A Study of Compressed Natural Gas Fuelling in a Downsized and Boosted, Multi-Cylinder, Direct Injection Spark-Ignition Engine

Tanmay Kar

ORCID: 0000-0002-2629-8058

Submitted in total fulfilment of the requirements of the degree of

Doctor of Philosophy

July 2020

Supervised by

Prof. Michael Brear

Asst. Prof. Joshua Lacey

Department of Mechanical Engineering

The University of Melbourne

Australia

Abstract

Improvement in the fuel economy of the internal combustion engine is imperative given the demand of increasingly strict fleet average carbon dioxide (CO_2) emissions limit. Compressed natural gas (CNG) has emerged as a promising automotive fuel to meet this demand due to its favorable fuel properties. However, today's CNG fuelled engines with port fuel injection technology have inferior peak performance compared to gasoline direct injection (GDI) engines, primarily due to lower volumetric efficiency. CNG direct injection technology has the potential to overcome these limitations.

Therefore, this study investigates the performance of a 4-cylinder, downsized and boosted, spark-ignited production engine when employing directly injected compressed natural gas (DI CNG) and gasoline direct injection (GDI). This work first examines the impact of various injection timing strategies with DI CNG operation and SOI timings in the range of 240 to 280 deg bTDC$_{Fire}$ are shown to be optimal for engine performance. A comparison of part-load performance with CNG and gasoline then shows similar fuel efficiency under stoichiometric conditions. DI CNG operation with fuel injection after IVC also achieves the same peak torque as GDI operation at low engine speeds with substantial fuel economy benefits.

The impact of charge dilution with both EGR and excess air is then examined with DI CNG and GDI operation. For equivalent dilution levels with CNG fuelling, air dilution demonstrates higher brake thermal efficiency (BTE) than that with stoichiometric EGR dilution. Both DI CNG and GDI exhibit similar engine performance at a given level of air dilution, although higher BTE is observed with GDI than that with DI CNG at a similar EGR rate.

Premixed turbulent combustion simulations are then performed for both fuels under stoichiometric, EGR, and lean conditions. The theory of Bradley is then used to establish a relationship between the modelled onset of flame quenching and increased COV_{IMEP} and UHC emissions for both fuels and both charge dilution strategies. This provides physical insight into the role of charge dilution on combustion and engine performance.

Finally, this work shows that a DI CNG engine utilizing stoichiometric, EGR, and lean-burn operation consistently demonstrates lower engine-out total CO_2 equivalent emissions than the baseline stoichiometric GDI engine over a range of operating conditions. Furthermore, several forms of advanced DI CNG engine operation are examined, including internal EGR, multi-pulsing, and the combined use of air and EGR dilution. The latter is shown to avoid high engine-out NO_x emissions at some operating conditions, and may potentially be superior to the sole use of air or EGR dilution.

Declaration

This is to certify that:

1. this thesis comprises only my original work towards the Doctor of Philosophy degree,
2. due acknowledgement has been made in the text to all other material used,
3. this thesis is fewer than 100,000 words in length, exclusive of tables, figures, bibliographies and appendices.

Tanmay Kar, July 2020

Acknowledgements

I would like to express my gratitude and sincere appreciation to the following people for their help and support throughout my study. This work would not have been successful without them.

- Michael Brear, Joshua Lacey, and Yi Yang

Thanks for their invaluable guidance, consistent encouragement, and suggestions during this research work. It was a great privilege and honor to study under their supervision.

- Zhenbiao Zhou

I want to extend my special thanks to Zhou for his contribution to developing our experimental setup and conducting experiments. It was such an incredible journey to work with him.

- Ulrich Kramer and his team (Ford Motor Company)

Thanks for sharing their expertise and financial support in this project.

- Al Knox, Michael Zammit and his team, and Daniel Jones

I wish to thank all of them for their useful technical support. Al Knox helped to build the safety system for CNG flow network. Michael Zammit and his team developed various components of the test bench, and Daniel helped a lot in fixing issues of the test engine.

- Monica Pater and Jan May

Thanks, Monica and Jan, for their help with administrative work and purchasing research equipment.

- Friends in the Thermodynamic lab and the University

I am grateful to all my friends for making my life at UoM enjoyable and memorable over these years.

- My parents and younger brother Molay

I want to express my heartfelt thanks to my parents and younger brother Molay for their love and support throughout my life.

- Reshmi (wife) and little Tanuva (daughter)

I am forever indebted to my wife for her care, most vital support, and encouragement throughout my Ph.D. study. Without her, I would not have completed this work. Little Tanuva, your presence in my life is the revitalizer during this arduous journey.

Contents

List of Figures

List of Tables

Nomenclature

List of Abbreviations

aTDC_{Fire}	After top dead center (firing)
BDC	Bottom dead center
BMEP	Brake mean effective pressure
BSFC	Brake specific fuel consumption
bTDC_{Fire}	Before top dead center (firing)
BTE	Brake thermal efficiency
CA	Crank angle
CH_4	Methane
CNG	Compressed natural gas
CO	Carbon monoxide
CO_2	Carbon dioxide
CO_{2e}	Total CO_2 equivalent emissions
COV_{IMEP}	Coefficient of variation of IMEP
CR	Compression ratio
DI	Direct injection
ECU	Electronic control unit
EGR	Exhaust gas recirculation

EGT	Exhaust gas temperature
EOI	End of injection
EVO	Exhaust valve opening
FEM	Full engine model
FSP	Fuel mass splitting percentage
GDI	Gasoline direct injection
GHG	Greenhouse gas
GWP	Global warming potential
i-EGR	Internal residual
ICEs	Internal combustion engines
IMEP	Indicated mean effective pressure
ITE	Indicated thermal efficiency
IVC	Intake valve closure
IVO	Intake valve opening
LHV_f	Lower heating value of fuel
MAP	Manifold air pressure
MAT	Manifold air temperature
MBT	Maximum brake torque
MFB	Mass fraction burned
MN	Methane number
NEDC	New European Driving Cycle
NGVs	Natural gas fuelled vehicles
PFI	Port fuel injection
PM	Particulate matter

PMEP	Pumping mean effective pressure
PP	Peak in-cylinder pressure
RGF	Total residual gas fraction
RON	Research octane number
RPM	Revolution per minute
SCM	Single cylinder model
SI	Spark-ignition
SOI	Start of injection
SOI2	Start of secondary injection
TDC	Top dead center
TWC	Three-way catalyst
UHC	Unburned hydrocarbon
VE	Volumetric efficiency
WLTP	World harmonized light-duty vehicles test procedure
WOT	Wide open throttle

Symbols

α	Thermal diffusivity
$\dot{m}_{air}$	Measured air flow rate
$\dot{m}_{fuel}$	Measured fuel flow rate
$\dot{m}_{total}$	Total flow rate combining fresh air and recirculated exhaust gas
η_e	Thermal efficiency
γ	Specific heat ratio
λ	Normalised air-fuel ratio
ϕ	Equivalence ratio

$\xi_{C,F}$	Carbon mass fraction of fuel
C_0	Convective heat transfer multiplier
C_{InPort}	Intake port heat transfer multiplier
l_T	Taylor micro-scale of turbulence
T	In-cylinder gas temperature
T_u	Unburned gas temperature
T_{Wall-F}	Wall temperatures calculated from full model run
T_{Wall-R}	Wall temperatures used in Reverse run
$\dot{H}_{Exh}$	Sensible enthalpy of exhaust gas
$\dot{H}_{UBF}$	Unburned fuel energy
$\dot{Q}_{Fr}$	Energy losses due to friction
$\dot{Q}_{In-Cyl}$	In-cylinder wall heat transfer
$\dot{Q}_L$	Total heat losses
$\dot{Q}_{misc}$	Heat transfer from external surface
$\dot{Q}_{Pump}$	Energy losses due to pumping
$\dot{q}_{Wall}$	Wall heat flux
$\dot{W}_b$	Brake work
λ'	Modified form of normalised air-fuel ratio
C_{DE}	Dilution multiplier
C_{FKG}	Flame kernel growth multiplier
C_{TFS}	Turbulent flame speed multiplier
C_{TLS}	Taylor length scale multiplier
h_w	Convective heat transfer coefficient
K	Karlovitz stretch factor

Le	Lewis number
P	In-cylinder pressure
P_{NRMSE}	Normalised root mean square error of pressure
S_L	Laminar flame speed
S_T	Turbulent burning velocity
T_{BDC}	Gas temperature at BDC
T_{Peak}	Peak in-cylinder temperature
u^t	Turbulent intensity
u^t_k	Effective turbulent intensity
V	Instantaneous cylinder volume
V_d	Displacement volume
AFR_{Stoic}	Stoichiometric air-fuel ratio

Chapter 1

Introduction

1.1 Transportation greenhouse gas emissions

The transportation sector is the fastest-growing contributor to global greenhouse gas (GHG) emissions and is currently responsible for 24% of direct carbon dioxide (CO_2) emissions from fuel combustion [1]. On-road vehicles such as motorcycles, cars, trucks, and buses account for nearly three-quarters of these emissions. To mitigate global climate change [2], legislation for fleet average CO_2 emissions worldwide has become more stringent in recent years, as shown in Fig. 1.1.

The carbon dioxide (CO_2) emissions from a vehicle can be viewed as [3],

$$\frac{dm_{CO_2}}{dx} = \underbrace{\left(\frac{\dot{n}_{CO_2}}{\dot{n}_{C,F}}\right)}_{=1} \underbrace{\left(\frac{M_{CO_2}}{M_C}\right)}_{=44/12} \underbrace{\left(\frac{\xi_{C,F}}{LHV_F}\right)}_{\text{a}} \underbrace{\left(\frac{1}{\eta_e}\right)}_{\text{b}} \underbrace{\left(m\left[gf_R + a\right] + \frac{\rho_{air}}{2} C_d A v^2\right)}_{\text{c}} \tag{1.1.1}$$

where the ratio of mole flow of CO_2 and carbon in the fuel, $\dot{n}_{CO_2}/\dot{n}_{C,F} = 1$ for complete combustion, M_{CO_2}/M_C is the ratio of mass of CO_2 molecule and carbon atom, $\xi_{C,F}$ is the carbon mass fraction of fuel, LHV_F is the lower heating value of fuel, and η_e is the thermal efficiency. As such, the term (a) depends only on fuel properties, (b) depends only on the powertrain efficiency, and (c) is only related to road loads. This fundamental expression has driven research to improve the fuel efficiency of conventional powertrains using engine technologies (e.g., turbocharging, dilute charge combustion) and low-carbon intensity fuels.

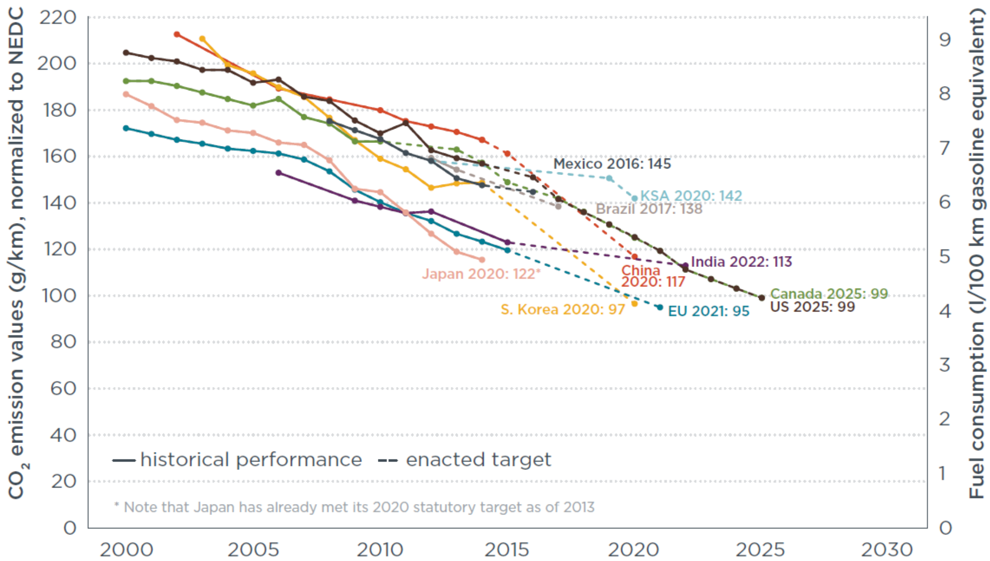

Figure 1.1: Historical fleet CO_2 emissions and current standards for passenger vehicles in major global markets [4, 5], where gCO_2/km is defined for the New European Driving Cycle (NEDC).

In the coming decades, while fully electric and fuel cell powertrains should displace conventional powertrains, internal combustion engines will remain in conventional and hybrid powertrains. At the same time, there should be greater use of alternative fuels, including those produced from renewable sources (e.g., electro-fuels and biofuels) [6].

1.2 Motivation for the research

Natural gas offers an approximate 23-24% tailpipe (tank to wheel) CO_2 emissions reduction compared to gasoline on an energy basis [7, 8]. Furthermore, compressed natural gas (CNG) can be blended with all types of renewably-sourced methane (i.e., bio-methane or power-to-gas methane) up to a blended rate of 100%, unlike ethanol-gasoline or biodiesel-diesel mixtures [9–12]. These factors, along with natural gas' high octane number [13, 14], enhance the carbon abatement potential of CNG compared to conventional fuels.

With more than 25 million natural gas fuelled vehicles (NGVs) and 32,577 refueling stations [15], the market for natural gas as an automotive fuel is global, though most NGVs are located in the Asia-Pacific region (Fig. 1.2). According to one source, by

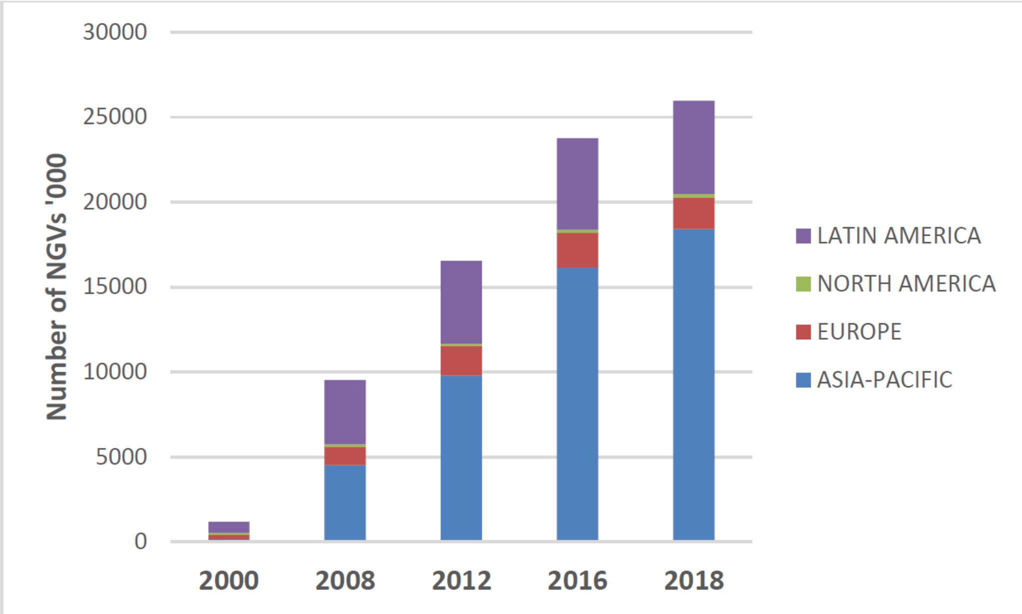

Figure 1.2: Global NGVs numbers by region, 2000 to 2018 [15].

2030 the number of NGVs is expected to rise to 15 million, with an additional 3,800 stations in Europe [16, 17].

However, CNG fuelled vehicles have traditionally inferior performance compared to liquid-fuelled vehicles because they have either port fuel injection (PFI) or throttle body injection. As an example, the performance comparison of the latest boosted European passenger cars (2014 year model) is shown in Fig. 1.3, where the average CNG PFI engine has reduced peak power and torque compared to an equivalent gasoline direct injection (GDI) engine [18]. This occurs because the port-injected natural gas displaces incoming air in the intake manifold, reducing the engine's volumetric efficiency and peak performance.

Direct injection (DI) of CNG into the combustion chamber can enhance cylinder charging compared to the PFI system. Furthermore, DI CNG allows improved scavenging and in-cylinder multiple injection capability as opposed to CNG PFI technology. Such opportunities are examined in this thesis using a combination of engine dynamometer experiments, theory, and simulation.

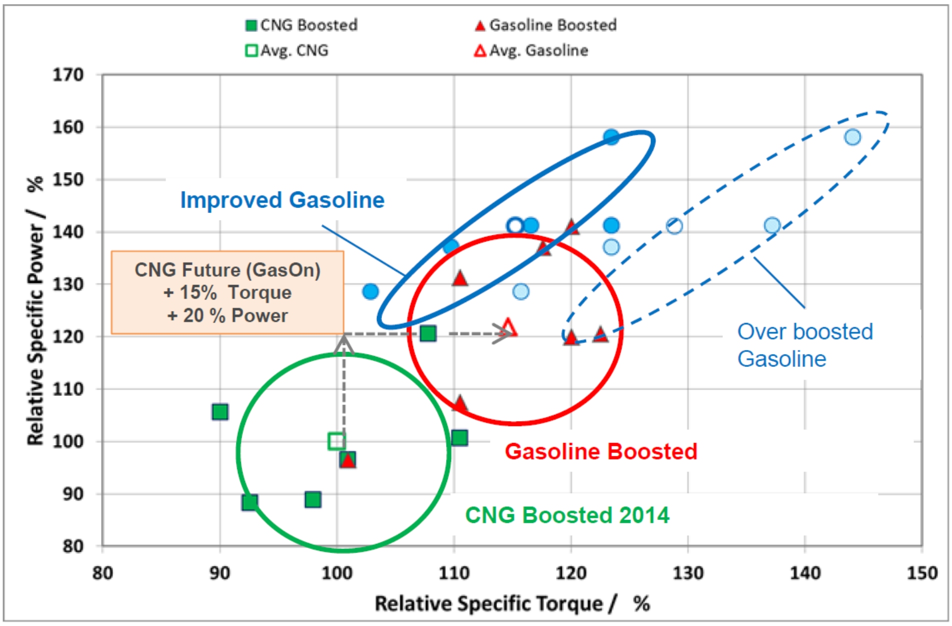

Figure 1.3: Performance comparison of boosted GDI and CNG PFI engine (Passenger car 2014 model) [12, 18].

1.3 Thesis layout

The layout of this thesis is now presented. Chapter 2 reviews the literature regarding CNG as an automotive fuel, focusing on its combustion and application in spark-ignited internal combustion engines. Chapter 3 describes the experimental engine setup and the methodology used. It also includes a description of the numerical methodology used to perform combustion and cycle analysis. Chapter 4 examines various direct injection timings' characteristics and their impact on engine performance with DI CNG fuelling. Chapter 5 evaluates the influence of exhaust gas recirculation (EGR) on stoichiometric DI CNG and GDI combustion and characterizes the resulting engine performance and emission trends. Chapter 6 presents a study of lean-burn and EGR dilute operation and probes the relationship between measured UHC emissions and the severity of turbulent flame quenching at dilute conditions. Chapter 7 explores further in-cylinder measures to reduce UHC emissions at dilute conditions. Finally, in Chapter 8, the important outcomes of this work are highlighted along with the recommendations for future studies.

Chapter 2

Literature Review

Internal combustion engines (ICEs) are one of the key drivers in the transportation sector and are generally categorized into two groups.

Spark-ignition (SI) engine: In traditional SI engines, a homogeneous mixture of air and fuel (e.g., gasoline) is compressed and then ignited by a spark plug's electrical discharge. This type of engine dominates the passenger car market due to its high power output. However, these engines have the drawback of lower thermal efficiency as a result of throttling and knock-limitation.

Compression ignition (CI) engine: In CI engines, fuel (e.g., diesel) is directly injected into the hot, compressed air of the combustion chamber and spontaneously ignited. Diesel engines are ubiquitous in the heavy-duty engine application owing to their higher thermal efficiency. However, these engines suffer from higher particulate and NO_x emissions, high noise level, and limited speed range compared to SI engines.

With recent trends of improving automotive fuel economy, researchers are focused on developing engines with fuel consumption like a diesel engine, while maintaining the specific power output of a spark-ignition engine in compliance with the stringent emissions legislations. This includes the introduction of high efficiency engine technologies (e.g., gasoline direct injection, homogeneous charge compression ignition, etc.), utilization of alternative fuels, loss reduction in powertrain, and improvements in vehicle aerodynamics.

2.1 Gasoline direct injection technology

Manufacturers have been adopting technologies that improve the efficiency of light-duty vehicles. Among all emerging technologies for SI engines, gasoline direct injection (GDI) technology has seen the highest level of adoption by manufacturers, reaching 51% for the 2018 model year [19].

In the GDI engine, gasoline is directly injected into the combustion chamber, and the air-fuel mixture is ignited by spark energy (Fig. 2.1). GDI concept has several advantages to overcome the basic limitations of traditional port fuel injection (PFI) gasoline engines such as an improved transient response, easy start-ability, and more precise air-fuel ratio control. GDI technology also offers in-cylinder

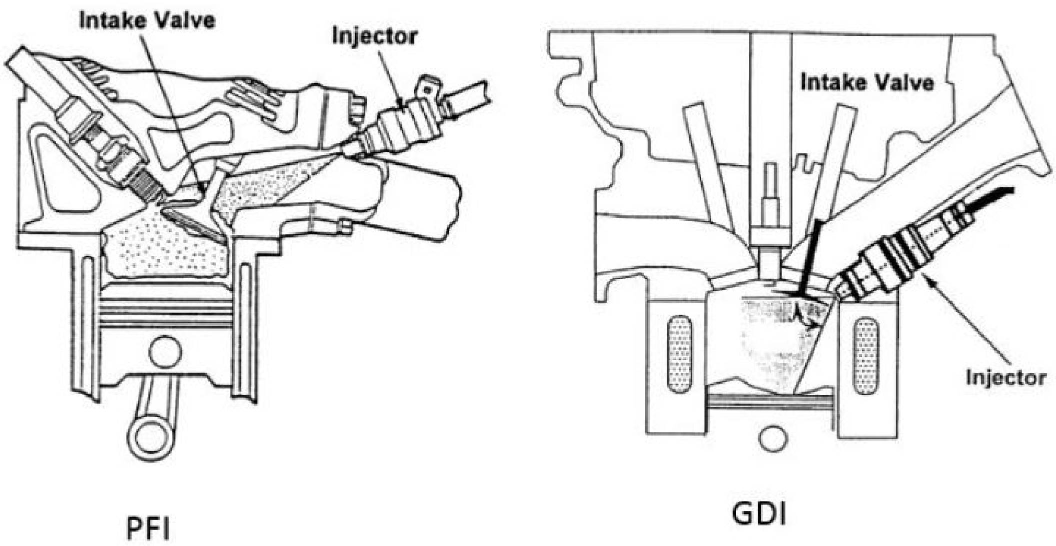

Figure 2.1: Traditional gasoline PFI vs. GDI technology [20].

charge cooling, which reduces the combustion temperature and allows a relatively high compression ratio operation, resulting in increased efficiency compared to the PFI engine. Furthermore, GDI operation reduces cold-start unburned hydrocarbon (UHC) emissions. Takigi et al. [21] has reported an approximate 30% lower cold start UHC emissions in the GDI engine compared to its PFI counterpart. However, the GDI engine emits higher UHC emissions at light load and high NO_x and particulate matter (PM) emissions at high load. Chad et al. [22] has demonstrated high NO_x, non-methane organic gas, and PM emissions for GDI operation compared to the gasoline PFI.

Exhaust emissions from automotive vehicles are growing as serious environmental and socio-economic concerns, signifying the implementation of stringent future emission legislation. Use of cleaner-burning alternative fuels as a replacement of conventional fuels is one of the key strategies to counter a range of issues such as health problems in polluted cities, climate change from increased greenhouse gas emissions, as well as political and social instabilities related to the conventional oil supply and price. In this context, natural gas has emerged as the most promising green transportation fuel among the other alternative candidates.

2.2 Natural gas

Natural gas is primarily composed of methane, but also contains the trace amounts of ethane, propane, butane, pentane, hexane, nitrogen, and carbon dioxide. The compositions of natural gas used in this study are shown in Table 2.1.

Table 2.1: Natural gas compositions [23]

Composition	**Volume (%)**
Methane (CH_4)	92
Ethane (C_2H_6)	4.3
Propane (C_3H_8)	0.4
Butane (C_4H_{10})	0.04
Pentane (C_5H_{12})	0.01
Hexane (C_6H_{14})	0.01
Nitrogen (N_2)	0.74
Carbon dioxide (CO_2)	2.5

2.2.1 Resource

Natural gas is one of the world's most abundant and widespread alternative fuels. The worldwide distribution of proven reserves for both natural gas and crude oil is shown in Fig 2.2. Natural gas is generally derived from conventional fossil sources. In addition, there are rapidly growing available resources of natural gas from shale deposits due to the advancement in hydraulic fracturing techniques. Scientific progression to produce methane from renewable resources (e.g. bio-activity, power-to-gas) is quite positive, and blending it to natural gas is very easy without

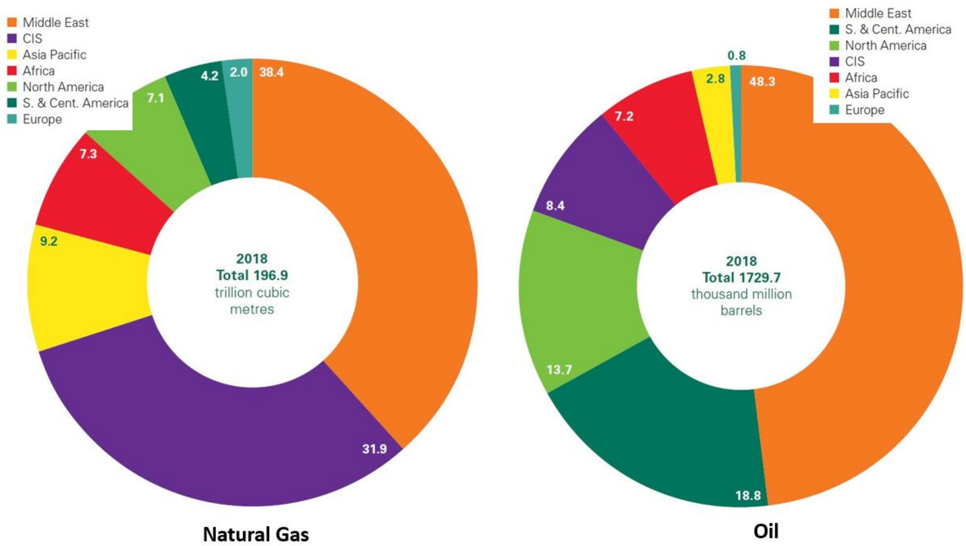

Figure 2.2: Distribution of proven natural gas and oil reserves in 2018 [24].

any blend limits such as those for ethanol in gasoline or bio-diesel in diesel [10, 11]. The existing supply of natural gas from traditional resources can therefore perform as an energy bridge to a renewable bio-methane future with continuous spectrum of blending being possible along the way.

2.2.2 Storage and safety

When used as a transportation fuel, natural gas is generally stored onboard either in liquid form as liquefied natural gas (LNG) at an extremely low temperature of -162°C or in compressed gaseous form as CNG at a pressure up to 200 bar. However, for the same energy content, CNG at 20.7 MPa has a volume disadvantage of 4:1 over gasoline and 5:1 over diesel, which poses a driving range limitation in transport applications [25]. Moreover, the requirement of a spacial storage tank for CNG with much thicker walls also contributes to a lower storage density compared to conventional fuels. With advancements in material technology such as fibre-reinforced aluminum alloy or even all composites, CNG pressure tanks can demonstrate an improvement in engine efficiency by weight savings of up to 57% over steel and an increased storage gas pressure capability, leading to higher vehicle range [26].

From the safety point of view, natural gas is safer than traditional fuels in many aspects. Unlike most conventional liquid fuels, CNG is non-toxic and non-caustic with no potential for groundwater contamination if leaked. Furthermore, an explosive mixture is unlikely to form in the event of a CNG leak due to its low density and high dispersal rates [27]. CNG is lighter than air and will dissipate upward rapidly if rupture occurs, while conventional liquid fuels will pool on the ground and increase the danger of fire [28].

2.3 Physio-chemical characteristics of CNG

Compressed natural gas (CNG) is regarded as one of the most promising alternative fuels due to its interesting physio-chemical properties, as shown in Table 2.2. CNG has a high H/C ratio and heating value compared to gasoline. These characteristics combinedly result in around 25% CO_2 reduction benefit with CNG due to fuel replacement only [18, 29]. Given its wider lean flammability limit, CNG fuelled engine can operate with higher normalized air-fuel ratio (λ) than that possible with gasoline [30].

Table 2.2: Properties of CNG and gasoline [13, 14, 23, 31]

Properties	**CNG**	**Gasoline**
H/C Ratio	3.96	2.026
Density (kg/m^3) at 16 °C and 1 atm	0.70	751
Autoignition Temperature (°C)	600	400
Research Octane Number (RON)	120	91.6
Stoichiometric Air-Fuel Ratio (mass)	16	14.1
Lower Heating Value (MJ/kg)	46	41.67
Combustion Energy (MJ/m^3)	24.6	42.7
Flammability Limits (V % in air)	5 - 15	1.4 - 7.6
Normalized fuel-air ratio limits (ϕ)	0.4 - 1.6	0.71 - 4
Laminar Flame Speed (cm/s)	41	50
Adiabatic Flame Temperature (°C)	1890	2150

2.3.1 Auto-ignition resistance

CNG has a very high research octane number that promotes the engine to operate at a higher compression ratio, particularly at mono-fuel mode (Fig. 2.3), resulting

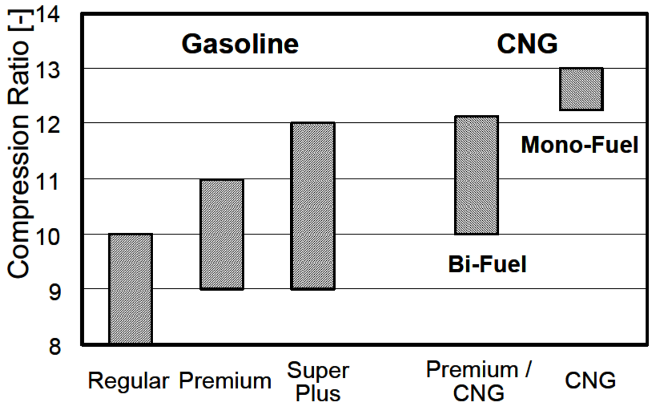

Figure 2.3: Compression ratio of gasoline and CNG fuelled powertrains [32].

in higher thermal efficiency [32, 33]. Furthermore, this allows optimal combustion phasing and negates the requirement of fuel enrichment at high load, resulting in additional improvement in fuel efficiency with CNG relative to gasoline fuelling [30, 34]. Higher octane rating also enables a higher downsizing potential, leading to improved fuel economy because of smaller engine architecture.

However, the conventional definition of octane rating is insufficient to describe the knock behavior of CNG, since the RON and MON scale end at approximately 120 before typical CNG starts to knock in a standard CFR engine [35] and no primary reference fuels (PRF) are available with RON and MON higher than 120.

Methane Number (MN) is introduced to describe the knock resistance of natural gas where H_2/CH_4 mixtures are used as PRF instead of iso-octane/n-heptane mixtures [35]. According to [36], a minimum MN of 70 is recommended for any methane-based fuel in the automotive application.

2.3.2 Volumetric efficiency

Volumetric efficiency (VE) is an important parameter used to measure the overall effectiveness of an engine's induction process and depends on the fuel type, engine design, and operating variables.

In a SI engine, the presence of gaseous fuel in the intake system displaces air, resulting in a lower amount of air in the intake (Fig. 2.4). For conventional fuels such as gasoline, the effect of fuel vapor is small due to liquid phase injection. Due to the low density of natural gas, a stoichiometric mixture of natural gas and air

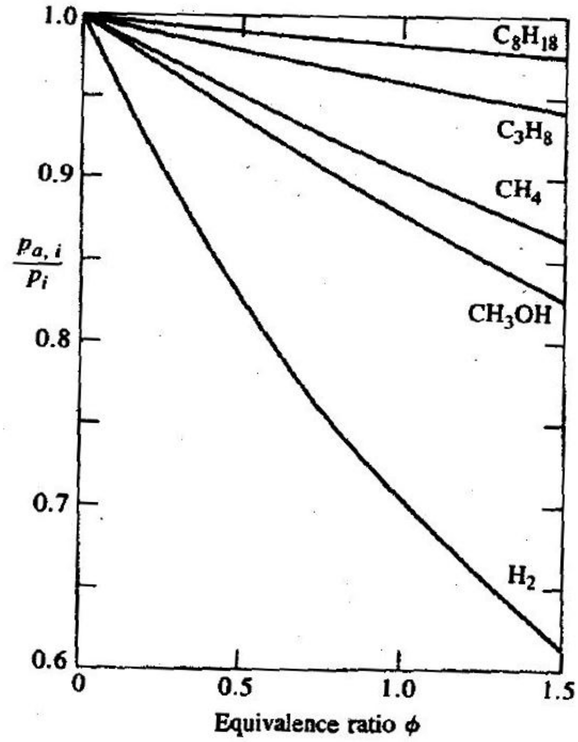

Figure 2.4: Effect of fuel vapour on inlet air partial pressure [37].

occupies about a 10% greater volume than a stoichiometric gasoline-air mixture with the same energy content [38].

Furthermore, the vaporization of liquid fuel decreases air temperature, resulting in increased volumetric efficiency as opposed to gaseous fuels. Experimental data shows that the decrease in air temperature due to liquid fuel evaporation has a more positive impact on volumetric efficiency compared to the detrimental effect of increasing the fuel vapor amount in the manifold [39].

2.3.3 Flame development, propagation and quenching

In the spark-ignition engine, flame generally begins as a laminar-like structure after the ignition. In the beginning, the small flame kernel is not exposed to the full spectrum of turbulence and is affected only by the higher frequencies [40, 41]. As the kernel grows with time, the flame is wrinkled by only the smallest scales of turbulence and larger length scales just convect the flame kernel bodily without affecting the flame front. With the continuous growing, the kernel becomes progressively wrinkled by the larger length scales until the size of the kernel is sufficient for it to experience the entire turbulence spectrum [42].

There have been several experimental studies of flame propagation in premixed charge SI engines to improve the understanding of certain global features of engine combustion [43–46]. Various spark-ignition zero-dimensional combustion models have also been developed and used for this purpose such as mean flame front model, flame sheet model, and entrainment and burn up flame model [45, 47–49].

Laminar flame speed (S_L) is an important property of a combustible mixture. This depends on the thermo-physical properties of the unburned mixture and is defined as the velocity at which unburned gases move into the flame front and transform to products under laminar flow conditions. Jones et al. [50] has demonstrated a lower S_L of natural gas compared to gasoline under engine-like conditions. This lower S_L necessitates a more advanced spark timing for natural gas in general [34, 51], with a more pronounced effect with the dilute operation [52–54]. However, Thurnheer et al. [55] has observed similar ignition timings for both gasoline and methane at part load under similar engine operating conditions. This is primarily due to less favourable thermodynamic conditions for chemical reactions with gasoline, resulting from lower intake pressure. It is reported that the 0-1% MFB duration is longer with natural gas operation than that with gasoline due to slower S_L, whereas the 1-90% MFB duration is comparable for both fuels due to the dominant turbulence effect at this stage [50, 51].

The impact of dilution on laminar flame speed is shown in Fig. 2.5 (a), where S_L decreases significantly with the increase of diluent such as burned gas, likely due to the reduction in mixture heating value. Furthermore, the presence of triatomic species such as CO_2, H_2O in the burned gas will have more heat sink effect due to their higher specific heat capacity (Fig. 2.5-b). It is also reported that for a similar dilution level, EGR has a much larger effect on S_L than the excess air due to its higher heat capacity [56].

Another important parameter is the turbulent burning velocity (S_T) at which mean flame contour propagates into the unburned mixture. This is calculated based on the following equation [37]:

$$\frac{u_b}{S_T} = \frac{\frac{\rho_u}{\rho_b}}{\left[\left(\frac{\rho_u}{\rho_b}\right) - 1\right] MFB + 1}, \tag{2.3.1}$$

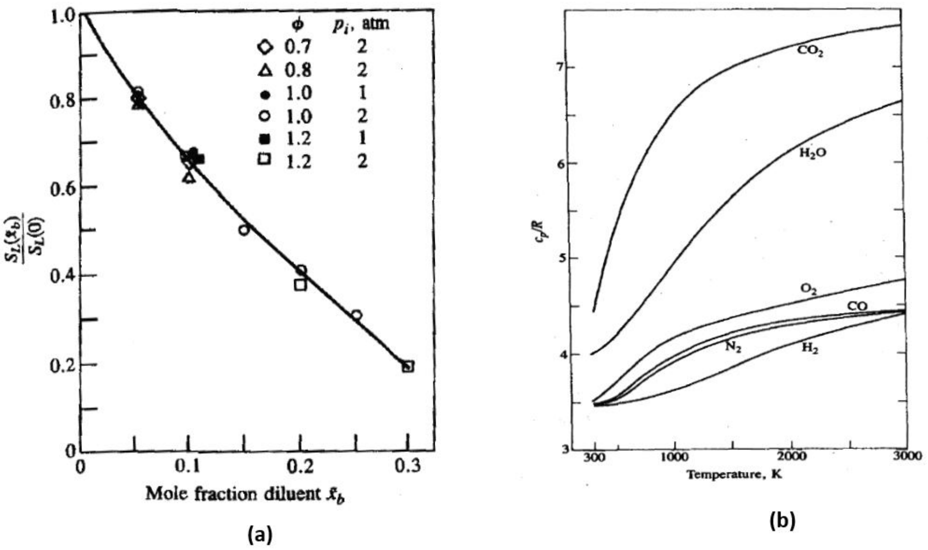

Figure 2.5: (a) Effect of burned gas mole fraction on the laminar burning velocity [56] and (b) specific heat capacity at constant pressure as a function of temperature for exhaust species [57].

where MFB is the mass fraction burned, ρ_u and ρ_b are the densities of unburned and burned gases, respectively. u_b is the mean expansion speed of the burned gas (or apparent burning velocity) and is defined as $u_b = S_T + u_g$, where u_g is the unburned gas speed just ahead of the flame front [37, 42].

Turbulence contributes to the wrinkling of the flame front and thus promotes its propagation [58–63]. The structure of the turbulent flame front has been characterized using several dimensionless parameters such as Damköhler and turbulent Reynolds numbers [37, 64]. The Damköhler number measures the relative importance of turbulence to fuel chemistry and is defined as the ratio of characteristics turnover time of an eddy to laminar burning time and is expressed as:

$$Da = \frac{\tau_{flow}}{\tau_{chemical}} = \left(\frac{l_0}{u^t}\right) / \left(\frac{\delta_L}{S_L}\right) = \left(\frac{l_0}{\delta_L}\right)\left(\frac{S_L}{u^t}\right), \tag{2.3.2}$$

where l_0 is the integral length scale which measures the size of the large energy containing structures in the flow, u^t is the turbulent intensity, S_L is the laminar flame speed, and δ_L is the laminar flame thickness. δ_L is estimated based on the following approximation given by Turns [65]:

$$\delta_L \simeq \frac{2\alpha}{S_L}, \tag{2.3.3}$$

where α is the thermal diffusivity. The turbulent Reynolds number, which characterizes the turbulent flow, is defined as:

$$Re_T = \frac{u^t l_0}{\nu}, \tag{2.3.4}$$

where ν is kinematic viscosity.

Using the non-dimensional Da and Re$_T$, Abraham et al. [64, 66] delineated the regimes of turbulent combustion, as shown in Fig. 2.6. This classification is based on the assumptions that the mass diffusivity is equal to kinematic viscosity, and the turbulence is homogeneous and isotropic. The combustion regimes are:

(A) The reaction sheets regime with wrinkled and convoluted flame fronts, which occurs when $l_k \gg \delta_L$, where l_k is the Kolmogorov length scale;

(B) The flamelets-in-eddies regime which occurs when $l_0 > \delta_L > l_K$;

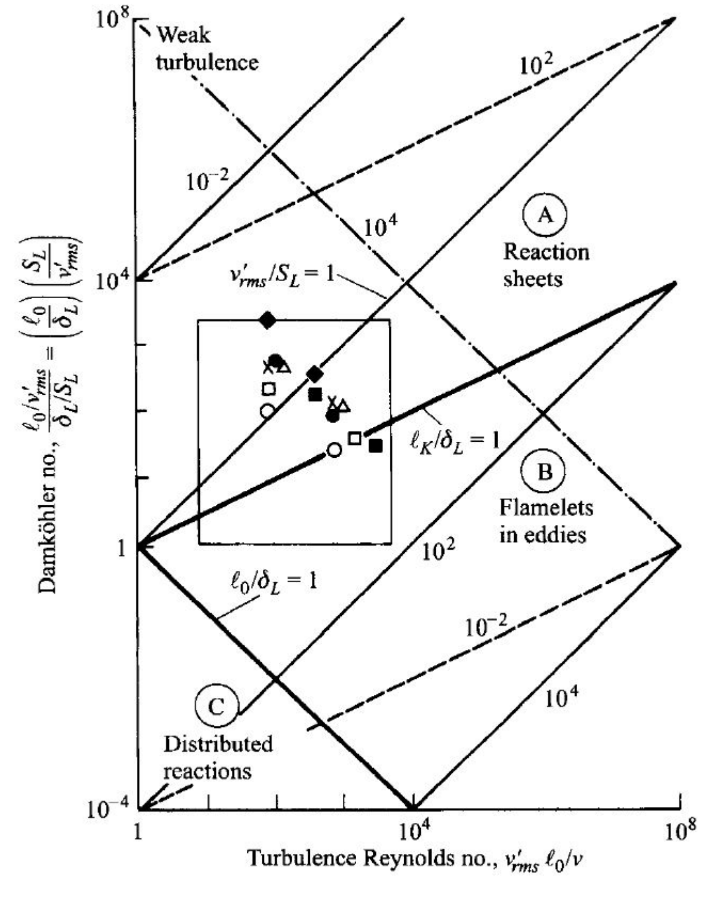

Figure 2.6: Premixed, turbulent combustion regime for a range of Da and Re$_T$ [64, 65].

(C) The distributed reactions regime without any flame sheet which occurs when $l_0 \ll \delta_L$.

Overall, this illustrates the importance of turbulence intensity, laminar flame speed, and gas properties on the flame structure and consequently establishes the combustion regime. The engine combustion regime is generally expected to be either in the wrinkled laminar flames or flamelets-in-eddies regime [43, 64]. This area is indicated by the box-shaped region in Fig. 2.6. Structural form of flame front under the influence of turbulence is also studied using the 'Borghi diagram' [67–69].

The effect of turbulence on the flame front varies at different stages of the combustion process, particularly for a transient flame such as that in an engine. Abdel-Gayed et al. [61] has introduced the concept of an effective turbulent intensity (u_k^t) embodied in the turbulent intensity (u^t) to quantify the degree of turbulence affecting the flame kernel growth. The correlations used to calculate u_k^t are as follows:

$$\left(u_k^t\right)^2 = \left(u^t\right)^2 \int_{\bar{F}_k}^{\infty} \bar{S}\left(\bar{F}\right) d\bar{F}, \tag{2.3.5}$$

$$\bar{S}\left(\bar{F}\right) = \frac{3.3}{1 + \left(2\pi\bar{F}\right)^{\frac{5}{3}} + \left(0.25\bar{F}\right)^4 + \left(0.08\bar{F}\right)^7}, \tag{2.3.6}$$

where dimensionless frequency $\bar{F}_k = t_k^{-1}\tau_a$ and infinite frequency is associated at the time zero, t_k is the elapsed time from flame initiation, and τ_a is the integral timescale which is calculated based on [70]:

$$\tau_a = \frac{l_0}{u^t}\left(\frac{\pi}{8}\right)^{0.5}. \tag{2.3.7}$$

While turbulence wrinkles the flame front, it is also subjected to a large traverse velocity and curvature due to the intense turbulence strain, which can result in flame stretch. To measure the magnitude of flame stretch, Karlovitz et al. [71] has introduced the concept of non-dimensional turbulent flame stretch K, which is known as the Karlovitz stretch factor and defined as:

$$K = \left(\frac{u^t}{l_T}\right) / \left(\frac{S_L}{\delta_L}\right), \tag{2.3.8}$$

where the numerator is the turbulent strain rate (in which l_T is the Taylor microscale of turbulence) and the denominator represents the chemical strain rate.

The flame stretch also affects the turbulent burning speed and the molecular diffusion processes. This can be accounted for using the Lewis number, which is defined as:

$$Le = \frac{\alpha}{D_{ij}} = \frac{k_t}{\rho c_p D_{ij}}, \tag{2.3.9}$$

where α is the thermal diffusivity, D_{ij} is the diffusion coefficient of the deficient reactant, k_t is the thermal conductivity, c_p is the specific heat capacity at constant pressure, and ρ is the density.

Bradley et al. [60, 62, 70] has studied the effect of turbulent strain on flame stretch and potential quenching by correlating the burning velocities with the product of the Karlovitz stretch factor (K) and the Lewis number (Le) using the 'Bradley diagram', as shown in Fig. 2.7. According to the 'Bradley diagram', a wrinkled laminar flame region exists at the low values of KLe. Flame sheets start to break up at the value of KLe $\sim$ 0.15 and continues up to the value of KLe $\sim$ 0.3. With a further increase

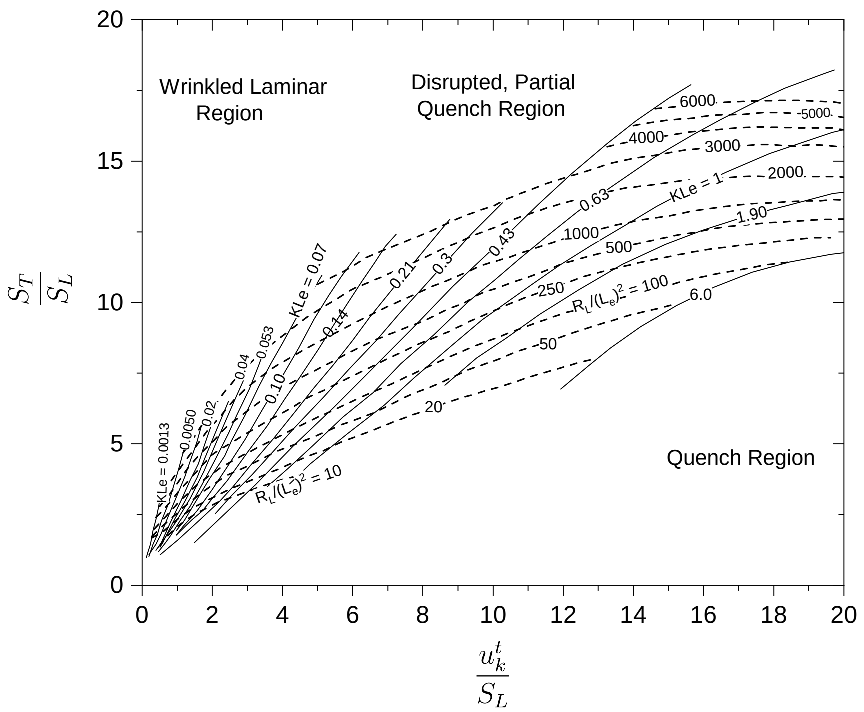

Figure 2.7: An example of the Bradley diagram [44, 60, 62].

of KLe, the flame becomes fragmented with the potential for partial quenching due to the higher flame stretch. Finally, a complete bulk flame quenching occurs at high values of KLe.

To link the flame quenching theory with engine operation, Merdjani et al. [44] has plotted the loci of gasoline combustion obtained from turbulent premixed simulation for different engine operating parameters in the Bradley diagram, as shown in Fig. 2.8. As shown, engine operation with higher engine speeds and lean mixtures shifts the combustion loci to a higher value of KLe and towards the partial quenching regime due to the increased u_k^t and lower S_L, respectively. Atibeh et al. [72] has also found that with the increase of λ (i.e. $\lambda = \frac{1}{\phi}$), the loci of lean-burn natural gas combustion move progressively deeper into the Bradley's quench region, particularly during initial stages of the flame propagation.

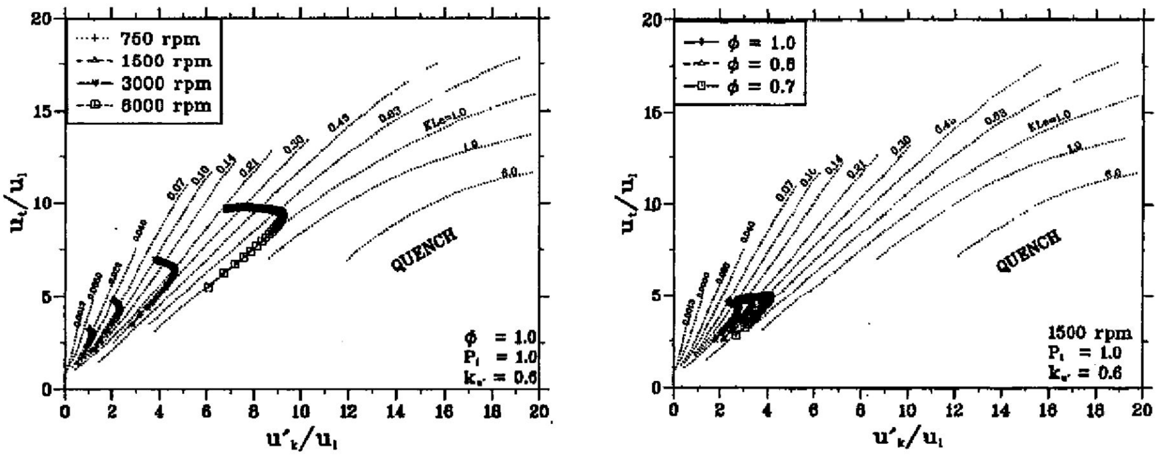

(a) Effect of engine speed (turbulence)

(b) Effect of mixture strength

Figure 2.8: Loci of gasoline combustion on Bradley diagrams for different engine operating conditions. Flame progression is anti-clockwise [44].

2.4 CNG engine technology

CNG has long been used in vehicles since 1930, but the application of CNG as a transport engine fuel has been considerably advanced over the last decade with the development of lightweight high-pressure storage cylinders [29]. There are many CNG engine technologies in use worldwide as shown in Fig 2.9, reflecting specific strategies for mixture preparation, combustion control, and emissions reduction.

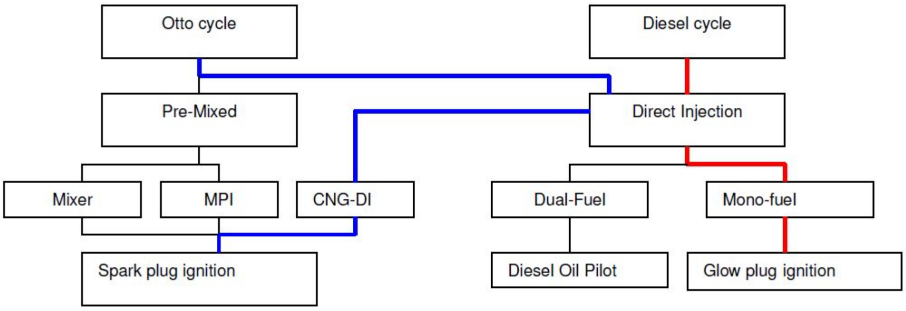

Figure 2.9: CNG Engine Technology [73].

2.4.1 CNG induction system for SI engine

The technologies mentioned above differ in the way of introducing CNG into the engine cylinder, and are evolved from basic venturi to efficient sequential injection and then to the modern direct injection system, as shown in Fig. 2.10. In general, CNG induction systems for SI engines are primarily categorized into two types: port fuel injection and direct injection.

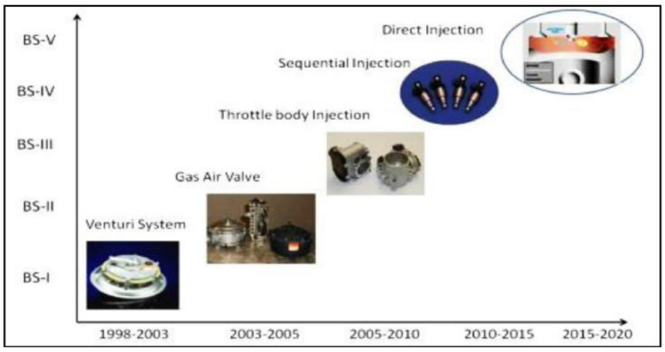

Figure 2.10: Evolution of CNG induction techniques [74].

Port fuel injection (PFI)

In this technology, CNG is injected into the intake manifold, and a premixed air-fuel mixture is ignited near the top dead center (TDC) by a spark plug. Today's CNG fuelled engines primarily use the PFI system, and the injectors available in the market for this application can achieve a maximum injection pressure of up to 8 bar. However, this technology suffers from a reduced volumetric efficiency due to the displacement of the incoming air by CNG [18]. Furthermore, this injection technology has limitations such as less scavenging capabilities and the inability of multiple injections per cycle.

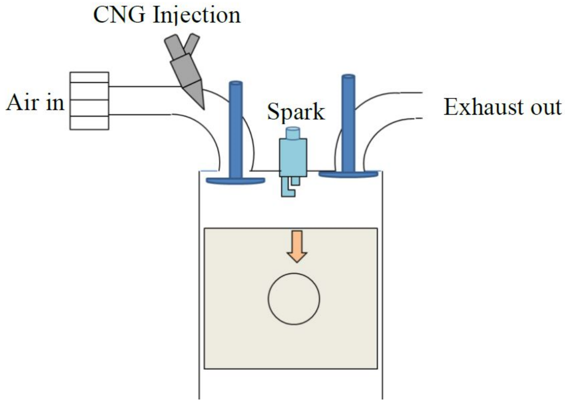

Figure 2.11: Port fuel injection (PFI) technology.

Direct injection (DI)

In this method, CNG is injected directly into the combustion chamber at high pressure. The air-fuel mixture is then compressed and ignited by the spark plug before TDC_{Fire}. The use of DI CNG technology allows the restoration of low-end torque by improving the volumetric efficiency and utilizing scavenging application as opposed to CNG PFI mode. This gives an equivalent engine performance on par with modern GDI engines through enhanced downsizing [75].

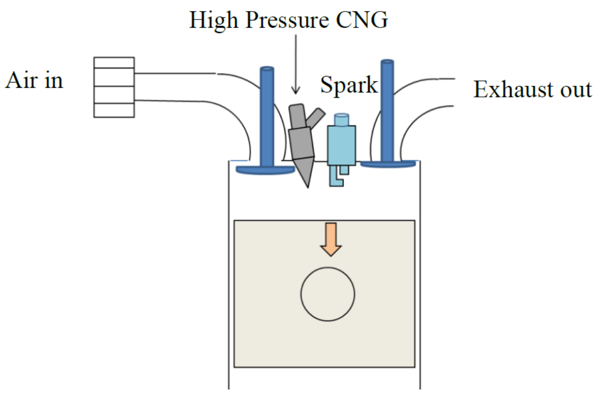

Figure 2.12: Direct injection (DI) technology.

An example of the impact of CNG direct injection strategy on the volumetric efficiency is shown in Fig. 2.13, where volumetric efficiency is lower with a fuel injection during the intake stroke but increases with a fuel injection after the intake valve closure. Furthermore, this approach allows an easy conversion of GDI engines to DI CNG types by a simple swapping of a GDI injector with a same form factor DI CNG injector either in central or side mount location, as shown in Fig. 2.14. The critical component of this technology is the DI CNG injector. It requires

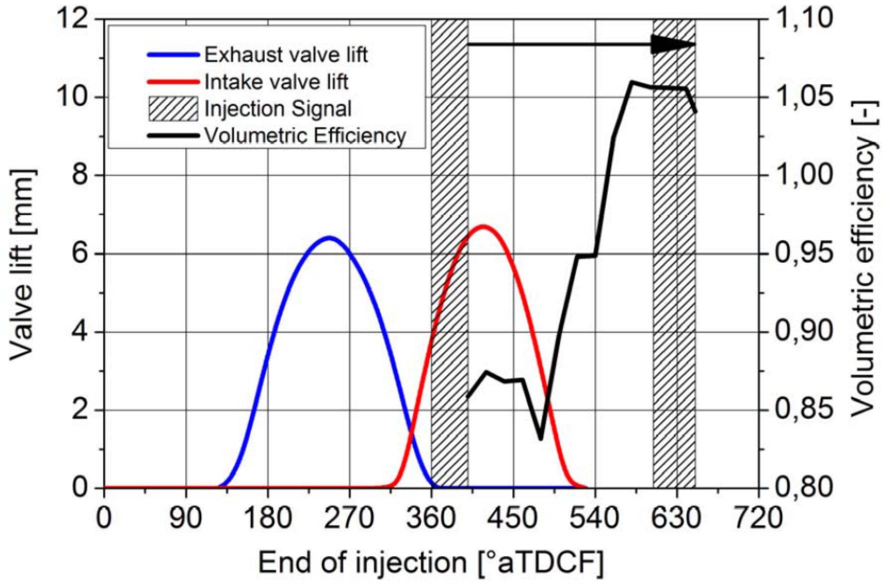

Figure 2.13: Impact of CNG direct injection strategy on the volumetric efficiency at WOT [76].

to deliver a high flow rate with low leakage, as well as to maintain an extended durability in the absence of self-lubricating properties of CNG, unlike conventional liquid fuels. The injectors available for delivering CNG in SI engine application are PFI type with a limited peak injection pressure capability, which can increase the vehicle range but lacks the high flow rate. The majority of previous research works on DI CNG have used high-pressure injectors such as a modified version of GDI injector, or a spark plug fuel injector (SPFI) with injection pressure in the range of 50-100 bar [77–79]. However, these high-pressure injectors are unrealistic in practical scenarios due to lower vehicle range and injector tip leakage issues [80]. Fig. 2.15 demonstrates the impact of injection pressure on vehicle range, where a 6.6% loss in vehicle range is observed if the injection pressure increases to 30 bar from a baseline value of 16 bar. On the other hand, the choice of 8 bar operating

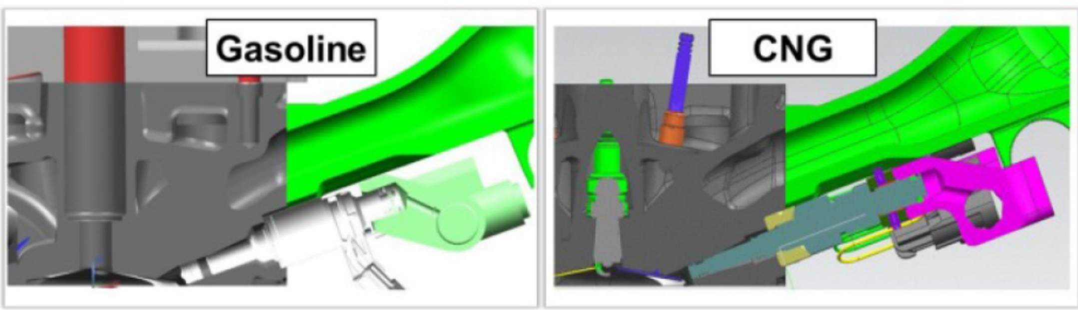

Figure 2.14: Side mounted injector position layout: GDI vs. DI CNG [81].

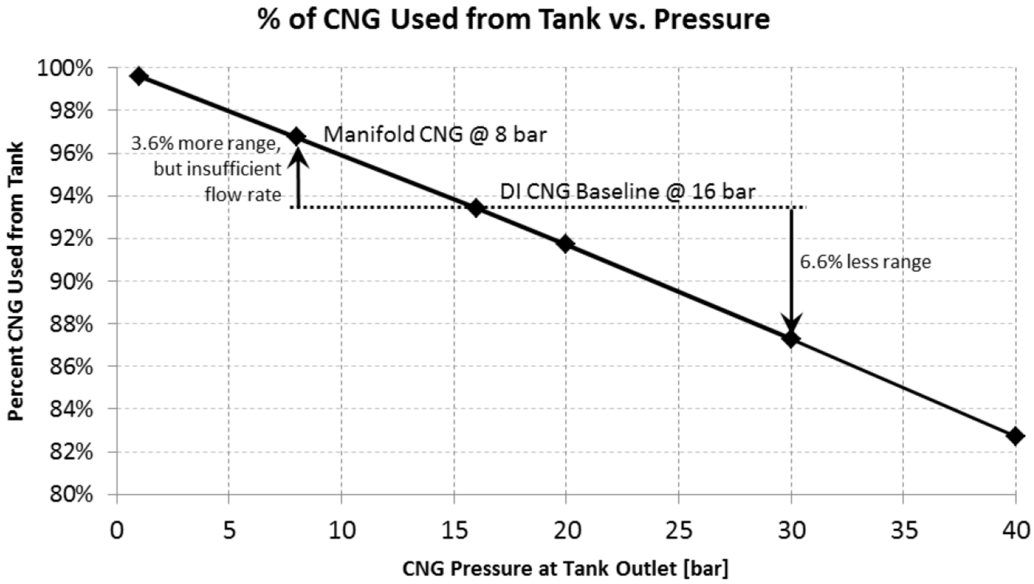

Figure 2.15: Percent of CNG used from tank vs. injection pressure [75].

pressure (i.e., similar to PFI injector operation) improves the vehicle range by 3.6%, but suffers from an insufficient flow rate [75]. A low-pressure DI system is generally suitable for low compression ratio SI engine [80, 82]. Dedicated DI CNG injectors for SI engine applications have been developed at the prototype level considering these design parameters by automotive industries such as Delphi, Continental, Westport Innovation, and Orbital. In this work, one such injector type from Continental is used, and details are provided in Table 3.2.

2.4.2 Vehicle application

Based on the CNG induction technologies discussed in Section 2.4, vehicles equipped with CNG fuelled SI engines can be categorized into following types:

Bi-fuel

In this type, a conventional SI engine adopts two separate fueling systems based on the PFI technology, enabling the engine to run on either CNG or gasoline. The bi-fuel conversion may utilize the original engine management system with the addition of gas flow controlling features and revised ignition timing, or can use a standard CNG kits. However, the conversion of a traditional SI engine to bi-fuel type prevents the engine from fully utilizing CNG's favourable characteristics.

Monovalent

In this category, CNG is used as an only fuel to run the vehicles. These engines are either derived from traditional SI engines or designed for the purpose. For CI engine to CNG SI conversion, modification in the piston to reduce the original compression ratio and the addition of an high-energy ignition system are necessary.

Light-duty vehicles are typically bi-fuel or monovalent SI types, while small commercial vehicles, heavy-duty automotive (i.e., buses, trucks) can be found with monovalent CNG application [83].

2.5 Operation of CNG fuelled SI engine

An overview of the operational limit of CNG fuelled engines under different conditions is shown in Fig. 2.16. The engine stability limits the external dilution level (i.e., excess air or EGR) at low to medium loads due to the presence of high amounts of residual gases from the previous combustion cycle. An insufficient boost pressure due to the lower exhaust energy limits the maximum dilution level at high loads, whereas autoignition limits the high load when the dilution decreases [84]. There is an ongoing emphasis on improving the CNG fuelled engine performance using traditional methods of integrating the state-of-the-art technologies and the development of efficient combustion concepts using dilution.

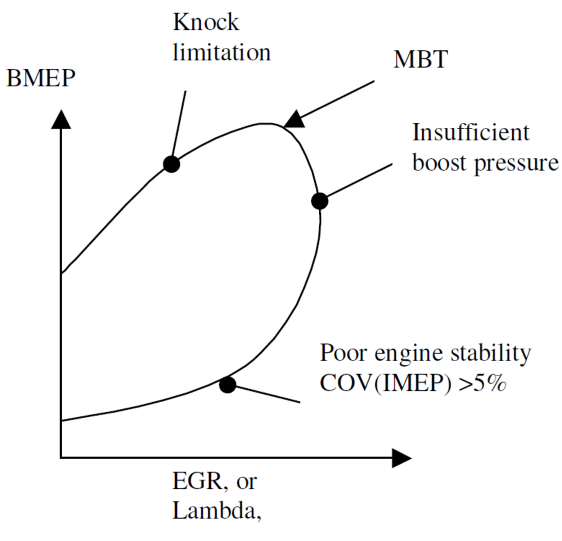

Figure 2.16: Limits of engine operating range under different conditions [84].

2.5.1 Modes of engine operation

Mixture composition during combustion is the most critical as it determines the development of combustion processes. Therefore, engine operation can be categorized into two modes: one with a stoichiometric mixture and another with charge dilution (either with excess air or with recirculated exhaust gas).

Stoichiometric operation

In stoichiometric operation, the air-fuel mixture is maintained at $\lambda = 1$ to achieve higher power output and stable combustion. Furthermore, a three-way catalyst (TWC) converter is used to control the emissions within the legislation limit. However, this approach suffers from a lower thermal efficiency due to higher in-cylinder wall heat losses and higher pumping work at low to medium loads. Moreover, an excessive thermal loading and auto-ignition tendency at high load may also reduce the engine durability [85].

Diluted operation

In this mode, the engine is generally operated either with excess air (i.e., $\lambda > 1$) or with exhaust gas recirculation (EGR) at $\lambda = 1$. Engine operation with charge dilution generally improves the part load fuel conversion efficiency primarily due to the following reasons [86, 87]:

(1) increase of expansion stroke work for a given expansion ratio, as the burned gases expand through a larger temperature ratio due to the change in mixture's specific heat ratio. Note that the ratio of specific heats (i.e., $\gamma = \frac{c_p}{c_v}$) primarily depends on the mixture property and temperature. In general, γ increases with the increase of λ (i.e., decrease in equivalence ratio, ϕ) for most of the fuels and also increases when the temperature decreases (Fig. 2.17-a).

(2) decrease of pumping work as the intake pressure increases with the higher charge dilution for a given mean effective pressure.

(3) reduction of the in-cylinder wall heat transfer due to the lower burned gas temperature.

However, lean-burn operation with excess air beyond a specific limit drops combustion temperatures considerably. This results in an extended burn duration due to the slower flame speed, which decreases the thermal efficiency. Ayala et al. [88] has demonstrated the individual contribution of various characteristics of lean-burn operation on the fuel efficiency as a function of λ. As shown in Fig. 2.17 (b), the specific heat ratio (γ), pumping work, and in-cylinder heat transfer have positive contributions on efficiency, though these are negated by the impact of longer burn duration beyond a certain λ threshold.

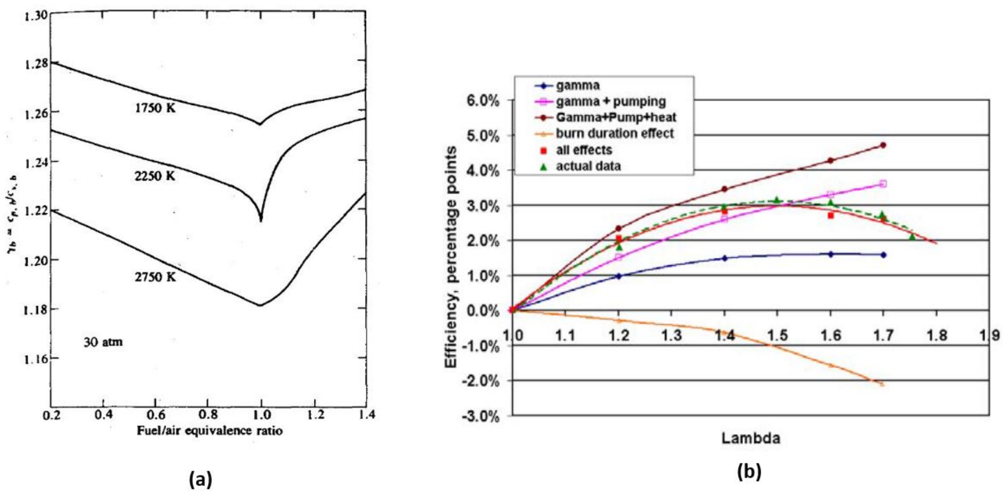

Figure 2.17: (a) Ratio of specific heats for burned gases as a function of equivalence ratio, ϕ [37] and (b) Effect of normalized air-fuel ratio, λ on efficiency [88].

Natural gas engines can operate with higher excess air than that possible with gasoline due to its substantially higher lean flammability limit [30]. An example of limiting combustion regimes for lean engine operation with methane is shown in Fig. 2.18. As the mixture is leaned out, normal combustion changes to partial burning and then further progresses towards the ignition limit in some cycles. This indicates that the lean limit of CNG operation can be extended to as close as $\phi = 0.625$ (i.e., $\lambda = 1.6$).

Exhaust gas recirculation (EGR) is another way to dilute the fresh mixture and can be classified as two types [90]:

- Hot EGR: here, exhaust gases are recirculated directly to the intake system. The engine using hot EGR uses exhaust gases to heat the intake mixture, which promotes combustion and thus improves the thermal efficiency.

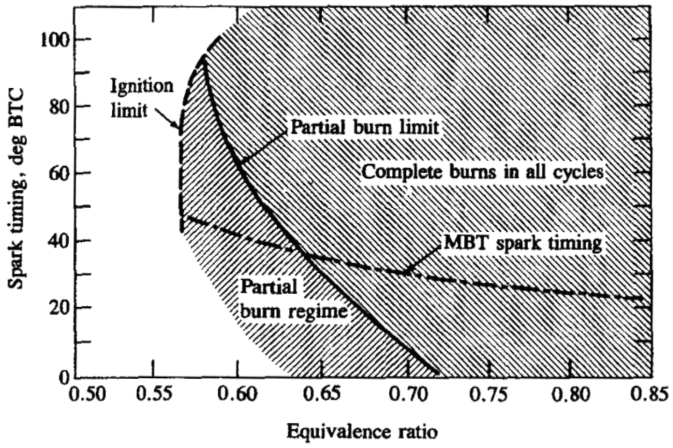

Figure 2.18: Limiting combustion regimes for lean operation with methane [89].

- Cooled EGR: here, recirculated exhaust gases are cooled before mixing with the intake air. Cooled EGR increases the volumetric efficiency of the engine. In addition, the lower mixture temperature further reduces NO_X emissions, but UHC emissions and cycle-to-cycle variations are increased compared to that with hot EGR.

In general, EGR can improve the fuel economy, reduce NO_X emissions, and inhibit the auto-ignition tendency [91, 92]. Besides, it also allows stoichiometric air-fuel operation in combination with the utilization of three-way catalyst. Cooled EGR dilution is a crucial technology in downsized SI engines to improve power output and reduce NO_X emissions [93, 94]. However, a high level of EGR reduces the combustion speed due to a reduction in available oxygen concentration, resulting in increased burn duration. This causes high cyclic variation, incomplete combustion, and finally misfire [95]. The impact of increasing EGR rate on the combustion process is shown in Fig. 2.19, where EGR rate $> 20\%$ increases the frequency of partial burn and misfire cycles. This limits the level of EGR dilution, with 15-

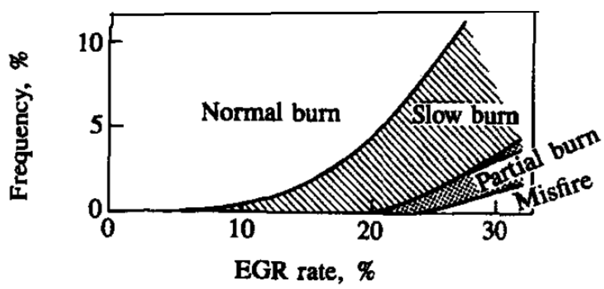

Figure 2.19: EGR limit for combustion with different frequency of normal, slow, partial-burn, and misfire cycles [96].

30% EGR rate being the maximum limit in a SI engine under normal part-throttle conditions [37, 96].

An example of mixture composition requirements for different operating modes over a range of engine speed and load is presented in Fig. 2.20. Top diagram shows that the mixture can be leaned out with the increase of mass flow rate at low loads. However, an air-fuel ratio close to stoichiometry is required when engine operation approaches WOT to achieve the maximum BMEP. The bottom diagram demonstrates a stoichiometric operation with EGR dilution, where the EGR rate varies from zero at light load to a maximum at medium load and then decreases at WOT to facilitate maximum BMEP.

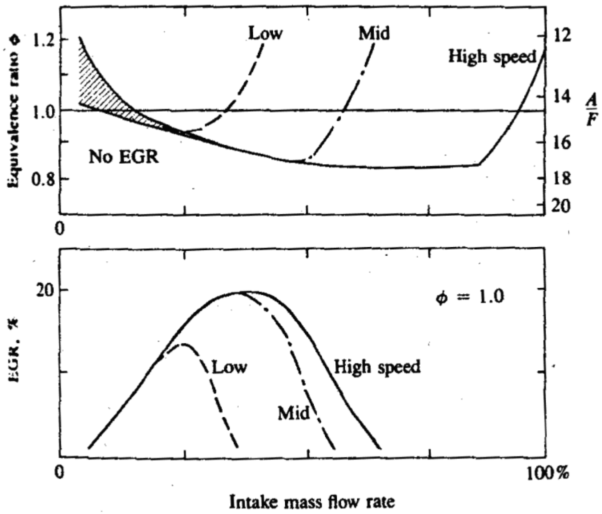

Figure 2.20: Mixture requirement for operating strategies at low, mid, and high engine speeds: variation of ϕ with the intake mass flow rate (top) and EGR rate for stoichiometric operation as a function of intake flow rate (bottom) [37].

2.5.2 Engine performance

Over the years, various studies have been performed in SI engines with CNG fuelling. Operation of a naturally aspirated, gasoline PFI engine on CNG typically results in power and torque losses over 10% at stoichiometric air-fuel ratio and WOT condition [73, 97–104]. This is primarily due to the reduction in volumetric efficiency (around 10% due to displacement of air by CNG in the intake manifold and 3% due to the absence of charge cooling [102]) and low burning velocity of CNG [38, 103]. However, brake specific fuel consumptions are lower with CNG relative to gasoline operation due to its higher calorific value. These peak performance losses can be recovered in part by increasing the compression ratio, turbocharging, and lean burn concept, as shown in Fig. 2.21.

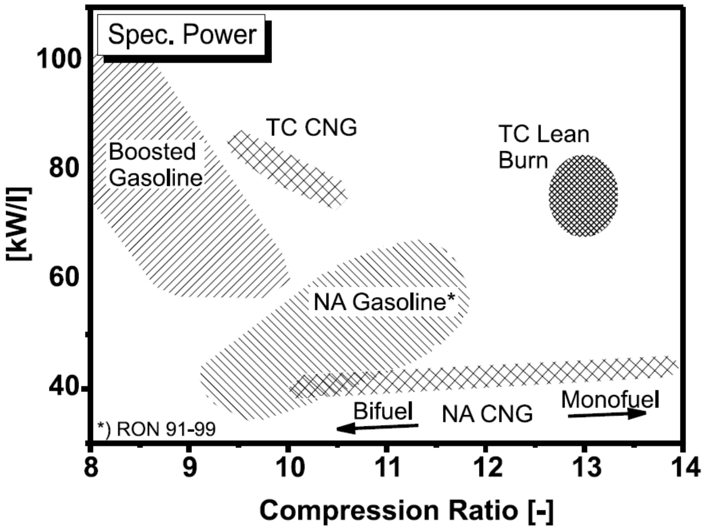

Figure 2.21: Specific engine power and compression Ratio [30].

In a recent study [18], a comparison between modern GDI and CNG PFI engine shows that a CNG PFI engine in a 2014 boosted European passenger car has an approximately 15% less peak torque and 20% less peak power compared to an equivalent GDI engine in the same vehicle. These performance losses are primarily at lower engine speeds below 2000 RPM when boosting is not sufficient to compensate the displaced air by port fuel injection, as shown in Fig. 2.22 (a). Despite this, thermal efficiency is higher with CNG compared to gasoline operation (Fig. 2.22-b) due to knock-limited combustion phasing and fuel enrichment for gasoline at high loads [105, 106].

Development of direct injection (DI) system for CNG fuelling has made a progressive breakthrough in recent years, and a lot of research works have been done to assess the performance of the DI CNG technology at stoichiometric air-fuel ratio conditions [76, 77, 81, 91, 107–114]. Studies about the effect of direct fuel injection timing on engine torque (Fig. 2.23: a and b) have demonstrated that the start of injection (SOI) after the intake valve closure (IVC) improves torque characteristics by increasing the volumetric efficiency at low engine speeds. Nonetheless, CNG needs to be injected before IVC at high engine speeds due to the requirement of longer fuel injection

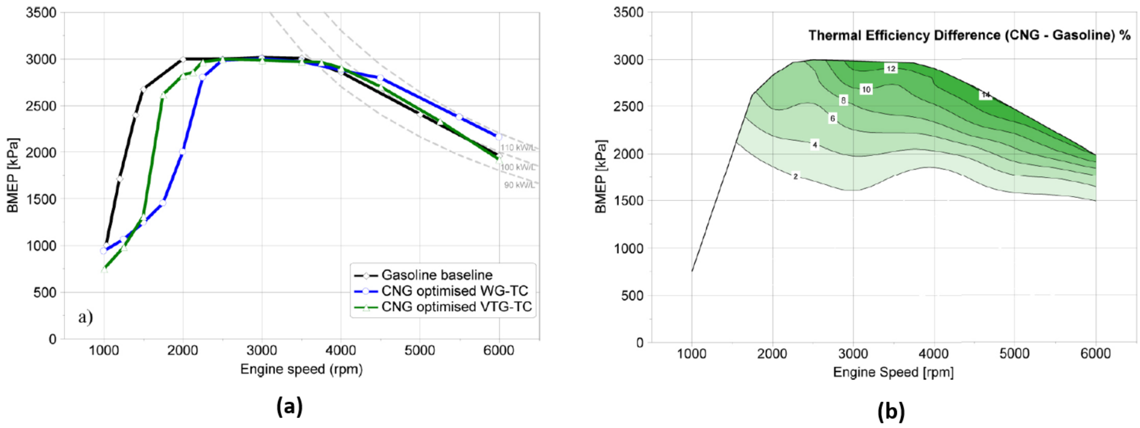

Figure 2.22: Comparison of (a) peak torque and (b) thermal efficiency between the boosted CNG PFI and GDI engine [105].

duration [75, 115]. Sevik et al. [111] has demonstrated that delaying the SOI for DI CNG systems helps to increase the load to a level higher than what is possible with the gasoline PFI operation at WOT conditions. Song et al. [113] has studied the effect of fuel injection pressure on the DI CNG combustion and found that the injection pressure variation has a minimum influence on combustion trends. Zeng

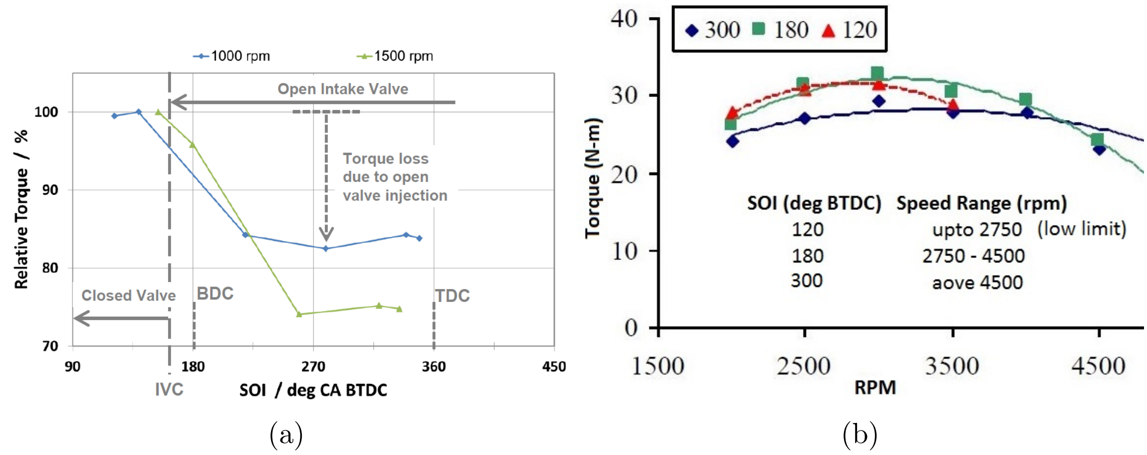

Figure 2.23: Effect of the start of injection timing (SOI) on engine torque: (a) Husted et al. [75] and (b) Rashid et al. [115].

et al. [77] has investigated the effect of various fuel injection timings on DI CNG combustion characteristics and found that the over retarded injection (i.e., closer to TDC_{Fire}) results in slower combustion due to inhomogeneous mixture by the insufficient fuel-air mixing time, whereas a fuel injection timing between the retarded and early injection (i.e., closer to $TDC_{Gas-exchange}$) demonstrates the maximum rate of heat release (Fig. 2.24). A comparison of combustion characteristics shown in Fig. 2.25 demonstrates that the DI CNG operation has a shorter 0-10% MFB duration

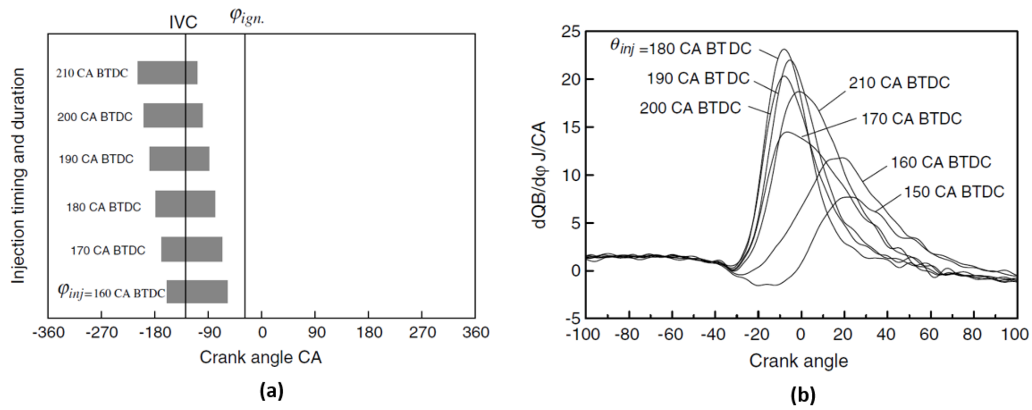

Figure 2.24: (a) Injection timings and duration and (b) Heat release rate versus fuel injection timings [77].

than that of CNG PFI and GDI operation. However, the 10-90% MFB duration with DI CNG is longer than that of GDI but shorter than CNG PFI operation. Recent works [18, 75] have shown that a DI CNG engine can match the peak performance of a GDI engine at low speeds using a combination of strategies such as late direct injection, enforced scavenging, and retarded ignition (Fig. 2.26). [75, 81]. Finally, the most recent work under EU Horizon 2020 framework has demonstrated that a DI CNG engine with the state-of-art technologies outperforms the modern GDI engine both in terms of peak power and torque [116].

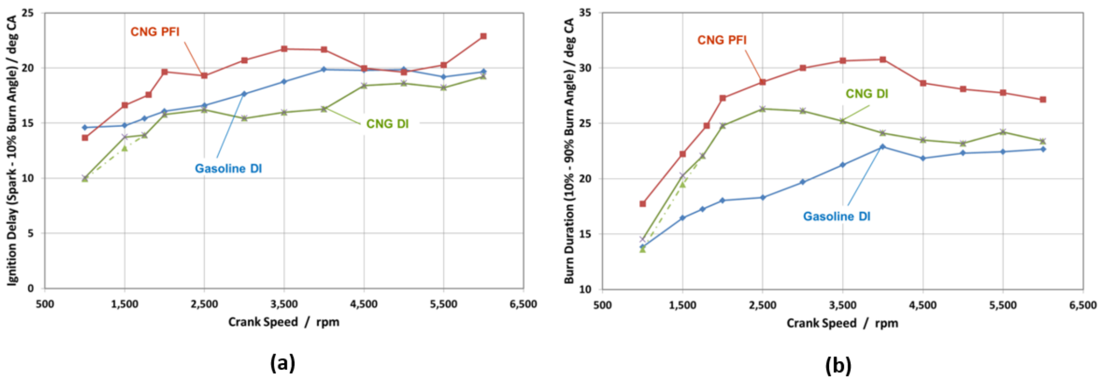

Figure 2.25: Comparison of (a) ignition delay and (b) burn duration for CNG PFI, DI CNG, and GDI operation [75].

Effect of charge dilution

Over the years, the effect of charge dilution (both with EGR and excess air) on the engine performance has also been studied for CNG fuelled operation. Loric et al. [91] has examined the performance of a DI CNG engine with EGR dilution

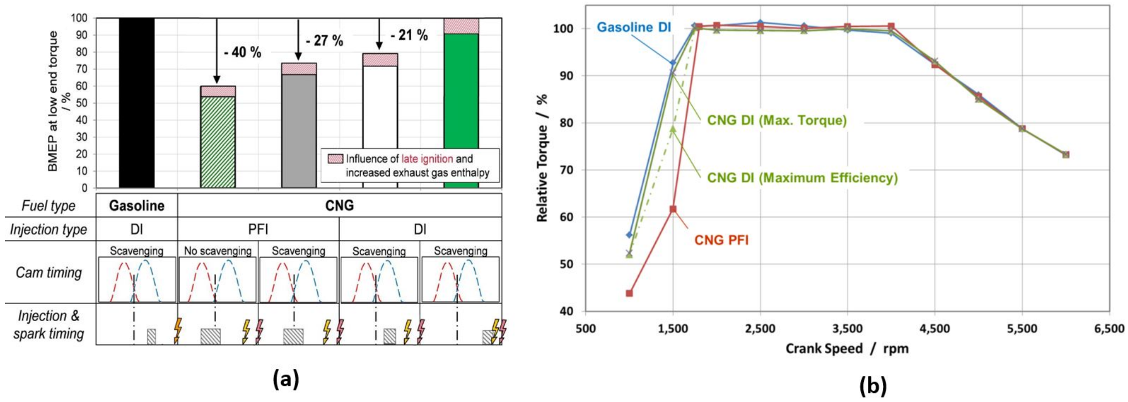

Figure 2.26: (a) Engine operating strategy for low end torue and (b) Relative engine torque: CNG DI, CNG PFI, and GDI operation [18, 75].

at part load (Fig. 2.27), where an improvement in fuel consumption with optimal EGR dilution is observed primarily due to the lower in-cylinder heat transfer and reduced pumping losses. However, an excessive cyclic variation with the high EGR rate usually prevents a substantial fuel economy improvements in practice. Figure 2.28 shows that the CNG fuelled engine operation with EGR significantly decreases the exhaust gas temperature at high engine speeds and full load conditions while maintaining the acceptable combustion variability limit[85].

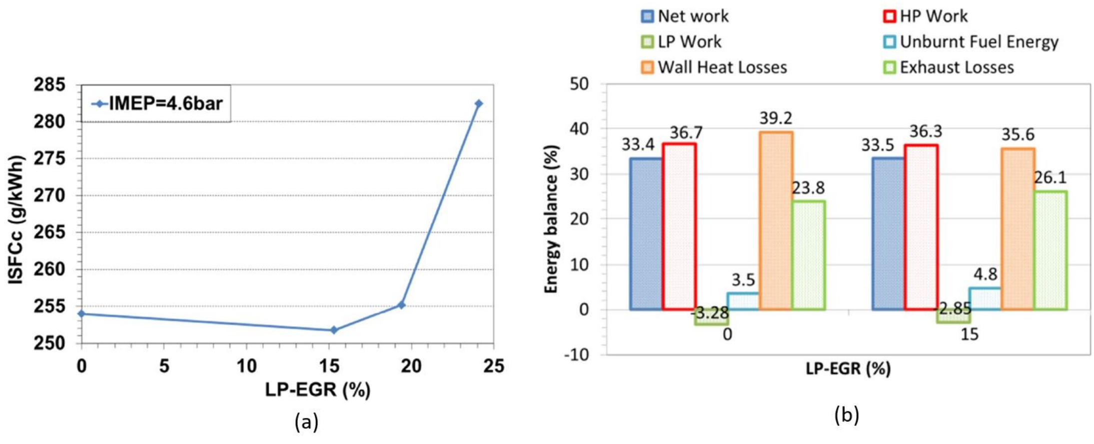

Figure 2.27: (a) Indicated specific fuel consumption (ISFC) as a function of EGR rate and (b) Energy balance without and with EGR for DI CNG operation at 2000 RPM and 4.6 bar IMEP [91].

EGR application also needs the consideration of fuel properties, as burning velocities in the presence of a diluent can differ significantly depending on the fuel type. This is particularly the case during the initial flame kernel development stage [117, 118]. Neame et al. [119] has studied the tolerance limit of EGR with three different fuel

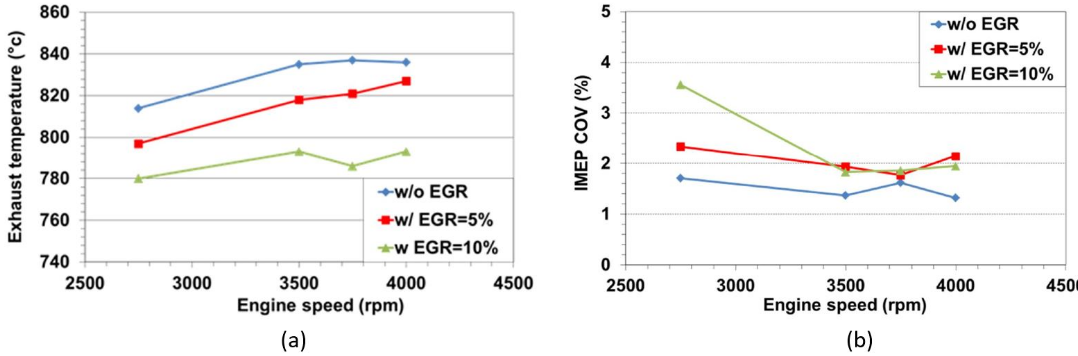

Figure 2.28: (a) Exhaust gas temperature and (b) COV_{IMEP} as a function of speed at full load with various EGR rate for DI CNG operation [91].

types and demonstrated that EGR tolerance of methanol is better than that with gasoline and natural gas.

Lean-burn natural gas engines offer the potential of higher thermal efficiency than conventional stoichiometric SI engines [25, 84, 85, 120]. Engine operation with CNG can be ultra-lean. This allows a higher compression ratio and boost pressure without autoignition due to the lower in-cylinder temperature, leading to higher fuel economy and power output [121, 122]. A turbocharged lean-burn concept is introduced to extend the CNG fuelled operation range to a higher compression ratio and more excess air using improved charge motion shown in Fig. 2.29. This enables the use of lean-burn over the whole engine operating range, resulting in fuel economy benefits with CNG fuelling compared to naturally aspirated gasoline operation with PFI strategy (Fig. 2.30). However, flame quenching, partial burn, and combustion instabilities could be expected for extremely lean mixtures, particularly $\lambda > 1.6$ [95, 120]. Lean combustion with a pre-chamber ignition system is also introduced to improve the engine efficiency and reduce the cyclic variation for CNG fuelled operation [123].

Higher cycle-to-cycle variability and poor combustion phasing, therefore, set a limit on the use of extremely high dilution levels [122]. A high level of turbulence accelerates combustion processes and reduces cyclic variability, though it may extinguish the flame completely, particularly at higher levels of dilution [124, 125]. It is therefore necessary to control the in-cylinder turbulence to enhance its positive effects and minimize its negative effects, thus optimizing combustion at a higher dilution level [126].

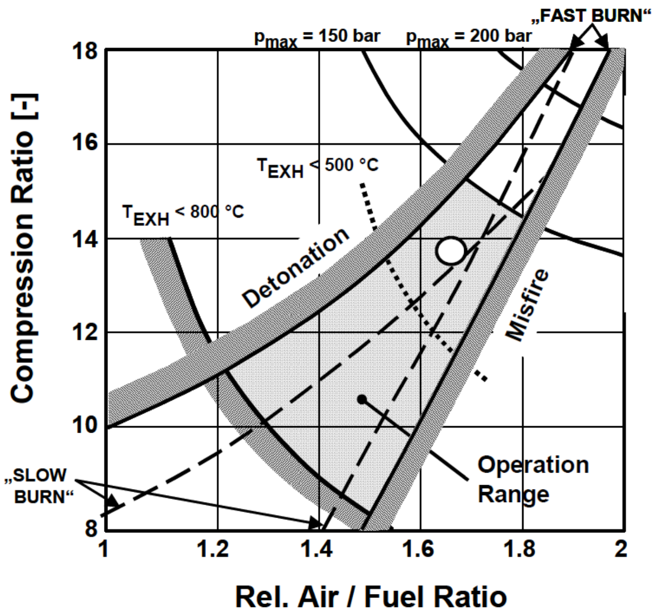

Figure 2.29: Turbocharged lean-burn concept for CNG engines [32].

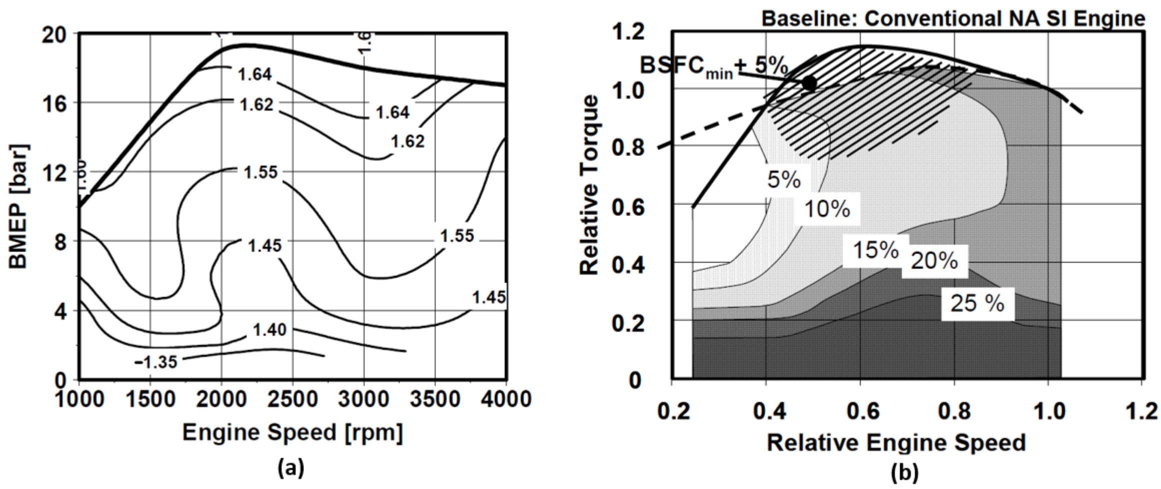

Figure 2.30: (a) operating λ and (b) fuel economy benefits of turbocharged lean-burn concept with CNG fuelling compared to gasoline NA PFI operation over the operating map [32].

2.5.3 Exhaust emissions

Exhaust emissions from a SI engine contain carbon monoxide (CO), oxides of nitrogen (NO_x), unburned hydrocarbon (UHC), particulate matters (PM) and other species besides carbon dioxide (CO_2) and water (H_2O). Fig. 2.31 shows the variation of CO, NO_x, and UHC emissions as a function of equivalence ratio for a typical SI engine.

Carbon monoxide (CO): In a SI engine, CO is generally formed under rich operation such as startup, wide-open throttle (WOT) conditions when there is not enough oxygen to convert all carbon to CO_2. Furthermore, CO can also form in stoichiometric and slightly lean mixture due to the dissociation of CO_2 at typical combustion temperature [65].

$$2CO_2 + Heat \rightarrow 2CO + O_2. \tag{2.5.1}$$

CO is not only considered as an undesirable emission but also represented as a loss of unburned fuel energy.

Oxides of Nitrogen (NO_x): Oxides of nitrogen (primarily NO and NO_2) are other important emission species from combustion that are produced in the post flame region by the oxidation of N_2 [65]. Though the highest flame temperature occurs at a slightly rich condition (i.e., $\phi = 1.1$), NO_x emissions generally peak at a slightly lean condition due to the presence of both sufficiently high temperature and excess air, as shown in Fig. 2.31. The use of exhaust gas to dilute the engine intake mixture lowers NO_x levels as it reduces flame temperatures by increasing the heat capacity of the cylinder charge per unit mass of the mixture [37].

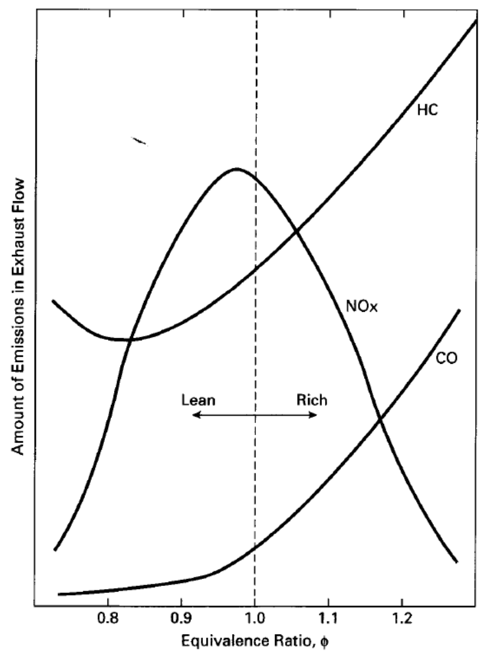

Figure 2.31: Exhaust emissions of an SI engine [127, 128].

Unburned Hydrocarbon (UHC): Figure 2.32 highlights the primary sources of UHC emissions. Several mechanisms that contribute to UHC emissions are:

(1) flame quenching near the combustion chamber walls due to the increased heat loss to the wall, leaving a layer of unburned fuel-air mixture adjacent to the wall.

(2) restrained flame propagation in crevices, resulting in escape of a trapped unburned mixture from the crevice volume.

(3) flame extinction in the bulk gas (i.e., bulk flame quenching) before reaching to the walls due to inhomogeneous charge distribution and poor combustion quality (e.g., inadequate control of excess air dilution, EGR, and ignition timing).

(4) any fuel stored in the intake port scavenged through the exhaust port as UHC emissions.

(5) absorption of fuel vapour in piston deposits or lubricant film. Note that methane is about two to three orders of magnitude less soluble in the oil layer than a larger parafin, such as octane [51].

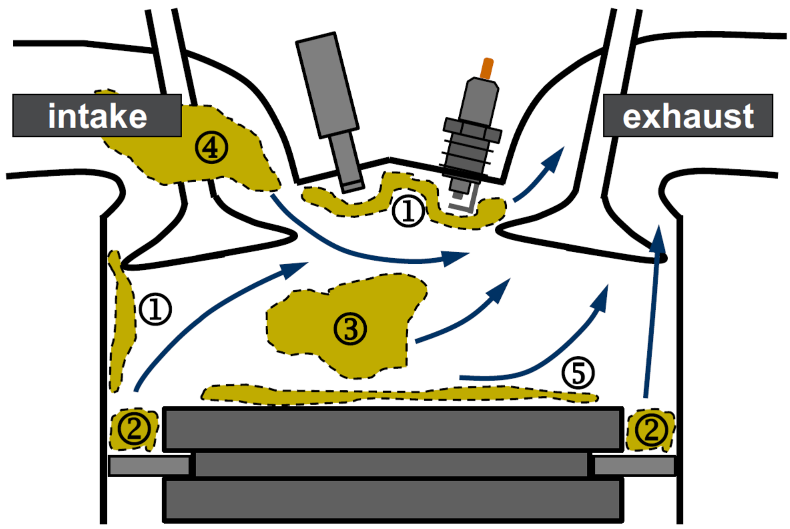

Figure 2.32: Sources of engine-out UHC emissions in the combustion chamber [129].

Particulate matter (PM): Emissions of particulate matter in premixed combustion can only result from the rich operation or fuel additives, lubrication oil, and depends on the fuel structure and flame temperature. There is no legislation limit of PM emissions for gasoline PFI engines due to a negligible or no

PM formation. However, PM emissions need to be considered in GDI engines as per Euro VI SI engine emission legislation [130].

Various researchers have studied engine-out emissions from stoichiometric CNG PFI engines and compared with baseline gasoline PFI engines at different operating conditions [97–100, 131]. In general, both UHC and CO emissions are lower with CNG fuelled operation due to the better mixing, lower oil film adsorption–desorption, and elimination of wall wetting effects on the intake manifold and the cylinder liner, particularly during the cold start conditions [51, 95, 102, 132]. NO_x emissions are normally lower with CNG than those with gasoline due to the higher stoichiometric air-fuel ratio and lower combustion velocity. However, considerably different results can be found due to its dependence on other engine operating parameters such as ignition timing, engine speed, and load [34, 132, 133]. Natural gas engines also produce relatively lower particulate matter emissions because they do not contain aromatic compounds such as benzene, and have less dissolved impurities (e.g., sulphur compounds) than those with petroleum fuels [134, 135]. Furthermore, evaporative emissions from natural gas fuelled vehicles (NGVs) are significantly lower than conventional vehicles as the fuel system for CNG is completely closed, and total in-use reactive organic gas (ROG) emissions from fuel storage and refueling of gas tanks are small [136].

Emissions from DI CNG engines have also been studied by various researchers. Sevik et al. [111] has demonstrated a 33-50% decrease in UHC emissions, as well as lower NO_x and similar CO emissions with DI CNG compared to gasoline PFI operation at the stoichiometric conditions. Zeng et al. [77] has shown that a highly stratified DI CNG engine increases UHC emissions and decreases NO_x emissions, while it demonstrates the opposite trends at homogeneous charge conditions. Ferrera et al. [81] has also observed similar UHC trends with the DI CNG operation, as shown in Fig. 2.33. The late injection results in higher UHC emissions because of less homogeneous mixing, whereas lower UHC emissions at early injection indicate a good mixture homogeneity due to the sufficient mixing time.

A comparison of drive cycle emissions behavior between gasoline and CNG fuelled

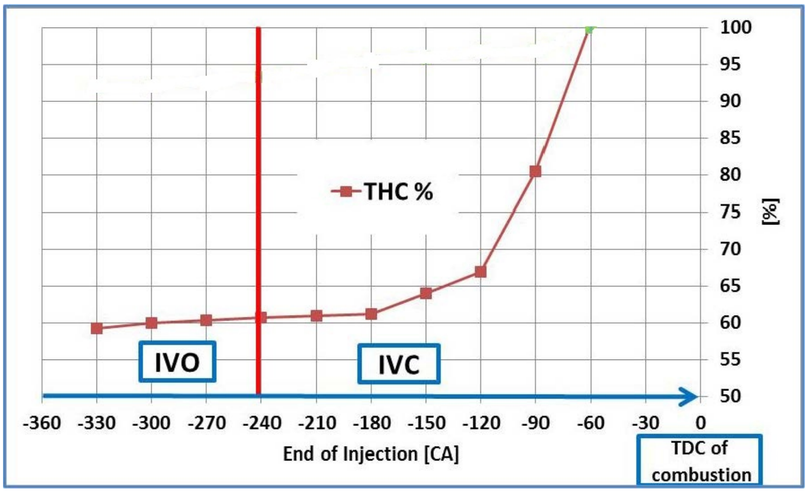

Figure 2.33: Unburned hydrocarbon (UHC) emissions as a function of the end of injection with DI CNG operation at 2000 RPM and 4 bar BMEP [81].

operation in a 1.6L CNG bi-fuel engine with PFI system is shown in Fig. 2.34, where CNG fuelling demonstrates lower tailpipe emissions in general. CNG powertrain induces higher UHC emissions during cold start, but it reduces immediately after that, resulting in comparable UHC emissions with gasoline fuelling over the drive cycle [32].

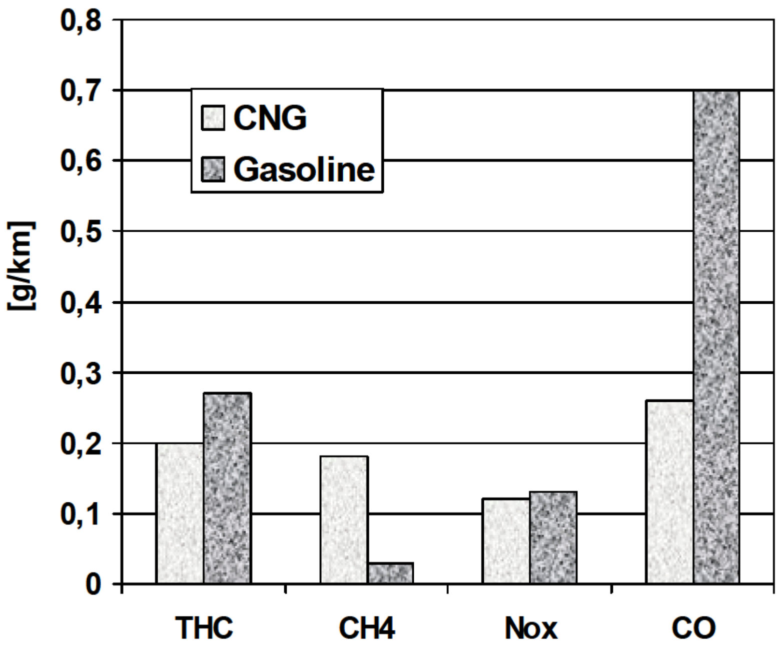

Figure 2.34: EUIII emission results from a 1.6L CNG bi-fuel engine, NEDC cycle [32].

EUVI emissions results of a C-segment European vehicle with a stoichiometric DI CNG engine are shown in Fig. 2.35. All NEDC, WLTP emissions of CO, NO_x, PM, total hydrocarbon (THC), and non-methane hydrocarbon (NMHC) are below EUVI limits. Furthermore, PM emissions are extremely low without any particulate filter [137].

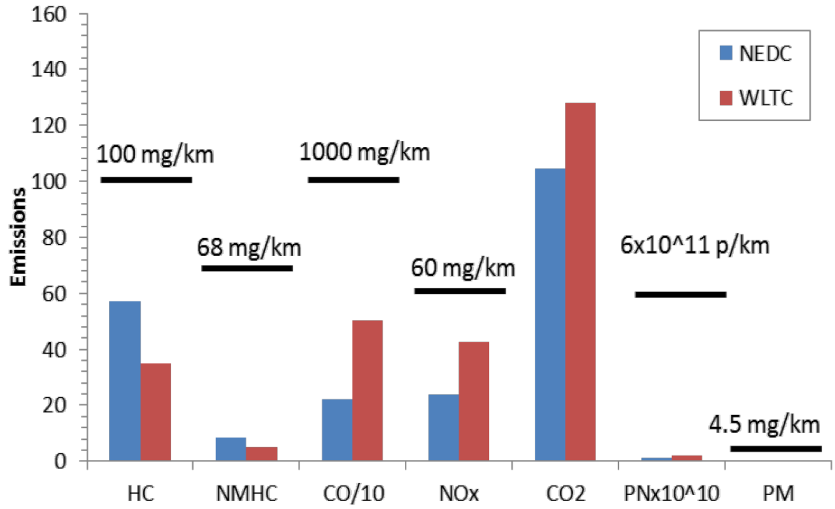

Figure 2.35: EUVI emission results in NEDC and WLTC drive cycle from a 1.0 L dedicated DI CNG engine on C-Segment Vehicle, GasON project [137].

The impact of charge dilution on emissions is now discussed. The application of EGR dilution results in a substantial reduction in NO_x emissions due to lower in-cylinder temperatures (Fig. 2.36). This is attributed to the higher heat capacity of EGR dilute mixture (thermal effect) and lower heat release due to the reduction of in-cylinder oxygen concentration (dilution effect) [37, 92]. With the increase of

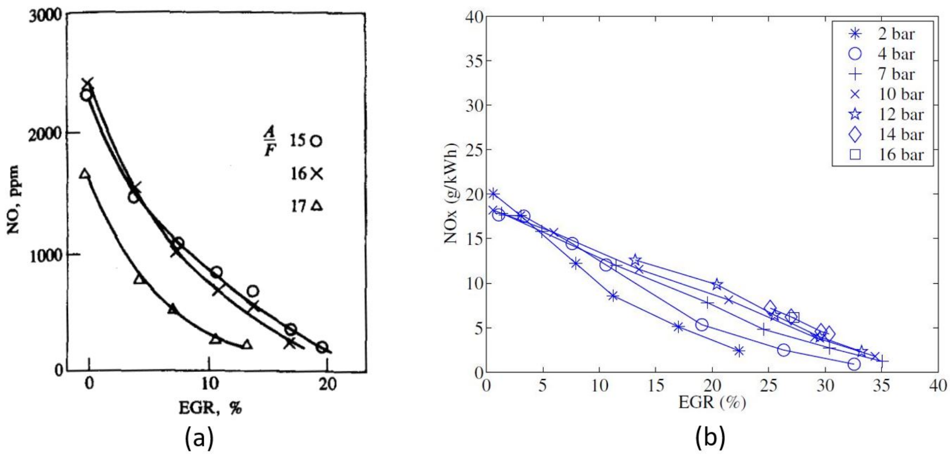

Figure 2.36: Engine-out NO_x emissions as a function of EGR rate (a) Sakai et al. [138] and (b) Einewall et al. [84].

EGR rate, the heat release rate decreases due to lower burning speeds resulting from lower in-cylinder temperatures and mixture inhomogeneity (Fig. 2.37-a), which increases UHC emission and combustion instability as shown in Fig. 2.37 (b). Initially, the increase in UHC emissions is modest and caused primarily by crevice flame quenching mechanisms. However, UHC emissions increase rapidly with the occurrence of a partial burning cycle at a higher EGR rate, indicating an incomplete combustion due to the potential bulk flame quenching [96].

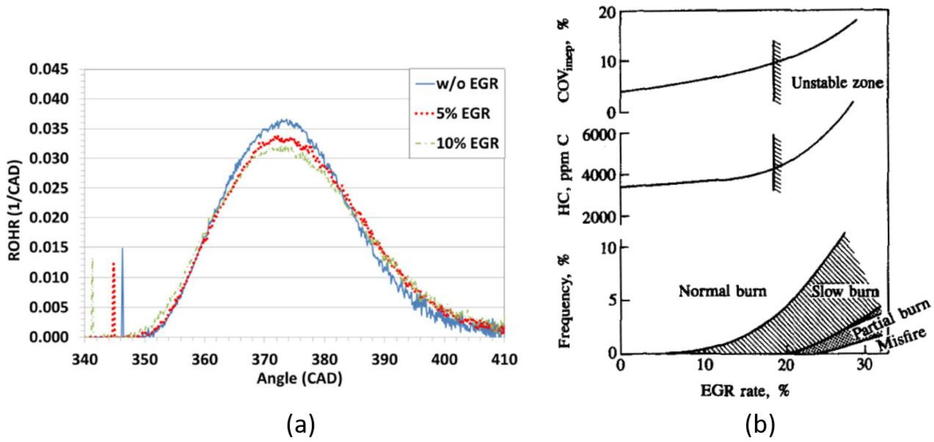

Figure 2.37: (a) Heat release rate [91] and (b) UHC and COV_{IMEP} [96] as a function of EGR rate.

With lean-burn operation, as shown in Fig. 2.38, engine-out UHC emissions decrease with the increasing λ due to decreased unburned fuel trapped in crevices. Furthermore, the post-combustion oxidation of the crevice gas is more effective during the expansion and exhaust strokes due to the presence of excess air. However, when the mixture is very lean, UHC emissions tend to increase due to the slow flame propagation, incomplete combustion, and misfire [84, 126]. Engine-out NO_x emissions decrease significantly as the mixture is leaned out due to lower in-cylinder temperatures. Dimitri et al. [129] has investigated multiple injection strategies as an internal measure to reduce UHC emissions and demonstrated that the double-injection (i.e., an early first injection containing 90% of the total fuel amount followed by a second injection close to the ignition timing with 10% fuel amount) reduces the UHC emissions by up to 25% compared to the best point of the single injections.

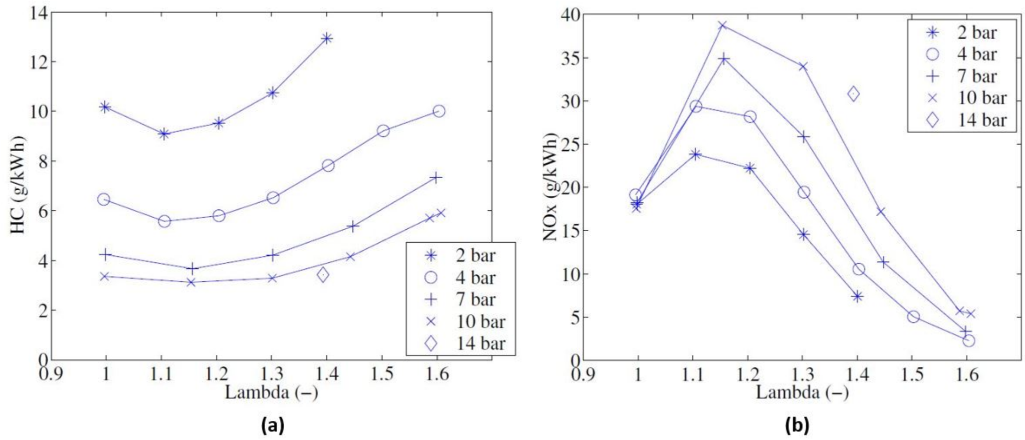

Figure 2.38: Engine-out (a) unburned hydrocarbon (UHC) and (b) NO_x emissions as a function λ [84].

2.5.4 After treatment of exhaust gas

Contemporary CNG-fuelled engines are designed for stoichiometric operation (i.e. $\lambda = 1$), where the existing three-way catalyst (TWC) technology of a typical SI engine is used for emissions control. With the CNG fuelled operation, the majority of engine-out UHC emissions are methane (> 80%) [37]. The conversion of methane requires a relatively higher oxidation temperature due to its compact molecular structure, as shown in Fig. 2.39. Higher methane-based UHC conversion thus requires a careful control of lambda, high light-off temperature (> 400^0C), and methane focused catalyst. With DI CNG, a catalyst heating strategy with the post injection is also investigated to improve the UHC conversion efficiency [139].

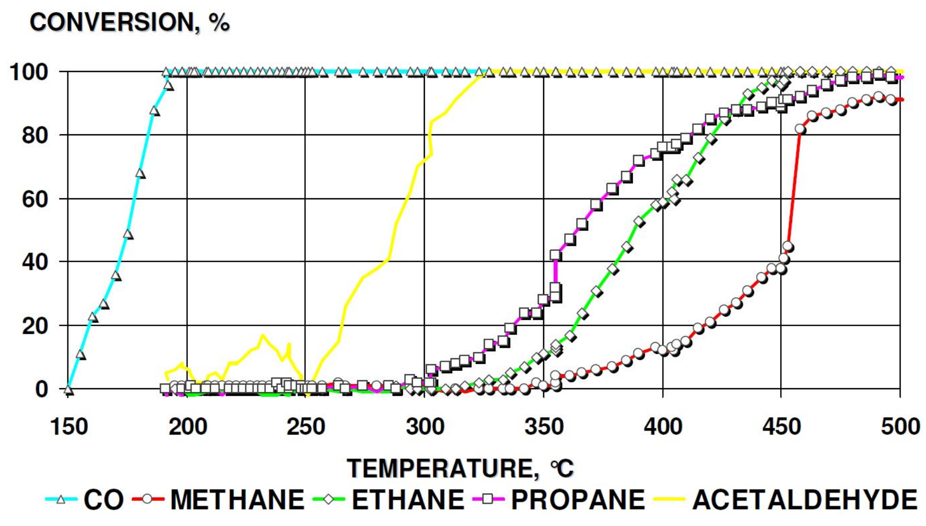

Figure 2.39: Typical conversion behavior of different exhaust gas components [140].

Furthermore, researchers are currently developing innovative coating technologies to reduce the methane light-off temperature compared to baseline technology. One example of these is shown in Fig. 2.40.

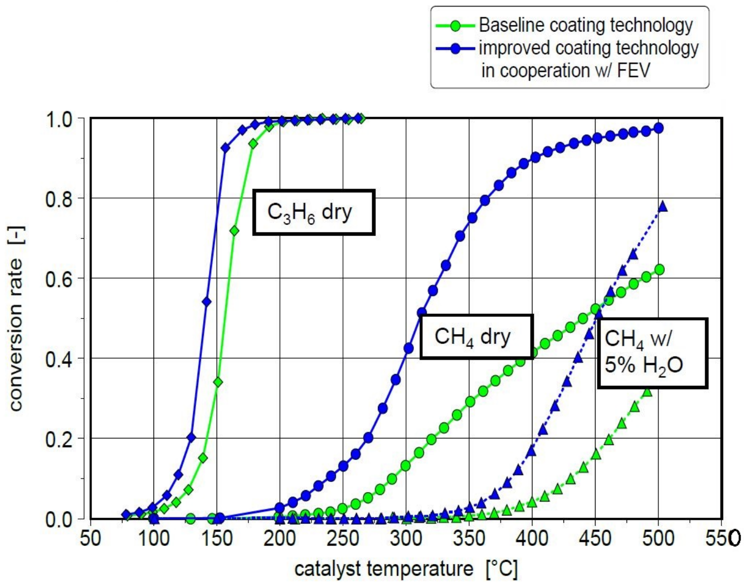

Figure 2.40: Methane light of temperature with improved coating technology [141].

CNG fuelled engine can operate ultra-lean to decrease CO_2 emissions, but high engine-out UHC emissions combined with low exhaust gas temperatures (EGTs) for lean-burn operation necessitate a more demanding catalytic performance. Gluck et al. [142] has suggested a Pd based oxidation catalyst for the methane conversion during CNG fuelled lean-burn engine operation.

2.6 Greenhouse gas emissions

Carbon dioxide (CO_2) increases the atmosphere's heat-trapping capability, resulting in increased average global temperatures. Therefore, CO_2 emissions are considered as the greenhouse gas emissions and regulated in the world's most of the automotive markets.

Figure 2.41 shows the energy-specific CO_2 formation for various fuels. Given its lower C/H ratio, methane offers an approximate 25% CO_2 reduction compared to conventional fuels such as gasoline and diesel [30]. Harry et al. [75] has shown that with a dedicated CNG engine and state-of-the-art technologies, DI CNG

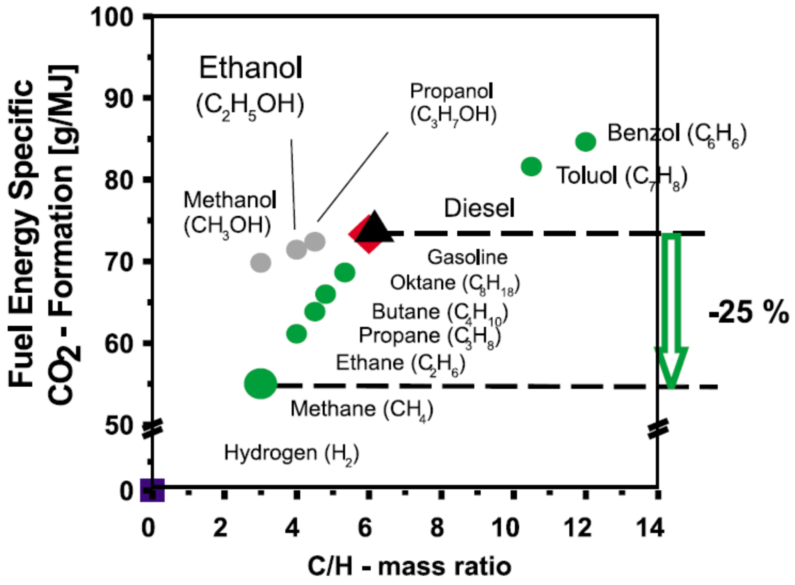

Figure 2.41: Fuel energy specific CO_2 formation [30].

combustion system can exhibit a substantial reduction in CO_2 emissions (i.e., ∼16%) compared to CNG PFI engines (Fig. 2.42). Thomas et al. [76] has demonstrated a 33% reduction in CO_2 emissions with DI CNG operation (having optimized combustion chamber, high compression ratio, and direct injection) compared to a GDI engine over NEDC cycle, as shown in Fig. 2.43. Finally, an overview of emissions reduction potential of CNG fuelling compared to gasoline operation is shown in Fig. 2.44, where the total impact of greenhouse gas emissions based on the GWP of CO_2 and CH_4 (CNG only) is also highlighted.

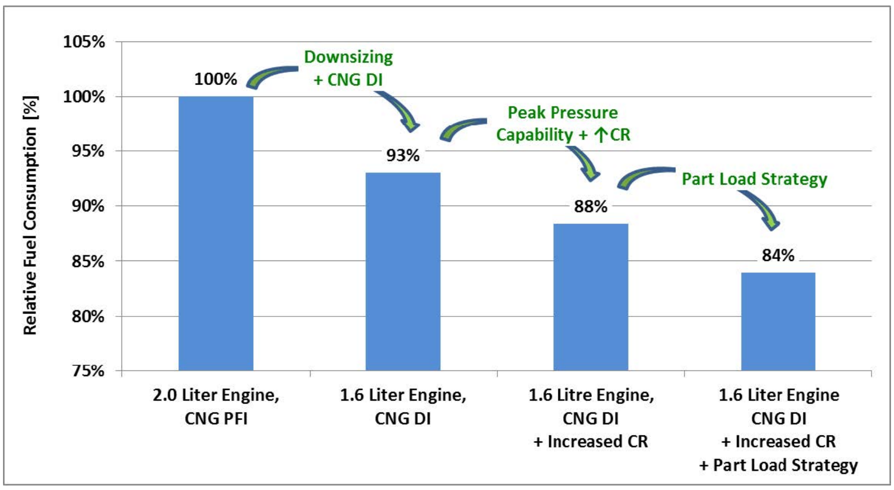

Figure 2.42: CO_2 emissions improvements, NEDC cycle [75].

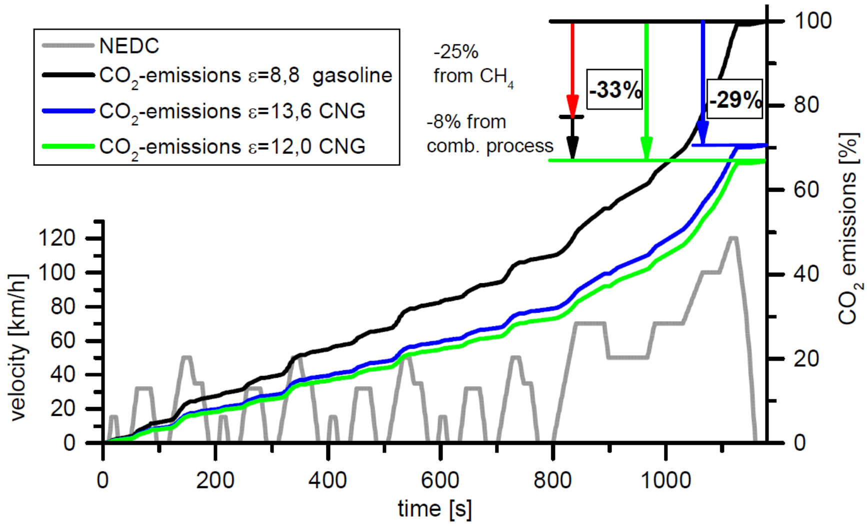

Figure 2.43: Comparison of CO_2 emissions with DI CNG over GDI operation [76].

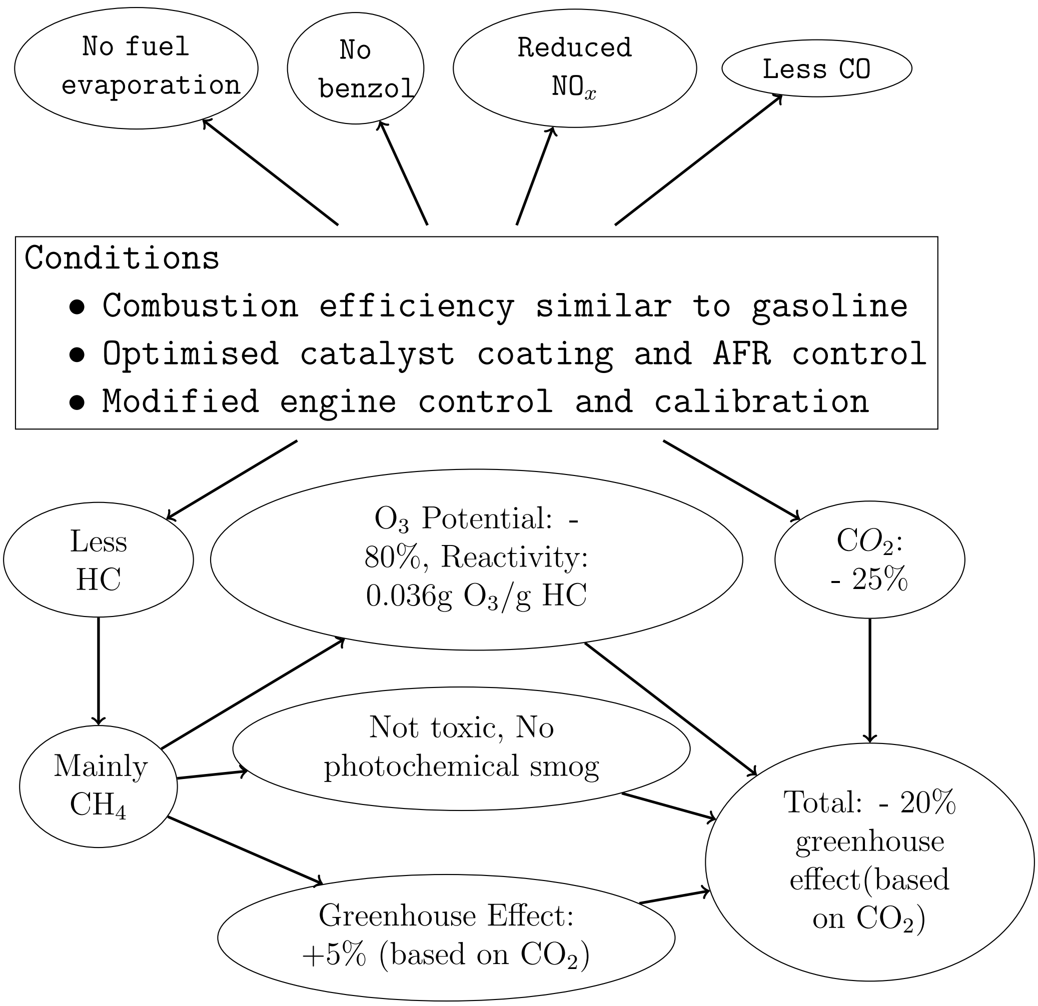

Figure 2.44: Emission reduction potential of CNG compared to gasoline [32].

2.7 Engine durability

Unlike gasoline, CNG lacks the latent heat of evaporation and lubrication property, which leads to higher metal temperatures when used as an automotive fuel (Fig. 2.45). This may lead to thermal failure of the engine parts [102, 143]. The durability

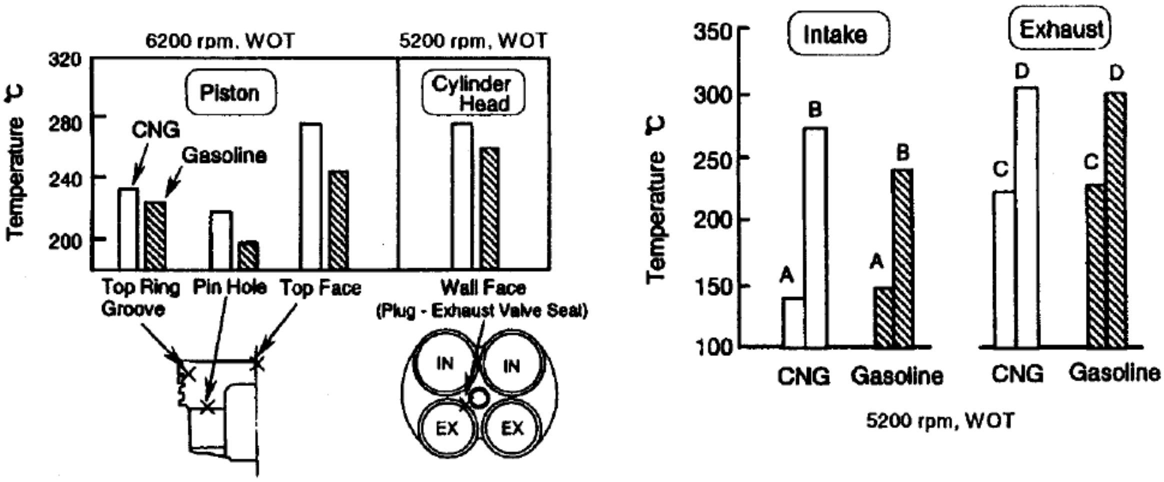

Figure 2.45: Temperature of various components with gasoline and CNG fuelled operation [102].

of a CNG engine with higher CR can be improved by selecting suitable materials and surface treatment methods for valves, valve seats, and spark plugs, and using high strength piston and modified water jacket design [95, 102].

2.8 Summary

This chapter outlined the details of CNG fuelled SI engine with both port fuel and direct injection systems and presented a performance comparison with the conventional gasoline engine at stoichiometric conditions. Today's spark-ignited CNG engine operating with the PFI technology suffers from a lower volumetric efficiency, resulting in an inferior peak performance compared to a modern GDI engine. An optimized mono-fuel natural gas engine with the DI technology is emerging as a potential solution to overcome these CNG PFI engine shortcomings. However, DI CNG technology's impact is not well charcterised for modern, production SI engines in the literature.

This chapter also presented an overview of CNG fuelled engine operation with external dilution (i.e., EGR, excess air) comprising the engine operating envelope, fuel economy, emissions, and strategies to achieve a stable combustion, particularly with the PFI technology. The status of current exhaust gas after-treatment systems and engine durability issues with CNG fuelled operation were briefly discussed. Implementation of the EGR dilution strategy to a stoichiometric SI engine operation improves the fuel economy, knock-limit, and in-cylinder NO_x production while maintaining the functionality of TWC for exhaust emissions reduction. The lean-burn natural gas engine achieves a relatively higher thermal efficiency due to CNG's extended lean flammability limit. Nevertheless, higher cycle-to-cycle variation, incomplete combustion, and misfire have been reported while using the extremely lean or high EGR dilution.

CNG fuelled operation overall reduces all engine-out exhaust emissions compared to the gasoline-fuelled engine. Furthermore, a significant CO_2 reduction potential is demonstrated for CNG fuelled operation due to favorable fuel properties and efficiency improvement. However, the methane slip can negate these benefits due to its higher GWP. Therefore, an adequate knowledge of UHC emission formation mechanism and it's control management are necessary for the optimal DI CNG engine performance, particularly with external charge dilution.

2.9 Research questions

Based on the current state of knowledge present in the literature, the following research questions are proposed for this work to improve further the knowledge base of DI CNG fuelled SI engine technology.

1. **How do the performance and greenhouse gas emissions of a modern, DISI production engine compare when fuelled with gasoline and CNG at stoichiometric conditions?**

   The majority of previous DI CNG research was conducted using single-cylinder engines or multi-cylinder, bi-fuel SI engine systems without state-of-the-art technologies. Furthermore, these studies compared the performance of DI CNG operation to that of gasoline PFI operation. While there are obvious CO_2 emissions benefits from replacing gasoline with CNG in modern SI engines, there are no studies to date that have characterised the additional carbon abatement gained through the implementation of DI CNG technology nor the associated injection or combustion strategies required to realize these benefits.

2. **How does the charge dilution strategy impact the fuel efficiency and emissions of a DI CNG engine?**

   Engine research involving external charge dilution with either excess air or EGR are well documented for SI engine operation, highlighting the benefits and drawbacks of each approach. However, there are no studies to date that consider DI CNG engine performance when employing each of these dilution strategies. Furthermore, previous works have not demonstrated the best methods to use external dilution to improve fuel economy and GHG emissions over a production engine's operating range. This optimal utilization, which is not established for DI CNG operation, requires a thorough understanding of the underlying mechanisms connecting turbulent flame propagation to pollutant formation. Therefore, this research effort will characterise and analyse DI CNG engine operation with charge dilution using EGR and air.

3. **Can advanced DI CNG combustion strategies address the trade off between fuel efficiency and emissions when charge dilution is used?**

   The use of lean-burn and EGR dilution with CNG fuelling improves the engine's fuel efficiency versus baseline GDI operation. However, excessively lean fuel-air mixtures or high EGR rates cause increased UHC emissions due to incomplete combustion, which is not studied in the literature for charge dilute DI CNG engine operation. As the large majority of these UHC emissions will be a high GWP methane, understanding the impact of various in-cylinder techniques on UHC emissions is necessary utilizing the capability of the DI system, particularly with the dilute operation. Moreover, lean-burn strategies should avoid mixtures near stoichiometry due to high NO_x production, which also has a significant GWP. Therefore, this work will consider all primary greenhouse gas production to determine the best approach for fuel-efficient, low emission, DI CNG operation at part-load.

Chapter 3

Experimental Setup and Numerical Method

This chapter describes the research engine, test cell facilities, and instrumentations used to conduct all experiments in this work. The methodology implemented to design the matrix of experimental operating conditions is also discussed. Further, a detailed numerical methodology is presented to perform the combustion analysis using Gamma Technologies' GT-Suite software.

3.1 Experimental setup

An experimental test-bench was prepared in the Thermodynamics Laboratory at the University of Melbourne to perform both gasoline and CNG fuelled experiments. The test engine was instrumented with various actuators and sensors to operate and acquire experimental data under different test modes. The existing AC dynamometer and coolant conditioning unit of the test cell were connected to the test engine for speed and coolant temperature control, respectively. Details of each system are discussed in what follows.

3.1.1 Test engine

A 2.0L four-cylinder, downsized and turbocharged, direct injection (DI) Ford EcoBoost engine with a compression ratio of 9.3 was used to conduct the experimental investigation. The cylinder head of the engine features a pent-roof combustion chamber with a centrally mounted spark plug, as well as dual overhead cam shafts (DOHC) with independent variable cam timings, allowing for intake advance and exhaust retard up to 50 crank angle degrees. The engine was also equipped with four side-mounted injectors (Bosch HDEV 5.1) to enable direct injection of gasoline into the cylinder. In this work, the gasoline used is a regular grade US EPA Tier 3 Certification Fuel [31]. Although the compression ratio of the engine appears relatively low for CNG fuelled operation considering its high knock resistance, the engine architecture was kept the same as production engine to allow for a direct performance comparison between gasoline and CNG fuelled operation. Note that this work didn't use any after-treatment system with the test engine. The specifications of the test engine are outlined in Table 3.1. The test

Table 3.1: Test engine specifications

No of Cylinder	4
Bore x Stroke	87.5 mm x 83.1 mm
Displacement	2.0 L
Compression Ratio	9.3:1
Valve Train	DOHC
Injection System	Side mounted DI
Firing Order	1-3-4-2
Peak Power	159 kW (91 RON) and 177 kW (98 RON)
Peak Torque	340 Nm at 1750-4000 RPM
Maximum Boost	110 kPa (gauge) at 5000 RPM
Manufacturing Year	2012
Vehicle Application	Ford Falcon

engine, along with all the subsystems, were rigidly mounted on a testbed with proper alignment between the engine and dynamometer shaft to ensure its safe, reliable, and vibration-free operation. Support accessories required to mount the engine on the testbed had been conceptualized and designed based on the new product development (NPD) approach using CATIA tool, as shown in Fig. 3.1. Parts were then manufactured in the UoM Physics Workshop.

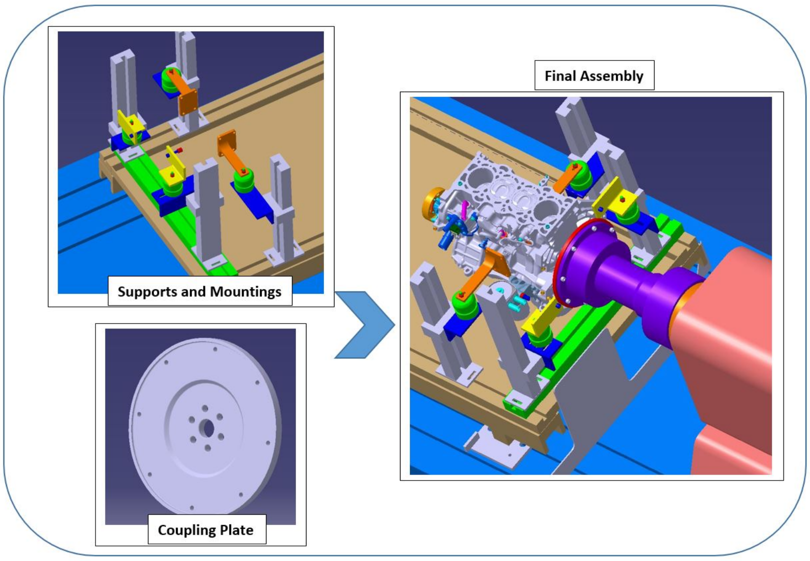

Figure 3.1: Engine mounting design and assembly.

3.1.1.1 CNG fuelling system

A schematic diagram of the CNG fuelling system is shown in Fig. 3.2, demonstrating the fuel path from gas storage at 200 bar to fuel injection at 16 bar. A Coltri MCH5 compressor with a charging rate of 5 m^3/hr was used to compress the mains natural gas, which was then stored in three steel tanks at a pressure of 200 bar. A high-flow reducing regulator from Aqua Environment was installed to reduce gas pressure from 200 bar to 40 bar before entering into the test cell. Natural gas flow experiences the Joule-Thomson cooling effect when subjected to a large pressure drop through the regulator. Therefore, a water heating module was incorporated into the system to avoid the regulator freezing. An additional low-pressure regulator was installed inside the test cell to maintain the fuel rail pressure at 16 bar during the engine operation. A normally closed, electro-pneumatic valve was also installed upstream of the high-pressure regulator to isolate the storage tank from the rest of the fuel system. Further, a safety control logic was implemented to allow CNG flow only when the heating water temperature was above 20°C and injectors were switched on. Additionally, a solenoid type shut-off valve was installed on the gas line upstream of the low-pressure (LP) regulator to locally control the gas flow.

In this work, four DI CNG prototype injectors developed by Continental Automotive Systems were used to supply CNG directly into the combustion chamber [144]. The

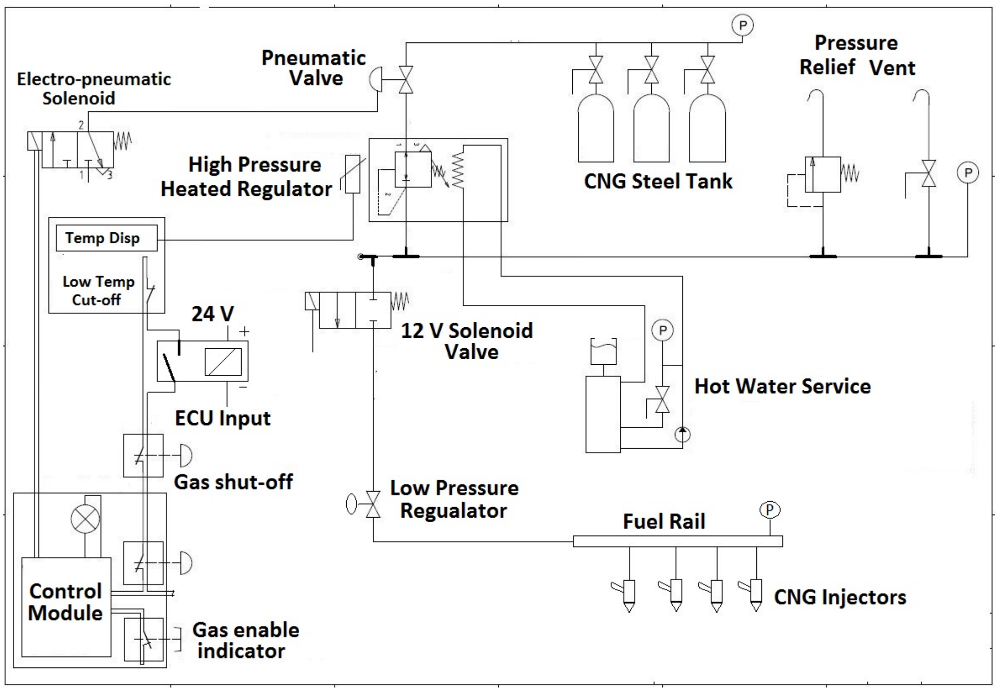

Figure 3.2: CNG fuelling system layout.

injector has an outward opening mechanical valve (hot valve) and an inward opening solenoid valve (cold valve). The form factor of this injector is nearly identical to the Bosch HDEV 5.1 GDI injector, enabling a simple swap of liquid fuel delivery with that of gas. The specifications of the DI CNG injector are presented in Table 3.2.

Table 3.2: DI CNG injector specifications

Maximum injection pressure	20 bar (absolute)
Static flow rate	12 $\pm$0.6 g/sec at 20 bar with N_2
Flow cone angle	80-100^0
Boost power supply	48 V
Peak sustain time	1 ms

3.1.1.2 Exhaust gas recirculation system

A cooled, external exhaust gas recirculation (EGR) system was designed and integrated with the test engine to extract the exhaust gas downstream of the turbine and reintroduce it upstream of the compressor. Figure 3.3 demonstrates the schematic of this system. An EGR cooler featuring spiral tube construction was used to cool the hot exhaust gas using the engine coolant. The temperature of exhaust gas downstream of the EGR cooler was maintained above 100°C by controlling the coolant flow rate using a globe valve, which helped to avoid any water condensation issue. A DC motor-driven exhaust flap was installed downstream of the EGR cooler to control the proportion of EGR going back to the engine. An additional flap was also mounted on the exhaust path to control the back pressure where necessary. The temperature of total charge (air + EGR if recirculated) downstream of the charge cooler was kept at 38 - 40°C for all engine experiments. Three k-type thermocouples and one sensor were installed to monitor the temperatures and pressure at different locations of the EGR system. Two air mass flow meters (details in Section 3.1.1.3) were incorporated to measure the fresh air flow rate ($\dot{m}_{air}$) and flow rate of air-exhaust gas mixture ($\dot{m}_{total}$), respectively. The measured mass flow rates were then used to calculate the EGR rate based on Eq. 5.1.1.

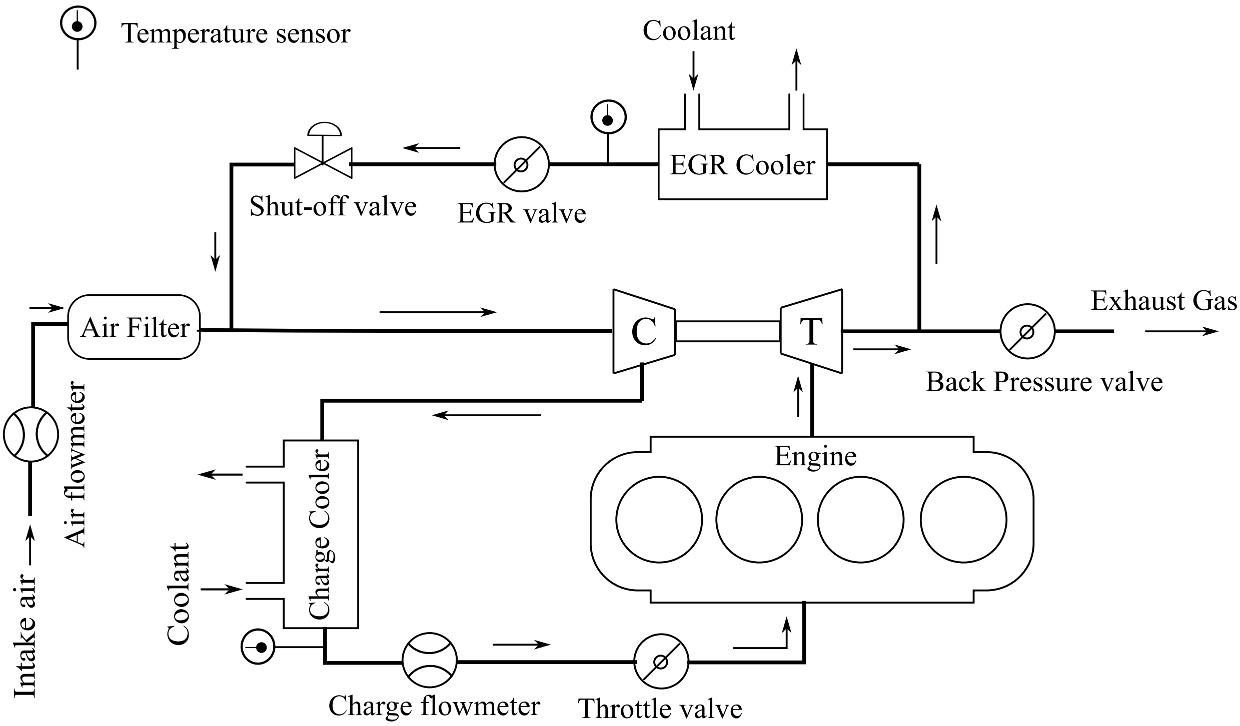

Figure 3.3: Cooled, external EGR system layout.

3.1.1.3 Engine instrumentation and management

The test engine was instrumented with various actuators and sensors, either factory mounted or installed in-house. Actuators such as throttle servo, injection and ignition controller, variable cam, and boost solenoid were used to control the subsystems based on OEM settings and user-given commands.

A Coriolis flow meter (Micro Motion elite series CMF010M) with a maximum flow capacity of 65 kg/hr (measurement accuracy of ± 0.35%) was used in this work to measure both gasoline and CNG flow rate. The analogue voltage output from the flow meter corresponding to a particular flow rate was recorded in the ECU during experiments for engine diagnosis and performance calculation.

A Bosch HFM5 hot-film, mass air flow meter with a measurement range of 15-850 kg/hr (measurement accuracy of ± 3%) was installed downstream of the air filter to measure the flow rate of incoming air. An additional air flow meter with similar specifications was installed upstream of the throttle body to measure the total charge flow rate (fresh air + EGR flow) as a part of the external EGR circuit. The corresponding voltage signal was acquired through the ECU to calculate the required fuel quantity for injection.

A wide-band lambda sensor (Bosch LSU 4.9) was installed on the exhaust pipe to monitor the air-fuel ratio during the experiments. MoTeC LTC (Lambda to CAN) module was incorporated into the engine set up to control the lambda sensor and transmit the readings to ECU via can bus. A closed-loop lambda control module integral to ECU maintained the operating λ by performing a trim operation on the fuel quantity to be injected. Note that the time for closed-loop lambda control trim update was observed in the range of 0.5 to 1 second.

A Bosch 5 pin sensor was installed on the intake manifold to measure pressure and temperature of the intake charge. Sensors were also used to monitor pressure at various other locations such as fuel rail, exhaust pipe, and compressor downstream. Two k-type thermocouples were mounted on both upstream and downstream of the turbocharger to measure exhaust gas temperatures. Coolant, oil, and air temperature (upstream and downstream of inter-cooler) were also monitored. Various position sensors were used to provide information about the crank and cam shaft position (hall effect type), valve timing, and throttle position as part of the feedback control loop.

A MoTeC M142 ECU with fully open, developmental access was used to control and monitor the engine operation. A customized firmware was developed and implemented in the ECU to control different modes of engine operation by communicating with various actuators and sensors. An overview of the ECU process flow is presented in Fig. 3.4.

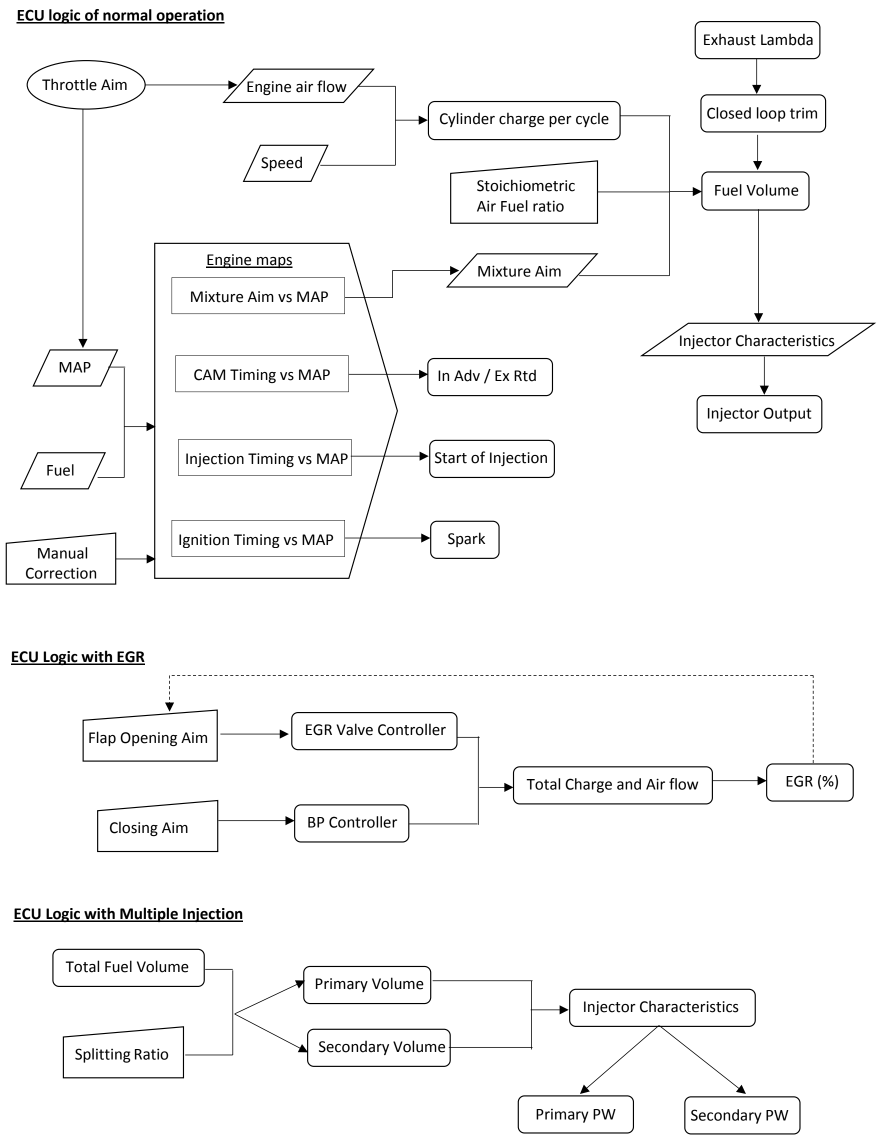

Figure 3.4: Overview of ECU process flow.

3.1.2 Test-bench facilities

3.1.2.1 Dynamometer

The research engine was tested using a Titan T460 Horiba-Schenck AC dynamometer with a capacity of 460 kW rated power and a maximum speed of 8030 rpm. The engine and dynamometer were mounted on an air-cushioned bed to absorb the vibrations during engine testing. A custom-designed flexible connecting shaft was installed between the dynamometer and engine to avoid torsional vibrations. The SPARC^{E} test stand controller was used to operate the dynamometer at a constant engine speed and to measure torque output for different operating conditions. Important safety features such as over speed and torque limit were added in the controller to protect the engine and dynamometer in an emergency situation.

3.1.2.2 Cooling conditioning system

The cooling system of the test cell was used to remove heat from the engine and to maintain the coolant at a specified temperature. Figure 3.5 presents the schematic of the cooling system. Due to the implementation of an external cooling circuit, engine components such as radiator, thermostat, and water pump drive belt were removed from the test engine. The system used a heat exchanger (W1) to cool the hot coolant from the engine using cold water from the university cooling tower, and an electrical heater (H1) to heat the coolant if necessary. The temperature of the coolant going to the engine was maintained at 90°C by mixing cold and heated fluid using a PID controller. Another cooling system with similar architecture was used to maintain the temperature of the incoming air after the liquid-to-air charge cooler around 38 to 40°C. This system also helped to cool the engine oil.

3.1.3 Combustion data acquisition

Four uncooled piezoelectric transducers (Kistler 6125C, 300 bar) were used to measure the in-cylinder pressure traces in all four cylinders. A specially designed tube was installed into the cylinder head to accommodate the pressure transducer and prevent any water leakage from the machined path close to the cooling jacket.

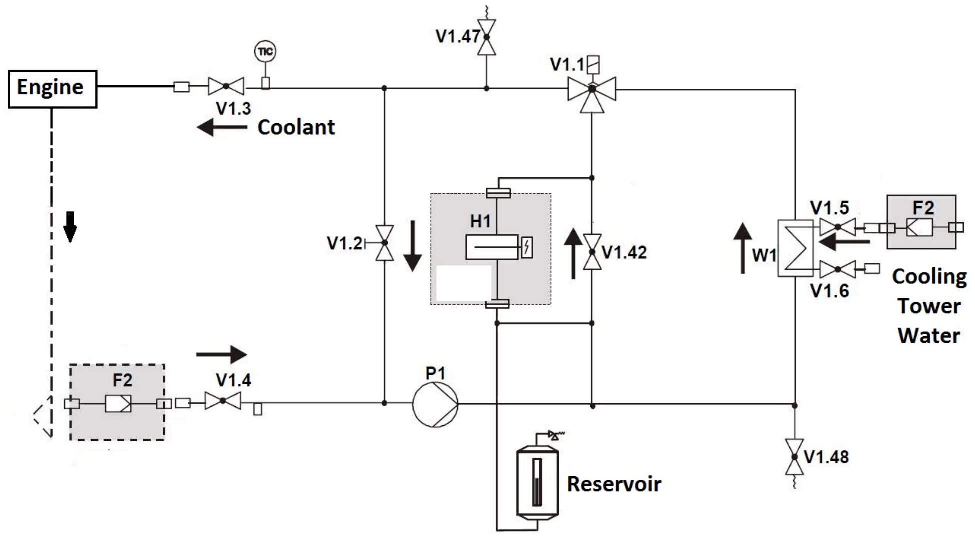

Figure 3.5: Engine cooling circuit of the test cell.

The pressure signal from the transducers was transmitted through low noise cables to a charge amplifier (Kistler 5064D) and then to a high-speed data acquisition system comprising NI cDAQ$^{\text{TM}}$ 91740, NI 9402, and NI 9222 modules from the National Instruments. A rotary encoder with 0.1 crank angle degree resolution was mounted on the crankshaft to synchronize the in-cylinder pressure with the crank-angle position. Pressure pegging was performed using the measured manifold air pressure (MAP) and averaged in-cylinder pressure signal at BDC (averaging window $\pm$ 4° crank angle) [145]. An in-house combustion code was also developed and incorporated in the LabVIEW program to provide the real-time information on the location of 50% MFB, cyclic variability (COV_{IMEP}) for engine optimisation and diagnosis.

In this work, a "trace-knock" or "borderline-knock" condition, which is the transition between knock-free normal combustion and continuous knocking, was determined by both audible signals from a microphone installed on the engine block and in-cylinder pressure oscillations measured by the data acquisition system [146]. For the latter, a cycle was deemed to be knocking if the peak-to-peak oscillation exceeded a threshold value of 0.5 bar at 1000 – 3000 RPM. Finally, an operating condition was defined to be trace knocking when the oscillation of 5% of every 300 cycles exceeded the threshold. Note that all the measured results both for gasoline and CNG fuelled operation were at knock-free conditions in this work, as ignition timings were retarded by the ECU if a trace-knock was detected with MBT ignition timing. In-cylinder pressure was recorded from all four cylinders for 300 consecutive cycles as it was found that these number of cycles allowed the convergence of indicated mean effective pressure (IMEP) for the steady-state condition. IMEP is calculated as

$$IMEP = \frac{\int_\theta PdV}{V_d} \tag{3.1.1}$$

where P is the measured in-cylinder pressure, V is the instantaneous volume, V_d is the engine displacement volume, and θ is the crank angle ranging a complete cycle.

A low-pass Butterworth filter with a cut-off frequency of 3 kHz was used to filter the noise from raw in-cylinder pressure traces [147]. Note that the 3 kHz cut-off frequency was selected based on the spectrum analysis as it preserved the peak pressure fluctuation for both gasoline and CNG fuelled operation, which were at knock-free conditions in this work. The in-cylinder combustion analysis was performed using a representative pressure trace selected from the filtered, measured pressure traces of one of the four cylinders. This trace was obtained from the all 300 recorded cycles at each operating point by minimizing the cost function [148, 149].

$$\mathrm{COST} = \left[\left(\frac{\mathrm{IMEP}_i - \mathrm{IMEP}_{avg}}{\mathrm{IMEP}_{avg}}\right)^2 + \left(\frac{\mathrm{PP}_i - \mathrm{PP}_{avg}}{\mathrm{PP}_{avg}}\right)^2\right], \tag{3.1.2}$$

where IMEP is the indicated mean effective pressure, PP is the peak in-cylinder pressure, and the subscripts i and avg denote the i^{th} cycle and the average quantity (evaluated from all cycles), respectively. Furthermore, cyclic variability of measured pressure traces is generally represented by the coefficient of variation of the net indicated mean effective pressure (COV_{IMEP}), which is calculated as per Eq. 3.1.3.

$$COV_{IMEP}(\%) = \frac{\sigma_{IMEP}}{IMEP_{avg}}, \tag{3.1.3}$$

where σ_{IMEP} is the standard deviation of IMEP over 300 cycles recorded pressure traces. In this work, COV_{IMEP} was maintained below 5% for all operating conditions. This relatively high value compared to what is typically employed (less than 3% limit) in the industry was used to probe the engine's performance with charge dilution at the limits.

3.1.4 Exhaust emissions measurement

AUTOTEST 5 Gas Analyzer was used to measure the engine-out exhaust emissions such as CO, UHC, CO_2, O_2, and NO_x. This device utilizes the non-dispersive infrared (NDIR) sensing technology to measure the concentrations of CO, CO_2, and UHC emissions. It also has two electrochemical sensors to measure O_2 and NO_x concentration. An overview of the analyzer's gas flow path layout is shown in Fig. 3.6. The analyzer uses a diaphragm type gas pump to circulate the exhaust gas

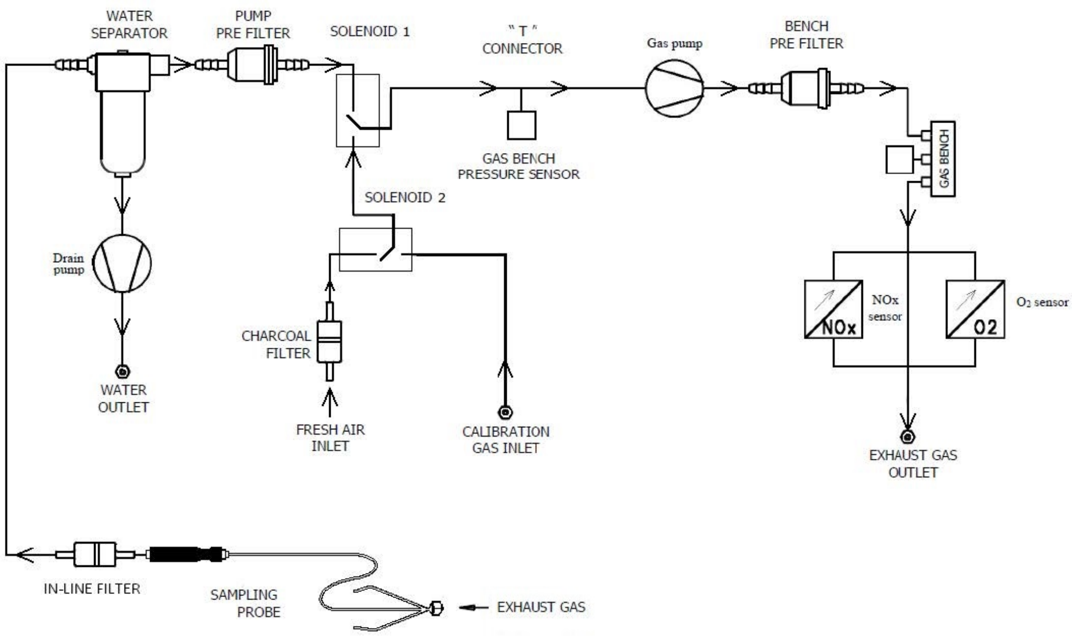

Figure 3.6: Flow diagram of the gas analyzer [150].

through a set of filters into the bench board and two electrochemical sensors, where contents of the sampled gas are analyzed. A water separator is used to trap the water content of the exhaust gas before entering into the NDIR detectors as water vapour's infrared absorption overlaps CO and CO_2 absorption bands. The temperature of the gas bench is also maintained at around 40 - 45°C to prevent any condensation building up inside the gas bench tube. The analyzer's proprietary software was used to perform exhaust emissions sampling and data recording. The specifications of the gas analyzer are presented in Table 3.3. Note that the response time of this analyzer is less than 10 seconds for a sample probe of 5-meter length. The measurement accuracy of the analyzer was verified by performing the sample test with the known concentration of calibration gases in the Thermodynamics Laboratory. The obtained results were appeared well within the accuracy limit of the analyzer for all calibration gases, as shown in Fig. 3.7.

Table 3.3: AUTOTEST 5 gas analyzer specifications

Exhaust Gas	Range	Resolution	Accuracy
CO	0 - 15 %	0.01 %	± 3 % rel
CO_2	0 - 21 %	0.10 %	± 4 % rel
UHC	0 - 20,000 ppm	1 ppm	± 5 % rel
NO_x	0 - 5,000 ppm	1 ppm	± 4 % rel
O_2	0 - 25 %	0.01 %	± 3 % rel

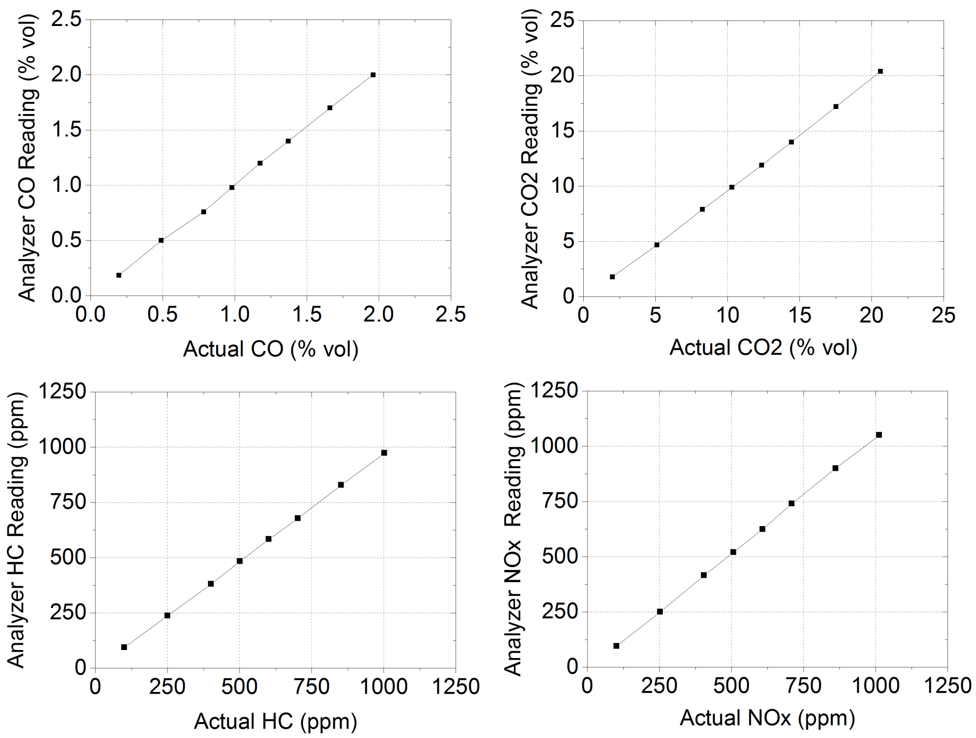

Figure 3.7: Gas analyzer's performance verification with calibration gases.

3.2 Design of engine experiments

3.2.1 Selection of engine speeds and loads

It is important to know an engine's most utilized operating range over the drive cycles. This helps to identify engine speeds and loads corresponding to this range over which engine's performance improvement is imperative. A basic vehicle simulation using GT-Power was therefore performed over drive cycles (such as NEDC, WLTC, UDDS, US06, and HWFET) to estimate plausible engine speed and load space. The vehicle data used was from the Ford Fusion model equipped with the 2.L EcoBoost engine. Figure 3.8 presents the time utilization histogram of engine speed and load over the aforementioned drive cycles grouped into two segments. Based on these cycle analyses, three engine speeds (1500, 2000, and 2500 RPM) and four loads (3, 6, 9, and 12 bar BMEP) were selected to form the speed-load matrix for engine experiments.

3.2.2 DI CNG injection timing limits

Fuel flow through a high-pressure CNG injector can be considered as a compressible flow. When the ratio of cylinder-to-injection pressure satisfies Eq. 3.2.1, then the gas flow is choked, resulting in a constant maximum fuel flow rate through the injector.

$$\frac{P_{\mathrm{cyl}}}{P_{\mathrm{inj}}} \leq \left(\frac{2}{\gamma+1}\right)^{\frac{\gamma}{\gamma-1}}, \tag{3.2.1}$$

where $\mathrm{P_{inj}}$ is the fuel injection pressure, $\mathrm{P_{cyl}}$ is the in-cylinder pressure, and γ is the specific heat ratio of fuel at the upstream condition.

For a constant fuel injection pressure, fuel flow regime transitions to an unchoked regime if the start of injection is sufficiently retarded. This can lead to considerable variations in the fuel flow rate depending on the chamber condition and result in improper performance calibration of the engine. Therefore, it is critical to ensure that the injector remains choked throughout the engine operation.

A basic calculation was performed to estimate the crank angle position of the end of injection up to which the choked flow condition can be maintained. As a part of

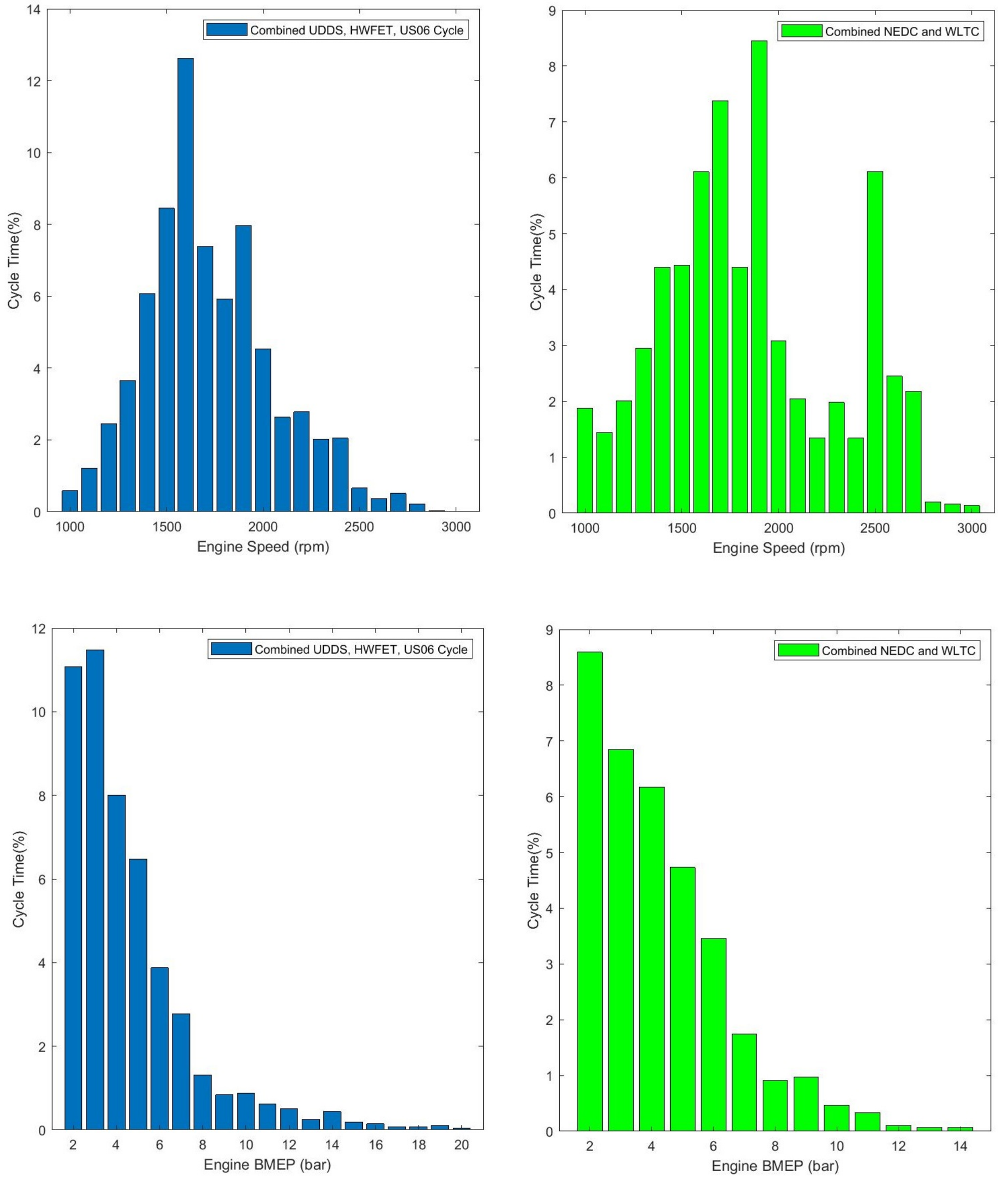

Figure 3.8: Estimated time usage of various engine speed and load over two sets of combined drive cycles.

this, Eq. 3.2.1 along with the fuel rail condition of P_{inj} = 16 bar and T_{inj} = 38 °C was used to estimate an upper limit for in-cylinder pressure resulting in choked fuel flow. Fig. 3.9 shows this upper limit ($P_{cyl\text{-}choke}$) superimposed onto the calculated in-cylinder pressure (P_{cyl}) based on the isentropic compression process using various manifold air pressures (MAP) as initial conditions. The crank angle location at the intersection of P_{cyl} and $P_{cyl\text{-}choke}$ indicates the maximum end limit of the fuel injection for a given MAP to ensure the choked flow. On the other hand, the maximum advanced start of injection in the intake stroke needs to avoid any CNG flow back into the intake manifold. Considering these criteria, the start of injection timing ranging from 320 to 80 deg bTDC$_{Fire}$ was initially selected, though this could be changed depending on the operating conditions during the engine experiments.

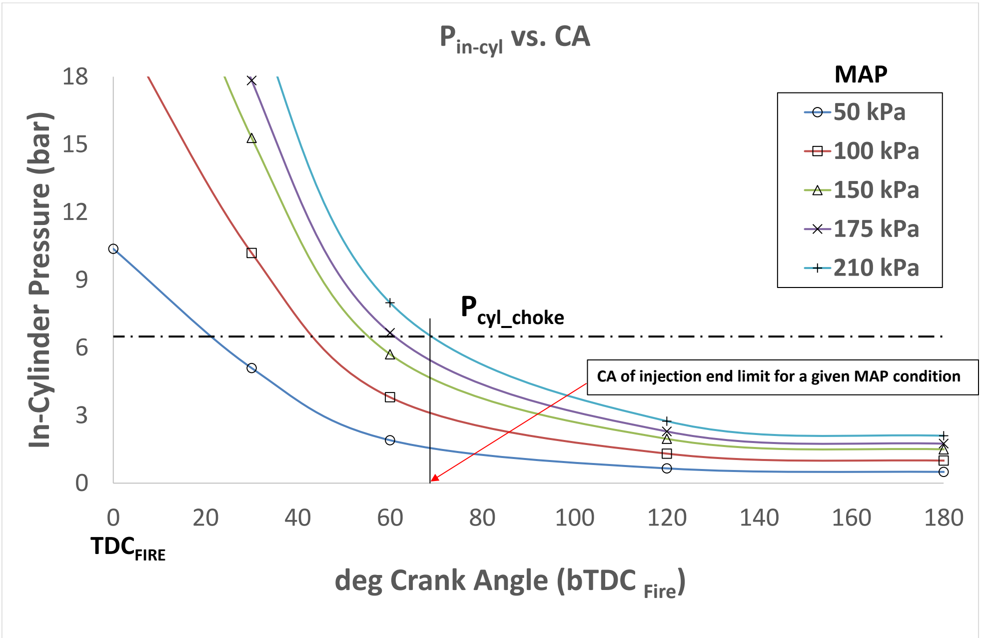

Figure 3.9: Estimation of injection end limit for choked flow.

3.2.3 Turbomachinery control for dilution tests

The experiments featuring air or EGR dilution deviate from the factory operation and therefore require an appropriate control strategy for the turbomachinery. One of the goals in the dilution tests, which are conducted at part-load conditions, is to maintain the atmospheric pressure in the intake manifold to avoid pumping losses and maximize the fuel efficiency. The engine controller has the flexibility to run the turbomachinery in two different modes to accomplish this objective.

Mode 1: Operate the turbomachinery with factory settings. Adjust the throttle position to maintain the manifold air pressure (MAP) at 1 atm for varying amounts of dilution.

Mode 2: Operate the turbomachinery with a fully open wastegate, which will prevent any boosting. Maintain wide open throttle (WOT) to ensure the atmospheric pressure in the manifold. In this mode, increasing the amount of dilution will decrease the engine torque.

For this study, 'Mode 2' is used in all experimental conditions featuring dilution for the following reasons.

1. When running with the wastegate fully open, no work is extracted from the waste heat of the exhaust by the turbomachinery. Thus, the exhaust temperature is higher than that of Mode 1. The increased temperature is preferred for better conversion of emissions in the catalytic converter, as exhaust gas temperatures (EGTs) are already low when using high dilution rates.

2. The pressure of the exhaust in Mode 2 is higher than in Mode 1 because the exhaust enthalpy is not utilized by the turbine. This allows for a higher maximum EGR flow rate through the engine's low-pressure EGR loop, which enables a broader range of engine load to be metered by EGR at WOT. This load metering method is favorable when operating the engine at stoichiometry with EGR, as the overall drive cycle efficiency will be increased by removing throttling at part load.

The reader is referred to Appendix B.1 for additional experimental results regarding these points. Note in instances where external dilution is unable to control the load due to excessive combustion instability and engine misfire, the throttle position was closed from WOT to decrease the load. Therefore, when the load was held constant with a varying amount of dilution at a given speed, the throttle position was also varied.

Table 3.4 presents an overview of a detailed test plan comprising various experimental modes and operating conditions with both GDI and DI CNG. To ensure the consistency of measured results, two sets of reference experiments, i.e., WOT motoring test at 1500 RPM and stoichiometric firing test at 1500 RPM and 6 bar BMEP, were repeated regularly. The peak pressure variation is observed less than 1% for both motoring and firing experiments, ensuring the repeatability of operating conditions. Once the steady-state condition was reached, measurements were taken over two minutes for the engine performance analysis.

Table 3.4: Experimental test matrix for Gasoline and CNG experiment

<table>
<tr><th>Fuel</th><th>Test Mode</th><th>BMEP (bar)</th><th>Speed (RPM)</th><th>Lambda</th><th>EGR (%)</th><th>2nd inj (%)</th><th>Fuel Pr (bar)</th><th>SOI ($bTDC_{Fire}$)</th><th>Spark ($bTDC_{Fire}$)</th><th>Valve timing (deg)</th><th>Other Conditions</th></tr>
<tr><td rowspan="3">Gasoline</td><td>Stoichiometric</td><td>3, 6, 9, 12</td><td>1500, 2000, 2500</td><td rowspan="2">1</td><td>NA</td><td rowspan="3">NA</td><td>28-108</td><td rowspan="3">280</td><td>4 to 32</td><td>2-42 (InAdv)
0-28 (ExRtd)</td><td rowspan="9">T_{air} : 38^{0}C
(after charge cooler)
$T_{coolant}$: 90 ^{0}C</td></tr>
<tr><td>External EGR</td><td rowspan="2">6</td><td rowspan="2">2500</td><td>0-25 %</td><td rowspan="2">70</td><td>19 to 31</td><td rowspan="2">20 (InAdv)
0 (ExRtd)</td></tr>
<tr><td>Air Dilution</td><td>1.1, 1.2, 1.3</td><td>NA</td><td>19 to 29</td></tr>
<tr><td colspan="11"></td></tr>
<tr><td rowspan="5">CNG</td><td rowspan="2">Start of Injection Timing (SOI) Sweep</td><td>3, 6, 9
(Part Load)</td><td rowspan="2">1500, 2000, 2500</td><td rowspan="2">1</td><td rowspan="3">NA</td><td rowspan="4">NA</td><td rowspan="5">16</td><td>80 to 320
(increment 40^0)</td><td rowspan="5">MBT</td><td rowspan="2">2-42 (InAdv)
0-28 (ExRtd)</td></tr>
<tr><td>12
(High Load)</td><td>close to IVC</td></tr>
<tr><td>Air Dilution</td><td rowspan="2">3 to 8</td><td rowspan="2">1500-2500</td><td>1.1, 1.2, 1.3, 1.4, 1.5, 1.6</td><td rowspan="2">Optimized SOI</td><td rowspan="3">Similar to SOI mode Settings</td></tr>
<tr><td>External EGR</td><td>1</td><td>0 - 25 %</td></tr>
<tr><td>Multi-pulsing</td><td>6, 8</td><td>2000</td><td>1, 1.4</td><td>NA</td><td>40, 25</td><td>1st - Single inj
2nd - 110, 140,180</td></tr>
</table>

3.3 Combustion analysis

The underlying mechanisms governing the engine performance trends are generally explained using various aspects of the combustion process. Here, Gamma Technologies' GT-Suite software was used to perform the heat release analysis and characterise the combustion process. The stages involved in the performed analysis, including the model development and two-zone combustion analysis, are discussed in the following sections.

3.3.1 Engine model development

In this work, a single-cylinder and a detailed multi-cylinder full engine model were built based on the test bench set up using GT-Power. The single-cylinder model (SCM) consists of a cylinder and a crank-train object only, while the full engine model (FEM) includes all of the engine components of the test bench from air entry to exhaust gas out, as shown in Figure 3.10. Various GT templates were implemented in the model, incorporating parametric information of the test engine and other parts of the test bench (Table 3.5). The model building procedure and descriptions of various templates are detailed in GT-Power manuals [151, 152].

In this study, GEM 3D (a GT graphical tool) was used to capture accurate geometric

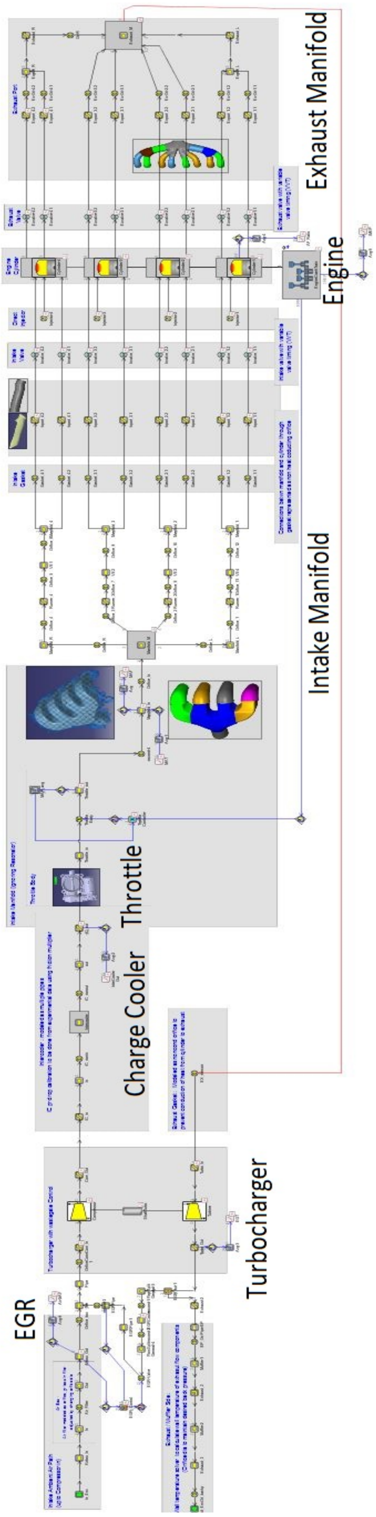

Figure 3.10: Full engine model.

Table 3.5: Parameters required to build an engine model in GT-Power

Engine characteristics	Compression ratio, firing order, no of stroke
Cylinder geometry	Bore, stroke, connecting rod length, pin offset, TDC clearance height, no of cylinder
Intake and Exhaust system	Geometry details of flow components such as manifolds, runners, ports, and exhaust tailpipe
Throttle body	Throttle diameter and location, discharge coefficients vs. throttle angle
Fuel injector	Location and number of injectors, Injection rate and timing, air-fuel ratio, fuel type, and LHV
Intake and Exhaust valves	Valve diameter and lash, lift profile, discharge coefficients, swirl and tumble coefficient
Turbocharger and intercooler	Turbine and compressor maps, intercooler geometry and effectiveness
Ambient state	Pressure, temperature, and humidity

information of intricated components such as intake and exhaust ports in the cylinder head. Once the 3D geometry is imported into this toolbox, it is then converted into regular shapes (e.g., pipes, flow-splits), and finally discretized for direct utilization in GT-Power model (see Fig.3.11) [153].

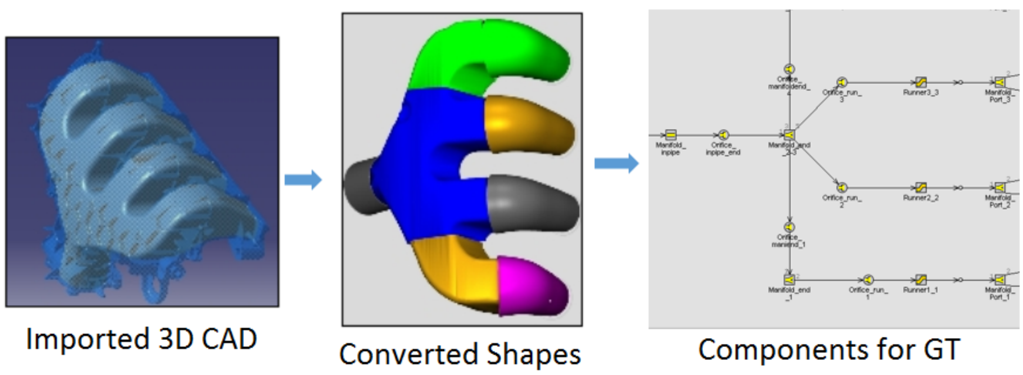

Figure 3.11: An example of intake port geometry import using GEM 3D [153].

Experimental data that were primarily utilized to tune and calibrate the engine model are presented in Table 3.6. Calibration of the full engine model, particularly at part load, requires the implementation of model-based controllers that match the experimental conditions at different flow path locations of the model. Here, the following controllers were used.

Table 3.6: Experimental data used for model calibration

In-cylinder pressure, manifold air pressure (MAP), and exhaust gas pressure
Manifold air temperature (MAT), compressor-out temperature, and EGT
Air and fuel flow rate, EGR rate
Fuel injection timing and pulse width, ignition timing
Engine speed, normalized air-fuel ratio (λ)

1. Throttle controller to match manifold air pressure.

2. Wastegate actuator for boost pressure matching.

3. EGR controller to target tested EGR flow rate.

Once the engine model was built, combustion analysis was performed using the measured experimental data. The detailed methodology of the combustion analysis is discussed in the subsequent sections.

3.3.2 MFB calculation methodology

This section presents the methodology used for mass fraction burned (MFB) calculation based on the two-zone combustion model. In this approach, the combustion chamber is divided into two zones: an unburned zone and a burned zone. At the time of ignition, all of the cylinder contents are assumed to be in the unburned zone. At each time step, a mixture of fuel and air is transferred from the unburned zone to the burned zone based on either the prescribed or calculated burn rate. The unburned and burned zone temperatures and cylinder pressure are then obtained using the energy equation.

Figure 3.12 shows the steps involved in the MFB calculation. The modeling procedure begins with the initial estimation of burn parameters using Rassweiler-Withrow (R-W) method followed by the GT-Power non-predictive forward and reverse run simulation for final burn rate calculation.

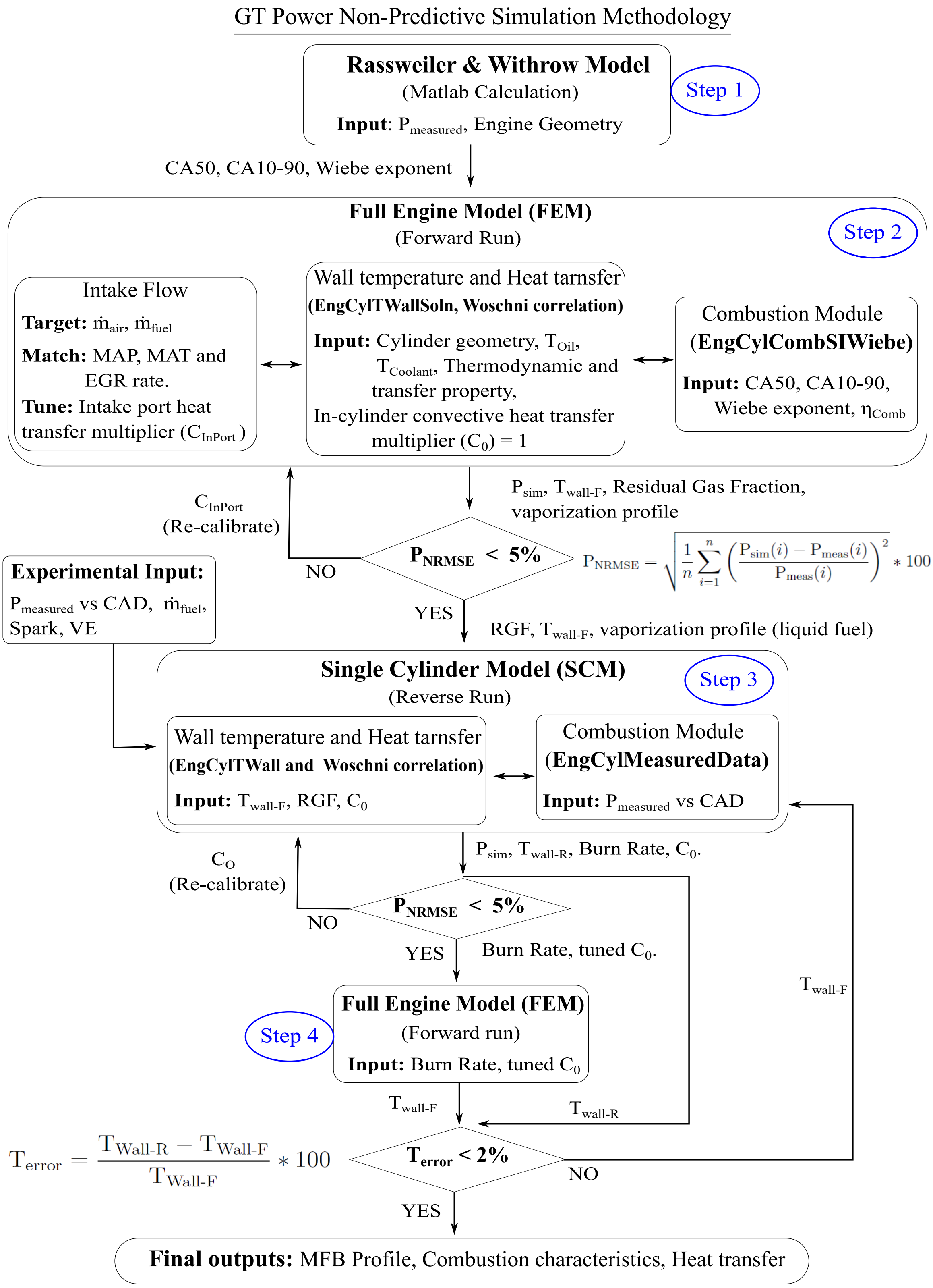

Figure 3.12: MFB calculation methodology.

3.3.2.1 Estimation of burn parameters by Rassweiler and Withrow principle

In this step, burn parameters such as the location of 50% MFB (CA50), the 10-90% MFB duration (CA10-90), and the Wiebe exponent (m) are estimated using the measured in-cylinder pressure and instantaneous volume data based on the Rassweiler and Withrow (R-W) method [37, 154]. The reader is referred to Appendix A.1 for the detailed calculation procedure. This method has limitations as it neglects the combustion efficiency and wall heat transfer, and uses an approximate polytropic index. Therefore, these parameters were only used for the initial estimation of wall temperatures and residual gas fractions.

3.3.2.2 Full engine simulation with Wiebe parameters

In this step, a non-predictive combustion simulation was performed using the full engine model to estimate wall temperatures, residual gas fraction, and fuel evaporation profile (for liquid fuel only). Here, the EngCylCombSIWiebe template was used to impose the estimated burn parameters by the R-W method as model inputs. In-cylinder heat transfer was modeled using Woschni's correlation combined with a thermal impedance network specifically developed for the engine under investigation. EngCylTWallSoln template, which incorporates the information regarding the engine's cooling passage and the state of cooling fluids was implemented to calculate the wall temperatures. Equation 3.3.1 was used to calculate the heat-transfer from the combustion gases to the chamber walls.

$$\dot{q}_{\text{Wall}} = C_0 h_w (T - T_{Wall}), \tag{3.3.1}$$

where $\dot{q}_{\text{Wall}}$ is the wall heat flux, h_w is the convective heat transfer coefficient based on Woschni's correlation, T and T_{Wall} are the temperatures of the gases and walls, respectively, and C_0 is the convective heat transfer multiplier used to calibrate the in-cylinder wall heat losses.

For accurate estimation of the residual gas fraction (RGF), particular attention was paid to model the intake and exhaust flow system with proper valve timings, lift profiles, and flow coefficients. For liquid fuel injection, a fuel evaporation model was also implemented to capture its impact on the volumetric efficiency and in-cylinder temperature history. Fuel distillation curve, DI injector geometry, and mass flow rate are all considered in this model.

Fluid dynamic calibration of the full engine model is vital as the air flow ($\dot{m}_{\mathrm{air}}$) entering into the cylinder determines the injected fuel mass for a given air-fuel ratio, thus influencing the in-cylinder pressure profile. To ensure that this parameter is captured accurately, experimentally measured manifold air pressure and temperature (i.e., MAP and MAT) and EGR flow rate (in case of EGR dilution) were matched using model controllers and multipliers. It is also imperative to tune the heat transfer through intake ports as the corresponding temperatures impact the density of the inducted air, hence the related airflow rate. As these temperatures were not measured, tuning heat transfer at these locations and thus calibration of the air flow rate was performed using the intake port heat transfer multiplier ($\mathrm{C_{InPort}}$).

Equation 3.3.2 shows the metric chosen for the comparison between simulated and measured in-cylinder pressure.

$$\mathrm{P_{NRMSE}} = \sqrt{\frac{1}{n}\sum_{i=1}^{n}\left(\frac{\mathrm{P_{sim}}(i) - \mathrm{P_{meas}}(i)}{\mathrm{P_{meas}}(i)}\right)^2} * 100, \tag{3.3.2}$$

where $\mathrm{P_{meas}}$ and $\mathrm{P_{sim}}$ are the in-cylinder pressure obtained from measurement and simulation over the crank angle, respectively, and n is the total number of crank angle samples. Here, a threshold of $\mathrm{P_{NRMSE}}$=5% was chosen as the convergence criterion for simulations [148]. The reason behind this selection was that the maximum allowable COV_{IMEP} was less than 5% in this work. The full engine model has two important multipliers, $\mathrm{C_{InPort}}$ and $\mathrm{C_0}$, that are generally tuned manually to calibrate the intake port and in-cylinder wall heat-transfer. As the simultaneous tuning of $\mathrm{C_{InPort}}$ and $\mathrm{C_0}$ would make the calibration process cumbersome, only $\mathrm{C_{InPort}}$ was tuned at this stage (keeping the value of $\mathrm{C_0}$ fixed at one) so that the trapped fuel mass matched the measured fuel mass and $\mathrm{P_{NRMSE}}$ was less than 5%. Once the model met the convergence criterion for a tuned $\mathrm{C_{InPort}}$, simulation results were used as inputs for the reverse run of the single-cylinder model in the next step.

3.3.2.3 Reverse run simulation of single cylinder model

In this step, a reverse run simulation of the single-cylinder model was performed only for the closed part of the engine cycle using 'Analysis, Closed Volume (CPOA)' simulation mode. Input parameters for reverse run analysis are presented in Table 3.7. Engine-out emissions (i.e., CO and UHC) were used for the estimation of

Table 3.7: Input data for reverse run simulation

Measured data	In-cylinder pressure, volumetric efficiency (VE), fuel flow rate ($\dot{m}_{fuel}$), state of incoming air, and concentration of engine-out CO and UHC emissions
Simulated data	RGF, fuel vapour fraction, and wall temperatures

combustion efficiency and, therefore, a more accurate calculation of MFB profile. The reverse run solver is unable to calculate in-cylinder wall temperatures as it runs only two cycles. Therefore, wall temperatures obtained from the full engine model were imposed into this model using an EngCylTWall template to allow the heat transfer calculation based on the Woschni's correlation.

In this simulation, the measured in-cylinder pressure profile was used as input using an EngBurnRate template. The combustion burn rate was calculated iteratively so that the simulated cylinder pressure matched the measured pressure trace. The convective heat transfer multiplier (C_0) was varied between 0.8 to 1.2 to calibrate the in-cylinder heat transfer and to obtain a close agreement between the simulated and measured in-cylinder pressure based on the $P_{NRMSE} < 5\%$ criterion discussed earlier. An example of the effect of convective heat transfer multiplier is shown in Fig. 3.13. Once an optimal C_0 is determined, this quantity and the corresponding burn rate profile are used as inputs to the final modeling step.

3.3.2.4 Final full engine model simulation with burn rate

In this step, full engine model simulation was performed using the burn rate profile calculated by the previously used reverse run model. All parameters incorporated earlier in the full model were preserved, except the followings:

- CylCombProfile template: this template was implemented instead of

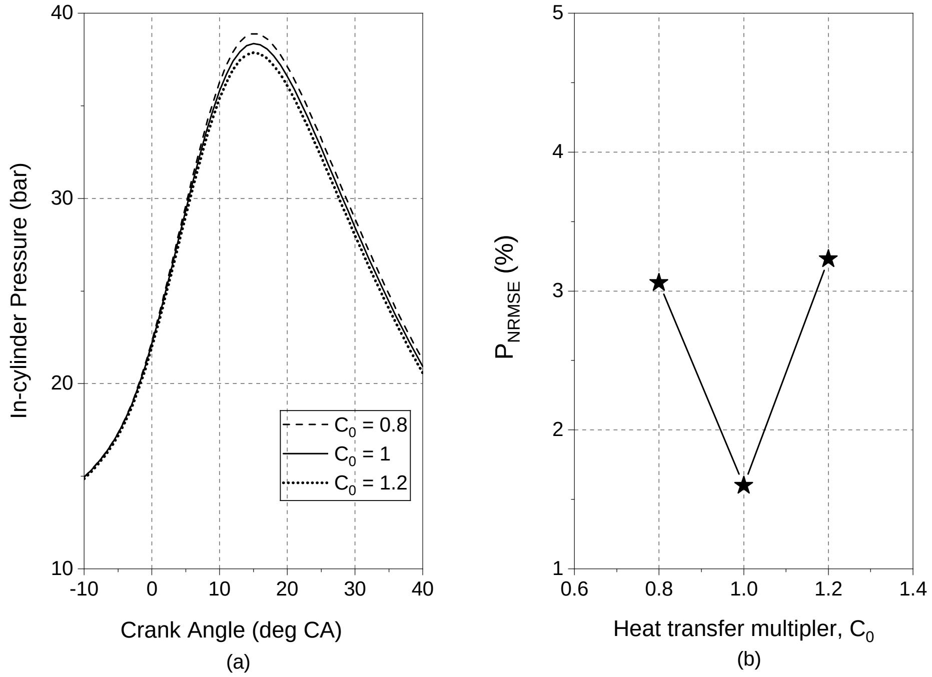

Figure 3.13: Single cylinder reverse run results: (a) simulated pressure and (b) P_{NRMSE} for different C_0 with CNG fuelling at 2500 RPM, 6 bar BMEP, and $\lambda = 1$.

'EngCylCombSIWiebe template' to input the burn rate profile.

- Tuned C_0: the convective heat transfer multiplier (C_0) that gave the best pressure match in reverse run simulation was used here as model input.

Once the full engine simulation is completed, it is essential to compare the calculated wall temperatures with those previously used in the reverse run model as they were initially estimated based on the Wiebe burn parameters. Equation 3.3.3 was used for this comparison.

$$T_{error} = \frac{T_{Wall\text{-}R} - T_{Wall\text{-}F}}{T_{Wall\text{-}F}} * 100, \tag{3.3.3}$$

where $T_{Wall\text{-}R}$ and $T_{Wall\text{-}F}$ are the wall temperatures used in the reverse run model and calculated from the final full engine model, respectively. T_{error} within 2% ensures that the applied wall temperatures in the reverse run of the single-cylinder model are reasonable. If T_{error} is not within the limit, the steps in Sections 3.3.2.3 and 3.3.2.4 are repeated with the latest T_{Wall} until simulation convergence is obtained. Once the temperature comparison was established within the limit, results from the final full engine model simulation were used for the combustion analysis. Fig. 3.14 presents such a result comparing the simulated and measured in-cylinder pressure for stoichiometric CNG fuelled operation at 2500 RPM and 6 bar BMEP.

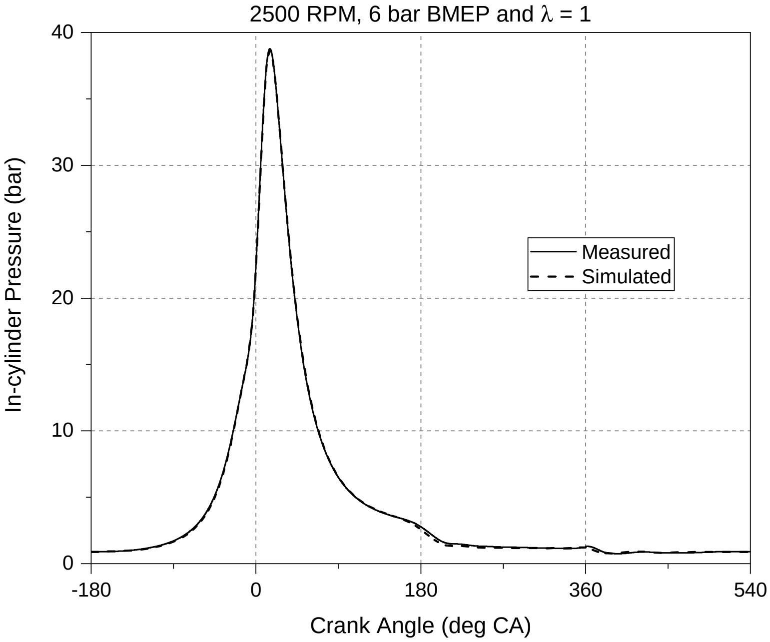

Figure 3.14: Full engine model simulation results: measured vs. simulated in-cylinder pressure for CNG fuelling at 2500 RPM, 6 bar BMEP, and $\lambda = 1$.

3.3.3 Predictive combustion simulation methodology

This section describes the predictive combustion simulation process which is used to gain an additional insight into the governing physics of premixed, turbulent combustion, particularly at the limits of bulk flame quenching. The combustion model is based on the 'Entrainment and Burn-up Flame' theory [45, 48, 49], which postulates that the unburned air-fuel mixture is entrained into the turbulent flame brush and then burns up at a rate governed by the amount of unburned mass within the flame divided by a characteristic time for eddy burn-up. The governing equations of the combustion model are as follows:

$$\frac{dm_e}{dt} = \rho_u A_e \left(S_L + u^t\right), \tag{3.3.4}$$

$$\frac{dm_b}{dt} = \frac{m_e - m_b}{\tau_b}, \tag{3.3.5}$$

$$\tau_b = \frac{l_T}{S_L}, \tag{3.3.6}$$

where m_e is the total mass entrained by the outer flame envelope surface, m_b is the total burned mass, ρ_u is the density of the unburned mixture, A_e is the area of flame front required to entrain m_e, S_L is the laminar flame speed, u^t is the turbulent intensity, τ_b is the characteristic time for eddy burn-up, and l_T is the Taylor micro-scale of turbulence.

The goal of the model calibration step is to predict a MFB profile similar to that obtained by the reverse run analysis. This is performed by tuning various multipliers that affect the combustion process. This includes tuning the turbulent flame speed (C_{TFS}) and Taylor length scale (C_{TLS}) multipliers to influence the turbulent intensity and length scale, the flame kernel growth multiplier (C_{FKG}) to impact the initial growth rate, and the dilution effect multiplier (C_{DE}) for any dilution impact on the flame speed. Figure 3.15 shows the stages involved in the predictive combustion simulation process, and details are discussed in the subsequent sections.

3.3.3.1 Calculation of in-cylinder flow parameters at IVC

The GT-Power full engine model (FEM) developed in Section 3.3.1 was used here to calculate the in-cylinder flow characteristics such as swirl and tumble number, turbulent intensity, and length scale at the intake valve closure. The 'EngCylFlow' module, which includes geometric features of the cylinder and piston, was implemented in the full model to provide the information regarding swirl, tumble, and turbulence. These parameters are pre-requisites for the final step of the premixed, turbulent combustion simulation. GT-Power flow model breaks the cylinder into four regions (i.e., central core, squish, head recess, and piston cup) and then calculates the mean radial, axial, and swirl velocities at each time step by taking into account the chamber geometry, piston motion, and flow rates of the incoming and outgoing gases through the valves [155]. The K_m-k-ϵ 0D in-cylinder flow model was used to calculate the turbulent intensity and length-scale by solving the mean kinetic energy (K_m), turbulent kinetic energy (k), and turbulent dissipation rate (ϵ) equations as described in [37, 155].

A forward run of the full engine model was performed using the burn rate data from the reverse run analysis. The results of the forward run such as wall temperatures, residual gas fraction, evaporation rate (liquid fuel only), and flow field parameters at IVC were then used as simulation inputs to the final step of the predictive calculation.

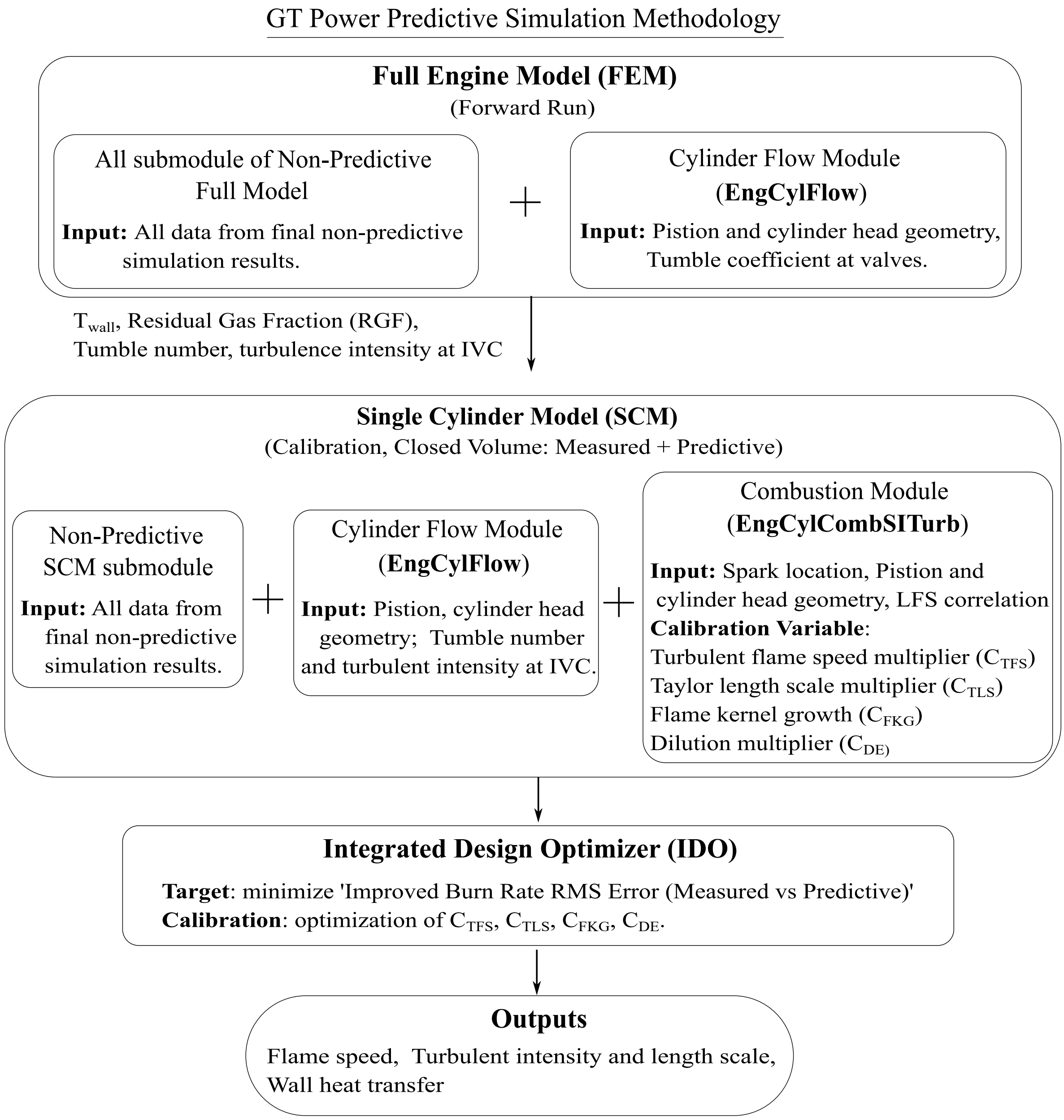

Figure 3.15: Predictive combustion simulation methodology.

3.3.3.2 Modelling laminar flame speed

The laminar flame speed for gasoline is modelled using Eq. 3.3.7, where the coefficients are given by Keck et al. [37, 56].

$$S_L = S_{L,0} \left(\frac{T_u}{T_{ref}}\right)^{\alpha} \left(\frac{P}{P_{ref}}\right)^{\beta} (1 - 2.06 * X)^{0.77}, \tag{3.3.7}$$

where T_u is the unburned gas temperature, P is the in-cylinder pressure, $P_{ref} = 1$ atm, $T_{ref} = 298$ K and X is the mass fraction of residuals in the unburned zone

For CNG, the laminar flame speed is modelled using the Eq. 3.3.8, and the coefficients are obtained from [152, 156].

$$S_L = S_{L,0} \left(\frac{\rho_u}{\rho_{ref}} \right)^{\epsilon} (1 - 2.06 * X)^{0.77} . \tag{3.3.8}$$

The effect of charge dilution can be modified using the dilution effect multiplier (C_{DE}).

3.3.3.3 Prediction of mass fraction burned

The single-cylinder model (SCM) along with inputs discussed in Section 3.3.2.3 was used here to predict the MFB profile. Additionally, the 'EngCylFlow' module was used to incorporate the flow characteristics at IVC obtained from the full engine model results (Section 3.3.3.1) as simulation inputs. An 'EngCylCombSITurb' module was implemented to perform turbulent combustion calculations based on the 'Entrainment and Burn-up Flame' theory taking into account the flame geometry information, laminar flame speed (S_L), and the effect of calibration multipliers (i.e., C_{TFS}, C_{TLS}, C_{FKG}, and C_{DE}) [151]. The predictive run was performed with the 'Closed Volume, Measured + Predicted (M+P)' analysis mode for the closed part of the cycle to predict the burn rate. The Integrated Design Optimizer (IDO) tool of GT-Suite was used to minimize the 'Improved Burn Rate RMS Error' between the reverse run and predicted MFB results. This was accomplished by performing an optimization sweep of calibration multipliers (i.e. C_{TFS}, C_{TLS}, C_{FKG}, and C_{DE}) within the range of 0.5 to 3 [151, 157].

3.3.3.4 Validation of predictive combustion model

Figure 3.16 (a) shows a comparison of the MFB profiles predicted by the turbulent combustion simulation and reverse run analysis for CNG fuelled operation at 2000 RPM, 3 bar BMEP, and $\lambda = 1$. As shown, the results are in a good agreement. Both measured and predicted results of in-cylinder pressure are also closely matching (i.e. $P_{\mathrm{RMSE}} << 5\%$) as shown in Fig. 3.16 (b). Furthermore, Fig. 3.17 shows a good agreement between predicted and non-predicted results in the case of

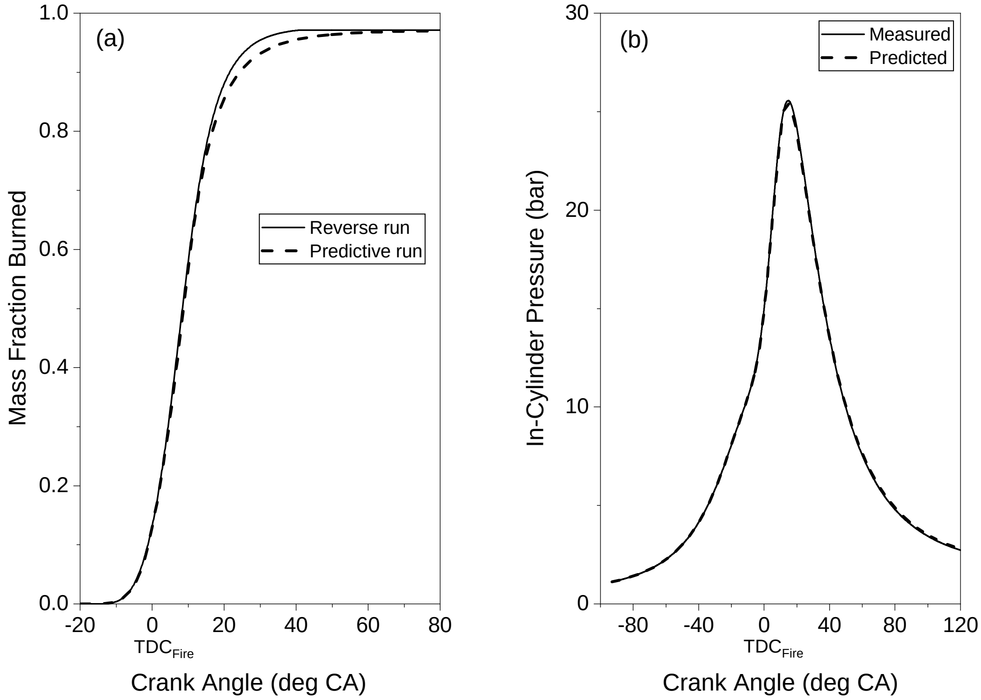

Figure 3.16: Predictive combustion simulation results at 2000 RPM, 3 bar BMEP, and $\lambda = 1$ with CNG fuelling: (a) MFB Profile comparison (reverse run vs. predictive run) and (b) In-cylinder pressure comparison (measured vs. predicted).

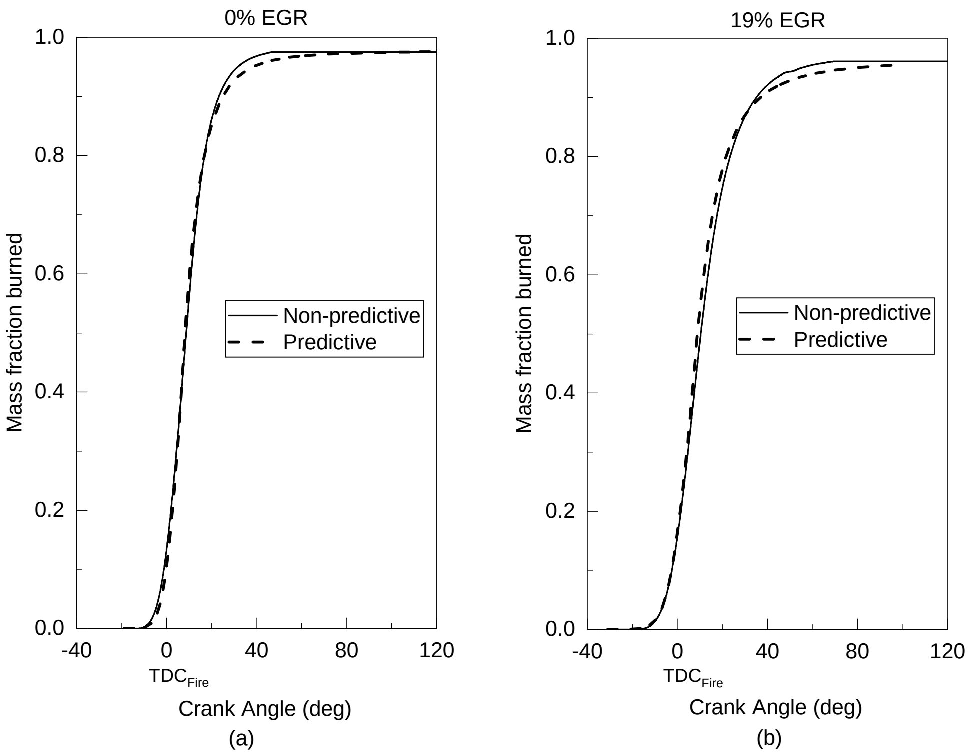

Figure 3.17: Comparison of mass fraction burned (MFB) profiles calculated from GT-power reverse and predictive model simulation for CNG fuelled stoichiometric operation with (a) 0% EGR and (b) 19% EGR at 2500 RPM and 6 bar BMEP.

stoichiometric operation with 0% EGR and 19% EGR at 2500 RPM and 6 bar BMEP conditions. These results confirm the predictive model's accuracy, and therefore, it is used extensively in the subsequent result chapters.

3.4 Analysis of cycle energy share and energy balance methodology

3.4.1 Cycle energy analysis

Cycle energy analysis is performed to obtain the share of input fuel energy at each of the four individual strokes in the engine cycle. This is determined by dividing the average work done during each stroke (calculated by integrating the in-cylinder pressure trace over the cylinder volume as a function of crank angle) by the input fuel energy. The percentage of input fuel energy share for expansion, compression and the gas exchange process are calculated as:

$$\text{Gas exchange energy}\,(\%),\; E_{GE} = \frac{\int_{\theta_{EVO}}^{\theta_{IVC}} PdV}{m_f * LHV_f} \times 100,$$

$$\text{Compression energy}\,(\%),\; E_{Comp} = \frac{\int_{\theta_{IVC}}^{\theta_{Spark}} PdV}{m_f * LHV_f} \times 100,$$

$$\text{Expansion energy}\,(\%),\; E_{Exp} = \frac{\int_{\theta_{Spark}}^{\theta_{EVO}} PdV}{m_f * LHV_f} \times 100,$$

$$ITE\,(\%) = E_{Exp} - (E_{Comp} + E_{GE}),$$

where m_f is the fuel mass per cycle per cylinder, LHV_f is the lower heating value of the fuel, P is the in-cylinder pressure, V is the instantaneous cylinder volume, θ_{IVO} is the crank angle at the intake valve opening, θ_{IVC} is the crank angle at the intake valve closing, θ_{EVO} is the crank angle at the exhaust valve opening, θ_{Spark} is the crank angle at the point of ignition, and ITE is the indicated thermal efficiency. The gas exchange energy represents the combined energy share of both the exhaust and intake strokes in the engine cycle.

3.4.2 Energy balance methodology

A first law energy balance for an internal combustion engine provides a distribution of the injected fuel's chemical energy during the engine cycle. Therefore, it is utilized as an additional tool to explain engine performance trends. For the control volume around the engine shown in Fig. 3.18, the steady flow energy conservation equation representing energy flow into and out of the engine can be expressed as:

$$\dot{m}_f h_f + \dot{m}_a h_a = \dot{W}_b + \dot{Q}_L + \dot{m}_e h_e, \tag{3.4.1}$$

where $\dot{m}$ is the mass flow rate, h is the specific enthalpy, $\dot{W}_b$ is the brake work output, and $\dot{Q}_L$ is the total heat losses. Subscripts a, f and e denote the air, fuel and exhaust, respectively. The specific enthalpy (h) is composed of two parts, i.e. h= h_s + h'_r, where h_s is the sensible enthalpy and h'_r is reference state enthalpy. It is noted that $h_a = 0$ for air at reference state of 298 K and 1 atm.

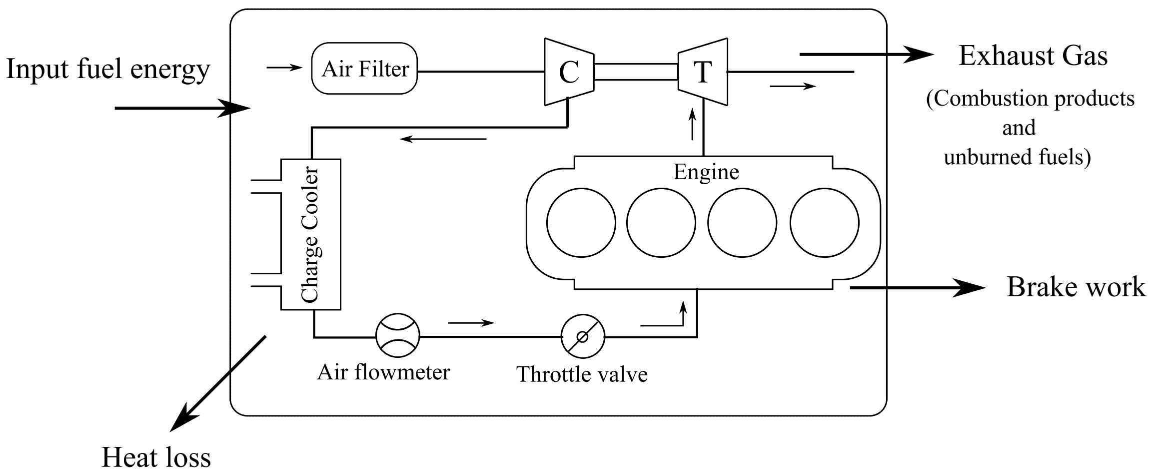

Figure 3.18: Control volume of an IC engine with energy flow in and out.

By considering the sensible part of the enthalpy, Eq. 3.4.1 can be written as [37, 158]:

$$\dot{m}_f LHV_f = \dot{W}_b + \dot{Q}_L + \dot{H}_{UBF} + \dot{H}_{Exh}, \tag{3.4.2}$$

where $\dot{H}_{Exh}$ is the sensible enthalpy of the gases in the engine exhaust and $\dot{H}_{UBF}$ is the loss of unburned fuel energy. These are calculated as:

$$\dot{H}_{Exh} = \sum_i \dot{m}_i \, h_{s,i},$$

$$\dot{H}_{UBF} = \dot{m}_{CO} \, LHV_{CO} + \dot{m}_{UHC} \, LHV_{UHC},$$

where $\dot{m}_i$ and $h_{s,i}$ are the mass flow and sensible enthalpy of the ith species in the exhaust, which are obtained based on the measured emission species, exhaust gas temperature and pressure. LHV$_{CO}$ and LHV$_{UHC}$ are the lower heating values of CO and UHC, respectively. After obtaining the values of input fuel energy ($\dot{m}_f LHV_f$), brake work output ($\dot{W}_b$), exhaust gas sensible enthalpy ($\dot{H}_{Exh}$), and unburned fuel energy ($\dot{H}_{UBF}$) from the measurement data, total heat losses ($\dot{Q}_L$) are inferred as a balance of remaining energy based on Eq. 3.4.2.

The inferred total heat losses ($\dot{Q}_L$) can be expressed as the sum of several terms:

$$\dot{Q}_L = \dot{Q}_{In-Cyl} + \dot{Q}_{Fr} + \dot{Q}_{Pump} + \dot{Q}_{misc}, \tag{3.4.3}$$

where $\dot{Q}_{In-Cyl}$ is the in-cylinder wall heat transfer between the hot combustion gas and the cylinder walls (calculated from the GT-Power full engine model simulation as described in section 3.3.2), $\dot{Q}_{Fr}$ is the energy losses due to friction, $\dot{Q}_{Pump}$ is the energy losses due to pumping, and $\dot{Q}_{misc}$ is the heat transfer from the engine's external surfaces (e.g., the outside surface of intake and exhaust valves, piping, etc.) needed to balance Eq. 3.4.3.

It is assumed that all of the engine pumping and friction work are dissipated as heat through the engine walls [158, 159], and therefore $\dot{Q}_{Pump}$ and $\dot{Q}_{Fr}$ are calculated as:

$$\dot{Q}_{pump} = \dot{W}_{iG} - \dot{W}_{iN},$$

$$\dot{Q}_{Fr} = \dot{W}_{iN} - \dot{W}_b,$$

where $\dot{W}_{iG}$ and $\dot{W}_{iN}$ are the indicated gross and net work, respectively. These are calculated from the measured in-cylinder pressure trace. Once all of these quantities related to energy flow into and out of the engine are obtained, they are plotted as a percentage of input fuel energy to demonstrate the distribution of initial fuel energy and characterize the engine performance.

3.5 Methodology of engine-out total CO_2 equivalent emissions calculation

CO_2 emissions from an internal combustion engine can be related to (a) fuel properties, (b) engine efficiency, and (c) actual road load [3]. One of the primary motivations to use CNG as a transportation fuel is the substantial abatement of CO_2 emissions that could be realized through this fuel substitution. However, methane, which is the main constituent of natural gas, has 25 times higher Global Warming Potential (GWP) than CO_2 over 100 years in the atmosphere [160]. Furthermore, engine-out NO_x emissions (considering only NO and NO_2) have also an estimated GWP of 7-10 for a time horizon of 100 years [161]. Therefore, all engine-out unburned hydrocarbon (UHC), assuming they are mainly methane (for CNG only), and NO_x are combined with measured CO_2 to form the engine-out total CO_2 equivalent emissions using Eq. 3.5.1.

$$CO_{2e} = CO_2 + 25 * UHC_{CH_4} + 10 * NO_x, \tag{3.5.1}$$

Note that this analysis overstates the importance of post-aftertreatment UHC and NO_x emissions, as the regulated pollutants would be reduced while CO_2 would not.

Chapter 4

Stoichiometric DI CNG and GDI Engine Operation

This chapter presents the engine performance and emissions observed from CNG and gasoline fuelled DI engine operation at stoichiometric conditions. The potential to improve engine fuel efficiency with CNG is investigated by varying injection timing under part load conditions and comparing against the engine's baseline performance with gasoline fuelling. Then, the benefits of using CNG over conventional fuels in a DI engine is considered for high load operation. Finally, a comparison of total engine-out greenhouse gas emissions from stoichiometric gasoline and CNG fuelled operation is presented at the engine load (3, 6, 9, and 12 bar BMEP) and speed (1500, 2000, and 2500 RPM) tested during experimentation.

4.1 Engine performance optimization with CNG at part load

There is strong motivation to focus on the part load performance of an SI engine, as these engines frequently operate in this load range and are inefficient at such conditions. In this section, the impact of the start of injection (SOI) timing of DI CNG on part load engine performance is examined, and the SOI that produces the highest fuel efficiency at a range of engine speeds and loads is determined.

4.1.1 Effect of injection timing on engine performance

An integral part of optimizing a DI system is the determination of an injection timing strategy that guarantees robust combustion and high fuel efficiency. The SOI is expected to impact both of these phenomena in a DI CNG engine, and therefore an injection timing sweep is necessary to realize peak performance from such an engine. For this work, SOI timings are classified into three different strategies as shown in Fig. 4.1 and referred to as:

- Advanced SOI: It represents the fuel injection timing occurring after 280 deg $bTDC_{Fire}$ and proceeding towards the intake valve opening (IVO).
- Retarded SOI: Injection timing occurring from 180 deg $bTDC_{Fire}$ towards the intake valve closure (IVC).
- Intermediate SOI: This is referred to as the injection timing that occurs between advanced and retarded SOI.

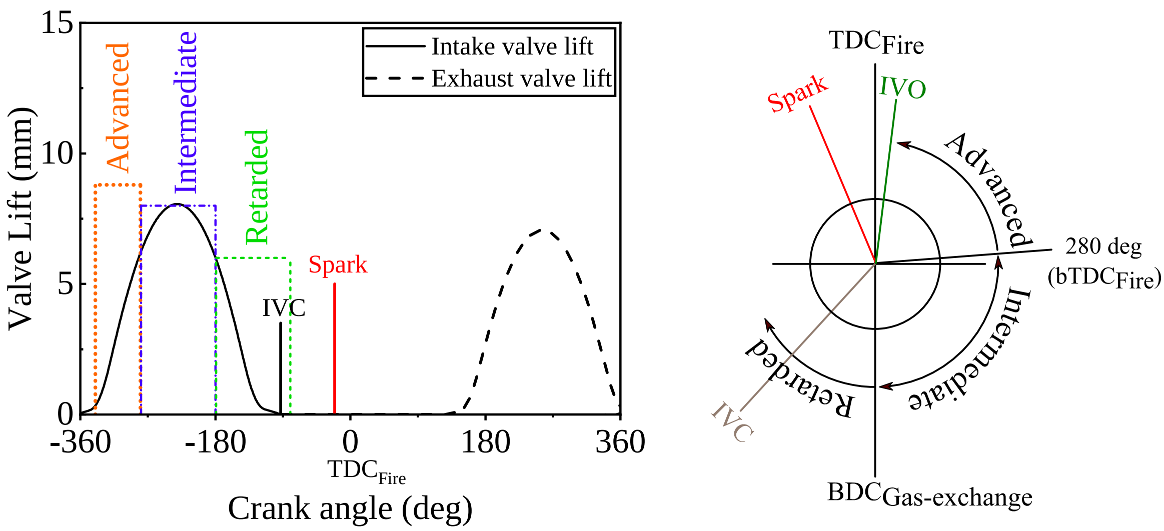

Figure 4.1: Classification of the start of injection (SOI) timing strategies.

Using DI CNG, the displacement of incoming air varies with the injection strategy, as shown in Fig. 4.2, which quantifies air displacement in terms of overall volumetric efficiency. For a given throttle position, i.e., a constant manifold air pressure (MAP), changing the start of injection from an advanced SOI of 300 deg $bTDC_{Fire}$ to a retarded SOI at 117 deg $bTDC_{Fire}$ increases the overall volumetric efficiency from 56% to 61%, indicating the reduction of air displacement by using a

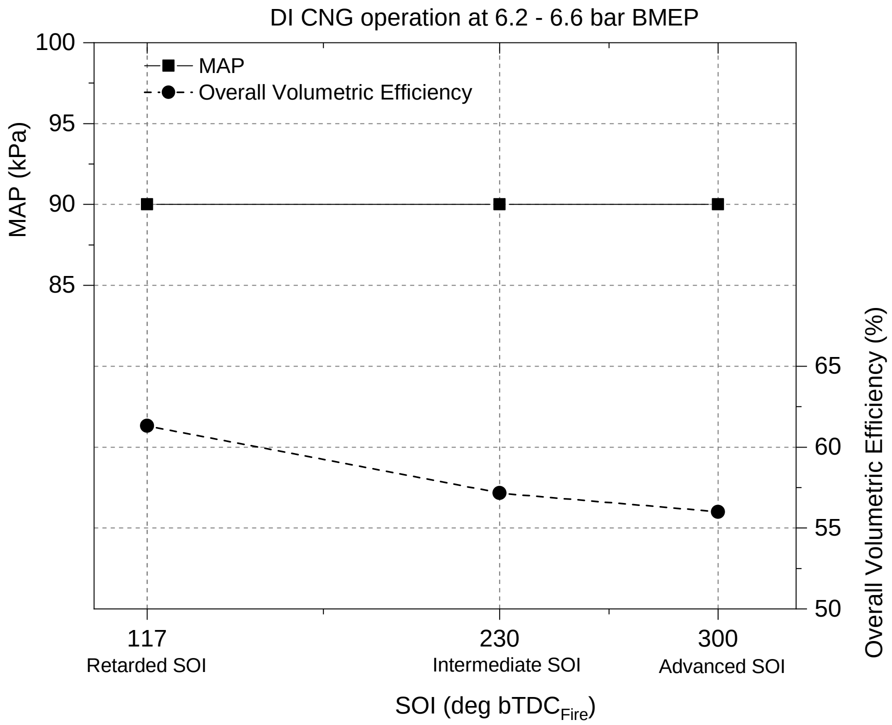

Figure 4.2: Effect of SOI timing on volumetric efficiency.

retarded injection strategy [91]. On the other hand, an advanced SOI can facilitate more time for enhanced fuel and air mixing before ignition. Because of these competing effects, it is hypothesized that there will be an optimal timing or range of SOI where engine performance is maximized. Therefore, SOI timing sweeps ranging from 107 deg bTDC$_{Fire}$ to 320 deg bTDC$_{Fire}$ are performed. Generally, the most retarded SOI timing is limited by the choked flow condition at the injector outlet (Section 3.2.2) and combustion stability criteria, whereas excessive flow of CNG back into the intake manifold appears to limit the most advanced SOI position. MBT ignition timing is maintained for all SOI sweep tests with CNG. Two engine operating conditions (i.e., 3 and 9 bar BMEP at 2000 RPM) are chosen as illustrative cases at low and mid-load to study the effect of SOI on engine performance.

Figure 4.3 shows the brake thermal efficiency (BTE) and volumetric efficiency for 3 and 9 bar BMEP cases as a function of SOI at 2000 RPM. For the 3 bar BMEP case, BTE peaks at 240 deg bTDC$_{Fire}$ with 23.5% and drops to a minimum of 22.7% at SOI 107 deg bTDC$_{Fire}$, whereas BTE varies from a maximum of 32% at 280 deg bTDC$_{Fire}$ to a minimum value of 30.7% at 130 deg bTDC$_{Fire}$ at 9 bar

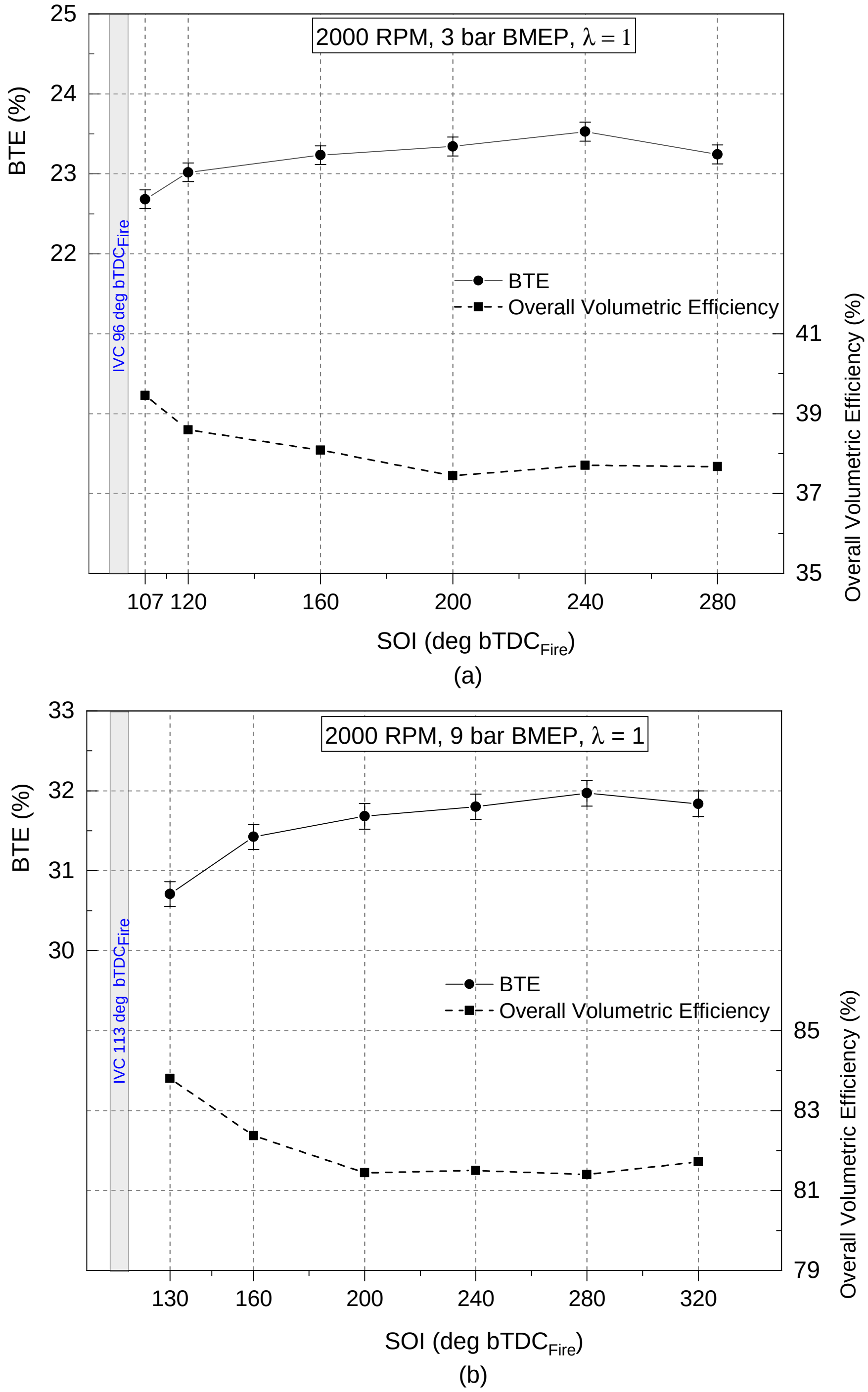

Figure 4.3: Brake thermal efficiency (BTE) and volumetric efficiency as a function of SOI at (a) 3 bar and (b) 9 bar BMEP, 2000 RPM, and $\lambda = 1$.

BMEP. For both load cases, there is no significant difference in BTE over the span of intermediate SOI relative to the maximum BTE value. However, lower efficiency is observed when using overly retarded SOI. The underlying physics of these observed BTE trends are discussed in the following sections based on the analysis of emission behaviour, combustion characteristics, and losses related to energy balance. As expected, a higher overall volumetric efficiency is measured for both load cases when fuel injection proceeds towards TDC_{Fire} (due to less air displacement), which is also consistent with the trend shown in Fig 4.2.

Figure 4.4 shows the end of injection (EOI) timing and the available air-fuel mixing time as a function of SOI. Here, the available air-fuel mixing time is defined as the difference in crank angle from EOI to ignition. In this figure, the ignition timing is fixed at X deg $bTDC_{Fire}$, which is MBT timing in all these cases. Advanced injection timings with longer available mixing time will generally promote a more homogeneous composition of the mixture before ignition, whereas retarded injection timings can result in partial stratification due to lower mixing time [109]. Furthermore, as shown in Figure 4.4, high load operation requires more advancement of SOI relative to low load to achieve similar mixing time. This is necessary to compensate for the available mixing time loss because of the longer injection duration.

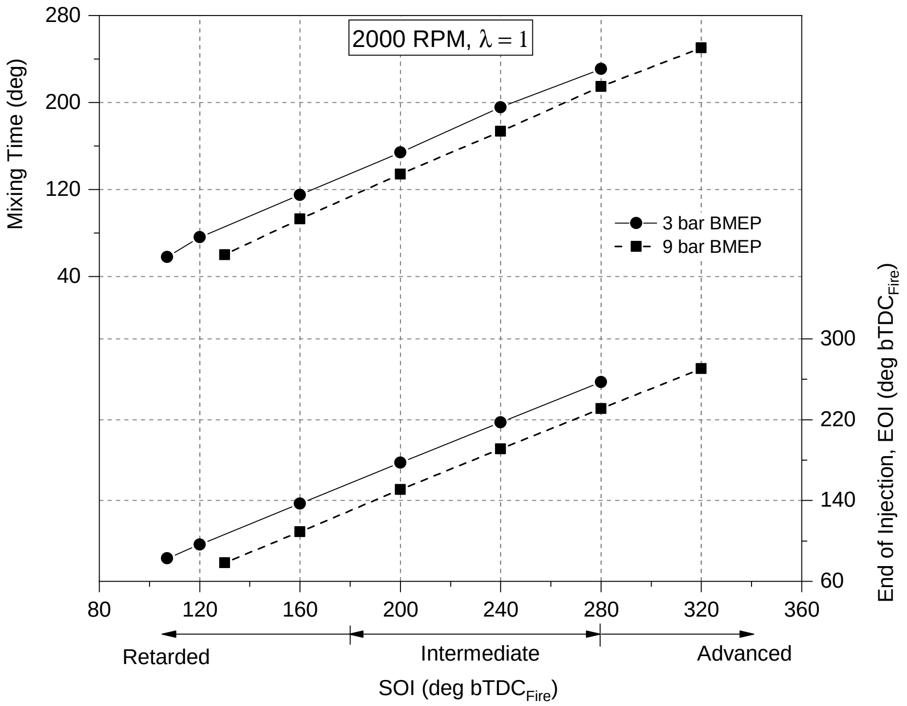

Figure 4.4: Mixing time and end of injection (EOI) as a function of SOI for 3 and 9 bar BMEP at 2000 RPM.

Figure 4.5 presents the engine-out unburned hydrocarbon (UHC) and carbon monoxide (CO) emissions as a function of SOI. With retarded injection, both UHC and CO emissions start to increase, which suggests a reduced mixture homogeneity with retarded SOI and is likely due to the reduced mixing time [81]. Both advanced and intermediate SOI with a longer mixing time appear to have a more homogeneous mixture, as CO and UHC emissions are lower.

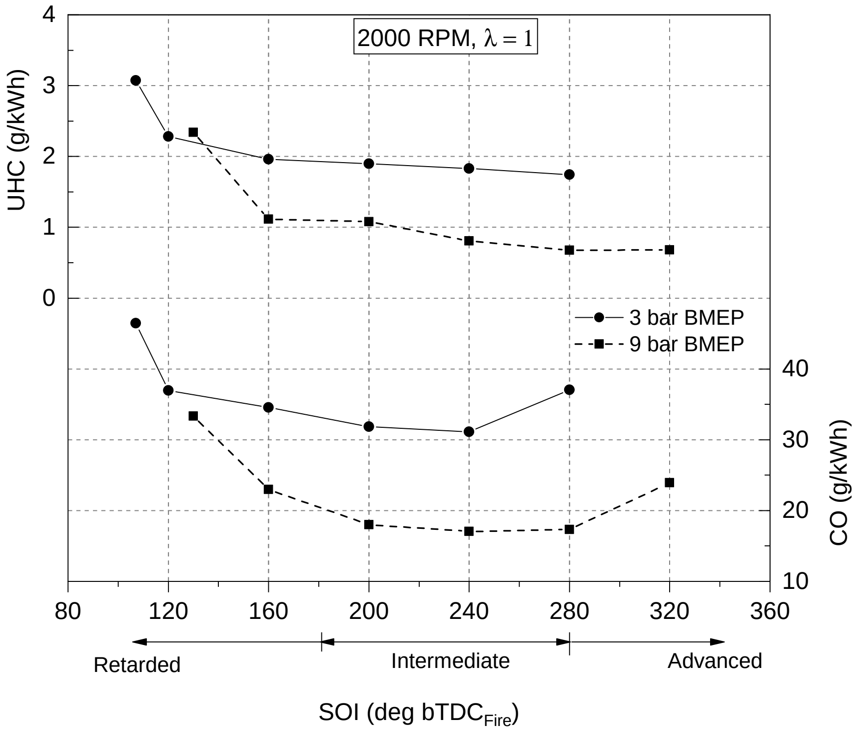

Figure 4.5: Engine-out UHC and CO emissions as a function of SOI for 3 and 9 bar BMEP at 2000 RPM, $\lambda = 1$.

This UHC trend is consistent with the coefficient of variation of IMEP (COV_{IMEP}) results shown in Fig. 4.6, where the COV_{IMEP} is maintained to less than 3% for most of the SOI timings, though there is a sharp increase with overly retarded SOI. Note that the selected COV limit is the typical value employed in the industry for stable engine combustion. This suggests that retarded injection timing creates poor combustion efficiency, resulting in a lower BTE than intermediate and advanced SOI timings. Figure 4.7 shows the crank angle position of SOI relative to the valve lift for 3 and 9 bar BMEP cases at 2000 RPM. For both load cases, the most advanced SOI timings begin at a low valve lift when the flow of intake air is low. This is potentially creating some locally rich areas in the combustion chamber, resulting in increased CO [111, 112]. On the other hand, the SOI corresponding to maximum BTE (Fig. 4.3) begins near the maximum valve lift where the intake air flow rate is at a maximum. These results suggest that an SOI timing at maximum valve lift helps to ensure a more homogeneous mixture of fuel and air. Nevertheless, a detailed

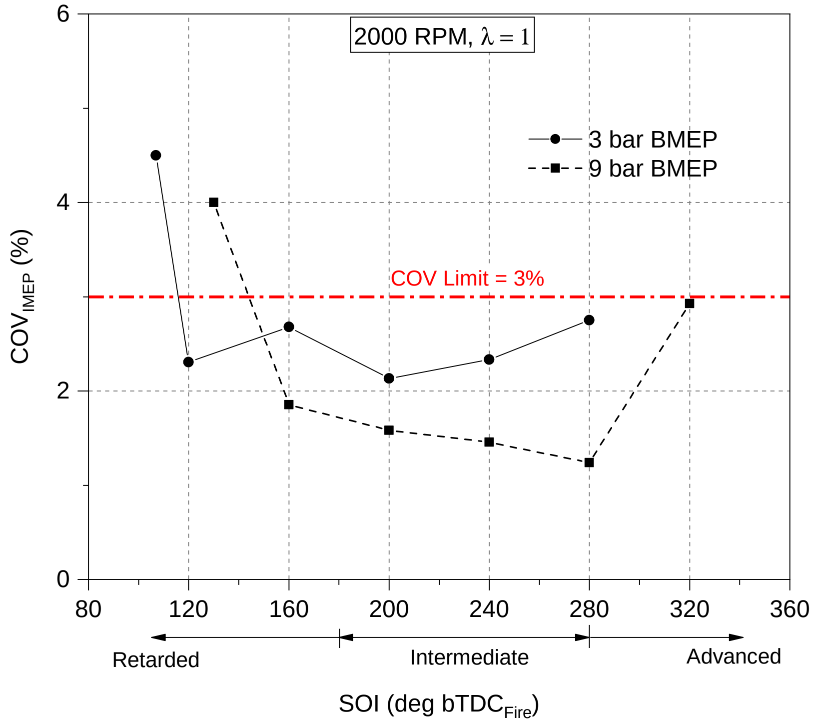

Figure 4.6: COV_{IMEP} as a function of SOI for 3 and 9 bar BMEP at 2000 RPM.

CFD analysis of incoming air and fuel jet interactions would be necessary to gain better insight into these trends.

4.1.2 In-cylinder pressure and combustion duration

In order to obtain a better understanding of the mechanism governing the engine performance trends presented in the previous section, detailed combustion analysis is considered. Figure 4.8 shows the logarithmic P-V diagram of representative pressure traces for three different SOI at 2000 RPM, 3 bar BMEP, and $\lambda = 1$. As SOI is advanced from 107 deg $bTDC_{Fire}$, the intake pressure increases as the engine is less throttled to compensate for the increasing amount of displaced air. This helps to reduce pumping losses and improve engine efficiency at intermediate and advanced SOI timings.

Changing the boundary conditions of the closed part of the cycle also influences the subsequent combustion event. This is now examined with two-zone combustion modelling using GT-Power, as detailed in Section 3.3.2 of Chapter 3. Figure 4.9 then presents the ignition timing and 0-90% MFB duration as a function of SOI for

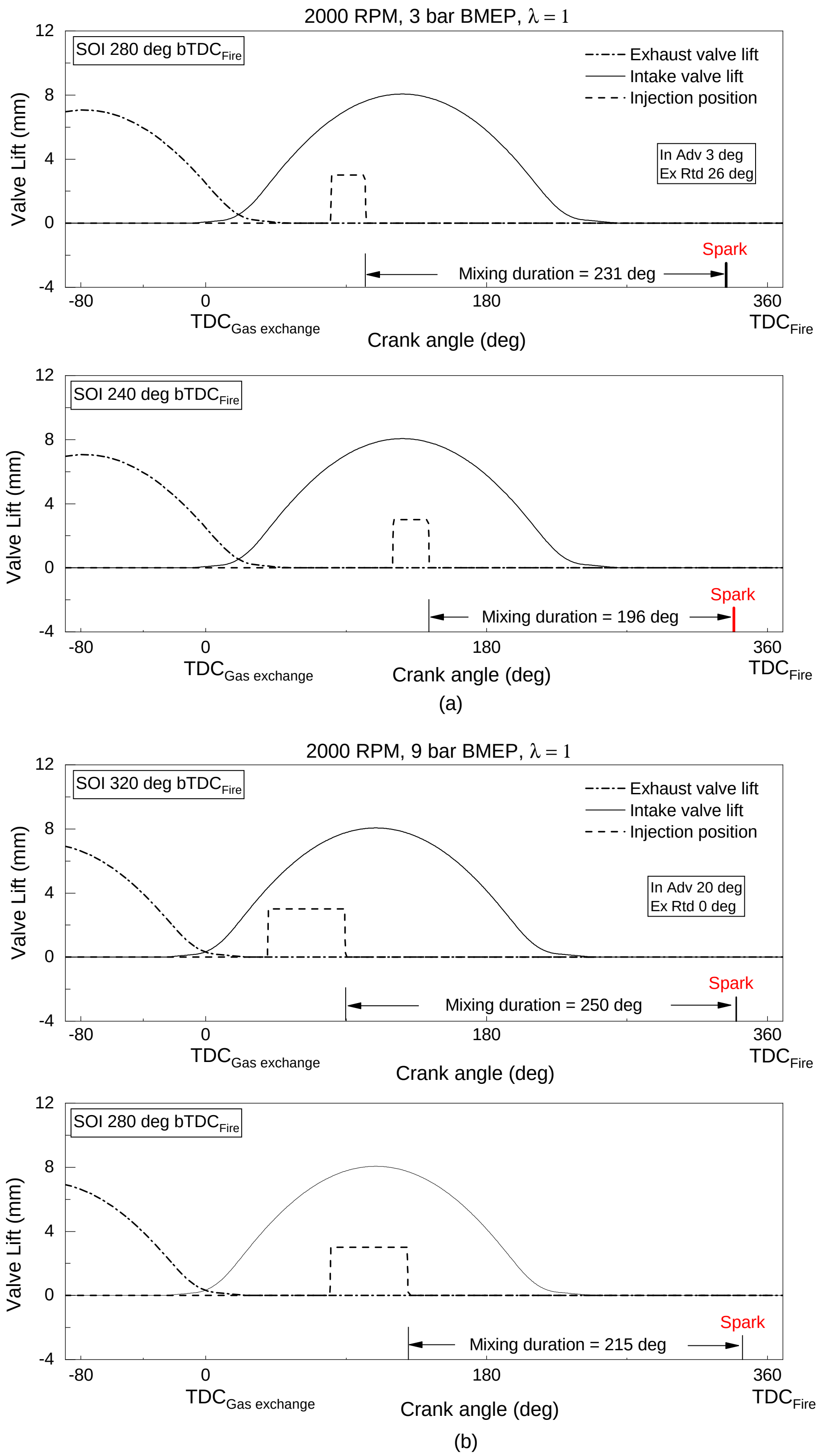

Figure 4.7: Valve lift and injection position versus the crank angle at 2000 RPM, λ = 1 for (a) SOI 280 and SOI 240 for 3 bar BMEP and (b) SOI 320 and SOI 280 for 9 bar BMEP.

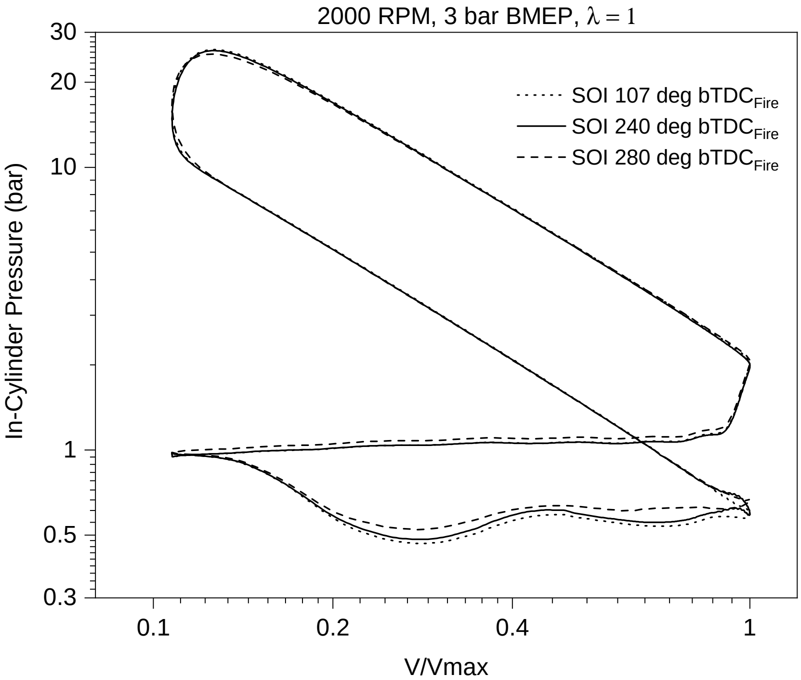

Figure 4.8: Pressure-volume trace comparison on a logarithmic scale for three different SOI timings at the operating condition of 2000 RPM, 3 bar BMEP, and λ = 1.

loads of 3 and 9 bar BMEP at 2000 RPM. As expected, the 0-90% MFB duration is shortest when the engine is operating at maximum BTE. For both load cases, advanced ignition timing and increased burn duration with the most retarded SOI suggest that there may be insufficient fuel-air mixing resulting in slower combustion. This is consistent with the earlier observations of lower BTE, higher UHC and CO, and increased COV_{IMEP} when the SOI was highly retarded. The trend of combustion duration is not monotonic; however, a relatively short burn duration is observed with SOI at 160 deg bTDC_{Fire}. For the most advanced SOI timings, advanced ignition timing and longer burn durations are measured for MBT operation despite a longer available mixing time.

4.1.3 Energy balance and loss analysis

Energy balance analysis based on the methodology described in Section 3.4.2 of Chapter 3 is now used to determine where losses occur as the injection timing strategy varies [37, 158]. Figure 4.10 (a) shows the distribution of input fuel energy with respect to measured and inferred quantities:

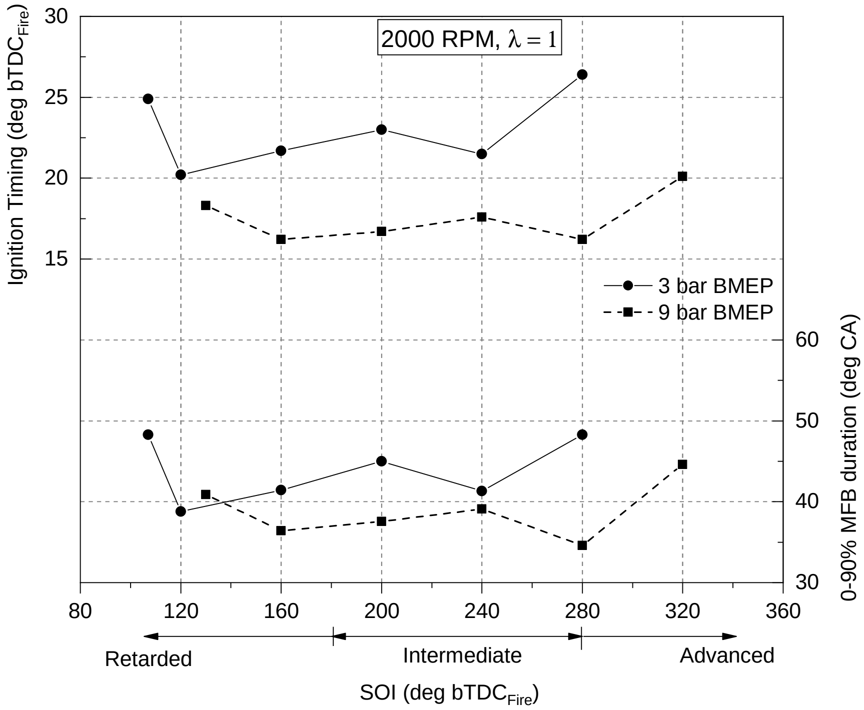

Figure 4.9: Ignition timing and 0-90% MFB duration as a function of SOI for 3 and 9 bar BMEP at 2000 RPM and $\lambda = 1$.

1. brake work ($\dot{W}_B$);
2. unburned fuel energy ($\dot{H}_{UBF}$);
3. exhaust gas sensible enthalpy ($\dot{H}_{Exh}$);
4. total heat losses ($\dot{Q}_L$).

The total heat loss ($\dot{Q}_L$) is further divided into various components, as shown in Fig. 4.10 (b). These include:

1. in-cylinder wall heat transfer between hot combustion gas and cylinder walls ($\dot{Q}_{In-Cyl}$);
2. energy losses due to friction ($\dot{Q}_{Fr}$);
3. energy losses due to pumping losses ($\dot{Q}_{Pump}$);
4. heat transfer from the engine's external surfaces ($\dot{Q}_{misc}$).

Note that the total value of the bars in Fig. 4.10 (b) is equivalent to the $\dot{Q}_L$ for each bar in Fig. 4.10 (a).

As shown from the energy balance in Figure 4.10 (a), the loss of unburned fuel energy due to incomplete combustion contributes to the variation of BTE with different SOI, suggesting that a sufficiently homogeneous air-fuel mixture before ignition is required for optimal BTE. Further investigation into the sources of heat loss (Fig. 4.10-b) shows higher in-cylinder wall heat losses with SOI 107 and SOI 280 compared to SOI 240 because of their longer combustion duration and hence more time for heat transfer. With injection proceeding towards advanced SOI at fixed load, the engine is less throttled, resulting in decreased pumping work. Similar trends are also observed with other speed and load as SOI is varied.

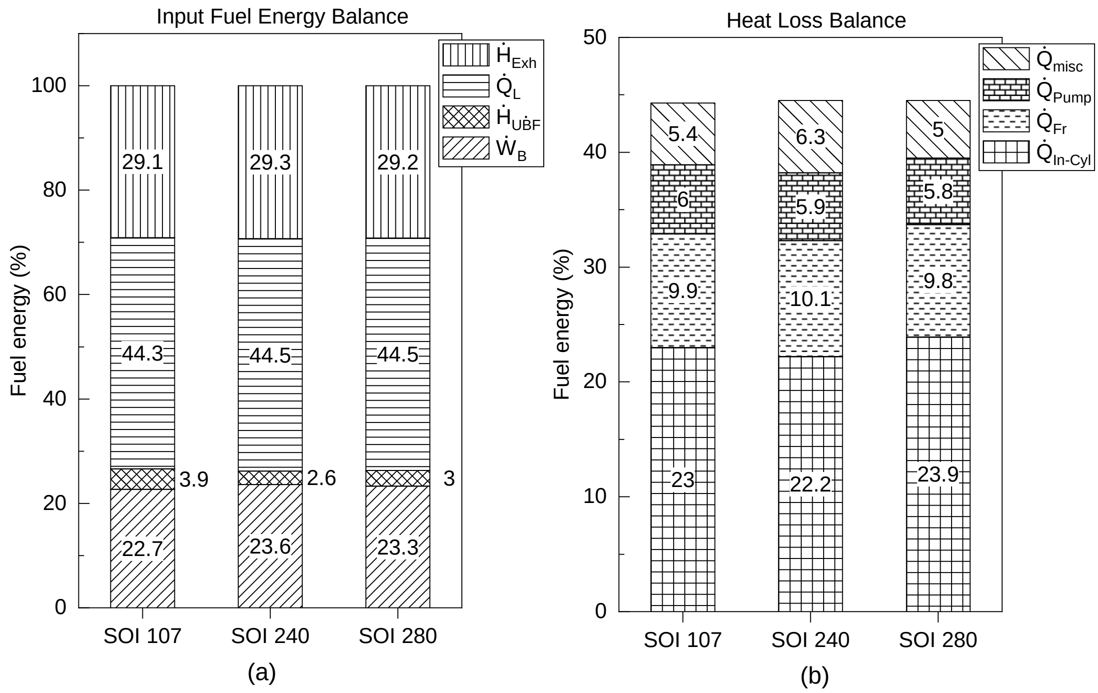

Figure 4.10: (a) Input fuel energy balance and (b) Heat loss balance for three different SOI at 2000 RPM, 3 bar, and $\lambda = 1$.

The results suggest that retarded SOI timings are a detriment to fuel efficiency at part load, though they could be applied at wide-open throttle or boosted conditions to mitigate the volumetric efficiency penalty from the use of gaseous fuel. At part loads, good mixture homogeneity appears to be the dominating factor in determining the optimum brake thermal efficiency. Thus, intermediate SOI timings in the range of 240 to 280 deg bTDC$_{Fire}$, which balance sufficient mixing time with engine de-throttling at a given load, have the highest brake thermal efficiency across the tested operating range.

4.2 Comparison of part load DI engine performance with Gasoline and CNG

In this section, a comparison of GDI and DI CNG engine performance is presented at stoichiometric conditions over a range of part load (i.e., 3, 6 and 9 bar BMEP). All baseline performance data with gasoline are obtained by running the test engine with the production engine's factory settings. The DI CNG results here correspond to the SOI timings that yield optimal part load performance, as discussed in Section 4.1. MBT ignition timing is maintained so long as trace knock is not encountered: DI CNG is never knock-limited for the tested conditions, though gasoline is in some cases. A linear interpolation method is used to generate the contour plots with measured data points indicated by black dots.

4.2.1 Thermal efficiency and fuel consumption

Figure 4.11 shows the brake thermal efficiency of both gasoline and CNG fuelled engine operation. These fuels exhibit similar part load brake thermal efficiency to

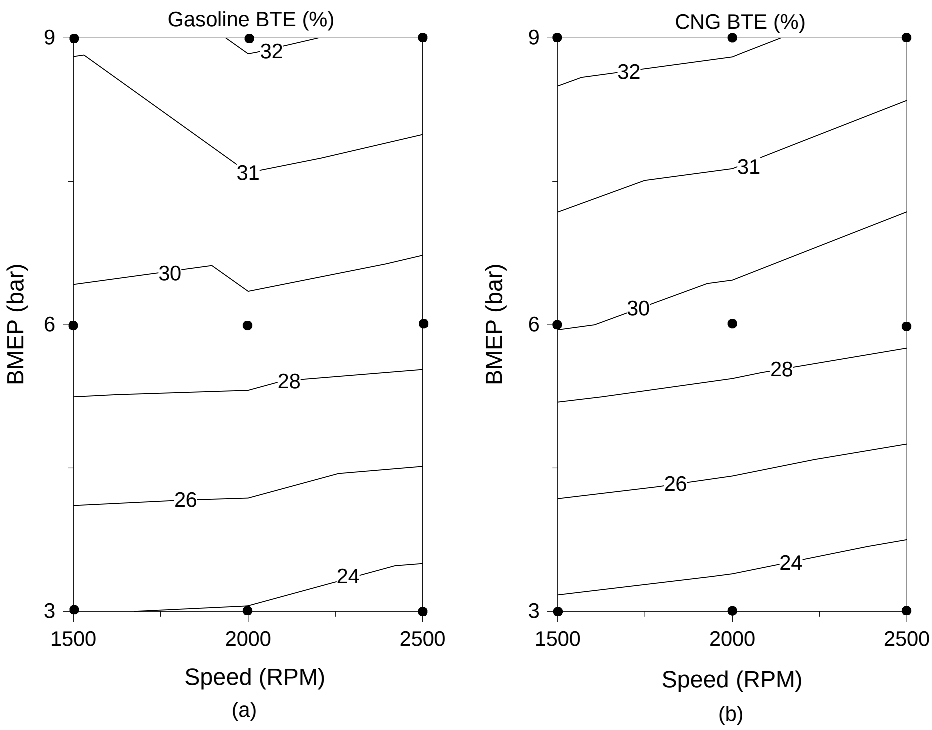

Figure 4.11: Maps of brake thermal efficiency (%) for (a) Gasoline and (b) CNG fuelled engine operation under part load conditions at $\lambda = 1$.

within experimental uncertainty [38, 111]. However, gasoline operation has around 1.3% lower BTE compared to CNG at the 1500 RPM, 9 bar BMEP condition because it is knock-limited. This drop in BTE with gasoline would be expected to increase with load, as combustion phasing becomes more retarded and fuel enrichment is required to prevent auto-ignition and protect the engine hardware. A comparison of brake specific fuel consumptions (BSFC) is shown in Fig. 4.12 for gasoline and CNG fuelled engine operation as a function of speed and load. BSFC with CNG is approximately 7-10% less than that of gasoline operation over the tested loads with MBT conditions (Fig. 4.13). This is mainly attributed to the lower heating value of CNG being around 10% higher than that of certification gasoline used in this study (refer to Table 2.2).

4.2.2 Engine-out emissions

Figure 4.14 compares the engine-out unburned hydrocarbon (UHC) emissions of the stoichiometric gasoline and natural gas fuelled DI engine operation under part load conditions. With gasoline, most of the UHC emissions are non-methane compounds, while around 90% UHC are methane when fuelling with natural gas [37]. The UHC emissions of CNG fuelled operation are generally lower than that of gasoline operation throughout all part load conditions, and UHC reductions of up to 60% are observed with CNG fuelling, as shown in Fig. 4.15 in terms of normalised UHC emissions. Greater mixture homogeneity and the elimination of fuel films on the surface of engine components are likely the major reasons for lower unburned hydrocarbon emissions with CNG [38, 99, 131]. Figure 4.16 shows the engine-out CO emissions for both gasoline and CNG fuelled engines. With CNG, around 25-55% lower CO emissions are observed relative to gasoline over the part load conditions (Fig. 4.17). Even though the SOI of gasoline is early, fuel on wetted walls can create localised rich regions in the later part of the cycle, which cannot occur with CNG. These locally rich regions possibly have a significant impact on CO formation [99]. Furthermore, the 1500 RPM and 9 bar BMEP gasoline condition is knock-limited and has higher CO, which also adds to overall engine-out CO emissions with GDI operation. Figure 4.18 shows a comparison of engine-out NO_x emissions for both fuels under part load conditions. NO_x is

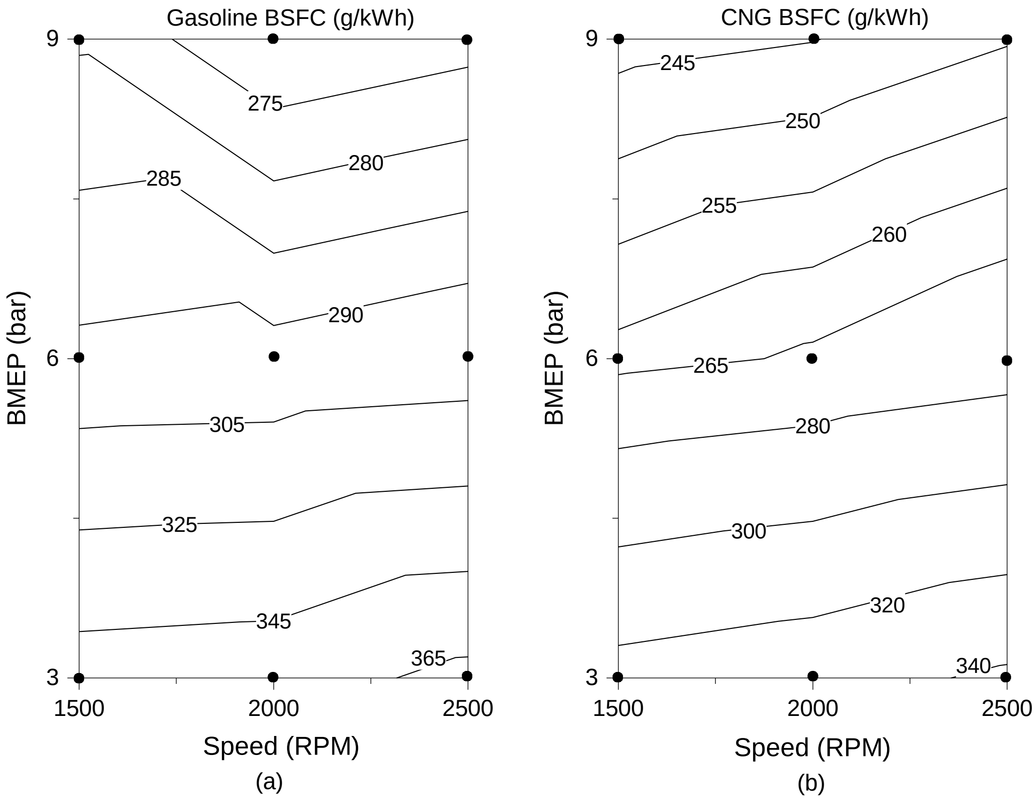

Figure 4.12: Maps of BSFC (g/kWh) for (a) Gasoline and (b) CNG fuelled engine operation under part load conditions at $\lambda = 1$.

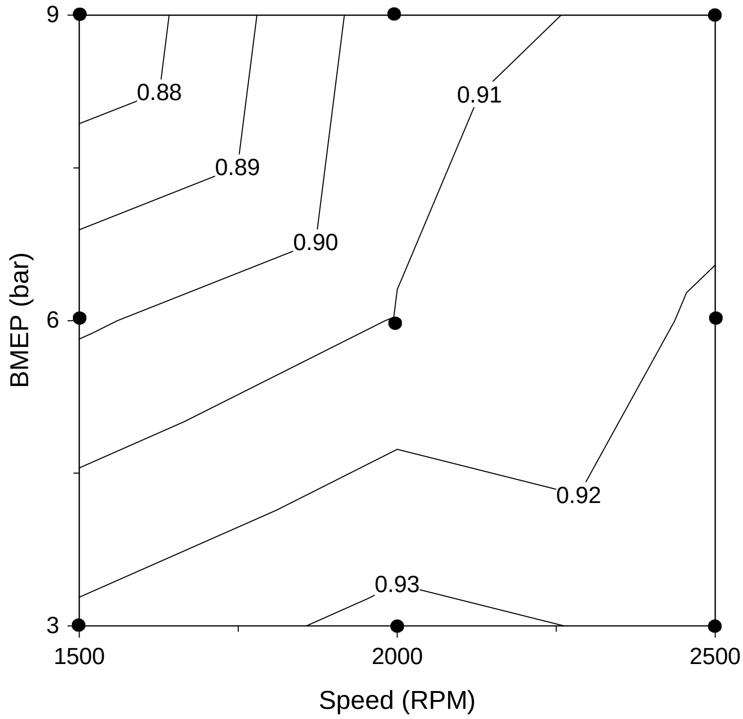

Figure 4.13: BSFC for DI CNG operation normalised by BSFC of GDI engine as a function of speed and load at $\lambda = 1$.

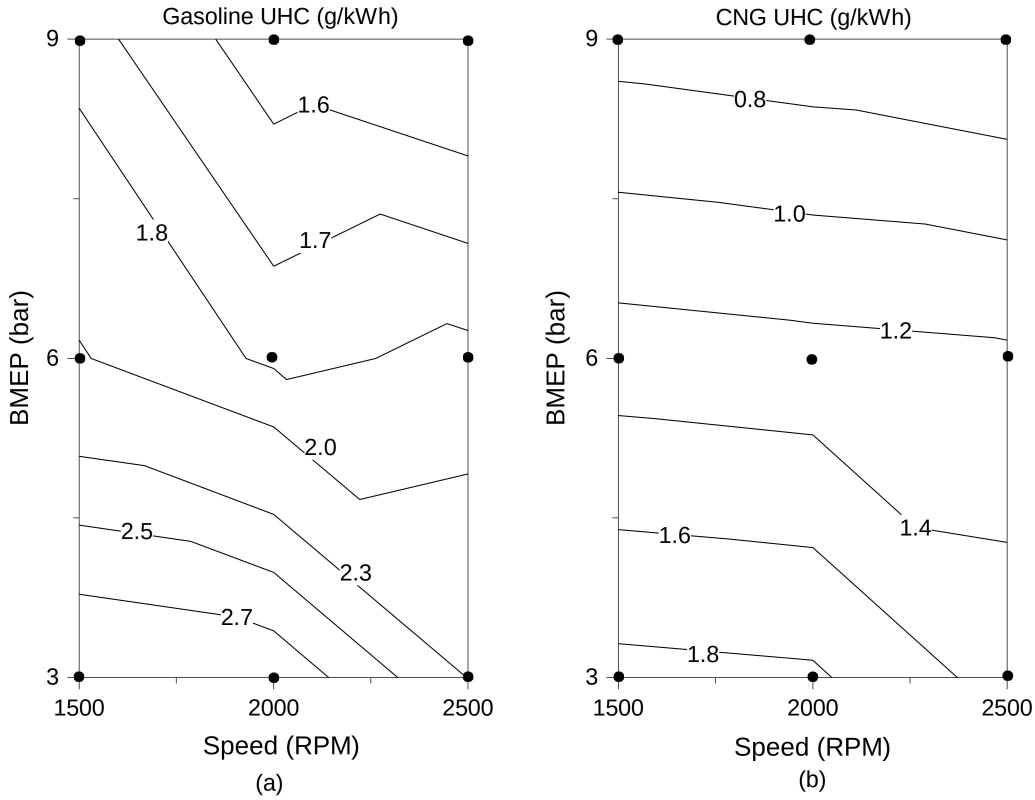

Figure 4.14: Maps of engine-out UHC emissions (g/kWh) for (a) Gasoline and (b) CNG fuelled engine operation under part load conditions at $\lambda = 1$.

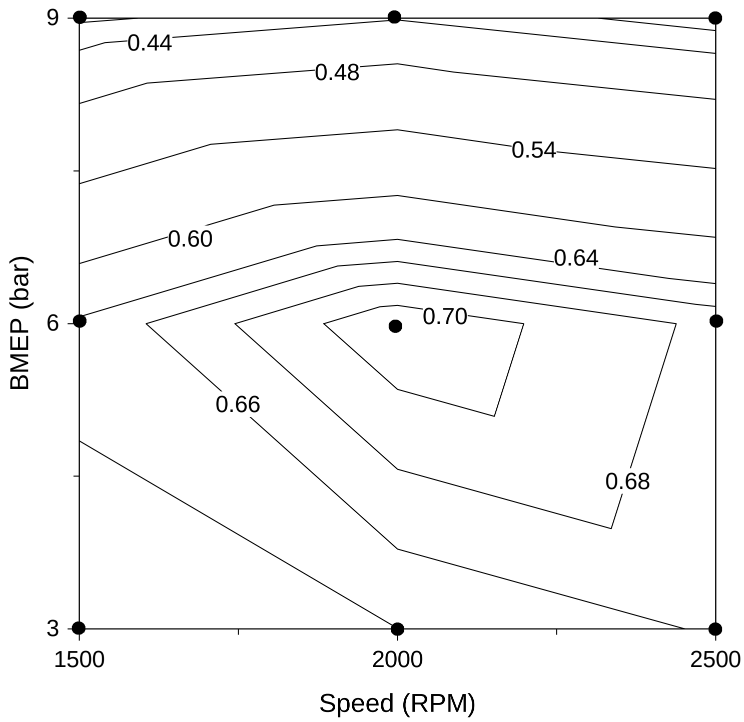

Figure 4.15: UHC emissions for DI CNG operation normalised by UHC emissions of GDI engine as a function of speed and load at $\lambda = 1$.

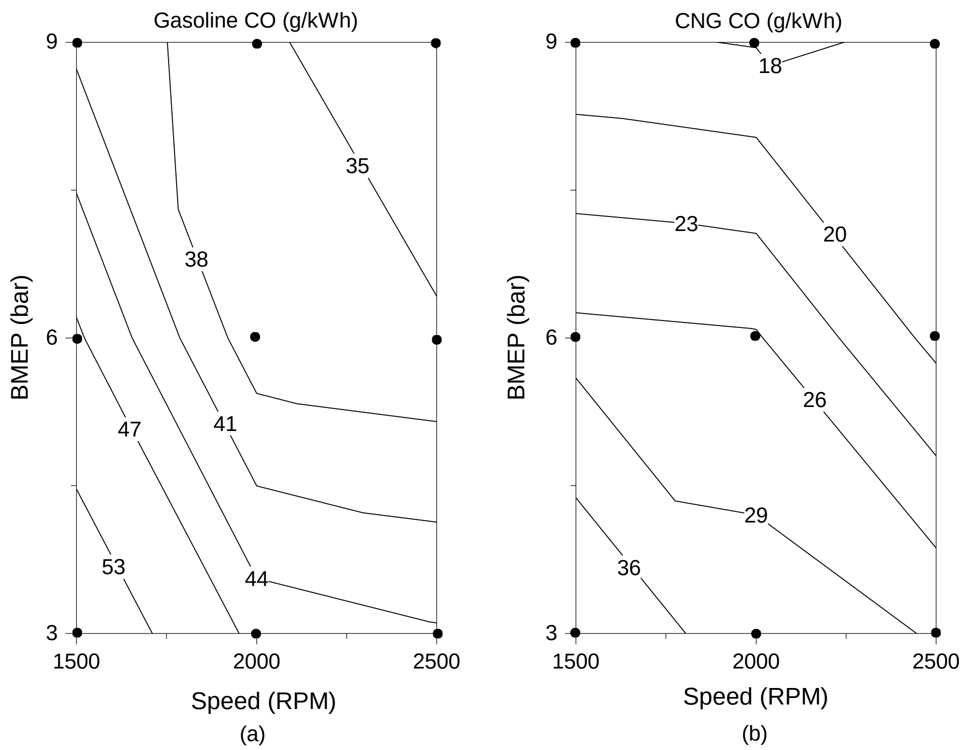

Figure 4.16: Maps of engine-out CO emissions (g/kWh) for (a) Gasoline and (b) CNG fuelled engine operation under part load conditions at $\lambda = 1$.

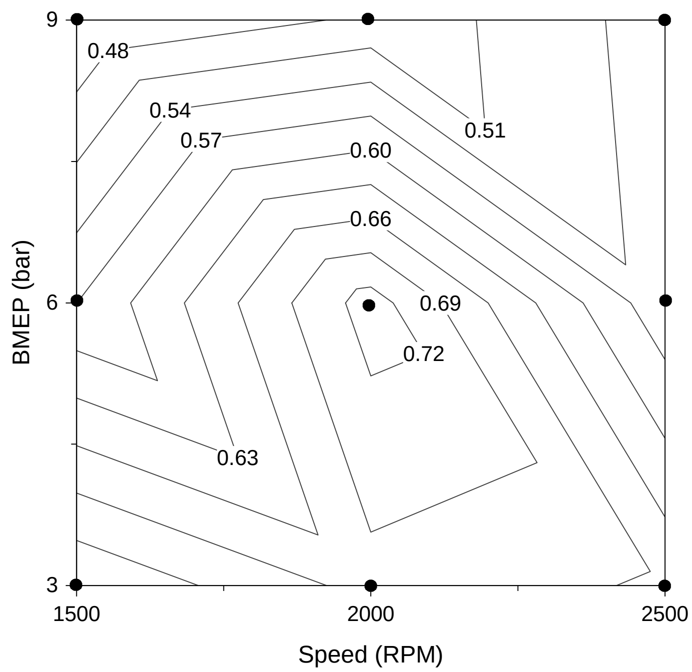

Figure 4.17: CO emissions for DI CNG operation normalised by CO emissions of GDI engine as a function of speed and load at $\lambda = 1$.

generally produced in post flame gases and is strongly related to peak combustion temperatures [37]. As shown in Fig. 4.19, higher engine-out NO_x emissions are observed with gasoline fuelled operation due to higher in-cylinder temperatures arising from gasoline's lower stoichiometric air-fuel ratio [111], except at the knock-limited conditions.

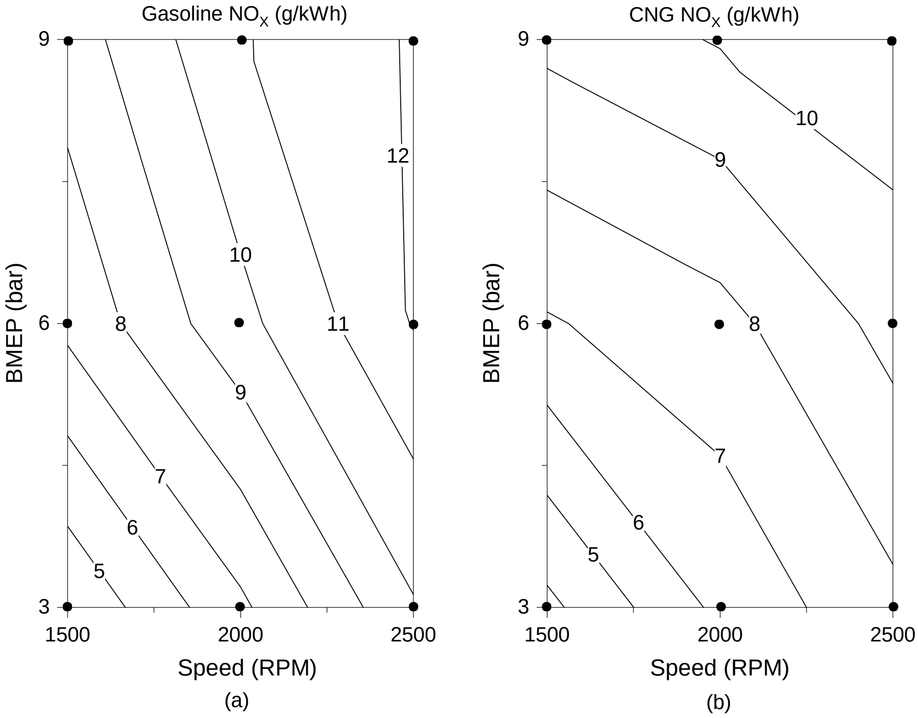

Figure 4.18: Maps of engine-out NO_X emissions (g/kWh) for (a) Gasoline and (b) CNG fuelled engine operation under part load conditions at $\lambda = 1$.

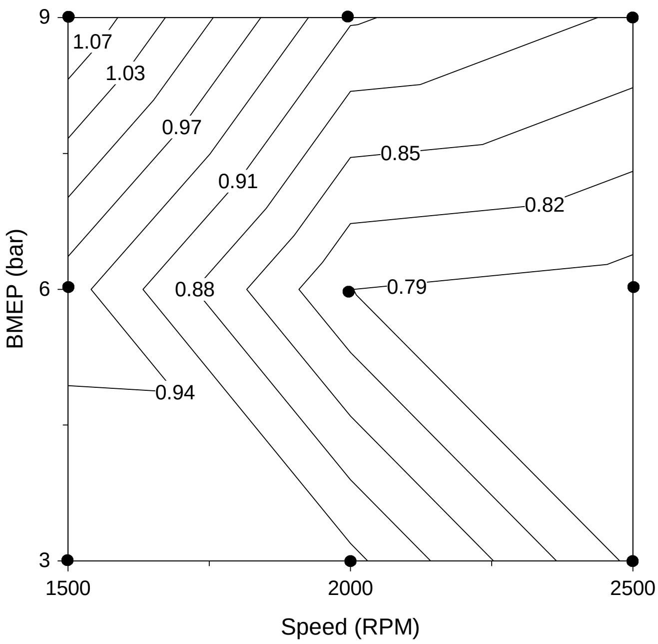

Figure 4.19: NO_x emissions for DI CNG operation normalised by NO_x emissions of GDI engine as a function of speed and load at $\lambda = 1$.

4.2.3 Combustion characterization and energy analysis

In this section, two different engine operating conditions (i.e., 2500 RPM, 3 bar BMEP and 2000 RPM, 6 bar BMEP) for both fuels are chosen and analyzed to explain the results obtained in Section 4.2.1. A comparison of representative pressure traces is shown in Fig. 4.20 for both (a) gasoline and (b) CNG fuelled operation at the two different engine operating conditions. As shown at both conditions, CNG fuelled operation has a higher pressure during the intake stroke, as the engine is less throttled to compensate for the displacement of air by CNG, resulting in less pumping work. Moreover, this higher intake pressure results in increased in-cylinder pressure, especially during the compression stroke, which has an impact on the thermodynamic conditions before ignition.

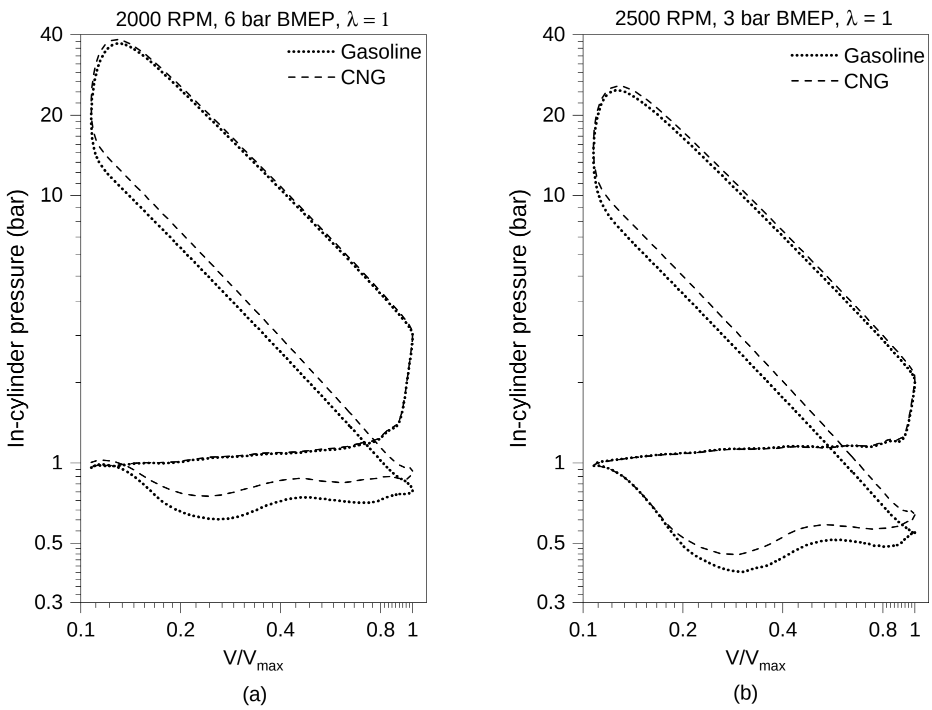

Figure 4.20: Pressure-volume trace comparison on a logarithmic scale for stoichiometric gasoline and CNG fuelled engine operation at (a) 2000 RPM, 6 bar BMEP and (b) 2500 RPM, 3 bar BMEP.

Figure 4.21 presents burn duration data obtained using GT-Power for both fuels. The 10-90% MFB burn durations are similar, but the 0-10% MFB duration for gasoline is longer than for CNG. This is likely because, under the same engine operating condition, lower intake pressure and in-cylinder vaporization of fuel with GDI operation generate less favourable thermodynamic conditions for chemical reaction compared to DI CNG. Figure 4.22 supports this, showing that the unburned gas temperature using gasoline is lower than that of CNG during the compression stroke. This necessitates more advanced ignition to maintain MBT

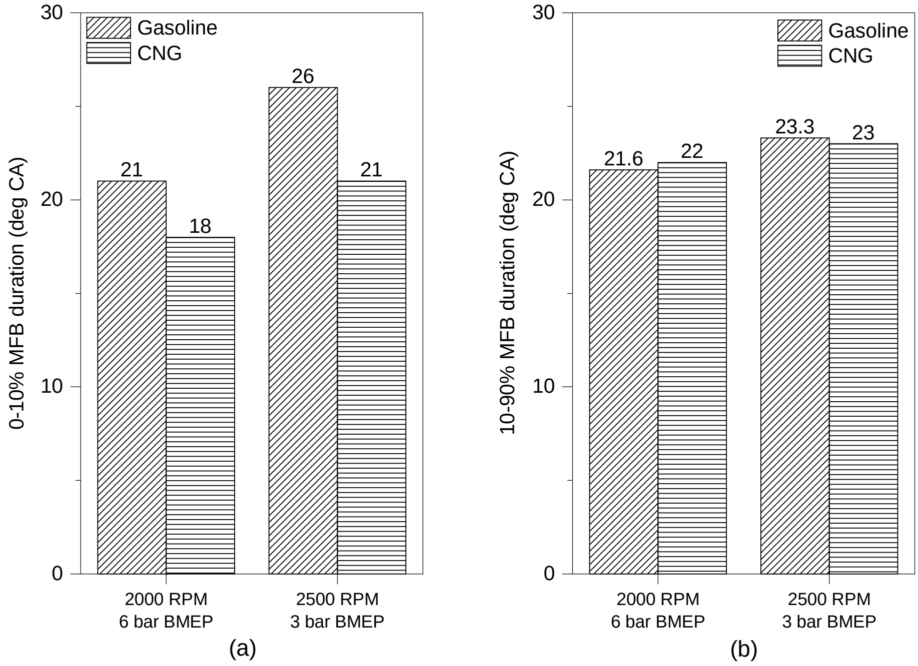

Figure 4.21: (a) 0-10% and (b) 10-90% MFB duration for stoichiometric gasoline and CNG fuelled operation at 2000 RPM, 6 bar BMEP and 2500 RPM, 3 bar BMEP.

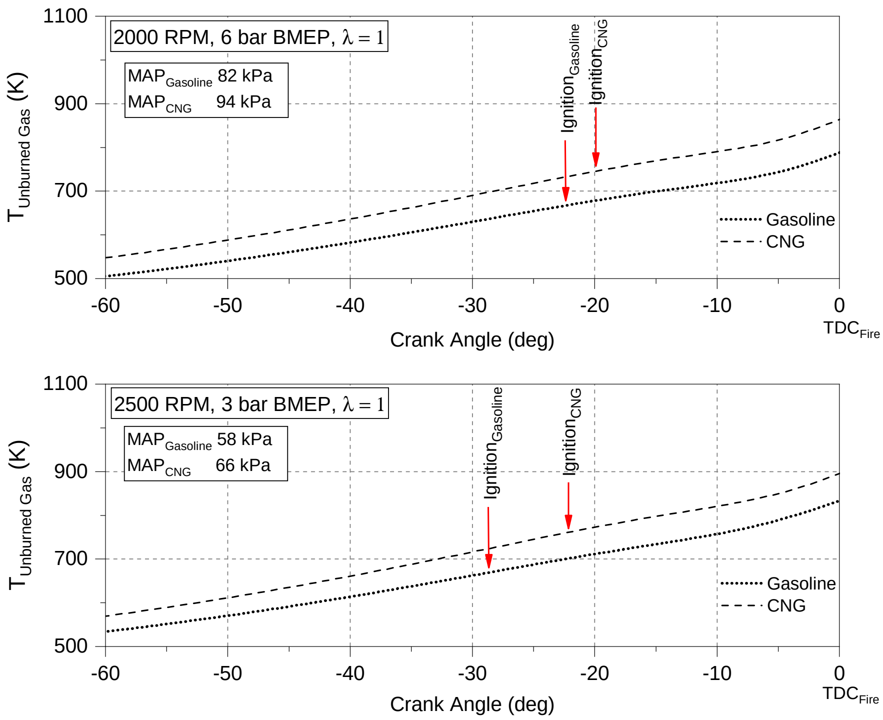

Figure 4.22: Simulated $T_{\text{Unburned Gas}}$ for stoichiometric gasoline and CNG fuelling at 2000 RPM, 6 bar BMEP (top) and 2500 RPM, 3 bar BMEP (bottom).

timing, resulting in a longer initial combustion duration with gasoline [55, 162]. While this finding may seem counterintuitive given that CNG is known to have a slower laminar flame speed than gasoline, this behaviour arises as a consequence of the load matching between fuels in the experiments, which necessarily causes the in-cylinder thermodynamic conditions to vary between each fuel at the same engine load.

Continuing such analysis for the rest of the cycle using the methodology described in Section 3.4.1, Figure 4.23 shows the energy share of the expansion, compression and gas exchange processes, as well as the indicated thermal efficiency (ITE) for stoichiometric gasoline and CNG fuelled engine operation at two different speed and load conditions. The expansion energy produced at both operating conditions is around 2% higher with CNG compared to gasoline operation. This can mainly be attributed to the short combustion duration of CNG, as shown in Fig. 4.21. In addition, the energy consumed during the gas exchange process is slightly lower with CNG due to less throttled engine operation. However, the energy consumed to

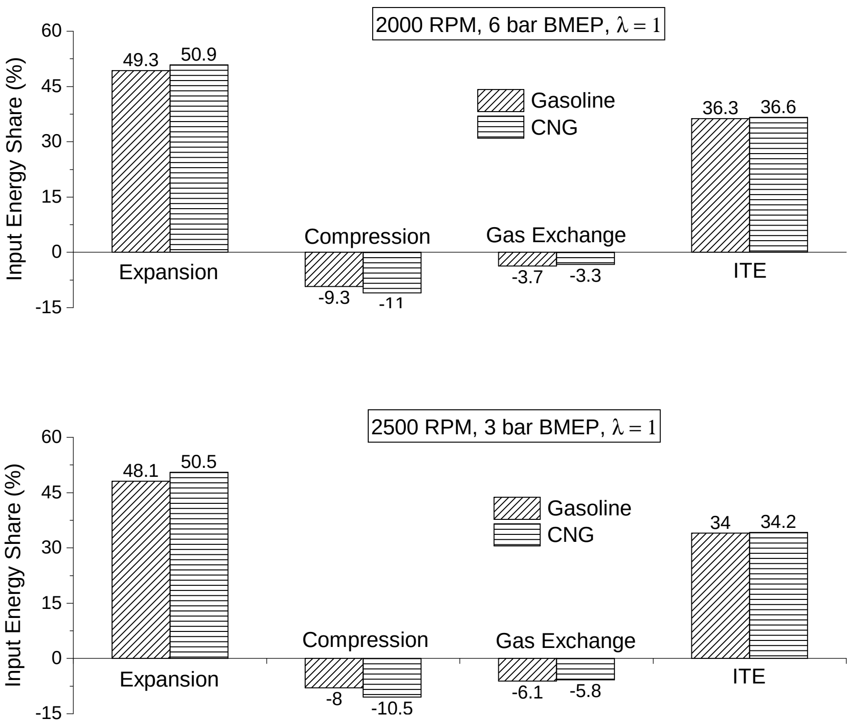

Figure 4.23: Cycle energy share for stoichiometric gasoline and CNG fuelled engine operation at 2000 RPM, 6 bar BMEP (top) and 2500 RPM, 3 bar BMEP (bottom) conditions. (+)ve and (-)ve value indicate generated and consumed energy in the cycle, respectively.

compress the natural gas is higher due to the higher in-cylinder pressure during the compression stroke, as shown in Fig. 4.20. This offsets the higher expansion energy and lower pumping loss with CNG, resulting in similar indicated thermal efficiencies for both fuels within experimental uncertainty. These ITE results are consistent with the previously examined BTE trends and also explain why the engine has similar thermal efficiency with both fuels even though DI CNG operation has less pumping loss and higher combustion efficiency than that of GDI operation.

4.3 High load operation with Gasoline and CNG fuelling

In this section, the high load potential of a DI CNG engine is presented in regards to the prospect of torque improvement at lower engine speeds and knock-resistance capability at high load as compared to gasoline operation. Experiments at peak engine load are not attempted in this study with DI CNG to preserve the test engine, as exhaust valve recession and damage on pressure transducer mountings are possible. This is due to increased wall temperatures at peak loads, as DI CNG can not provide charge cooling unlike conventional, liquid fuels. Therefore, the test engine is operated at a maximum of 12 bar BMEP (a condition where the engine is boosted) both with gasoline and CNG as a representative high load condition.

4.3.1 The prospect of high torque at low speeds with DI CNG

CNG fuelled vehicles equipped with PFI technology inherently have lower peak power than the same engine fuelled by gasoline due to the displacement of intake air by CNG [81, 111]. DI affords the capability to inject fuel near IVC as shown previously in Fig. 4.2, and in doing so, volumetric efficiency can be improved by allowing the increased filling of the cylinder with air. Moreover, if the fuel could all be injected after IVC, a given engine would have better volumetric efficiency than a liquid-fuelled equivalent, as the cylinder volume before IVC would be composed only of air and no fuel. Gaseous fuel has this additional flexibility in SOI timing because there is no fuel vaporization needed and the fuel can directly mix with the ambient air.

For high load operation, the SOI is therefore targeted to occur after or as close to IVC with CNG to realize high volumetric efficiency. Figure 4.24 shows the SOI used for 12 bar BMEP engine operation at 1500 and 2000 RPM with gasoline and CNG. SOI timing with gasoline operation is kept the same as the production engine at 280 deg bTDC$_{Fire}$. For CNG fuelled operation at 12 bar BMEP, SOI sweeps are performed at each speed by retarding injection towards IVC to achieve higher volumetric efficiency and identify the maximum possible retarded SOI that results in less than 3% COV$_{IMEP}$. Theses timings are 130 deg bTDC$_{Fire}$ at 1500 RPM and 165 deg bTDC$_{Fire}$ at 2000 RPM.

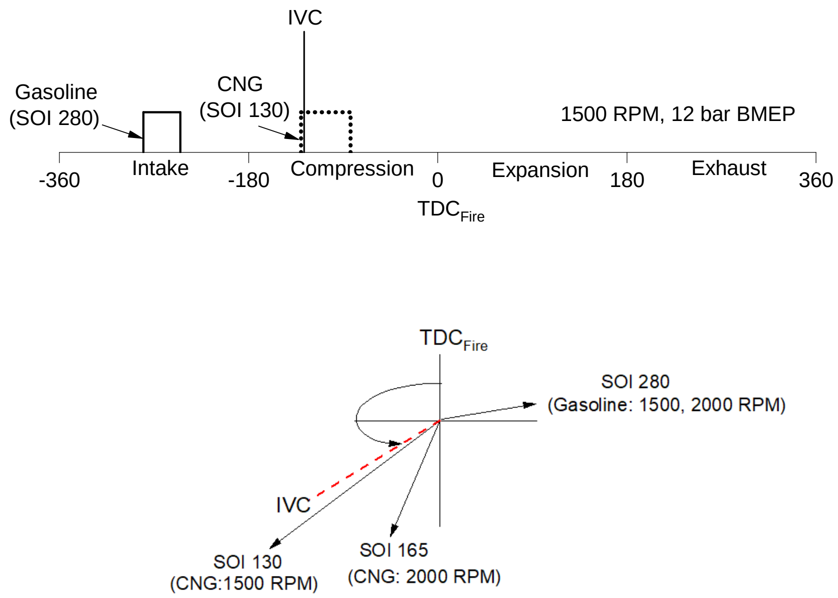

Figure 4.24: Fuel injection strategy for gasoline and CNG fuelled stoichiometric engine operation at 12 bar BMEP.

Figure 4.25 shows the manifold air pressure (MAP) required to produce 12 bar BMEP at 1500 and 2000 RPM with gasoline and CNG under stoichiometric conditions. As shown, engine operation with CNG requires a MAP of 131 kPa at 1500 RPM and 133 kPa at 2000 RPM to produce 12 bar BMEP, which is slightly lower than the MAP for gasoline fuelling of 136 kPa at 1500 RPM and 136.5 kPa at 2000 RPM. This shows that an engine of a given displacement fuelled with DI CNG can match the peak torque of a gasoline-equivalent when the CNG SOI is sufficiently retarded to mitigate any loss of volumetric efficiency.

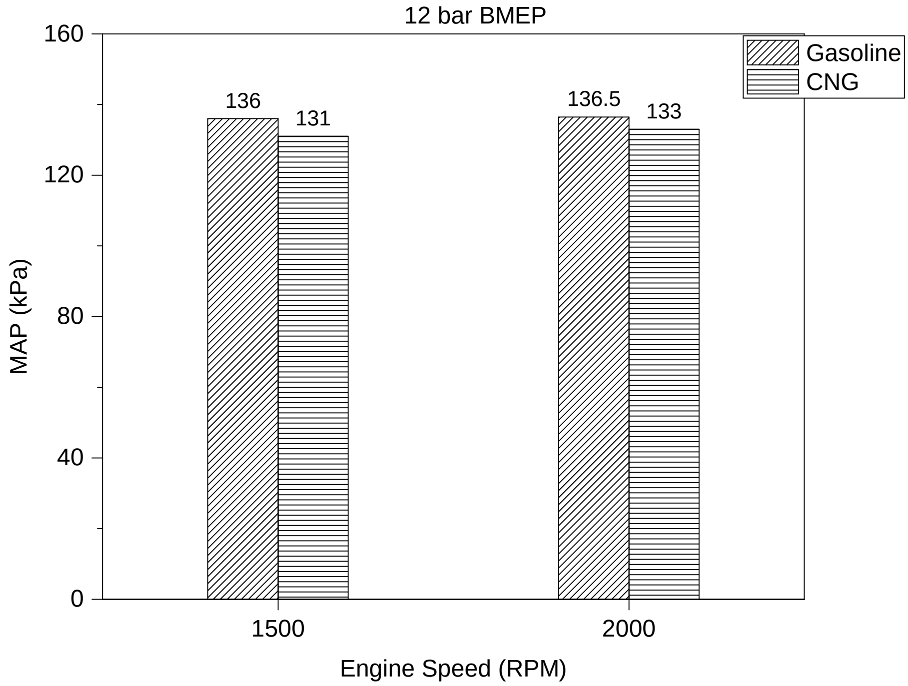

Figure 4.25: Comparison of manifold air pressure (MAP) at 12 bar BMEP, 1500 and 2000 RPM for stoichiometric gasoline and CNG fuelled engine operation.

4.3.2 Efficiency benefits of DI CNG at high load

Engine operation with gasoline is knock-limited at high load, particularly at highly boosted conditions, whereas an engine can be operated with significantly less or no knock with CNG due to its high octane rating. Figure 4.26 (a) shows that engine operation with CNG is able to maintain MBT timing at 12 bar for both tested engine speeds, but gasoline operation is knock-limited and therefore with compromised efficiency. A comparison of engine BTE is also presented in Fig. 4.26 (b) for gasoline and CNG fuelled operation at 12 bar BMEP. With DI CNG, a BTE up to 33% is achieved compared to 30% with gasoline, the latter of which is attributed to knock-limited, retarded combustion phasing. The relative difference in BTE between the gasoline and CNG operation would increase further with higher loads as the gasoline engine becomes more knock-limited.

As expected, ignition timings in Fig. 4.27 (a) are highly retarded towards TDC_{Fire} for gasoline cases to avoid knock and advanced with CNG to maintain MBT timing. A shorter burn duration with CNG in Fig. 4.27 (b) results from more advanced combustion phasing relative to that of gasoline [111]. This decreases the time for in-cylinder heat transfer and increases the BTE for CNG compared to GDI operation.

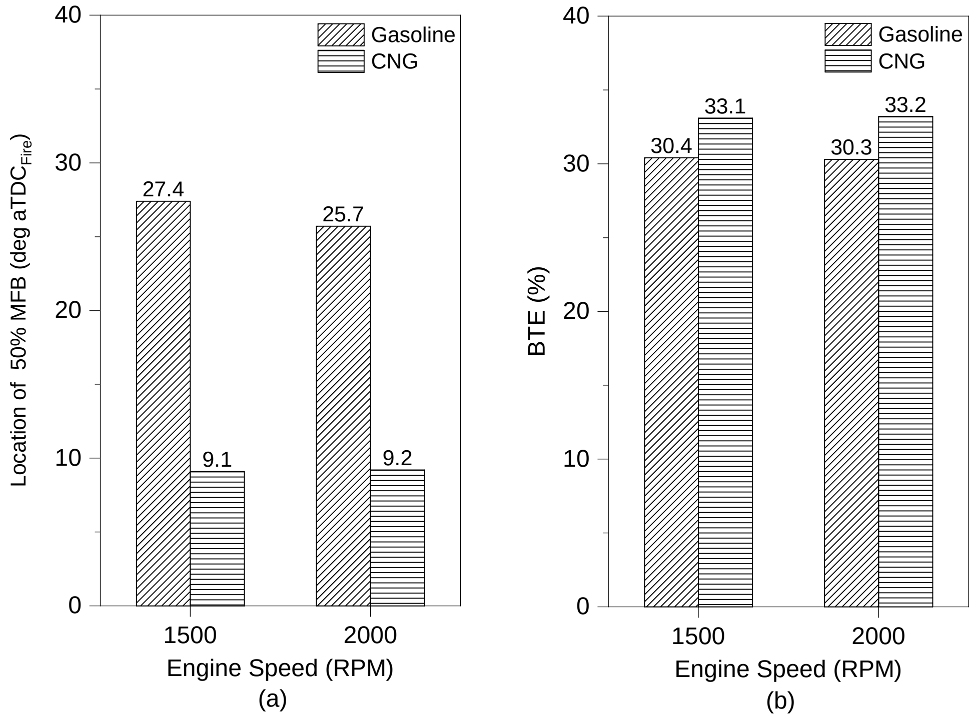

Figure 4.26: (a) Location of 50% MFB and (b) Brake thermal efficiency (BTE) for gasoline and CNG fuelled stoichiometric engine operation at 1500 and 2000 RPM, 12 bar BMEP.

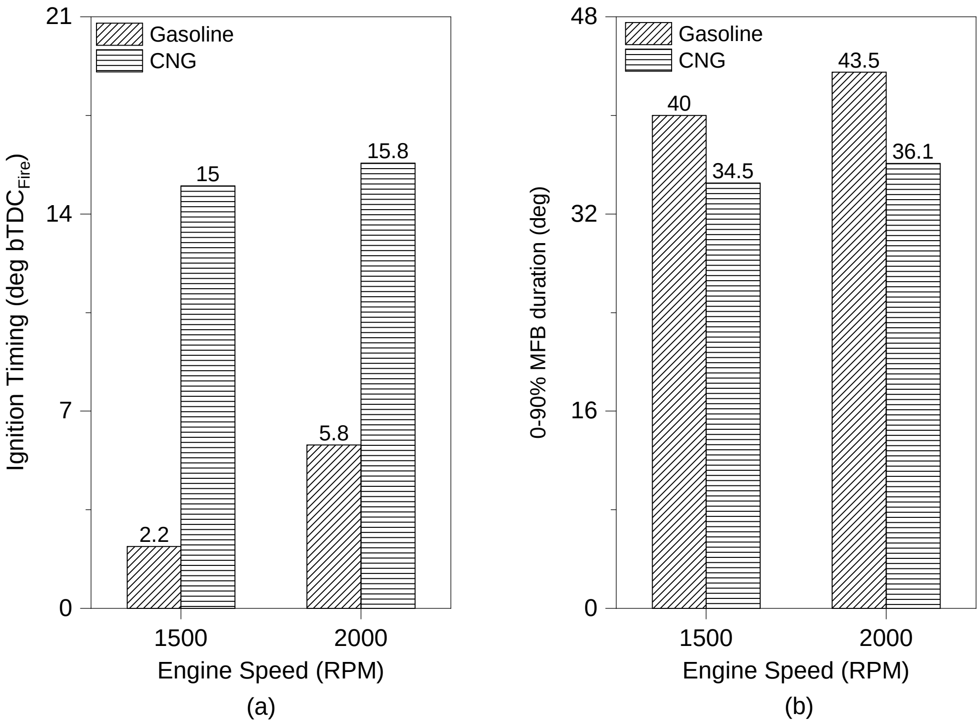

Figure 4.27: (a) Ignition timing and (b) 0-90% MFB duration for gasoline and CNG fuelled stoichiometric engine operation at 1500 and 2000 RPM, 12 bar BMEP.

While the use of retarded SOI with DI CNG has the capability to mitigate the peak power loss typical in gaseous-fuelled engines when compared with their liquid-fuelled counterparts, there is a drawback in regards to unburned hydrocarbon emissions. Higher engine-out UHC emissions are measured with CNG operation in Figure 4.28 (a), which is likely due to greater mixture inhomogeneity with retarded SOI timings. This is supported by Fig. 4.28 (b), where the advanced SOI at 280 deg bTDC$_{Fire}$ has lower UHC emissions relative to the retarded SOI at 120 deg bTDC$_{Fire}$ and 9 bar BMEP, 1500 RPM engine operation with CNG.

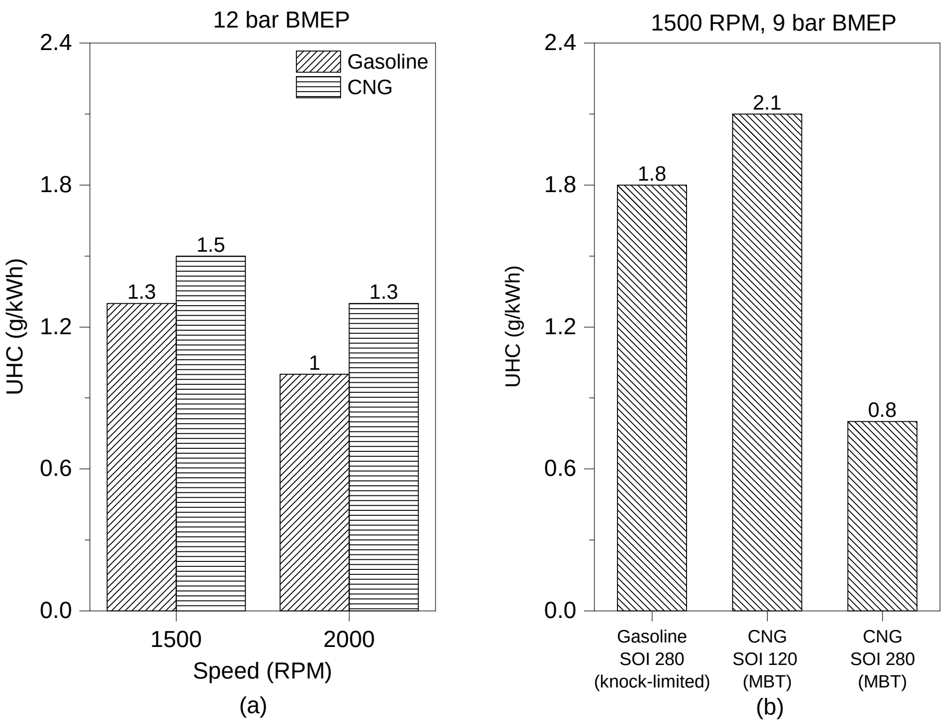

Figure 4.28: (a) UHC at 1500 and 2000 RPM, 12 bar BMEP, $\lambda = 1$ and (b) UHC as a function of SOI at 1500 RPM, 9 bar BMEP, and $\lambda = 1$.

4.4 Greenhouse gas emissions with stoichiometric DI CNG and GDI operation

Figures 4.29 (a) and (b) present the engine-out CO_2 emissions as a function of speed and load for both gasoline and CNG fuelled operation, respectively. As previously mentioned, the higher H/C ratio of CNG over gasoline provides a significant advantage in CO_2 emissions reduction when considering only fuel substitution. Based on the fuel compositions details in Table 2.1 and part (a) of

Eq. 1.1.1, changing fuel from certification gasoline ($\frac{\xi_{C,F}}{LHV_F}$ = 0.824/41.67 MJ/kg = 19.8 gCO_2/MJ) to CNG ($\frac{\xi_{C,F}}{LHV_F}$ = 0.71/46 MJ/kg = 15.4 gCO_2/MJ) reduces CO_2 by approximately 22% on its own. An additional 1-5% CO_2 reduction is then achievable by exploiting the favorable properties of CNG to better optimize engine fuel efficiency. This reduction would be increased at higher loads due to avoided knock and fuel enrichment.

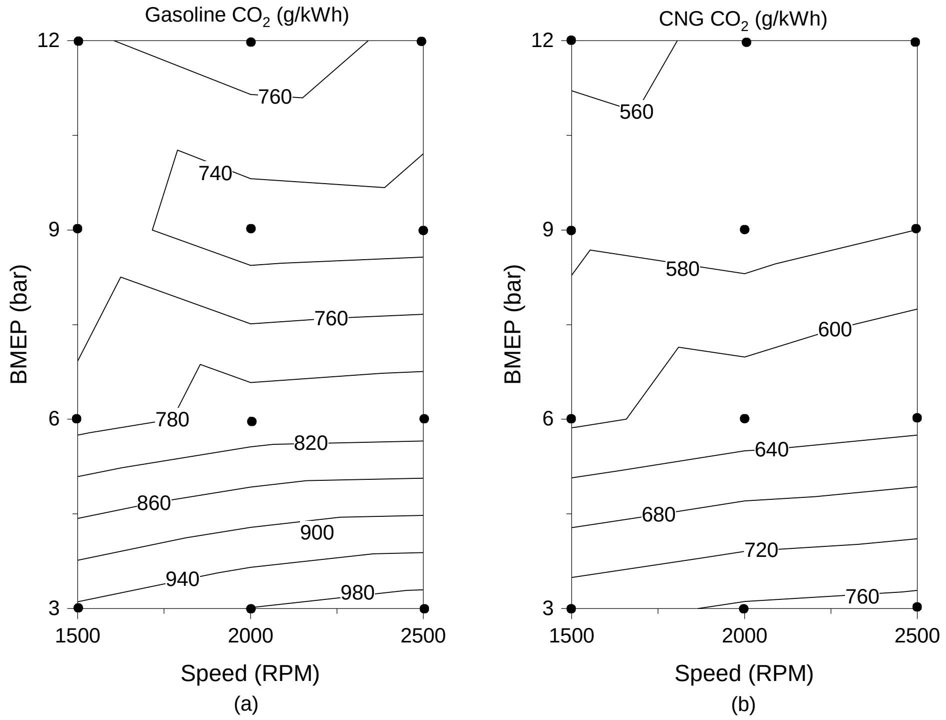

Figure 4.29: Maps of engine-out CO_2 emissions (g/kWh) for (a) Gasoline and (b) CNG fuelled engine operation as a function of speed and load at $\lambda = 1$.

Figure 4.30 shows the total CO_2 equivalent emissions based on engine-out GWP emissions for both gasoline and CNG fuelled engine operation. These are obtained using the CO_{2e} calculation methodology discussed in Section 3.5. Furthermore, normalized CO_{2e} emissions calculated as per Eq. 4.4.1 are also shown in Fig. 4.31.

$$\text{Normalized } CO_{2e} = \frac{[CO_{2e}]_{\text{CNG}}}{[CO_{2e}]_{\text{gasoline}}} \tag{4.4.1}$$

Accounting for GWP of CH_4 and NO_x emissions, an approximate 16-19% engine-out CO_{2e} reduction is observed with DI CNG relative to GDI operation. Note that the calculation of CO_{2e} for gasoline includes engine-out CO_2 and NO_x only as most of the UHC emissions with gasoline fuelling are non-methane compounds [37].

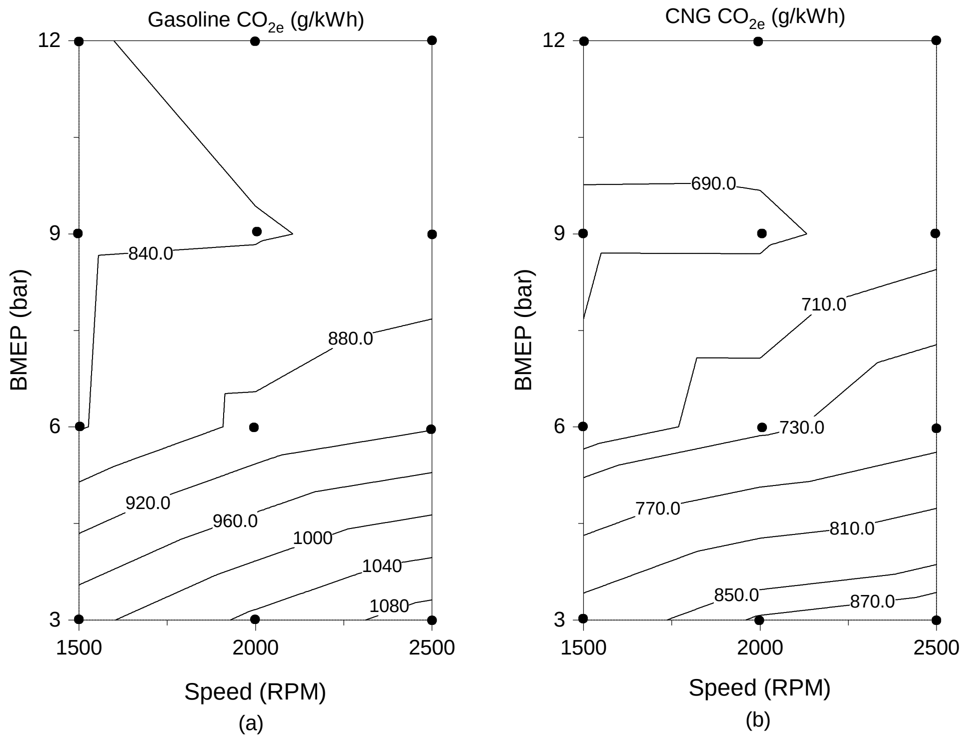

Figure 4.30: Map of engine-out CO_{2e} emissions (g/kWh) for (a) Gasoline and (b) CNG fuelled engine operation as a function of speed and load at $\lambda = 1$.

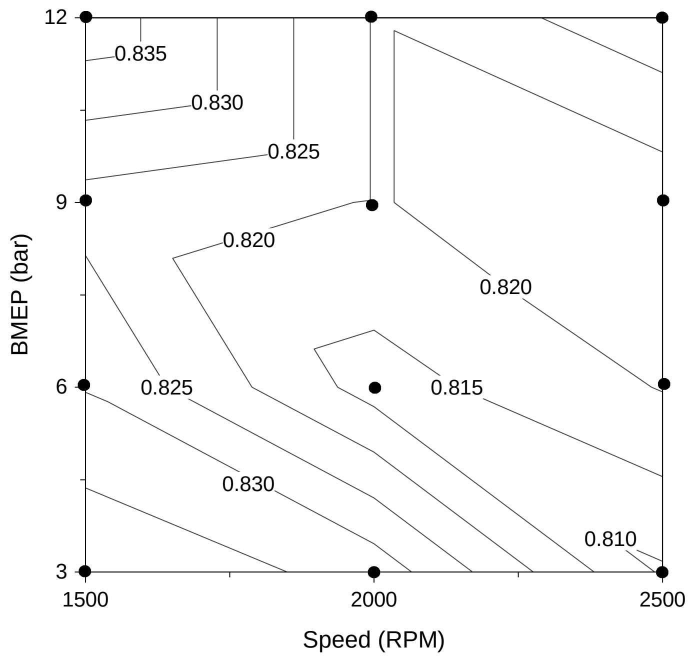

Figure 4.31: CO_{2e} emissions for DI CNG operation normalised by CO_{2e} emissions of GDI engine as a function of speed and load at $\lambda = 1$.

4.5 Summary

In this chapter, experimental results were presented both for CNG and gasoline fuelled DI engine operation under stoichiometric conditions. For DI CNG operation, start of injection (SOI) timing sweeps were first performed at part load conditions, and it was found that early injection promoting greater mixture homogeneity was beneficial. Retarded SOI timings performed worse at part loads, irrespective of volumetric efficiency benefits. An intermediate SOI timing in the range of 240 to 280 deg bTDC$_{Fire}$ therefore provided a balance of sufficient mixing time and engine de-throttling to realize the highest brake thermal efficiency.

This optimized part load engine performance with DI CNG was compared with the baseline GDI engine performance. DI CNG operation had lower UHC and CO emissions compared to those of gasoline, indicating increased combustion efficiency. It was nonetheless found that the higher compression energy needed during the compression stroke offsets the reduced pumping losses and higher combustion efficiency with DI CNG, resulting in similar thermal efficiency at part-load conditions for both fuels.

It was then demonstrated that CNG fuelled operation with retarded direct injection can achieve the same peak power relative to GDI operation at low speeds for a given engine. High load operation also demonstrated the superior knock resistance of CNG. This resulted in a substantial fuel consumption improvement at higher engine loads when utilizing DI CNG.

Finally, the total CO_2 equivalent emissions were calculated considering engine-out GWP emissions, and an approximate 16-19% CO_{2e} reduction was observed with DI CNG relative to GDI operation due to the fuel substitution and efficiency gain under stoichiometric condition.

Chapter 5

Stoichiometric DI CNG and GDI Engine Operation with Cooled, External Exhaust Gas Recirculation

The stoichiometric operation of spark-ignited DI CNG and GDI engines with no external diluent was discussed in Chapter 4. Despite the benefits demonstrated when replacing gasoline with CNG, this mode of operation is efficiency-constrained at low to medium loads due to engine throttling losses [84]. Since the vast majority of drive cycle time is spent at part load, improvement of engine efficiency at these conditions has significant ramifications for the overall drive cycle fuel economy.

One method to improve the part load efficiency is to control the engine load in part with dilution, and therefore reduce throttling, either by excess air or by external exhaust gas recirculation (EGR)[1]. With EGR, exhaust gases are extracted downstream of the turbocharger, cooled through a water-cooled heat exchanger, and circulated to the intake system upstream of the compressor where the cooled, external EGR mixes with incoming intake air (Section 3.1.1.2).

This chapter examines the impact of EGR on engine efficiency and emissions with

[1]Note: EGR refers to externally recirculated exhaust gas, and i-EGR denotes the internal residual based on valve timing throughout the thesis.

both CNG and gasoline fuelling at stoichiometric conditions. Combustion analysis is then used to gain insight into the physics governing the combustion process and understand the relationship between bulk flame quenching and measured engine-out UHC emissions when stoichiometric EGR operation is employed. The potential for greenhouse gas emissions abatement over a range of engine speeds and loads using stoichiometric CNG with EGR is also investigated.

5.1 Engine control strategy for EGR dilution

As discussed in Section 3.1.1.2 and 3.2.3, dilute operation with EGR is performed with the fully open wastegate, and the dilution level is varied by opening an EGR valve, which recirculates a portion of the exhaust gas back into the intake system.

In the current study, the start of injection (SOI) timing for gasoline fuelled operation with EGR is maintained at the factory timing of 280 deg bTDC$_{Fire}$. As demonstrated in Chapter 4 with stoichiometric DI CNG operation, mixture homogeneity is necessary for optimal BTE at part load. All CNG fuelled operation with EGR dilution are therefore performed with an intermediate SOI timing of 240 deg bTDC$_{Fire}$. MBT ignition timing is then maintained for all EGR levels with both fuels at part load. The valve timings for EGR operation are maintained at factory settings obtained from the baseline stoichiometric engine operation for a given load and speed. A closed-loop lambda control unit integral with the ECU maintains a stoichiometric air-fuel mixture at all times. The amount of EGR is based on measured mass flow rates and is calculated as follows [151]:

$$EGR(\%) = \frac{\dot{m}_{total} - \dot{m}_{air}}{\dot{m}_{total}} * 100 \tag{5.1.1}$$

where $\dot{m}_{air}$ is the fresh air flow rate measured upstream of the air filter and $\dot{m}_{total}$ is the total flow rate combining fresh air and recirculated exhaust gas measured immediately upstream of the throttle body.

5.2 Engine performance with EGR

5.2.1 The impact of EGR on engine efficiency and emissions with CNG and gasoline fuelling

Figure 5.1 shows the brake thermal efficiency and COV_{IMEP} as a function of EGR rate both for gasoline and CNG at 2500 RPM and 6 bar BMEP. Around a 0.7% and 1.6% increase in BTE is observed with the maximum amount of EGR dilution relative to the baseline condition for CNG and gasoline fuelled engine operation, respectively. Furthermore, CNG fuelled operation produces lower brake thermal efficiency compared to gasoline fuelling under similar EGR dilution, with the causes of these differences are discussed later in this chapter. Fig. 5.1 also shows that, for both fuels, the combustion variability (i.e., COV_{IMEP}) is below 5% over the range of EGR conditions tested. This relatively high COV_{IMEP} limit compared to what was used in Chapter 4 is employed to probe the engine performance with charge dilution at the limits. For gasoline, there is an overall lower COV_{IMEP} relative to CNG fuelled EGR operation, which can be attributed to the lower burning velocity

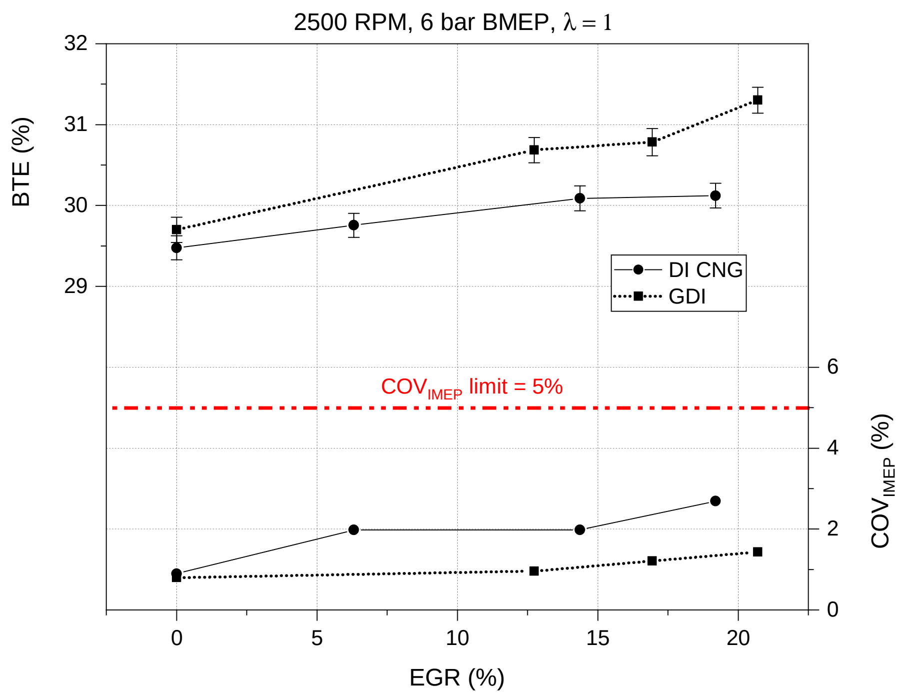

Figure 5.1: BTE and COV_{IMEP} for gasoline and CNG fuelled stoichiometric operation as a function of EGR at 2500 RPM and 6 bar BMEP.

of CNG in the presence of EGR diluent [119]. This trend is also consistent with gasoline's greater BTE improvement when using EGR.

Figure 5.2 shows that NO_x emissions decrease while exhaust gas temperatures (EGTs) increase with increased EGR dilution, as to be expected. Since NO_x is primarily formed in the post flame environment [37], this reduction in engine-out NO_x emissions is likely due to a significant reduction of in-cylinder temperatures with EGR dilution. For both fuels, an increasing trend of EGTs is also observed with an increasing EGR rate. This can be attributed to increased heat loss to the exhaust, likely due to the extended combustion duration into the expansion stroke with EGR.

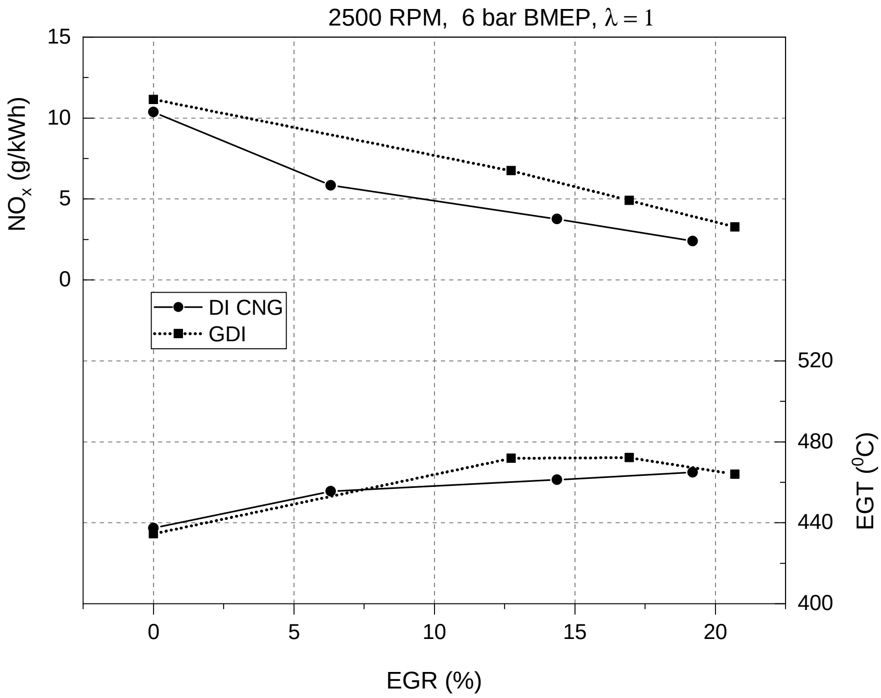

Figure 5.2: Engine-out NO_x and EGT for gasoline and CNG fuelled stoichiometric operation as a function of EGR at 2500 RPM and 6 bar BMEP.

Figure 5.3 shows engine-out CO and UHC emissions as a function of the EGR rate for CNG and gasoline fuelling at 2500 RPM and 6 bar BMEP. A weakly decreasing CO emissions trend is observed for both fuels with EGR dilution. For both fuels, engine-out UHC emissions increase with the increasing EGR rate. These UHC trends are consistent with the earlier observations of COV_{IMEP} results (Fig. 5.1). The potential causes of both of the trends will be discussed later in this chapter.

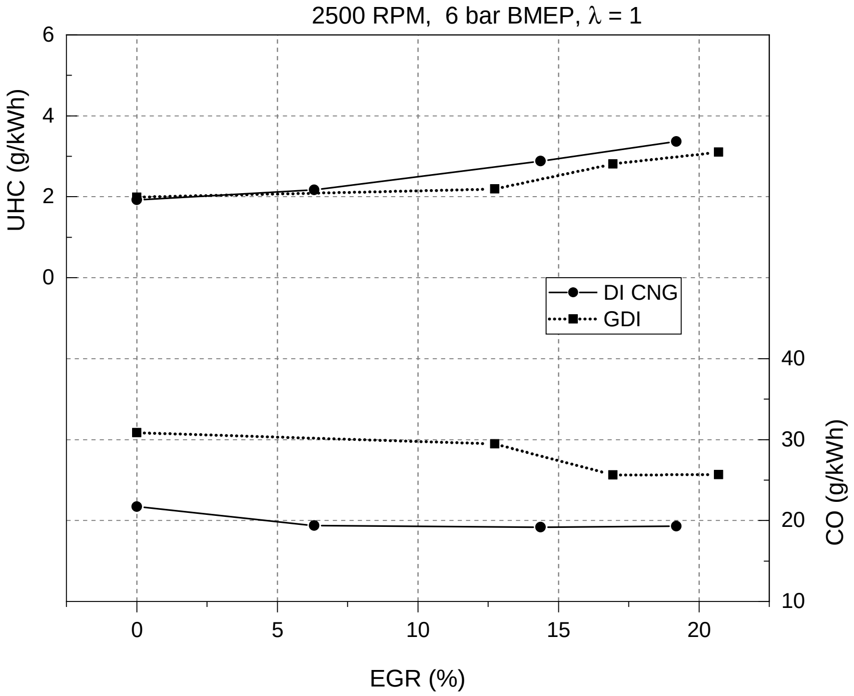

Figure 5.3: Engine-out CO and UHC emissions for gasoline and CNG fuelled stoichiometric operation as a function of EGR at 2500 RPM and 6 bar BMEP.

5.2.2 Comparison of part load engine operation with CNG and gasoline fuelling

Figure 5.4 shows the EGR rate, manifold air pressure (MAP), and COV_{IMEP} required to achieve a range of part load conditions for three different engine speeds with CNG fuelling. Engine operation begins with a MAP close to atmospheric pressure, which is close to representative WOT without boosting. The load then decreases with an increasing EGR rate. At a given throttle position, there is an EGR rate that causes COV_{IMEP} >5%. Once this threshold is reached, the decrease of engine load is thereafter achieved by closing the throttle position from WOT, resulting in lower MAP.

We now consider the effect of engine speed. Figure 5.5 compares the brake thermal efficiency of CNG fuelled stoichiometric operation with EGR relative to baseline gasoline and CNG fuelled stoichiometric operation without external dilution. For all three engine speeds, an improvement in BTE is observed in the mid load range, though BTE deteriorates at low load with EGR dilution. As expected, Fig. 5.6 shows that NO_x emissions are reduced significantly at part load for all three engine

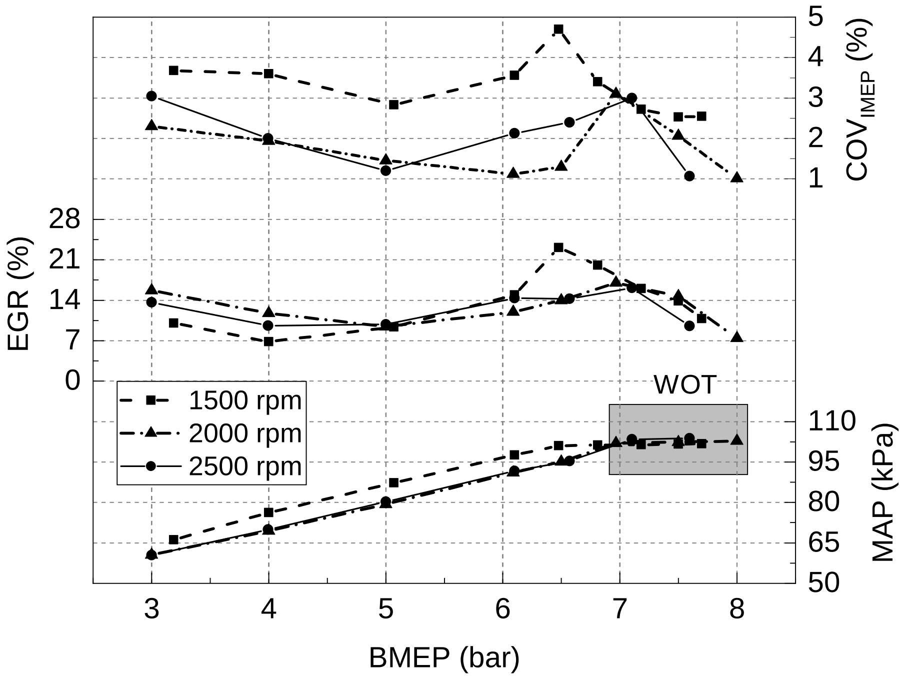

Figure 5.4: EGR rate, MAP, and COV_{IMEP} with CNG fuelled stoichiometric operation over the tested part load range.

speeds with EGR dilution. This is consistent with earlier results, and reasons will be discussed later in this chapter. The variation of EGTs with load is compared with the baseline operation in Fig. 5.7. For all three engine speeds, similar EGTs are observed with CNG fuelling over the part load range irrespective of the level of EGR dilution. This is consistent with the proposed benefits of the wastegate opening strategy for external dilution, as described in Section 3.2.3.

Figure 5.8 shows higher UHC emissions with EGR dilution compared to baseline operation for all three engine speeds over the part load range. This necessitates a trade off between the maximum EGR limit and effective control of a three-way catalyst (TWC) for CNG fuelled engine operation, as discussed in Section 2.5.4.

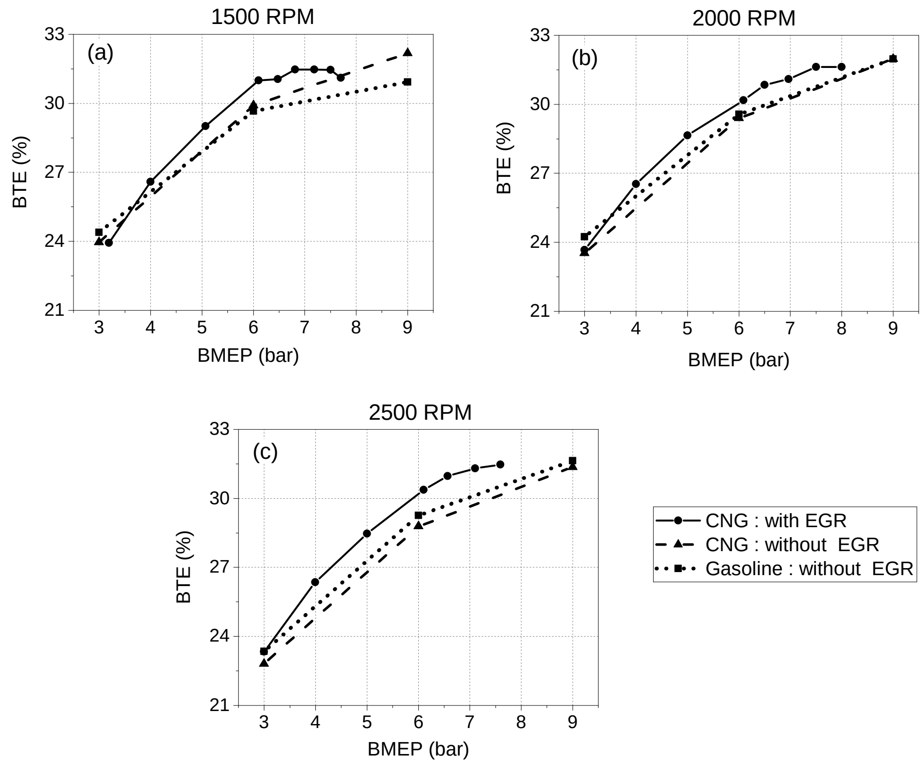

Figure 5.5: Part load BTE comparison at (a) 1500 RPM, (b) 2000 RPM, and (c) 2500 RPM for stoichiometric CNG fuelled operation with EGR, baseline stoichiometric gasoline and CNG fuelled operation without EGR.

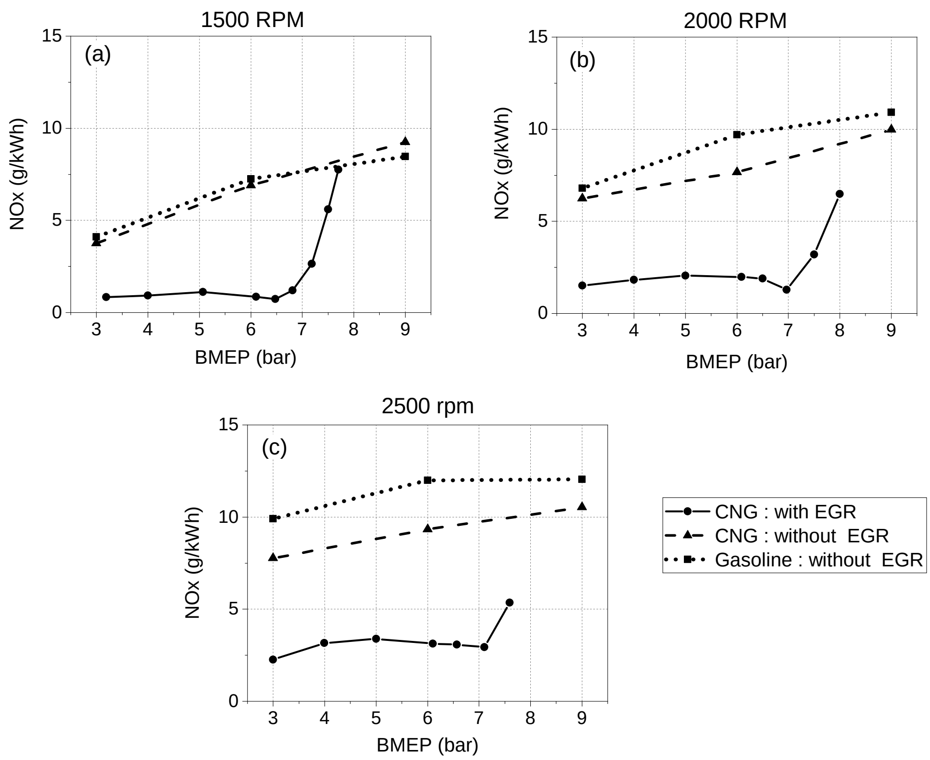

Figure 5.6: Part load NO_x emissions (g/kWh) comparison at (a) 1500 RPM, (b) 2000 RPM, and (c) 2500 RPM for stoichiometric CNG fuelled operation with EGR, baseline stoichiometric gasoline and CNG fuelled operation without EGR.

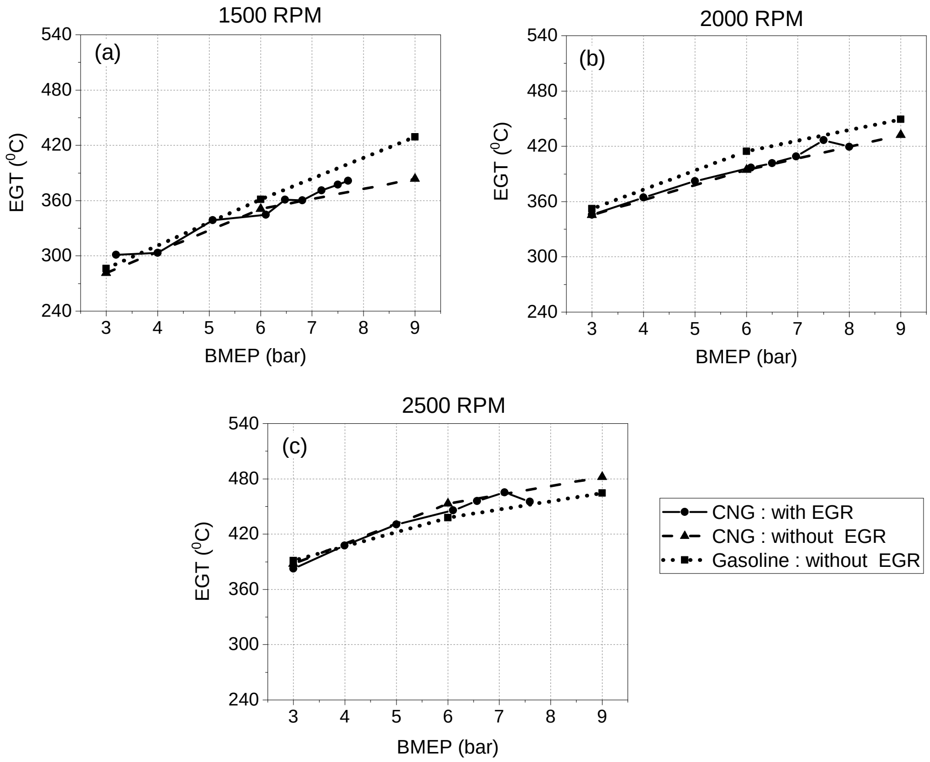

Figure 5.7: Part load EGT comparison at (a) 1500 RPM, (b) 2000 RPM, and (c) 2500 RPM for stoichiometric CNG fuelled operation with EGR, baseline stoichiometric gasoline and CNG fuelled operation without EGR.

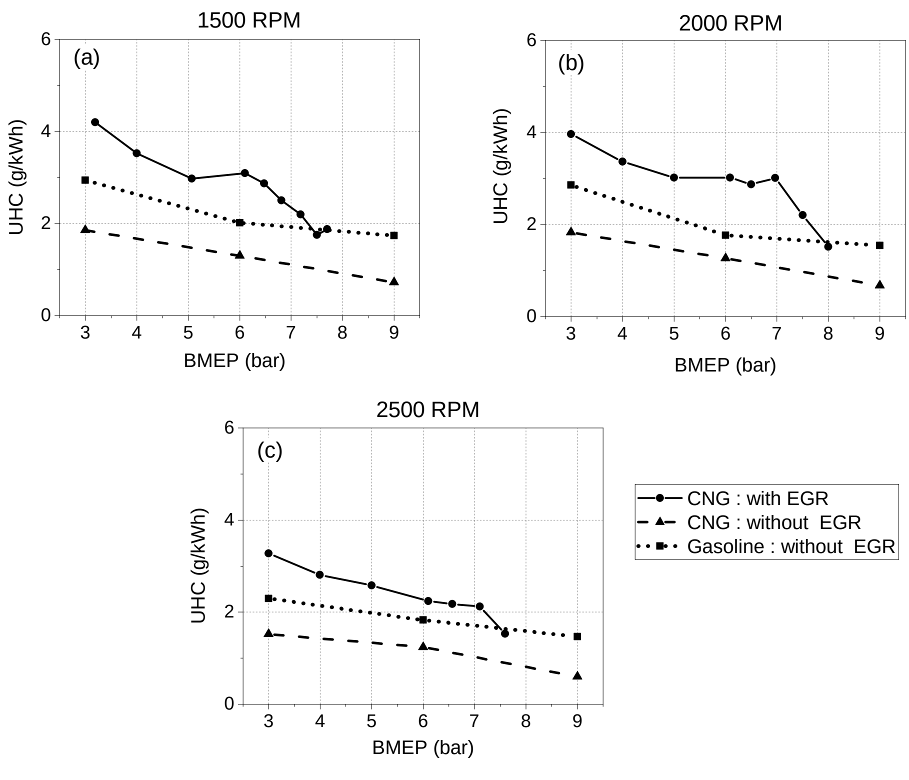

Figure 5.8: Part load UHC emissions (g/kWh) comparison at (a) 1500 RPM, (b) 2000 RPM, and (c) 2500 RPM for stoichiometric CNG fuelled operation with EGR, baseline stoichiometric gasoline and CNG fuelled operation without EGR.

5.3 Analysis of engine performance with EGR dilution

5.3.1 In-cylinder pressure and temperature during combustion

Figure 5.9 (a) shows the P-V diagram of representative pressure traces for stoichiometric DI CNG operation at 2500 RPM and 6 bar BMEP with 0% EGR and 19% EGR. These two EGR rates span those presented earlier in this chapter. The intake pressure is higher with 19% EGR, as the engine is less throttled to compensate for the displacement of fresh air by the recirculated exhaust gas. A comparison of pumping mean effective pressure (PMEP) calculated using Eq. 5.3.1 is also shown in Fig. 5.9 (b) as a function of EGR for both fuels.

$$PMEP = \frac{\int_{\theta_{EVO}}^{\theta_{IVC}} PdV}{V_d} \tag{5.3.1}$$

where P is the measured in-cylinder pressure, V is the instantaneous volume, V_d is the engine displacement volume, θ_{IVC} is the crank angle at the intake valve closure, and θ_{EVO} is the crank angle at the exhaust valve opening. As the EGR dilution rate increases at a given load and speed, the throttle is opened to match the load, decreasing pumping losses. For CNG fuelled operation, the displacement of fresh air by both natural gas and the recirculated exhaust gas necessitates less throttling relative to gasoline fuelled operation, resulting in lower PMEP with CNG at all EGR conditions.

Figure 5.10 (a) shows that the simulated in-cylinder burned and unburned gas temperatures reduce with increasing EGR dilution with CNG. These simulations were performed using GT-Power, with the methods discussed in Section 3.3.2. This lower burned gas temperature is consistent with the measurement of lower NO_x emissions with EGR, as observed in Figures 5.2 and 5.6. Furthermore, Fig. 5.10 (b) shows that CNG fuelling results in lower peak in-cylinder temperatures relative to gasoline fuelling, which is likely the cause of the earlier observations of lower engine-out NO_x and CO emissions when gasoline is substituted with CNG.

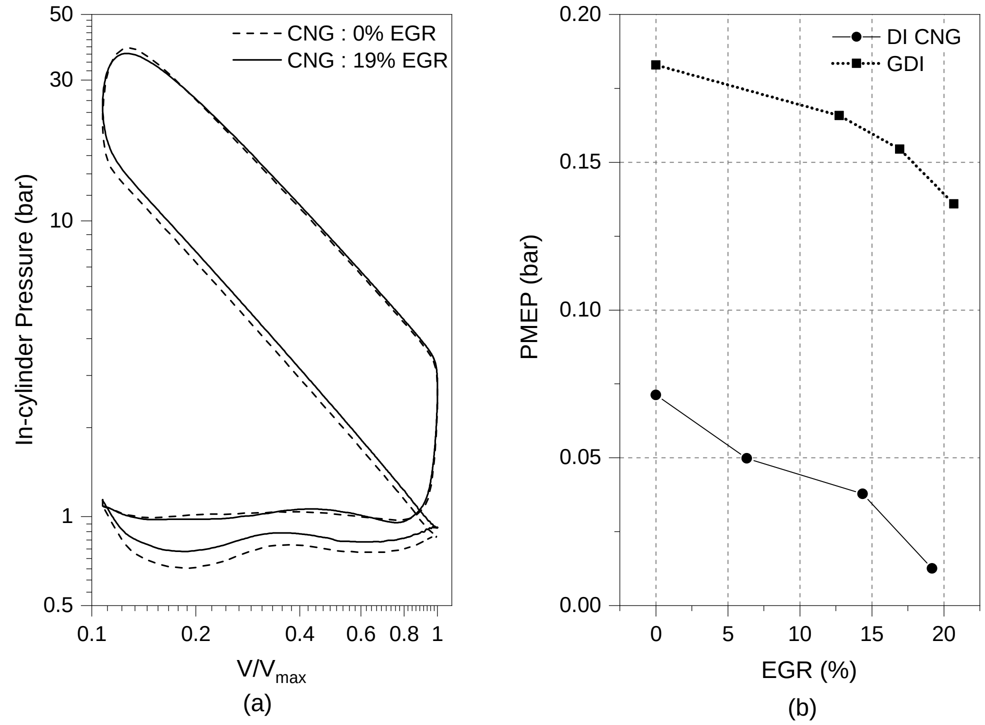

Figure 5.9: (a) Pressure-volume trace comparison on a logarithmic scale for stoichiometric CNG fuelled engine operation with 0% EGR and 19% EGR, (b) Pumping mean effective pressure (PMEP) comparison for CNG and gasoline fuelled operation as a function of EGR at 2500 RPM and 6 bar BMEP.

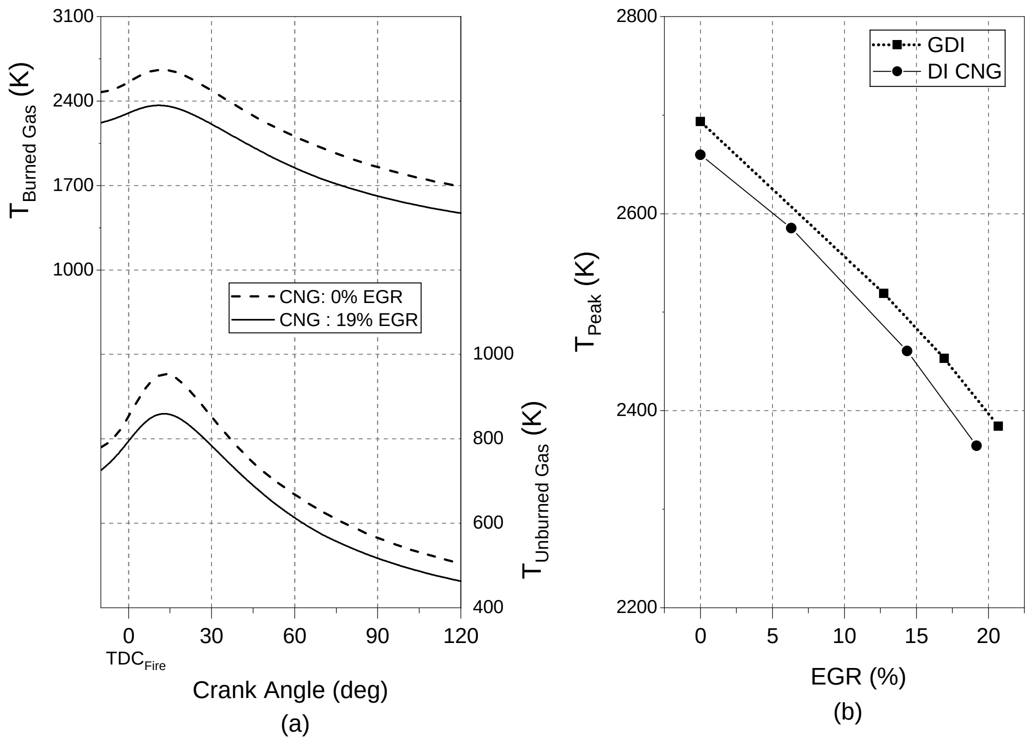

Figure 5.10: (a) In-cylinder burned and unburned gas temperature for stoichiometric CNG fuelling with 0% EGR and 19% EGR, (b) Peak temperature comparison for CNG and gasoline fuelling as a function of EGR at 2500 RPM and 6 bar BMEP.

5.3.2 Combustion duration

Figure 5.11 presents the MBT ignition timing and 0-90% MFB duration as a function of EGR at 2500 RPM and 6 bar BMEP for gasoline and CNG fuelled operations. More ignition advance and longer burn durations are observed with increased EGR for both fuels, which likely account for some of the observed BTE reduction. This longer burn duration can be attributed to slower flame speeds due to a reduction of mixture heating value [163] and lower in-cylinder unburned gas temperatures (Fig. 5.10-a) with EGR addition. As expected, the CNG fuelled operation also requires more ignition advance and has a longer burn duration compared to gasoline fuelling due to its lower flame speed.

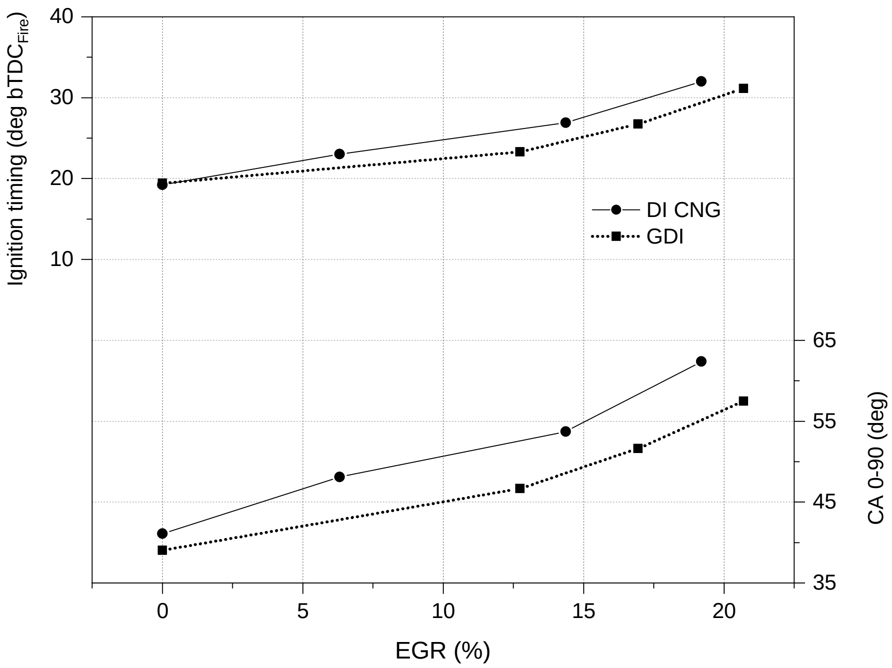

Figure 5.11: Ignition timing and 0-90% MFB duration for gasoline and CNG fuelled stoichiometric engine operation as a function of EGR at 2500 RPM and 6 bar BMEP.

5.3.3 Energy balance and loss analysis

Figures 5.12 (a) and (b) show a comparison of the energy balance and heat loss distribution, respectively, at 2500 RPM and 6 bar BMEP for DI CNG operation with 0% EGR and 19% EGR. The in-cylinder wall heat losses, $\dot{Q}_{In-Cyl}$ decrease with EGR addition compared to baseline operation due to lower in-cylinder temperatures (Fig. 5.12-b). Pumping losses given by $\dot{Q}_{Pump}$ also decrease with

EGR dilution, as throttling losses are minimized using the part load EGR strategy. These two effects are the primary sources for BTE improvement using EGR dilution. However, as shown from the energy balance in Fig. 5.12 (a), the unburned fuel energy, $\dot{H}_{UBF}$ increases with EGR dilution because of flame quenching due to a reduction in mixture heating value and lower in-cylinder temperatures. Furthermore, energy lost in the exhaust, $\dot{H}_{Exh}$ slightly increases with EGR operation, which is consistent with the higher measured EGTs in Fig. 5.2 and the longer burns in Fig. 5.11. These are the primary sources of efficiency loss when using EGR dilution. Therefore, the optimization of part load fuel efficiency with EGR dilution necessitates the management of two competing effects:

1. efficiency gain through lower in-cylinder wall heat losses and reduced pumping work;
2. efficiency loss through incomplete combustion and increased sensible enthalpy in the exhaust.

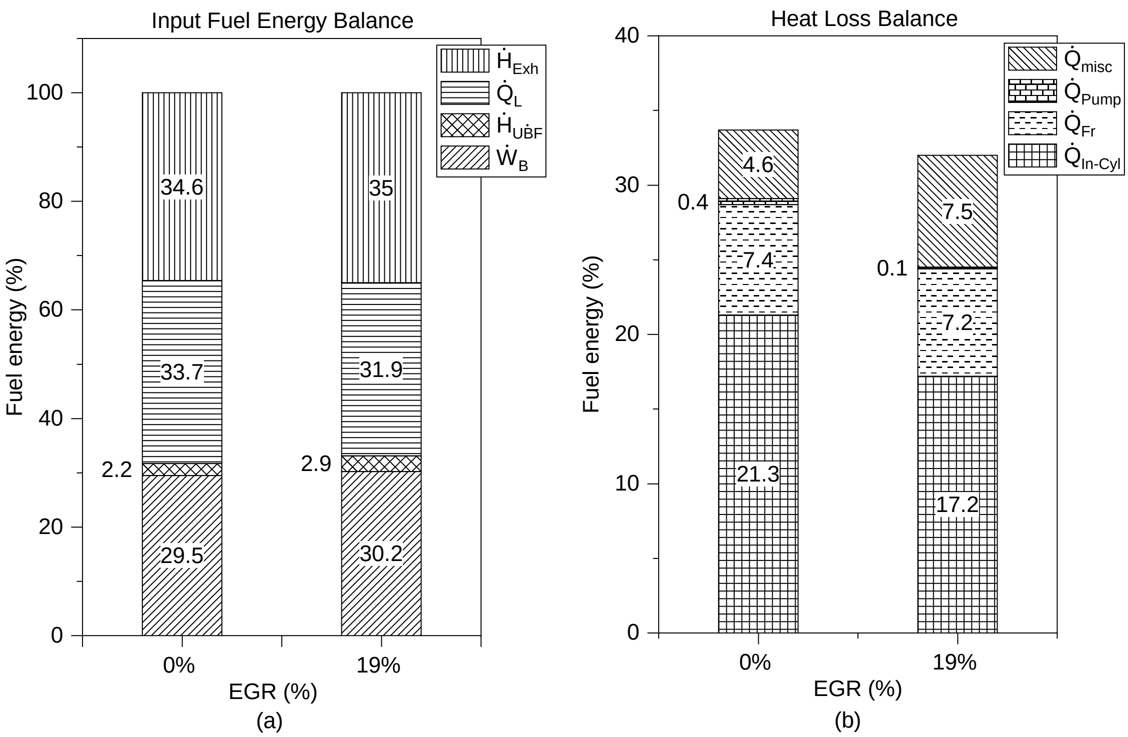

Figure 5.12: Comparison of modelled (a) input fuel energy balance and (b) heat loss distribution at 2500 RPM and 6 bar BMEP for DI CNG operation with 0% EGR and 19% EGR (obtained using the methodology described in Section 3.3.2 and 3.4.2).

5.4 Understanding UHC emissions trends

The use of EGR was earlier shown to increase engine efficiency for CNG and gasoline fuelling at part loads. However, an increase in UHC emissions was also observed with higher rates of EGR. It is hypothesized that the use of EGR dilution leads to increased flame quenching, which subsequently increases UHC emissions [37]. This phenomenon is investigated through the use of premixed, turbulent combustion analysis for both gasoline and CNG fuelling using GT-Power simulation. The reader is referred to Section 3.3.3 for more details of this methodology.

5.4.1 Flame speed

A comparison of the laminar flame speed (S_L) and turbulent burning velocity (S_T) across representative burns are shown in Fig. 5.13 for 0% EGR and 19% EGR for CNG fuelling. As expected, S_L decreases with the increase of EGR dilution due to a reduction in heating value per unit mass of the mixture [92, 164] and lower in-cylinder unburned gas temperatures (Fig. 5.10-a). For a given engine speed and load, S_T also decreases with EGR dilution due to S_L falling. Lower S_L and S_T then

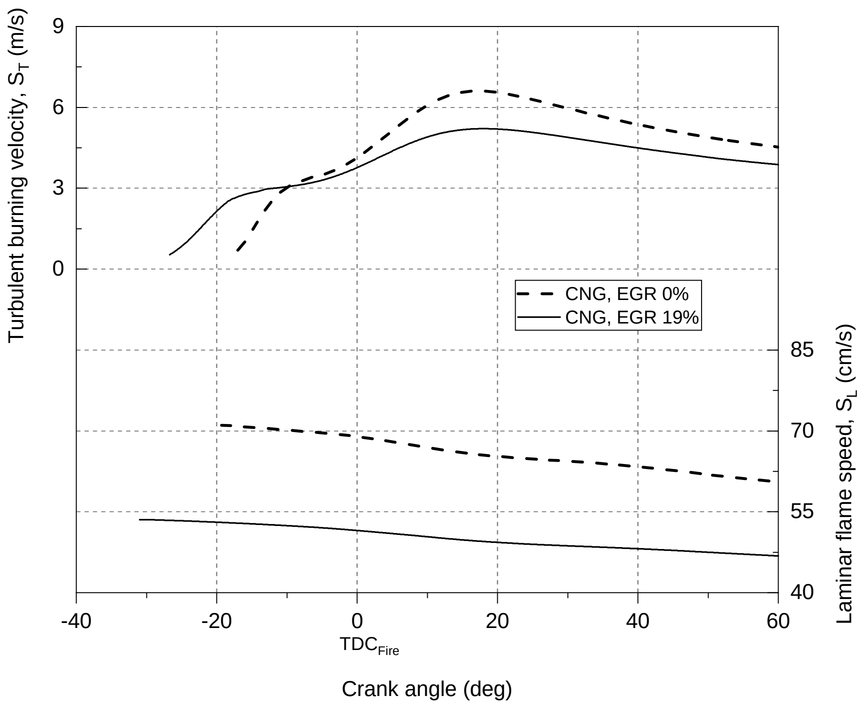

Figure 5.13: Comparison of S_L (cm/s) and S_T (m/s) for CNG fuelled stoichiometric operation with 0% EGR and 19% EGR at 2500 RPM, 6 bar BMEP.

necessitate an advancement of ignition timing to maintain MBT and therefore a longer combustion duration, as shown in Fig. 5.11.

A comparison of S_T and S_L for gasoline and CNG fuelling is shown in Fig. 5.14 for similar EGR rates at 2500 RPM and 6 bar BMEP. Unlike gasoline, the S_L of natural gas does not increase with temperature rise because of the modelled negative pressure coefficient (i.e., $S_{L,\,CNG} \propto P_u^{-0.51}$ and $S_{L,\,gasoline} \propto P_u^{-0.22}$) that works to offset the effect of high temperature during combustion [37, 56, 151, 156, 165]. A slightly higher turbulent burning velocity is also observed with gasoline relative to CNG under EGR dilution. These trends indicate slower combustion with CNG fuelling than gasoline with EGR dilution and are consistent with the combustion duration results for both fuels shown in Fig. 5.11.

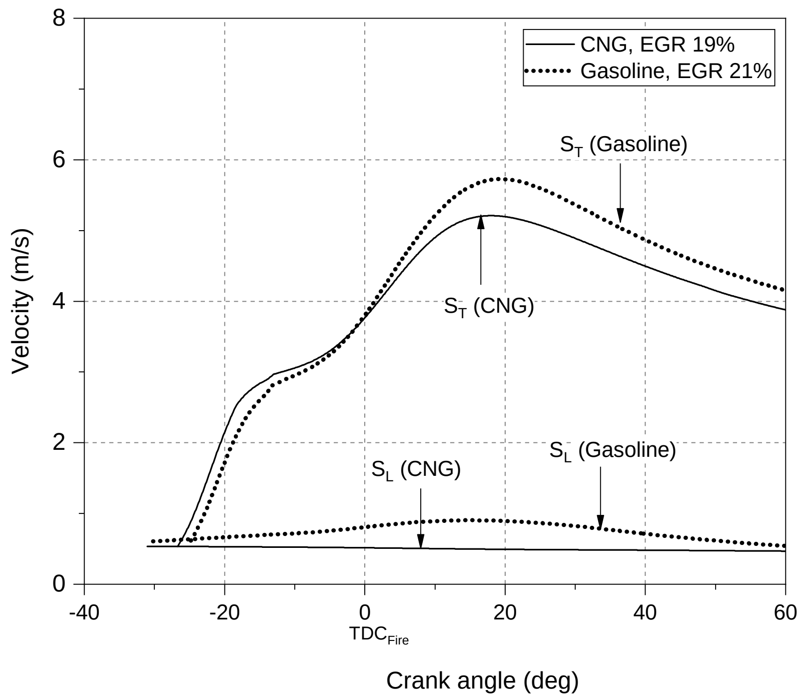

Figure 5.14: Comparison of S_L (m/s) and S_T (m/s) for gasoline and CNG fuelled stoichiometric engine operation with EGR at 2500 RPM and 6 bar BMEP.

5.4.2 Turbulent flame quenching and its relationship to UHC emissions

The effect of turbulence on flame quenching is shown in Fig. 5.15. Here, the ratio of the turbulent burning velocity to laminar flame speed, $\frac{S_T}{S_L}$ is plotted against the ratio of the effective turbulence intensity to laminar flame speed, $\frac{u_k^t}{S_L}$ in the 'Bradley' diagram. The locus of three representative burns at 2500 RPM and 6 bar BMEP are shown, along with four specific points in each burn defined by a given MFB. Substitution of gasoline with CNG with a similar level of EGR, or an increase in EGR rate, both shift these loci to a higher value of KLe and towards the quenching region, where K is the Karlovitz stretch factor and Le is the Lewis number.

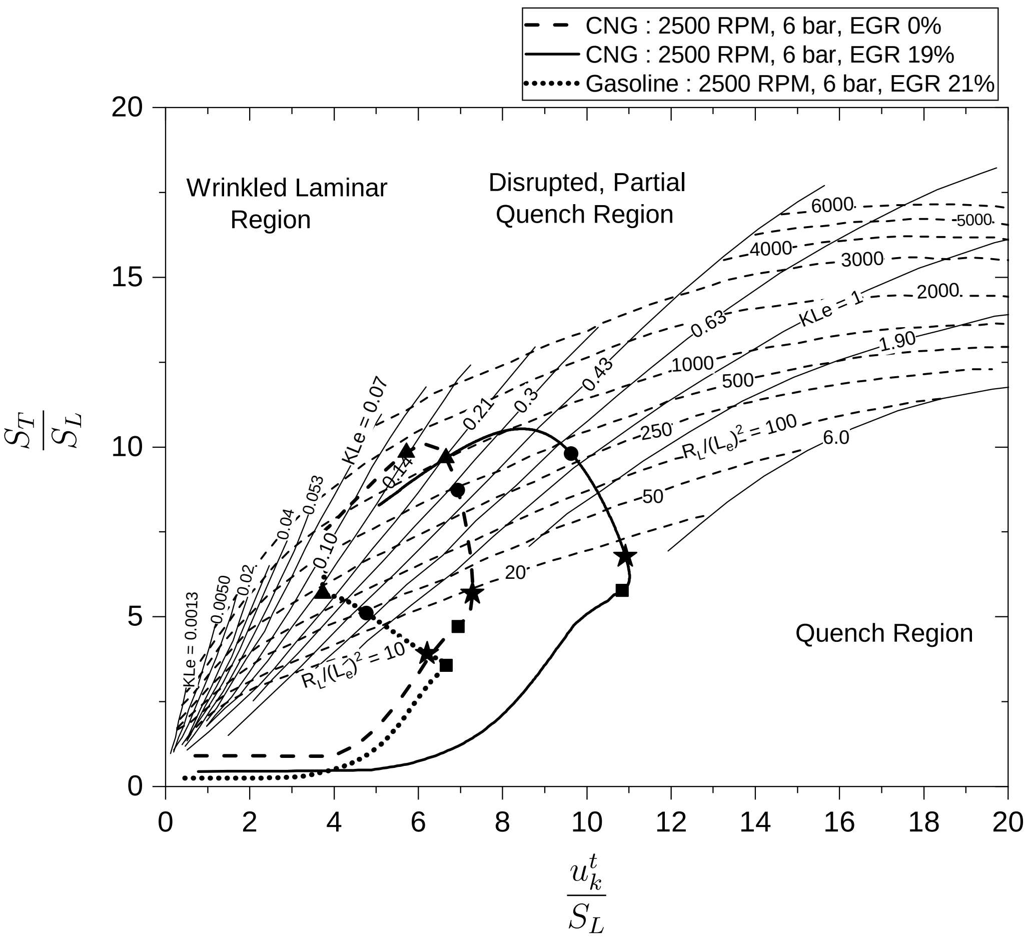

Figure 5.15: Loci of combustion events in the Bradley diagram for gasoline and CNG fuelled engine operation with different amount of EGR dilution at 2500 RPM, 6 bar BMEP, and $\lambda = 1$ [44, 60, 62]. Highlighted symbols represent combustion event at the location of 1% MFB (■), 10% MFB (★), 50% MFB (●), and 90% MFB (▲).

The effect of engine speed on flame quenching via turbulence is also shown in Fig. 5.16. With the increase of engine speed, S_L remains similar for a given mixture strength, but the turbulent intensity, u^t (and hence u_k^t) increases. This results in higher $\frac{u_k^t}{S_L}$, which again pushes the combustion locus to the right. This suggests that the flame quenching may offset the benefit of increased turbulence on flame propagation at higher engine speed with the use of EGR dilution. This may also explain why the higher EGR dilution is achievable at lower engine speeds (Fig. 5.4).

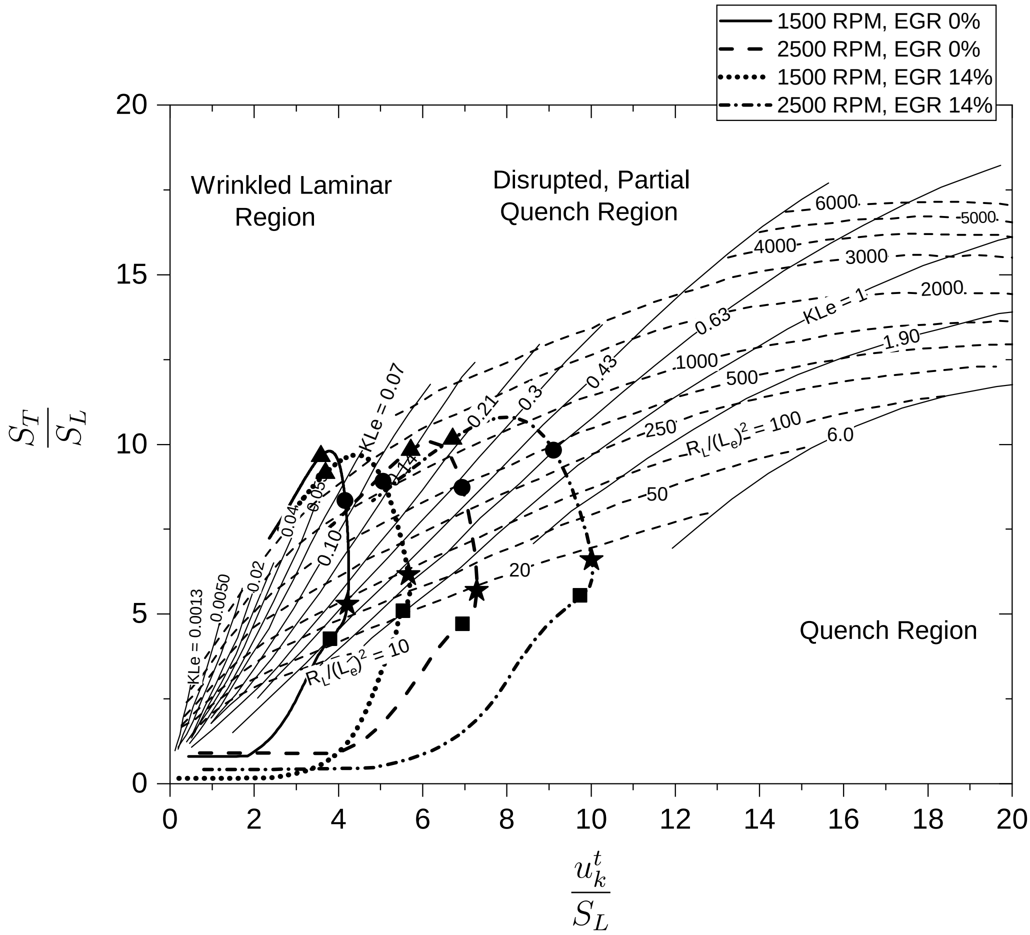

Figure 5.16: Engine speed effect: loci of combustion events in the Bradley diagram for CNG fuelled stoichiometric engine operation at 1500 and 2500 RPM, 6 bar BMEP, and $\lambda = 1$ [44, 60, 62]. Highlighted symbols represent combustion event at the location of 1% MFB (■), 10% MFB (★), 50% MFB (●), and 90% MFB (▲).

If this modelling and theory is reasonable, the expected increase in flame quenching via fuel substitution from gasoline to CNG, increased EGR, and increased engine speed should be observed in measured data. Measured engine-out UHC emissions and COV$_{IMEP}$ are therefore shown in Fig. 5.17 as a function of KLe at 1% MFB estimated from the Bradley diagrams (Fig. 5.15 and 5.16). The KLe values here are chosen at the 1% MFB location because the flame is more susceptible to quenching at the initial combustion stage [37, 42]. As shown in Fig. 5.17 (a), higher values of measured UHC and COV$_{IMEP}$ occur at higher KLe created by EGR dilution compared to the baseline condition for both fuels, and this effect is most pronounced with CNG fuelled operation. Furthermore, Fig. 5.17 (b) shows higher UHC and COV$_{IMEP}$ with larger KLe at 2500 RPM compared to 1500 RPM for two dilution levels, which supports the impact of engine speed on flame quenching as shown in Fig. 5.16. In both cases, the monotonic increase of UHC emissions and the COV_{IMEP}, both of which are measured quantities, with the modelled KLe suggests that flame quenching plays a significant role in determining engine performance.

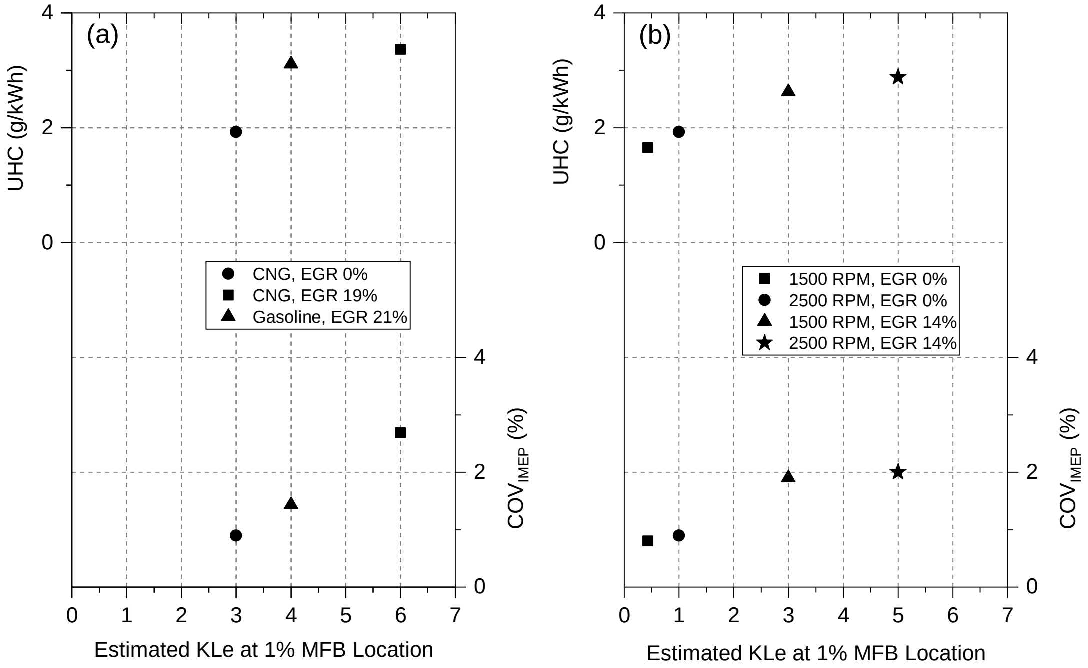

Figure 5.17: Unburned hydrocarbon (UHC) emissions and COV_{IMEP} as a function of KLe at the 1% MFB location (estimated from the Bradley diagrams) considering the (a) fuel substitution and EGR dilution effect at 2500 RPM, 6 bar BMEP, $\lambda = 1$ for both fuels, and (b) the engine speed effect at 1500 and 2500 RPM with CNG fuelling.

5.5 Greenhouse gas emissions with EGR

Figure 5.18 compares engine-out CO_2 emissions from CNG fuelled operation with EGR dilution over baseline operation with both CNG and gasoline. Considering a representative global warming potential of CH_4 (i.e. $GWP_{CH_4} = 25$ [160]) along with CO_2, engine-out CO_{2e} emissions (as per Eq. 3.5.1 in Section 3.5) of CNG fuelled operation with EGR dilution shown in Fig. 5.19 are not much higher than the baseline CNG fuelled operation, and are still lower than those with gasoline fuelling even after considering the high unburned hydrocarbons with EGR. Fig. 5.20 then shows CO_{2e} emissions considering the GWP of both CH_4 and NO_x (i.e., $GWP_{NO_x} = 10$ [161]) along with CO_2. CO_{2e} emissions with EGR dilution are now

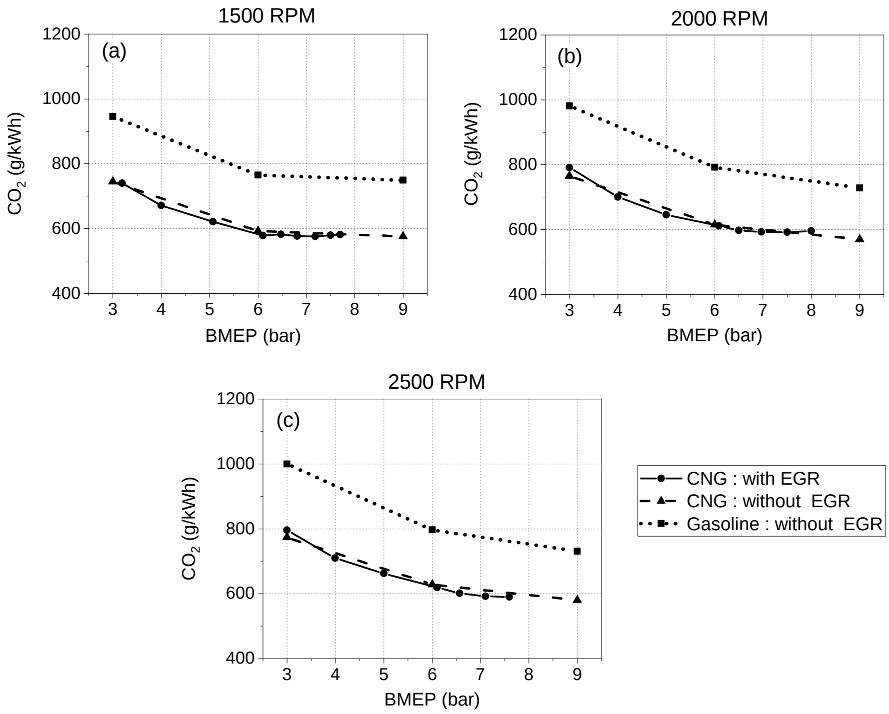

Figure 5.18: Part load CO_2 emissions comparison at (a) 1500 RPM, (b) 2000 RPM, and (c) 2500 RPM on CNG fuelled operation with EGR over the baseline gasoline and CNG fuelled operation without EGR at stoichiometric conditions.

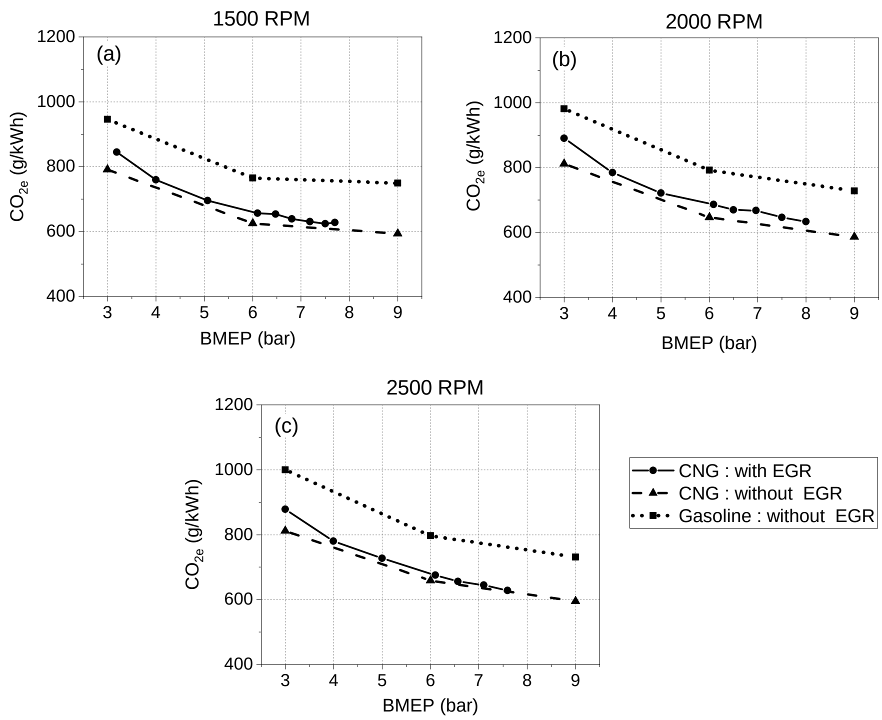

Figure 5.19: Part load CO_{2e} emissions comparison considering GWP of CO_2 and CH_4 at (a) 1500 RPM, (b) 2000 RPM, and (c) 2500 RPM on CNG fuelled operation with EGR over the baseline gasoline and CNG fuelled operation without EGR at stoichiometric conditions.

lower than the baseline CNG fuelled operation, particularly at mid load.

Furthermore, a conventional TWC can be used with EGR dilute operation as it maintains stoichiometric conditions, suggesting low tailpipe CO_{2e} emissions may also be achievable in this case. While the observed range of EGTs studied (Fig. 5.7) are likely sufficient for the oxidation of UHC from gasoline operation, further study of candidate TWC performance is required to determine the efficacy of TWC operation on CNG [140].

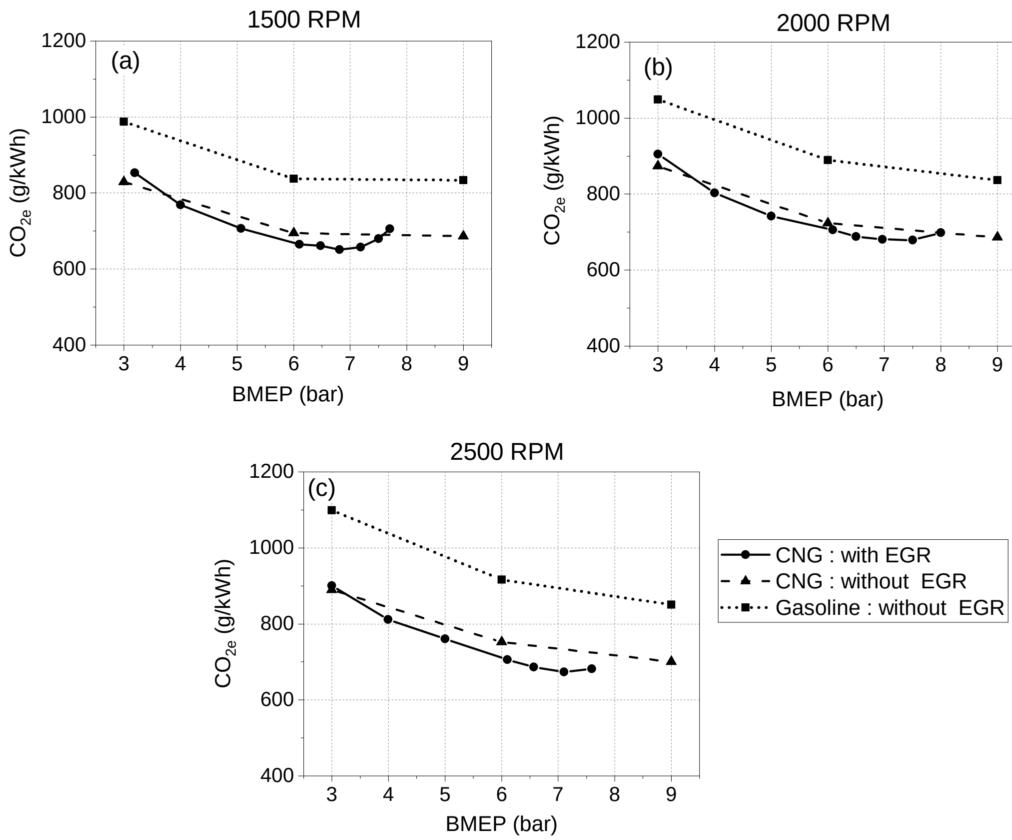

Figure 5.20: Part load CO_{2e} emissions comparison considering GWP of CO_2, CH_4, and NO_x at (a) 1500 RPM, (b) 2000 RPM, and (c) 2500 RPM on CNG fuelled operation with EGR over the baseline gasoline and CNG fuelled operation without EGR at stoichiometric conditions.

5.6 Summary

In this chapter, experimental results were presented for both gasoline and CNG fuelled stoichiometric engine operation with EGR dilution. EGR dilute operation resulted in an improvement in BTE relative to 0% EGR operation for both fuels. At a similar EGR rate, gasoline fuelled operation demonstrated higher brake thermal efficiency compared to CNG fuelling due to its faster combustion. The performance of CNG fuelled operation with EGR was also examined over a range of engine speeds and loads, and compared with the baseline operation with both fuels. DI CNG operation with EGR dilution exhibited overall higher BTE relative to baseline operation except at lower loads. This fuel economy improvement with EGR dilution was primarily attributed to the impact of reduced in-cylinder wall heat transfer and lower pumping work, which was dominant over the detrimental effect of energy lost in the exhaust.

For all three tested engine speeds, significantly lower NO_x emissions were observed with EGR dilution over the range of engine loads, and this was likely due to the reduction in in-cylinder temperatures.

To further investigate the observed UHC emissions trends, premixed turbulent combustion simulations were performed for both fuels. The resulting laminar and turbulent burning velocities fell with increasing EGR dilution, which was consistent with the longer combustion durations observed with EGR operation. Furthermore, the lower flame speed of CNG compared to gasoline under EGR dilution suggested that the effect of EGR dilution on the combustion was also fuel dependent. These results were then examined using the Bradley diagram, where lines of the product of the Karlovitz and Lewis numbers (KLe) indicate the susceptibility of turbulent premixed flames to quenching. Of note was the monotonic increase of engine-out UHC emissions and the COV_{IMEP}, both of which are measured quantities, with the modelled KLe at 1% mass fraction burned. These results appeared to accommodate variations in the fuel and the engine speed, and therefore suggest that flame quenching plays a role in determining engine performance.

Finally, EGR operation also demonstrated a slightly improved engine-out greenhouse gas emissions potential relative to baseline CNG operation over a range of part load conditions. It therefore appears that stoichiometric CNG fuelled operation with EGR dilution may be a viable strategy to improve fuel efficiency and mitigate carbon emissions in light-duty vehicles.

Chapter 6

DI CNG and GDI Lean Engine Operation and a Comparison between CNG Dilution Strategies

This chapter investigates the impact of lean-burn by air dilution on fuel economy and engine-out emissions, particularly NO_x in the presence of an oxygen-rich combustion environment, over the range of load and speed conditions mentioned in Table 3.6. Both EGR (as discussed in Chapter 5) and air dilution strategies have the potential for fuel economy improvement; however, the differing compositions of excess air and EGR suggest that each type of dilution will have different effects on the combustion process, which is also examined in detail.

To begin, lean-burn engine experiments are performed using the same fully open wastegate strategy adopted for EGR dilution in Chapter 5. The start of fuel injection (SOI) timing for gasoline fuelled engine operation with air dilution is maintained at the factory timing of 280 deg $bTDC_{Fire}$. All DI CNG operation with excess air dilution are performed with an intermediate SOI of 240 deg $bTDC_{Fire}$. This intermediate injection timing results in sufficient mixture homogeneity (Chapter 4) for optimal BTE at part load, irrespective of air dilution level. The reader is referred to Appendix B.2 for additional experimental details regarding this point.

MBT ignition timing is then maintained for all operating points with both fuels at part load. The valve timings for lean-burn operation are maintained at the factory settings obtained from the baseline stoichiometric engine operation at the same load and speed.

The amount of air dilution is quantified by the normalised air-fuel ratio λ,

$$\lambda = \frac{(\dot{m}_{air}/\dot{m}_{fuel})_{actual}}{AFR_{Stoich}} \tag{6.0.1}$$

where $\dot{m}_{air}$ and $\dot{m}_{fuel}$ are the measured flow rate of air and fuel, respectively. AFR$_{Stoic}$ is the stoichiometric air-fuel ratio. As a method to facilitate the comparison between dilution strategies, a modified form of the normalised air-fuel ratio λ' is also introduced. This term is defined as [166]:

$$\lambda' = \frac{(\dot{m}_{air} + \dot{m}_{TRG})/\dot{m}_{fuel}}{(\dot{m}_{air}/\dot{m}_{fuel})_{Stoich}} = \frac{\lambda}{1 - RGF}\,[1 + \frac{RGF}{\lambda\,(\frac{\dot{m}_{air}}{\dot{m}_{fuel}})_{Stoich}}] \approx \frac{\lambda}{1 - RGF} \tag{6.0.2}$$

where $\dot{m}_{air}$, $\dot{m}_{fuel}$ and $\dot{m}_{TRG}$ are the mass flow of air, fuel and total residuals respectively, λ is the measured normalised air-fuel ratio, and RGF is the total residual gas fraction, including both internal residual (i-EGR) and exhaust gas recirculation (EGR). Note that the i-EGR primarily depends on the intake pressure, valve timing, and engine speed [37]. The final approximation in Eq. 6.0.2 is commonly used [166] as the term $RGF/[\lambda\,(\dot{m}_{air}/\dot{m}_{fuel})_{Stoich}]^{-1}$ is generally small.

6.1 Engine performance

6.1.1 Comparing DI CNG with air dilution and stoichiometric EGR

Figure 6.1 shows the brake thermal efficiency as a function of λ' with CNG fuelling at 2500 RPM, 6 bar BMEP for each dilution strategy. The engine always has some internal residual, so λ' is never equal to unity. The values of λ and EGR rate corresponding to the calculated λ' are also presented in Fig. 6.1 using two

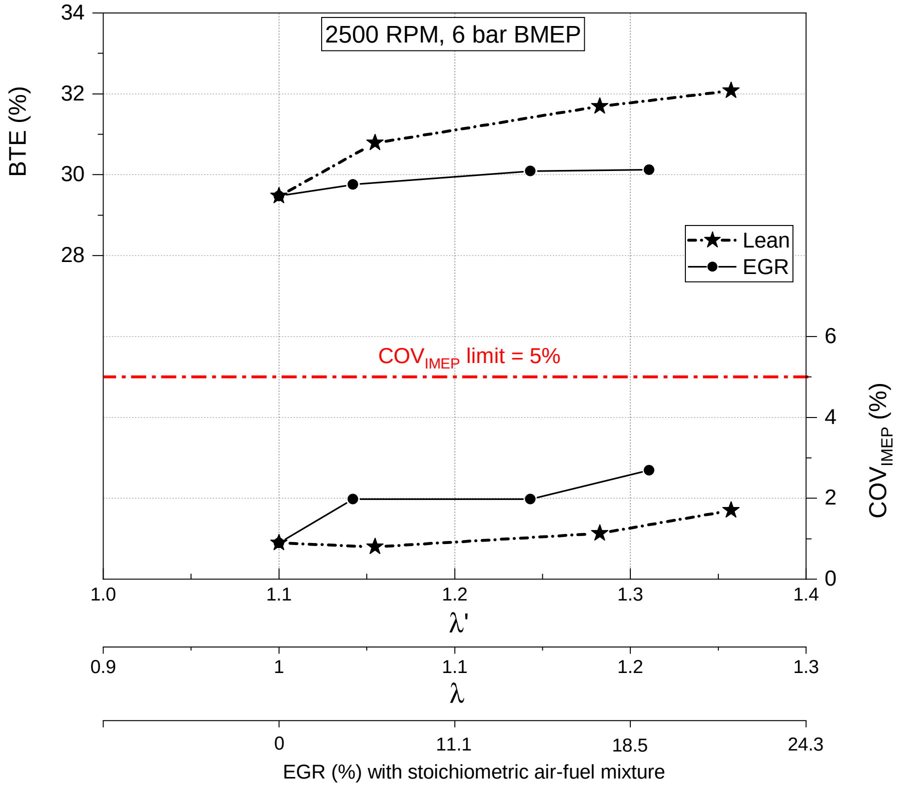

Figure 6.1: BTE and COV_{IMEP} for CNG fuelled operation with EGR and air dilution at 2500 RPM and 6 bar BMEP.

abscissas. At these tested conditions, a linear relationship is observed between λ' and dilution levels primarily because of the monotonic increase of both λ and EGR rate. Furthermore, the impact of i-EGR on λ' is very similar for different external dilution levels as the amount of i-EGR is nearly constant over these tested conditions at 2500 RPM and 6 bar BMEP. As shown in Fig. 6.1, thermal efficiency increases with the increase of λ' for both lean and EGR dilution. At their highest levels of dilution, lean operation demonstrates about a 2.6% increase in BTE relative to stoichiometric operation, whereas only a 0.7% increase in BTE is observed with EGR dilution. Figure 6.1 also shows a lower COV_{IMEP} with lean operation relative to EGR dilution. The presence of excess oxygen with lean operation likely promotes combustion, resulting in a lower COV_{IMEP} until the lean limit.

Figure 6.2 shows NO_x emissions as a function of λ' for both forms of dilution. With air dilution, NO_x emissions peak at around $\lambda = 1.1$ and then start to decrease. At similar λ' for both dilution strategies, EGR operation demonstrates a significantly lower NO_x emissions compared to lean operation. These different NO_x trends are clearly tied to the dilution strategies. Air dilution always has excess oxygen in-

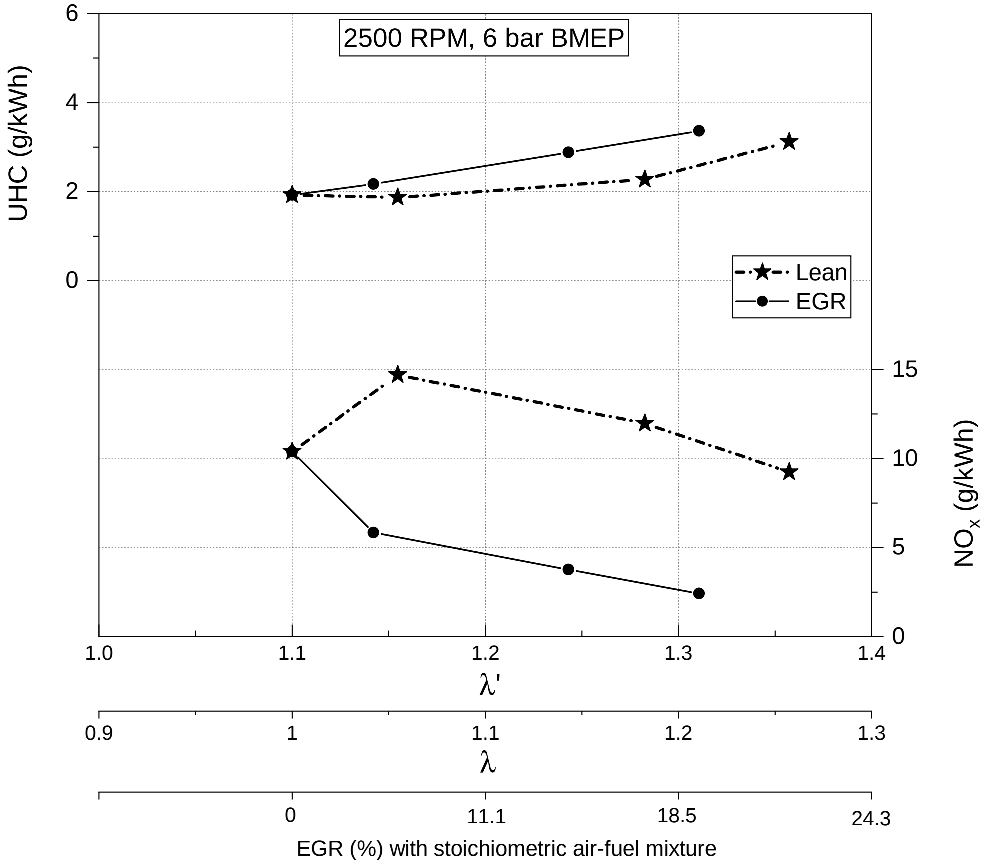

Figure 6.2: Engine-out UHC and NO_x emissions for CNG fuelled operation with EGR and air dilution at 2500 RPM and 6 bar BMEP.

cylinder, so the composition of the chamber is more favourable for NO_x formation than that of stoichiometric EGR dilution, where the overall oxygen concentration is reduced. Also, EGR dilution leads to lower in-cylinder temperatures, as shown later in this chapter, which is less favourable for NO_x production [84, 167, 168]. Figure 6.2 also shows that UHC emissions tend to increase with increased dilution, and lean-burn operation has lower UHC emissions than the EGR dilution. This trend is also consistent with the observed COV_{IMEP} for both dilution strategies (Fig. 6.1). The potential causes of this trend will be discussed later in this chapter.

Engine-out CO emissions are shown in Fig. 6.3 as a function of λ' for both lean and EGR dilute operation. Air dilution demonstrates significantly lower CO emissions than those from baseline operation as the presence of excess oxygen with higher λ promotes the oxidation of CO [37]. On the other hand, a small decrease in CO emissions is observed with increasing EGR dilution levels relative to baseline operation. The lower UHC and CO emissions suggest that the combustion efficiency

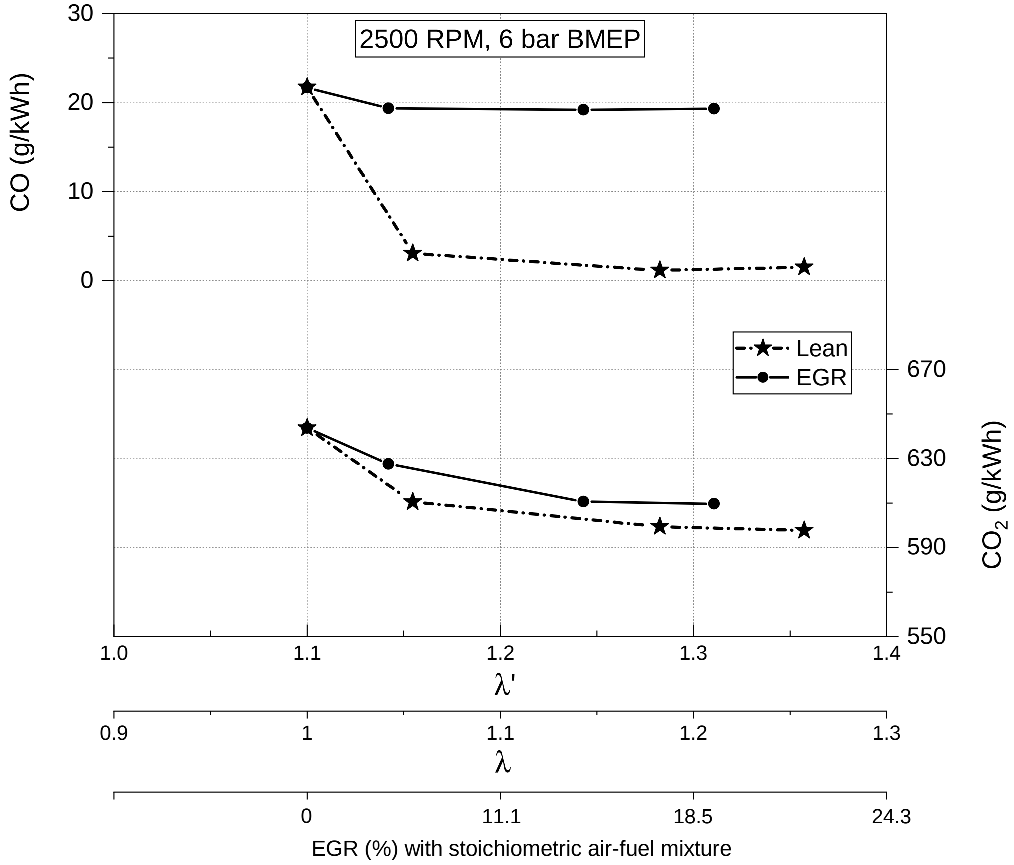

Figure 6.3: Engine-out CO and CO_2 emissions for CNG fuelled operation with EGR and air dilution at 2500 RPM and 6 bar BMEP.

of the engine is higher with lean-burn than with equivalent levels of EGR dilution. This also accounts for some of the BTE increase with the lean operation (Fig. 6.1). Fig. 6.3 also shows that CO_2 emissions decrease with the increase of λ' for both dilution strategies as the fuel efficiency increases with the increase of dilution level (Fig. 6.2).

6.1.2 Comparing DI CNG and GDI with air dilution

Figure 6.4 shows the COV_{IMEP} and brake thermal efficiency as a function of λ for both gasoline and CNG at 2500 RPM and 6 bar BMEP. The $COV_{IMEP} < 5\%$ is always observed for both fuels. However, engine operation with gasoline fuelling is limited to $\lambda = 1.3$ as higher combustion instability with $COV_{IMEP} > 5\%$ is observed with a further increase of λ. At this operating condition, DI CNG operation is limited to a peak of $\lambda = 1.4$ where the engine can maintain the tested load.

The peak BTE with gasoline fuelled operation is 32% with λ in the range of 1.2 to

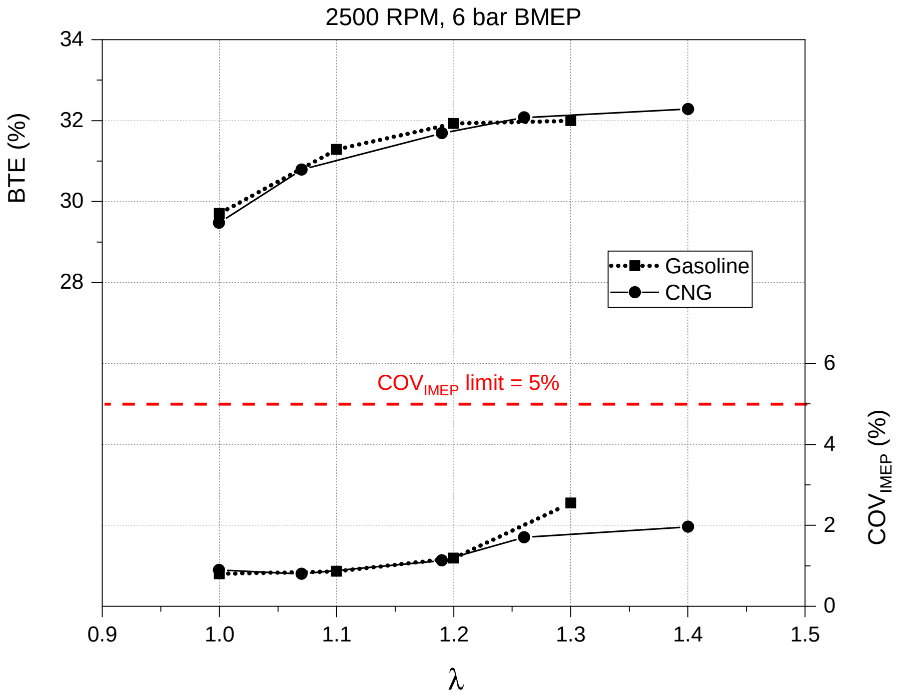

Figure 6.4: COV_{IMEP} and BTE for gasoline and CNG fuelled operation as a function of λ at 2500 RPM and 6 bar BMEP.

1.3. Further increase in λ results in lower BTE and higher COV_{IMEP}. CNG fuelled operation demonstrates a peak BTE slightly above 32% as the wider flammability limit of CNG is exploited to run as lean as $\lambda = 1.4$.

Figure 6.5 shows the NO_x emissions for gasoline and CNG fuelled operation under lean conditions. As expected, peak NO_x occurs at slightly lean conditions for both fuels, and overall lower NO_x is observed with CNG fuelling. Engine-out UHC emissions, as shown in Fig. 6.5, increase with the increased λ, and similar emissions are measured for both fuels over the λ range. Furthermore, lean operation with both fuels again demonstrates significantly lower CO emissions than those at stoichiometric baseline operation due to higher CO oxidation in the presence of excess O_2.

6.1.3 Comparing part load DI CNG with air dilution and stoichiometric EGR

Figure 6.6 shows the λ and manifold air pressure (MAP) required to achieve a range of part load conditions for three different engine speeds with lean-burn CNG fuelling. Engine operation is close to stoichiometric at WOT and with the MAP

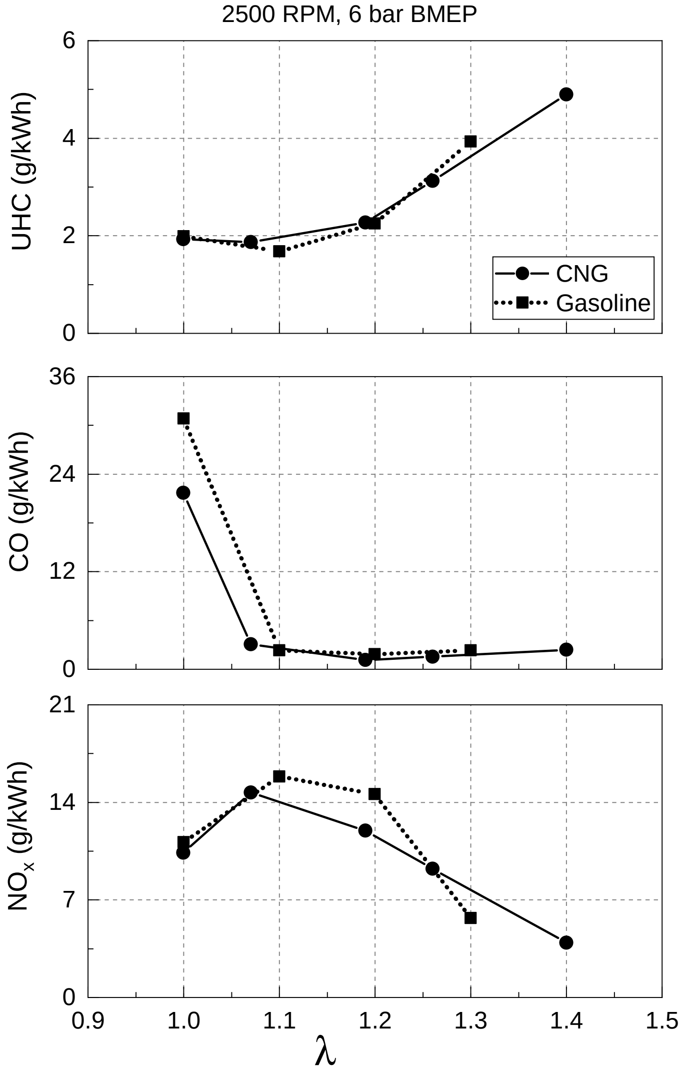

Figure 6.5: Emissions: UHC (top), CO (middle), and NO_x (bottom) for gasoline and CNG fuelled engine operation as a function of λ at 2500 RPM and 6 bar BMEP.

close to atmospheric pressure, and the load then decreases with the increase of λ. Also shown in Fig. 6.6, COV_{IMEP} increases with the increase of λ, and the maximum λ is limited to the range of 1.5 - 1.6 otherwise the COV_{IMEP} starts to exceed 5% limit. Therefore, some loads can only be achieved with intake throttling, resulting in a lower MAP.

Across the three engine speeds, the maximum air dilution tolerance is observed at 1500 RPM with $\lambda = 1.6$. This is discussed later in this chapter and can be attributed to a lower intensity of flame quenching at lower engine speed due to the reduced turbulence. Furthermore, the use of air dilution allows for a broader range of load control without throttling relative to EGR dilution (Fig. 5.4). This is due to the presence of excess oxygen with the lean operation, which likely helps to maintain

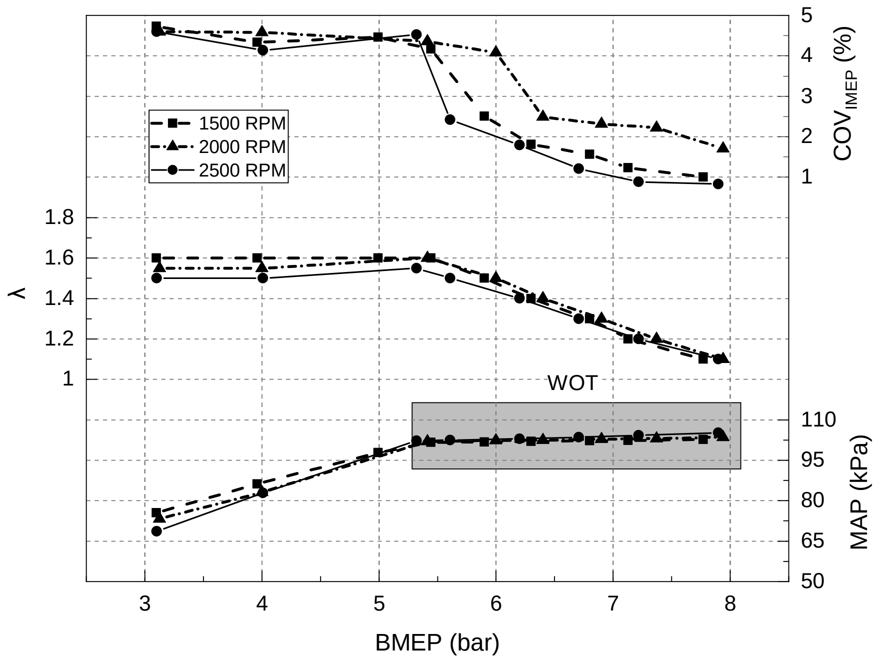

Figure 6.6: λ, MAP, and COV_{IMEP} for CNG fuelled operation with air dilution over the tested part load range.

mixture reactivity and therefore allows more air dilution at WOT before reaching the combustion stability limit.

Figure 6.7 shows the brake thermal efficiency with lean operation compared to the other two operating modes with CNG fuelling over the range of tested part load conditions. For lean operation, significant improvements in BTE are observed over EGR dilute operation at each part load condition across all three engine speeds.

Figure 6.8 shows the NO_x emissions of lean operation compared to the other two operating modes with CNG fuelling. At all three engine speeds, EGR operation demonstrates lower NO_x emissions than the baseline stoichiometric case at all the part load conditions. As expected (e.g. [37]), lean operation results in peak NO_x emissions at $\lambda = 1.1$. With a further increase of λ, NO_x emissions decrease, most likely due to the dominating effect of lower in-cylinder temperature [167]. It is also noted that lean operation starts to demonstrate NO_x emissions similar to those with EGR dilution at 6 bar BMEP operating points with $\lambda = 1.4 \sim 1.5$ for all three engine speeds. As engine load is decreased, the amount of dilution required to control the load is significantly higher when utilizing lean-burn as opposed to stoichiometric

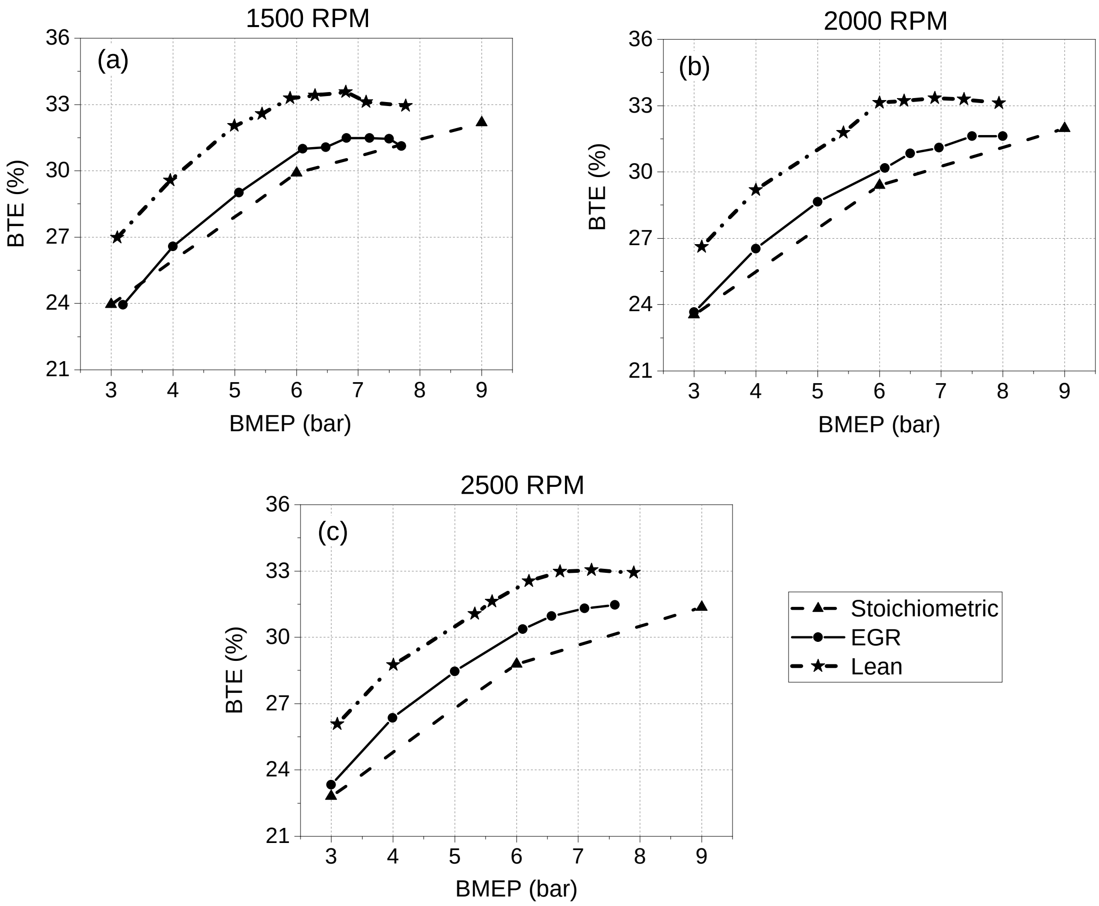

Figure 6.7: Part load BTE comparison at (a) 1500 RPM, (b) 2000 RPM, and (c) 2500 RPM for CNG fuelled operation with stoichiometric, lean, and EGR dilution.

operation with EGR, as shown in Fig. 6.9 with the calculated λ'. Note that the external dilution levels are not monotonically changing over the tested loads (for e.g., 17% EGR at 7 bar, 9% EGR at 5 bar, and 16% EGR at 3 bar BMEP) as the test procedure is different from what is done in Section 6.1.1, resulting in a non-linear relationship between λ' and dilution levels (i.e., λ and EGR rate) in Fig. 6.9 as opposed to the relationship observed in Fig. 6.1. This higher λ' should result in lower peak in-cylinder temperature with lean operation relative to EGR dilution at lower loads. It is likely because of this lower peak in-cylinder temperature due to higher diluent concentration that an air dilution strategy is able to achieve similar NO_x to that of EGR dilution despite the presence of extra O_2.

Figure 6.10 shows the variation of the measured exhaust gas temperature (EGT) with load for all three engine operating modes. Both baseline stoichiometric and EGR operation demonstrate similar EGTs at all three engine speeds. With air

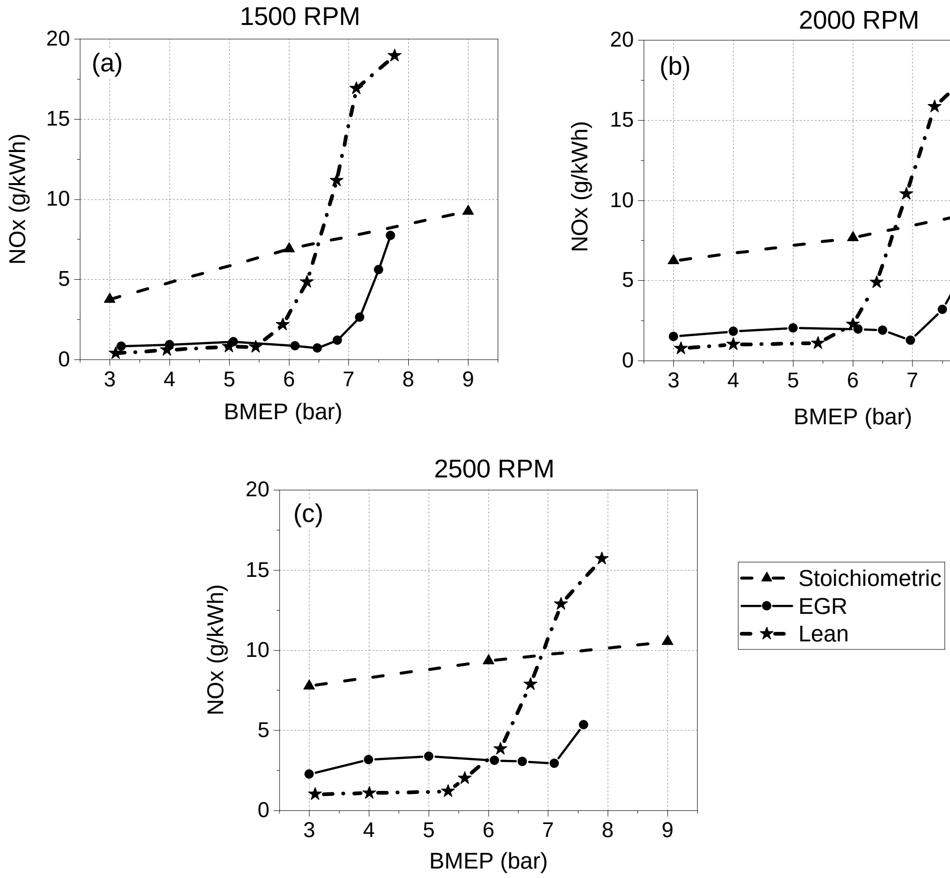

Figure 6.8: Part load NO_x comparison at (a) 1500 RPM, (b) 2000 RPM, and (c) 2500 RPM for CNG fuelled operation with stoichiometric, lean, and EGR dilution.

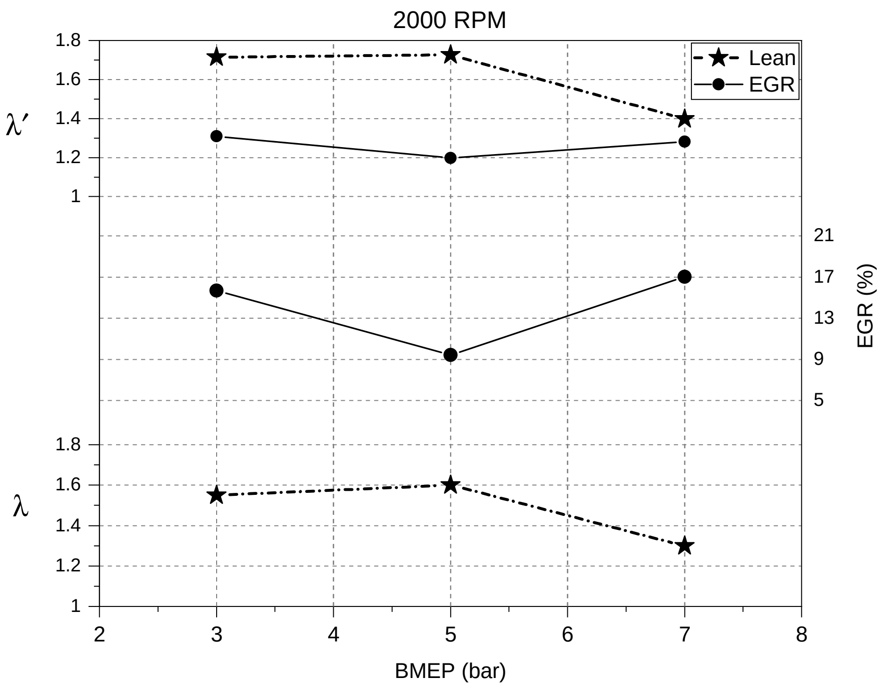

Figure 6.9: λ' with corresponding EGR rate and λ for CNG fuelled operation with EGR and air dilution over three different part load conditions at 2000 RPM

dilution, the EGTs are similar to other modes at higher loads but drop significantly at lower loads. This can be attributed to the lower in-cylinder temperatures with air dilution at a given low load compared to that of EGR dilution due to higher diluent concentration (Fig. 6.9) and is consistent with the NO_x results measured with lean operation at lower loads (Fig. 6.8).

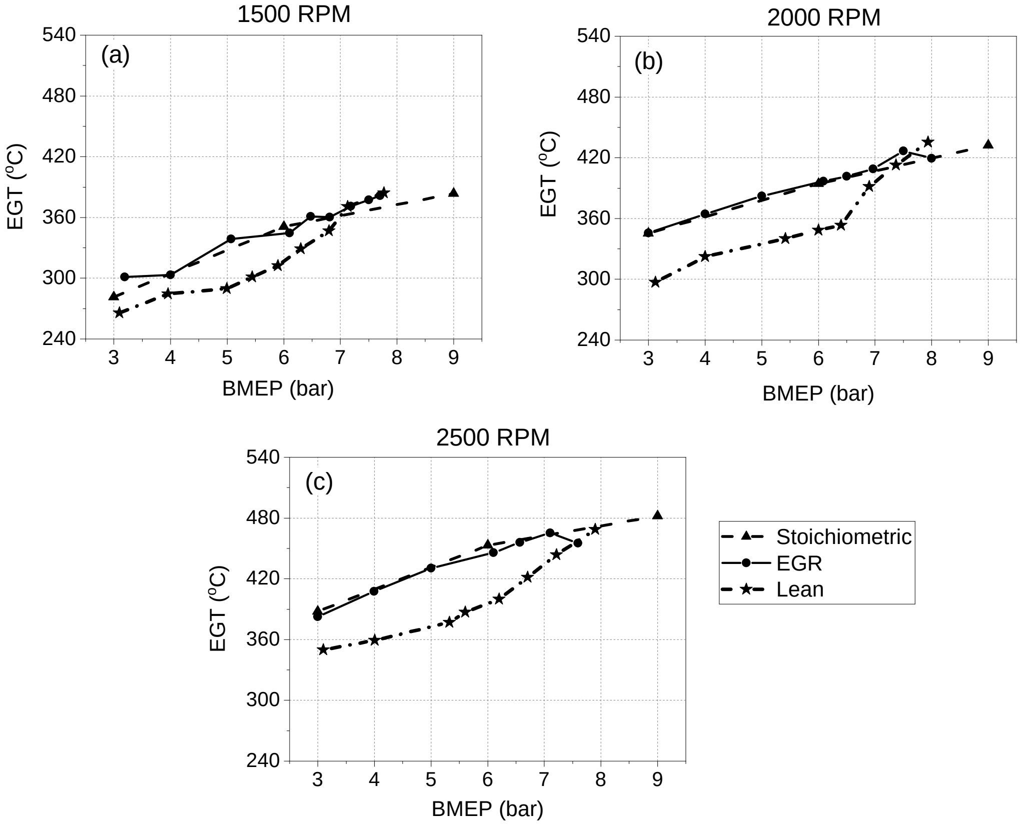

Figure 6.10: Part load EGT comparison at (a) 1500 RPM, (b) 2000 RPM, and (c) 2500 RPM for CNG fuelled operation with stoichiometric, lean, and EGR dilution.

Figure 6.11 shows the comparison of engine-out UHC emissions for the three different engine operating modes over the range of tested part load conditions. EGR operation has higher UHC emissions relative to baseline stoichiometric operation. For lean operation, lower UHC emissions are observed relative to EGR dilution above 6 bar BMEP, likely due to the oxygen-rich environment, and UHC emissions increase below 6 bar BMEP. Below 6 bar BMEP, lower in-cylinder temperatures due to higher dilution concentrations (i.e., larger λ') with lean operation likely increase the flame quenching and thus UHC emissions.

This behavior demonstrates a trade-off for lean-burn CNG engine operation. The use of air dilution to increase fuel efficiency must accommodate increasing UHC

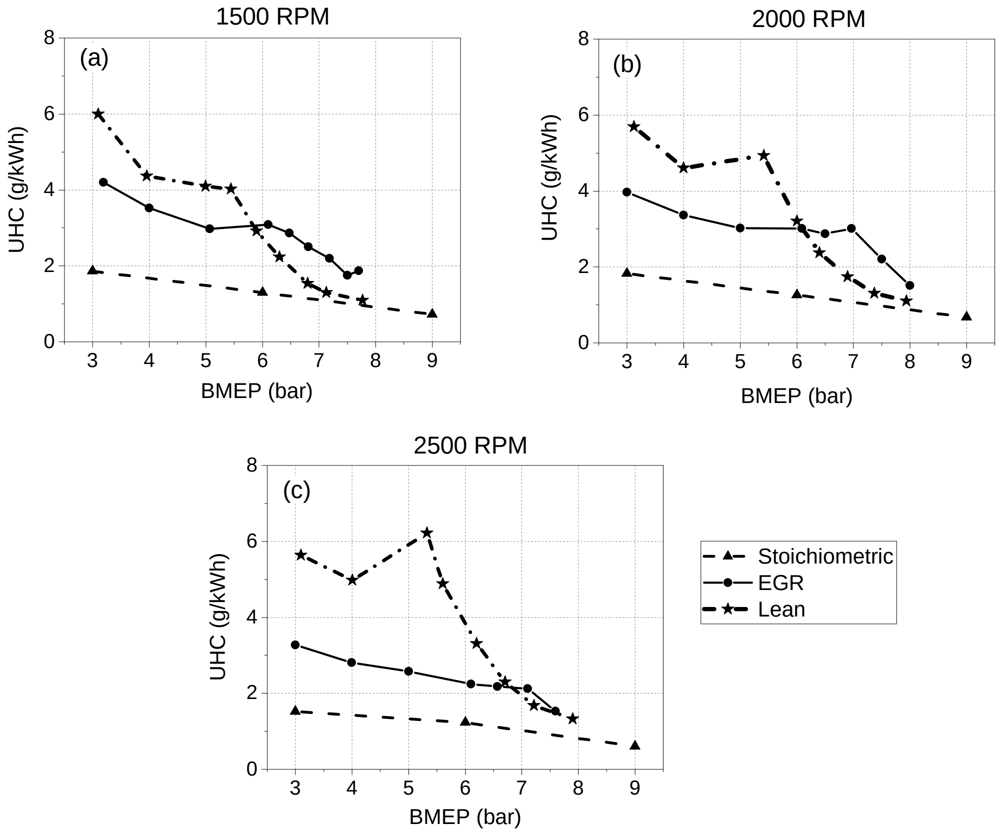

Figure 6.11: Part load UHC emissions comparison at (a) 1500 RPM, (b) 2000 RPM, and (c) 2500 RPM for CNG fuelled operation with stoichiometric, lean, and EGR dilution.

emissions and combustion instability when the lean limit is approached. An increase in methane emissions will negate the CO_2 reduction benefit from the use of higher engine efficiency, since methane is also a greenhouse gas. Such effects are considered later in this chapter.

6.2 Analysis of engine performance with air dilution

This section analyses the engine performance demonstrated earlier in this Chapter. A combination of measurement, theory, and the GT Power modelling discussed in Section 3.3.2 are used. This work intends to provide insights into the physical mechanisms by which dilution impacts engine performance.

6.2.1 In-cylinder pressure and combustion duration

Figure 6.12 (a) shows the P-V diagram of representative pressure traces for CNG fuelled operation with stoichiometric, lean, and EGR dilution at 2500 RPM and 6 bar BMEP. The intake pressure increases for both lean and EGR dilution relative to baseline stoichiometric condition as the engine is less throttled to allow the excess air for lean-burn operation and to compensate for the displaced air by exhaust gas for EGR dilution. Both dilution strategies employ similar throttle positions at this load, and therefore the pumping losses are similar (Fig. 6.12-b).

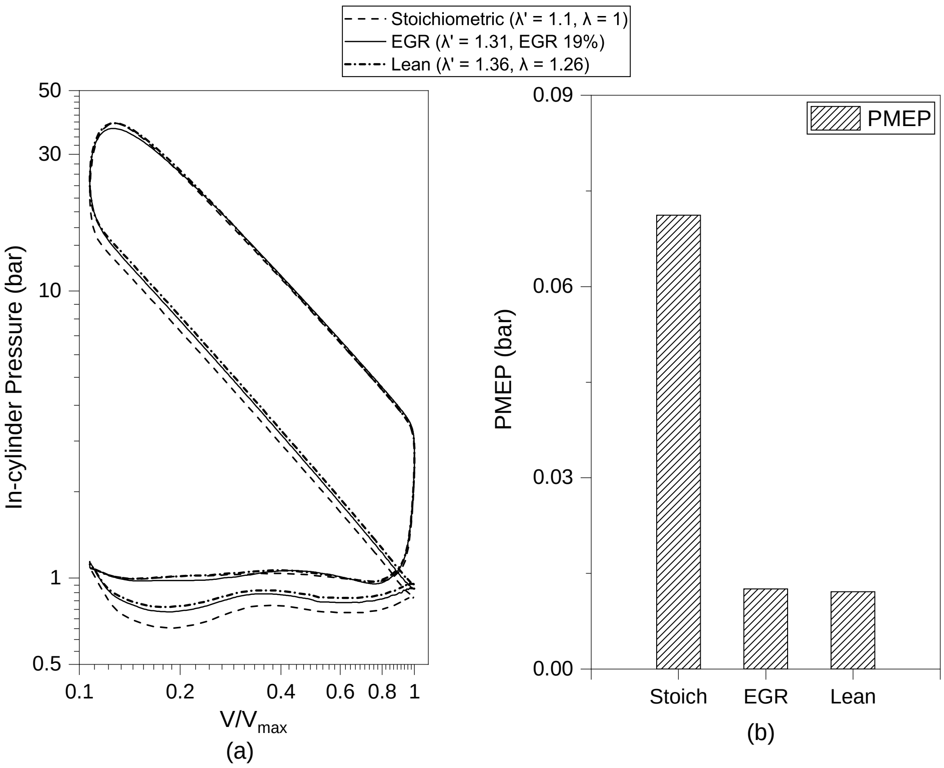

Figure 6.12: Comparison of (a) pressure-volume trace on a logarithmic scale and (b) pumping mean effective pressure (PMEP) for CNG fuelled operation with stoichiometric, lean, and EGR dilution at 2500 RPM, 6 bar BMEP.

Figure 6.13 shows the 0-10% and 10-90% MFB durations obtained using GT-Power as a function of λ' for both lean and EGR dilute operation. Ignition and subsequent flame kernel development at the initial combustion stage depend on the laminar flame speed [37]. With the lean operation, the presence of excess oxygen is more conducive to a higher laminar flame speed than that of stoichiometric CNG with EGR with a similar dilution level. This key difference between the two dilution strategies manifests itself in the 0-10% MFB burns. The 10-90% MFB duration

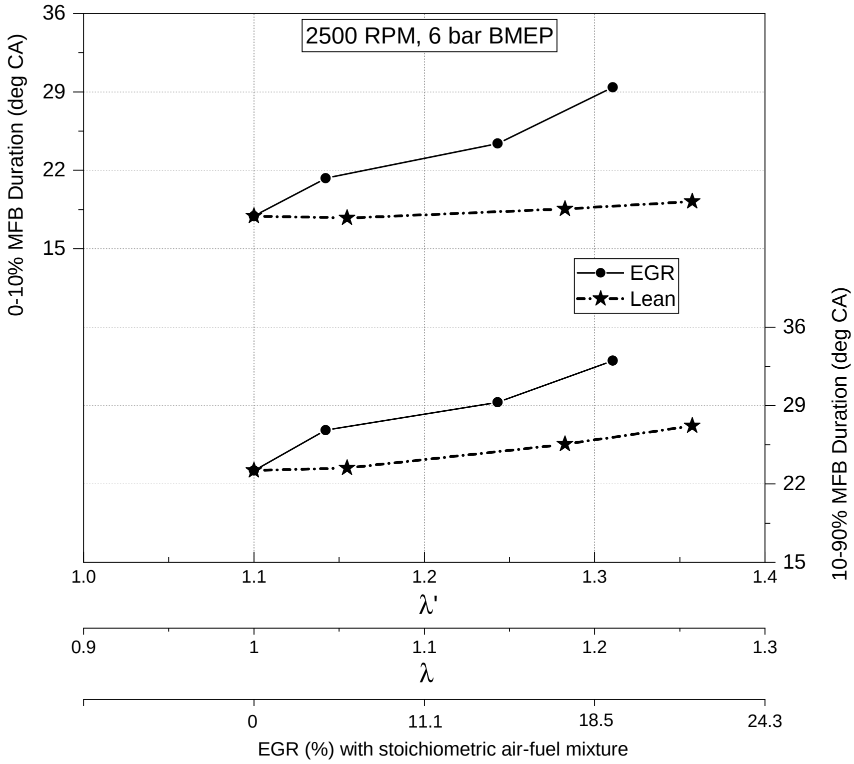

Figure 6.13: 0-10% and 10-90% MFB durations obtained using GT-Power for CNG fuelled operation with EGR and air dilution at 2500 RPM and 6 bar BMEP.

increases for both dilution strategies as λ' increases, which again arises from slower flame speeds due to reduction in mixture reactivity, and this effect is more significant with EGR dilution.

Longer burns are generally detrimental to fuel economy for several reasons, and this acts to negate some of the efficiency benefits gained by dilution and reduced pumping losses. A longer combustion duration also increases the cyclic variability as the variations in pressure arise from the combined effect of combustion variation and volume change [37]. The increased burn durations are consistent with the higher COV_{IMEP} results shown in Fig. 6.1 for dilute conditions.

6.2.2 Energy balance and loss analysis

Figures 6.14 shows a comparison of input fuel energy balance and heat loss distribution, respectively, at 2500 RPM and 6 bar BMEP for stoichiometric, EGR, and lean operation with CNG fuelling. The results for lean and EGR operation correspond to very similar λ' (i.e., $\lambda'_{EGR} = 1.31$ and $\lambda'_{Lean} = 1.36$). As shown in Fig. 6.14 (a), while lean operation reduces the unburned fuel energy, $\dot{H}_{UBF}$ in the

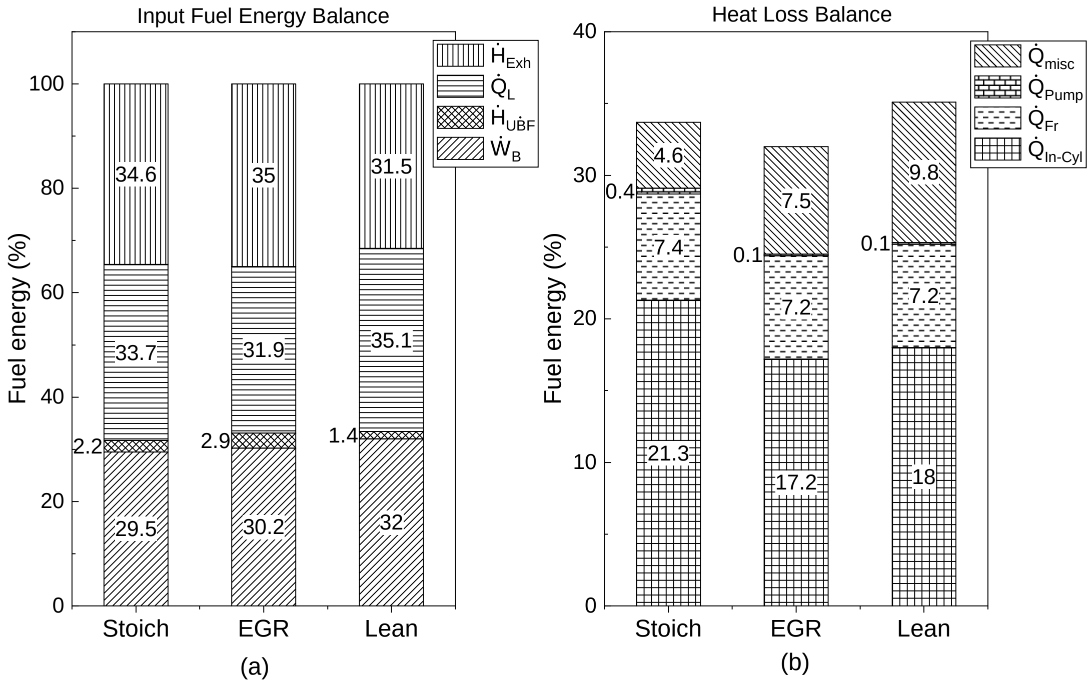

Figure 6.14: (a) Input fuel energy balance and (b) Heat loss analysis for CNG fuelled operation with stoichiometric, lean, and EGR dilution at 2500 RPM, 6 bar BMEP (obtained using the methodology described in Section 3.3.2 and 3.4.2).

exhaust, a larger $\dot{H}_{UBF}$ is observed with EGR dilute operation due to higher UHC and CO than air dilution at the same λ'. Furthermore, energy lost in the exhaust (i.e., $\dot{H}_{Exh} + \dot{Q}_{misc}$) is increased with EGR dilution due to its longer combustion duration. Note that the blowdown heat losses with lean operation are also expected to be higher than baseline stoichiometric operation due to a longer combustion duration, and a significant portion of these losses are expected to occur from surfaces outside the combustion chamber, particularly from the exhaust manifold. Figure 6.14 (b) shows that the in-cylinder wall heat losses, $\dot{Q}_{In-Cyl}$ are lower for both dilution strategies, particularly with EGR operation, relative to baseline stoichiometric condition due to lower in-cylinder temperatures as shown in Fig. 6.15. In addition, pumping losses, $\dot{Q}_{Pump}$ are also reduced from 0.4% to 0.1% with both dilution strategies due to less throttled engine operation.

These results suggest that optimizing fuel efficiency with dilution requires a balance between the positive impact of lower in-cylinder heat losses and less pumping work, and the negative impact of incomplete combustion and longer burn durations [91, 169]. Using the operating point at 2500 RPM and 6 bar BMEP as a representative example of part-load operation, it is evident that the use of dilution with CNG

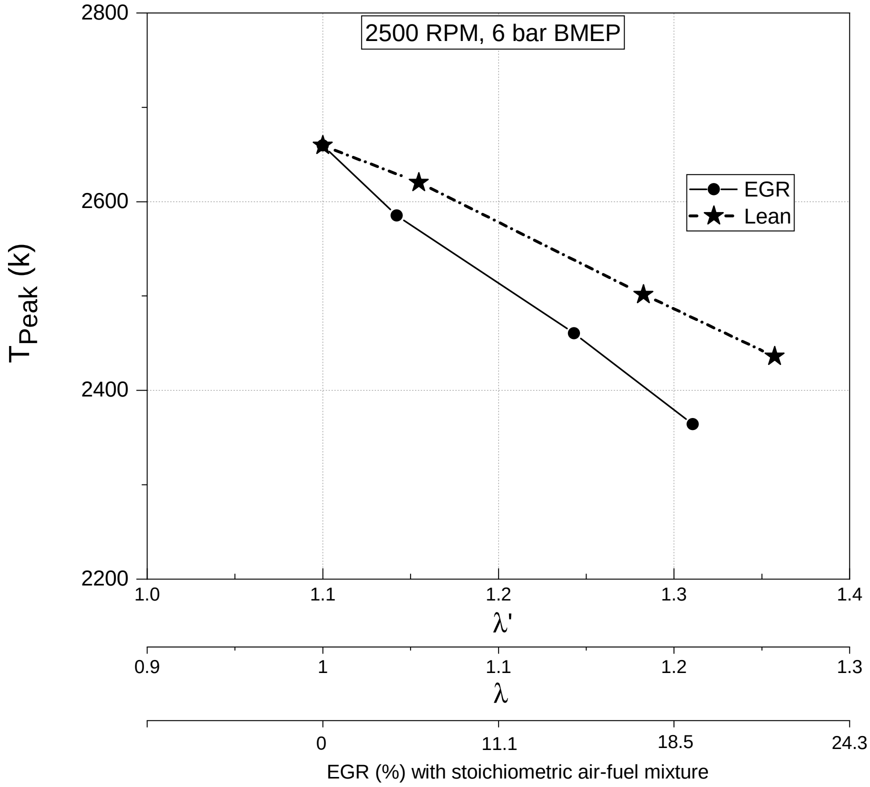

Figure 6.15: Comparison of simulated T$_{Peak}$ for CNG fuelled operation with EGR and air dilution at 2500 RPM and 6 bar BMEP.

improves fuel efficiency over stoichiometric operation due to lower in-cylinder heat losses and decreased pumping work.

6.3 Impact of dilution on combustion and UHC emissions

Lean operation with CNG fuelling can improve fuel economy with increasing λ. However, this benefit must be balanced against the concurrent increase in emissions, as these can negate the environmental benefit of lean-burn operation. Therefore, it is necessary to gain insight into the interplay between air dilution and UHC emissions to determine an optimal λ for CNG fuelled lean-burn engine operation.

As with EGR dilution, it is hypothesized that a reduction of in-cylinder temperature or mixture reactivity from increased air dilution leads to increased flame quenching and is, therefore, directly related to increased UHC formation. Premixed, turbulent combustion simulations of air dilute engine operation with

CNG fuelling are therefore performed using the GT-Power predictive combustion methodology, as described in Section 3.3.3. The results of the simulation are then compared with those using EGR dilution. Finally, the results are further generalized by including simulations of gasoline engine operation both with and without external dilution.

6.3.1 Flame speed variation with dilution strategy

Figure 6.16 shows a comparison of the laminar flame speed (S_L) and turbulent burning velocity (S_T) with CNG fuelled operation for stoichiometric, EGR, and lean dilution at 2500 RPM and 6 bar BMEP, where the diluted cases have similar λ'. As shown, baseline stoichiometric operation without any external diluent demonstrates a higher S_L than the dilute cases. At a similar λ', lean operation exhibits a higher S_L relative to EGR dilution as excess oxygen increases the heating value per unit mass of the mixture, resulting in increased flame temperatures and consequently higher flame speed [37, 92]. Furthermore, lean operation demonstrates a higher S_T compared to EGR dilution as S_L is higher for lean burns. These flame speed trends are consistent with the combustion duration results shown in Fig. 6.13.

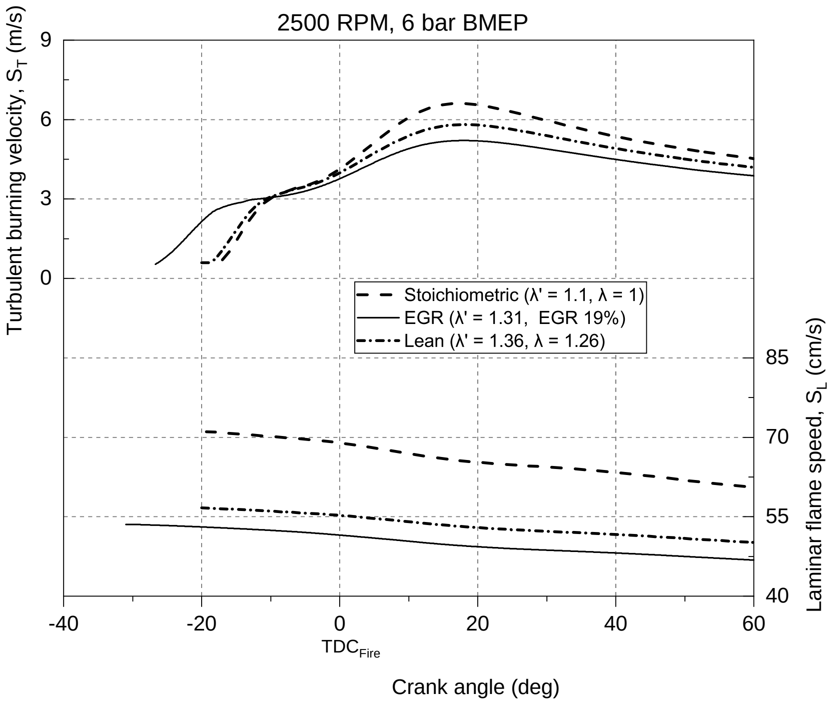

Figure 6.16: Comparison of laminar flame speed, S_L (cm/s) and turbulent burning velocity, S_T (m/s) for CNG fuelled engine operation with stoichiometric, lean, and EGR dilution at 2500 RPM, 6 bar BMEP.

6.3.2 Correlating flame quenching with UHC emissions

The effect of turbulence on flame quenching is now examined in Fig. 6.17. As in Chapter 5, the ratio of the turbulent burning velocity to the laminar flame speed ($\frac{S_T}{S_L}$) is plotted against the ratio of the effective turbulence intensity to the laminar flame speed ($\frac{u'_k}{S_L}$) in the 'Bradley' diagram. The locus of stoichiometric, EGR and lean burns at 2500 RPM and 6 bar BMEP are shown, along with four specific points in each burn defined by a given MFB. The loci of combustion with dilution are moved to higher values of KLe, and towards the quenching region relative to stoichiometric CNG combustion without dilution [159]. For lean operation, the loci of combustion are located at lower values of KLe compared to those with EGR dilution due to the higher S_L at a similar λ'. This suggests, at a given λ', that less flame quenching occurs with lean operation as opposed to stoichiometric fuel and air with EGR. This phenomenon explains the earlier trends in the COV_{IMEP} in Fig.

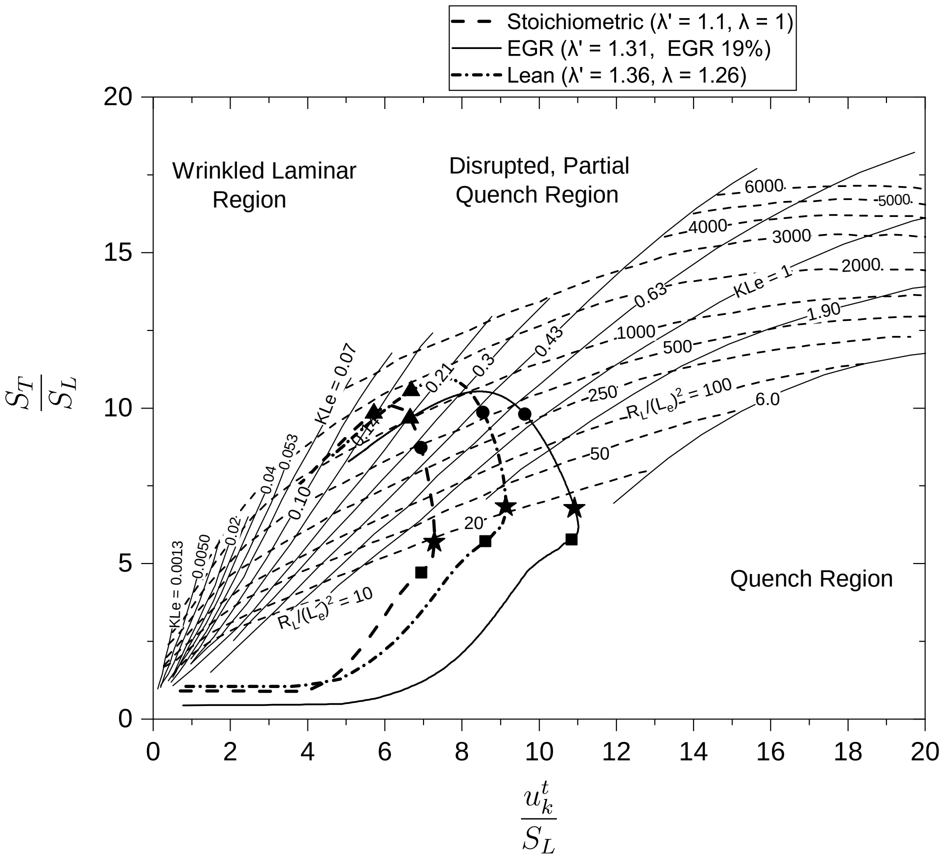

Figure 6.17: Loci of combustion events in the Bradley diagram for CNG fuelled operation with stoichiometric, lean, and EGR dilution at 2500 RPM, 6 bar BMEP [38, 60–62]. Highlighted symbols represent combustion event at the location of 1% MFB (■), 10% MFB (★), 50% MFB (●), and 90% MFB (▲).

6.1 and UHC emissions in Fig. 6.2, as lean-burn operation, which experiences less bulk flame quenching than that of EGR operation, has a lower COV_{IMEP} and less UHC emissions over the range of tested λ'.

The mechanism for UHC formation in SI engines occurs when the flame is quenched before reaching the last pocket of the unburned fuel. This is typically limited to quenching at the crevice volume [37, 42]. Therefore, bulk quenching of the flame should be correlated with UHC emissions because this represents a case where the flame is quenched earlier, resulting in more UHC emissions. This is illustrated in Fig. 6.18, which shows the measured UHC and COV_{IMEP} plotted against KLe at the points of 1% MFB on the Bradley diagram in Fig. 6.17. The 1% MFB locus is used because the effect of flame quenching is more significant at the early stage of flame development than it is at the later stages when the flame is more established [42, 47, 170]. Fig. 6.18 suggests a relationship between KLe and the measured UHC emissions.

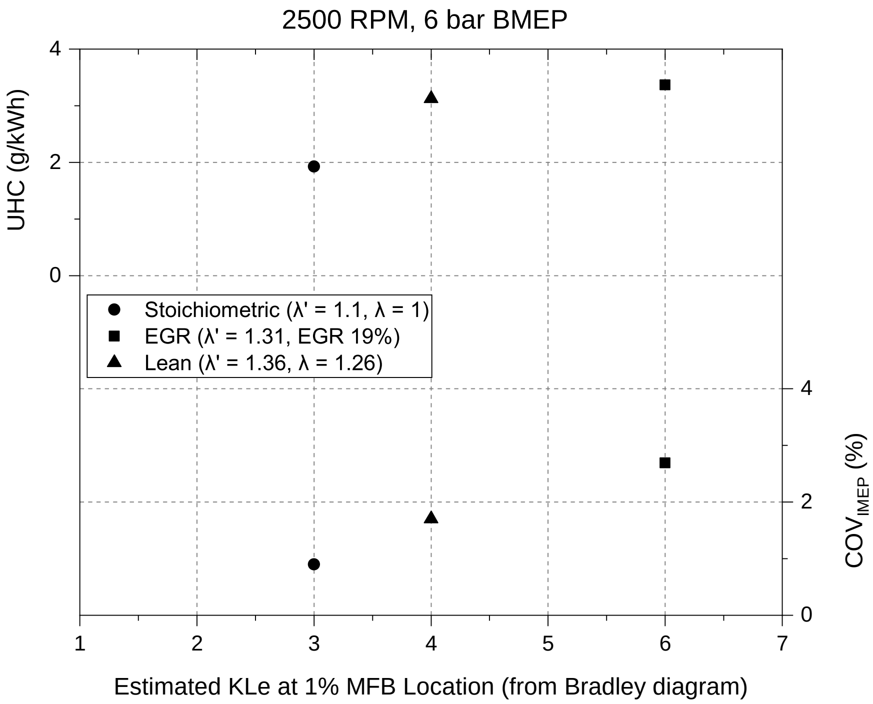

Figure 6.18: UHC emissions and COV_{IMEP} as a function of KLe at 1% MFB for CNG fuelling with stoichiometric, lean, and EGR dilution at 2500 RPM and 6 bar BMEP.

This correlation is expanded upon Fig. 6.19 and Fig. 6.20 using measured UHC emissions from all tested load conditions at two engine speeds of 2000 and 2500

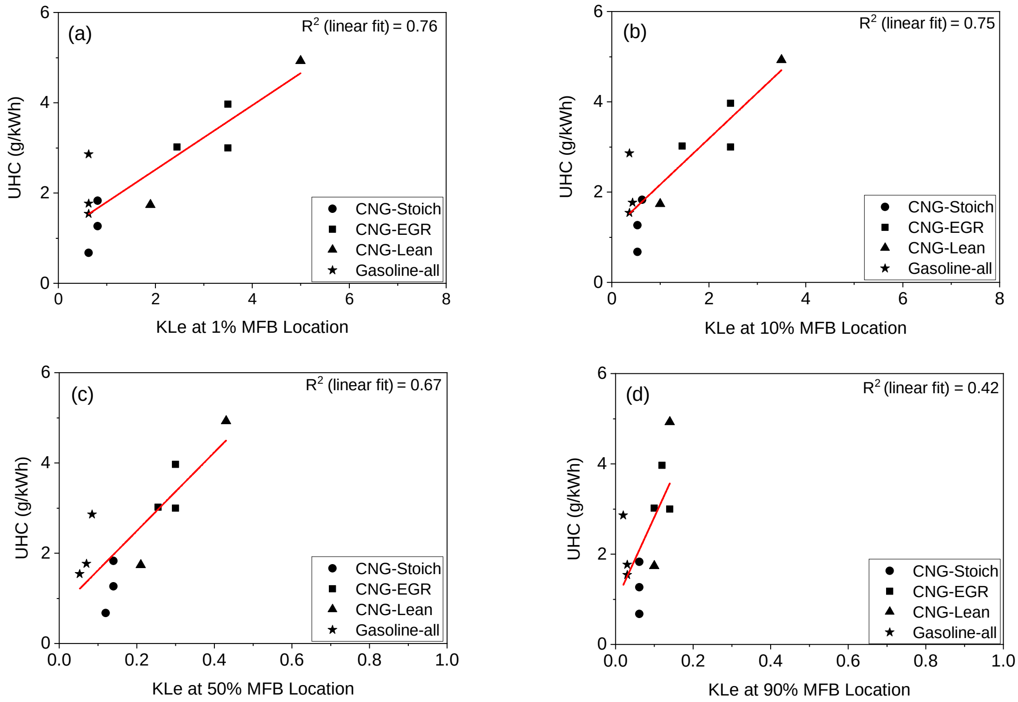

Figure 6.19: Relation between measured UHC and KLe at various MFB locations for stoichiometric, lean, and EGR dilute operation with both CNG and gasoline fuelling at 2000 RPM.

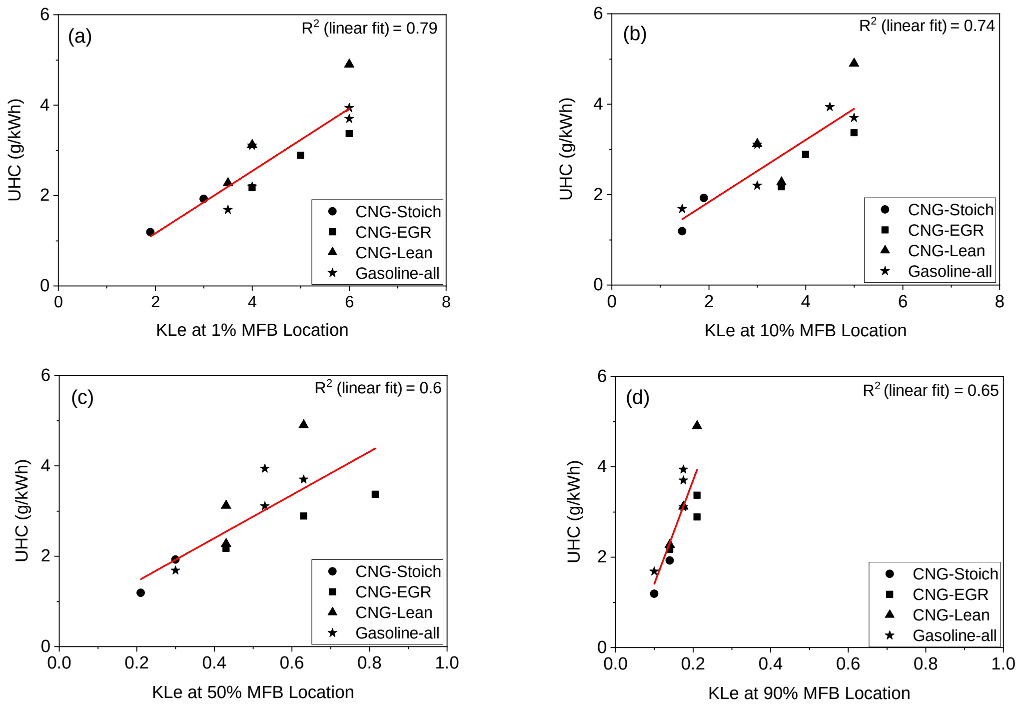

Figure 6.20: Relation between measured UHC and KLe at various MFB locations for stoichiometric, lean, and EGR dilute operation with both CNG and gasoline fuelling at 2500 RPM.

RPM, respectively. The estimated KLe at various MFB locations, again obtained from the Bradley diagram, for stoichiometric, lean, and EGR dilute operation with CNG and gasoline fuelling are also shown. As seen in the figures, the strongest correlation (i.e., largest R^2) occurs when using the KLe at the 1% MFB point, which is consistent with the view that the most significant impact of turbulent flame quenching occurs during the establishment of the flame.

6.4 Greenhouse gas emissions with air dilution

It has been demonstrated that DI CNG has the potential to mitigate CO_2 emissions relative to gasoline fuelled operation, and the use of dilution allows for further reduction in GHG emissions. However, the efficiency and CO_2 reduction benefits of each dilution strategy must be balanced against methane and NO_x emissions from CNG combustion, since these emissions also have a global warming potential, as discussed in Section 3.5. Therefore, Fig. 6.21 compares CO_2 emissions from CNG fuelled operation with stoichiometric, lean, and EGR dilution at part load. Lean operation demonstrates a significant reduction in CO_2 emissions relative to EGR dilution over these part load conditions. This occurs because of the higher BTE with lean operation than the other two operating modes (Fig. 6.7).

Considering the GWP of CH_4 along with CO_2, the engine-out CO_{2e} emissions of lean-burn CNG fuelled operation shown in Fig. 6.22 are very similar to the baseline stoichiometric operation at part load and all three engine speeds. Fig. 6.23 then shows CO_{2e} emissions considering the GWP of both CH_4 and NO_x (i.e., NO and NO_2) along with CO_2. Engine-out CO_{2e} emissions with air dilution are now lower below 6 bar BMEP but increase at higher loads.

Together, these results demonstrate that the choice of combustion strategy and the accompanying after-treatment system will have a significant impact on CO_{2e} emissions of CNG DI engines. In particular, should an oxidation catalyst and selective catalytic reduction (SCR) work well with the air dilution strategy and associated lower exhaust temperatures, this approach offers significant CO_{2e}

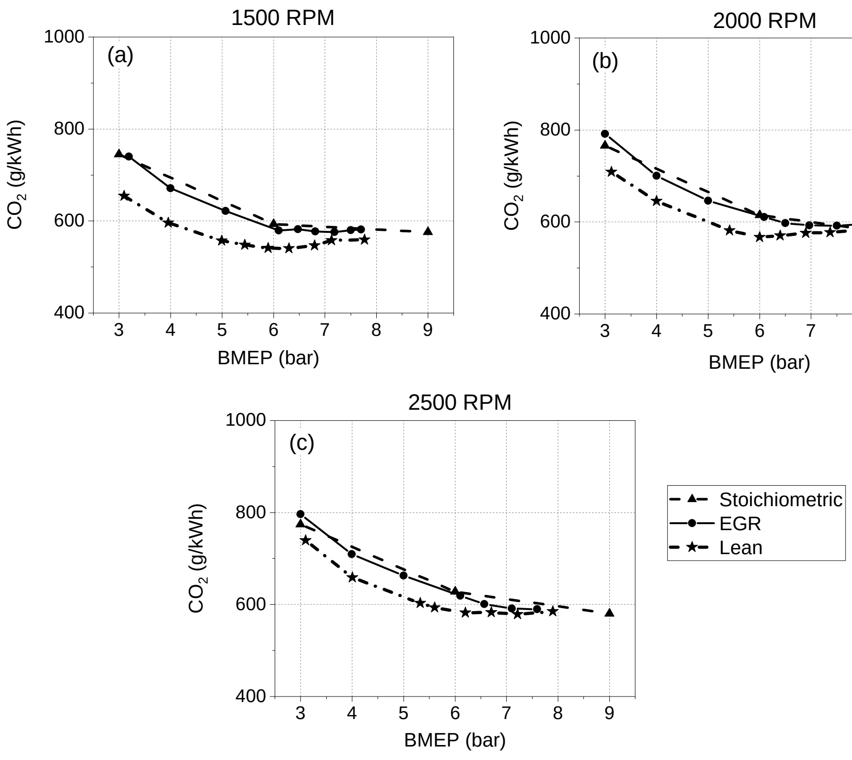

Figure 6.21: Part load CO_2 comparison at (a) 1500 RPM, (b) 2000 RPM, and (c) 2500 RPM for CNG fuelled operation with stoichiometric, lean, and EGR dilution.

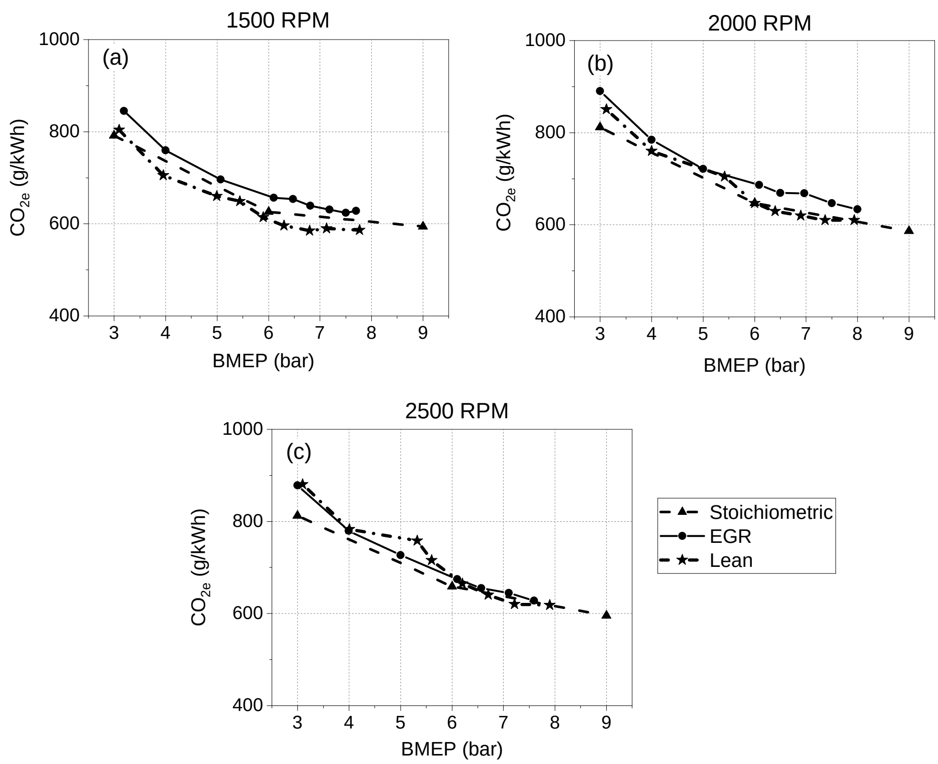

Figure 6.22: Part load CO_{2e} comparison considering GWP of CO_2 and CH_4 at (a) 1500 RPM, (b) 2000 RPM, and (c) 2500 RPM for CNG fuelled operation with stoichiometric, lean, and EGR dilution.

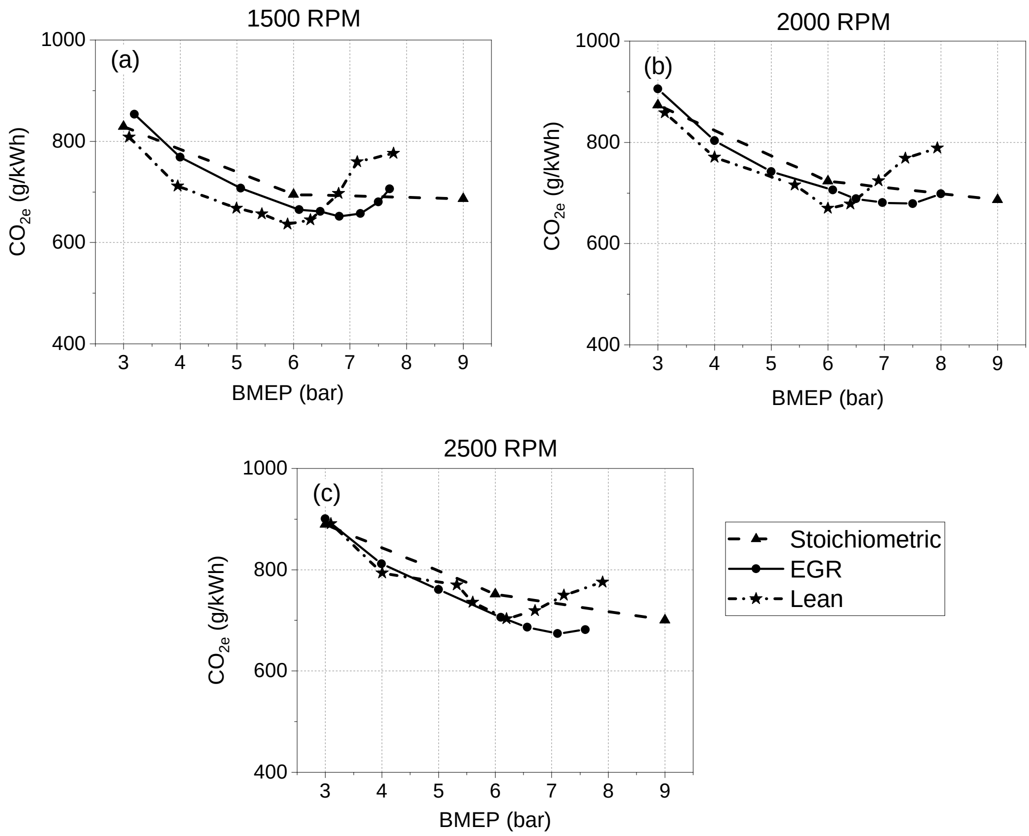

Figure 6.23: Part load CO_{2e} comparison considering GWP of CO_2, CH_4 and NO_x at (a) 1500 RPM, (b) 2000 RPM, and (c) 2500 RPM for CNG fuelled operation with stoichiometric, lean, and EGR dilution.

benefits over the other two. However, should this not be the case, use of a three-way catalyst with stoichiometric combustion or EGR may be superior. Such considerations are outside the scope of this work but need careful consideration in order to determine which combustion strategy is superior.

6.5 Summary

In this chapter, experimental results were presented for both CNG and gasoline fuelled operation with air dilution. The impact of excess air dilution on engine performance was first examined and compared with dilute operation with EGR at similar speed and load. For equivalent levels of dilution, lean operation demonstrated higher BTE than dilution with EGR. The presence of excess oxygen with air dilution also facilitated the reduction of both CO and UHC emissions, but promoted higher NO_x than an equivalent operation with EGR dilution.

The performance of CNG fuelled engine operation with air dilution was then examined at part load, and the fuel efficiency and emission outputs were compared with the baseline stoichiometric and EGR dilute operation. A significant BTE improvement was observed with lean operation relative to EGR dilution over the tested engine speeds and loads. For lean operation, lower UHC and higher NO_x were also observed relative to EGR dilution above 6 bar BMEP, and these trends were reversed below 6 bar BMEP. This switching in emission trends was a consequence of the load sweep strategy in this study. Because the charge dilution was used to control load through the sweep to minimize throttling, different quantities of charge dilution were required for a given load when using air dilution or EGR.

Premixed, turbulent combustion simulations were then performed for tested cases with air dilution, and results were compared with results from stoichiometric and EGR dilution. At similar dilution levels, the lean operation had a higher flame speed than that with stoichiometric EGR operation due to improved mixture heating value in the presence of excess oxygen. The Bradley diagram was then again utilised to determine if a correlation existed between measured UHC emissions and the severity of turbulent flame quenching. It was shown that UHC emissions and the KLe at the 1% MFB point were again correlated for all fuels and charge dilution strategies, further supporting the hypothesis that charge dilution promoted bulk flame quenching and thus an increase of UHC emissions. This appeared to be true of both gasoline or CNG fuelling, and with both air and EGR charge dilution.

Finally, CNG fuelled operation with air dilution demonstrated a significant reduction in CO_2 emissions compared to stoichiometric and EGR dilute operation. However, lean-burn CO_{2e} emissions, which account for the global warming potential of methane and NO_x, were not as favourable. This is because lean operation was shown to suffer from high NO_x emissions near stoichiometry and significant UHC emissions as the lean limit was approached at low loads. Careful consideration of the after-treatment system is therefore required before the best combustion strategy can be determined.

Chapter 7

Advanced Engine Operating Strategies with DI CNG

Chapter 6 showed that DI CNG with air dilution demonstrated a significant fuel economy improvement relative to other operating modes at part load. Despite this, increased NO_x and UHC emissions in certain parts of the load range increased the total CO_2 equivalent emissions significantly above the engine-out CO_2 emissions. For example, at higher loads approaching stoichiometric, the increase in NO_x emissions caused the engine-out CO_{2e} to be higher than stoichiometric operation. Chapter 5 also showed that UHC emissions were an issue when using EGR at low loads. Therefore, this chapter investigates the impact of internal residual gases, multiple fuel injections per cycle and the combined use of air and recirculated exhaust gas dilution to explore further the relationship between BTE and engine-out emissions.

7.1 Impact of internal residuals on DI CNG combustion

One approach to address high engine-out UHC emissions is to elevate the in-cylinder temperature and thereby encourage fuel oxidation via several mechanisms. The utilization of hot internal residual (i-EGR) is one means of achieving this [171]. The proportion of i-EGR is defined as the ratio of the mass remaining in-cylinder from the previous cycle to the total 'trapped mass' at the intake valve closure (IVC). It depends on several factors, such as the valve timing, the engine speed, and the pressure differential during gas exchange [37].

In this chapter, the amount of i-EGR is controlled by varying the valve overlap using the variable camshaft actuation system. The influence of i-EGR on combustion is examined for two different valve phasing strategies:

(a) intake valve advance for a fixed exhaust valve timing;

(b) exhaust valve retard at the intake valve timing that demonstrates the best performance.

The absolute valve timing of the intake valve advance and exhaust valve retard tests are presented in Table 7.1 and Fig.7.1.

Table 7.1: Valve timings for the intake valve advance and exhaust valve retard tests

Test mode	IVO (aTDC$_{Fire}$)	EVC (aTDC$_{Fire}$)	Overlap (deg)
1. 20 deg intake valve advance	335	384	49
2. 30 deg intake valve advance	325	384	59
3. 40 deg intake valve advance	315	384	69
4. 10 deg exhaust valve retard	335	394	59
5. 20 deg exhaust valve retard	335	404	69
6. 30 deg exhaust valve retard	335	414	79

7.1.1 Effect of intake valve advance

Figure 7.2 shows the calculated amount of i-EGR and the gas temperature at BDC (T$_{BDC}$) as a function of intake valve advance at 2000 RPM, 3 and 5 bar BMEP, and $\lambda = 1.4$. These quantities are determined using GT-Power simulations of the calibrated, full engine model, as described in Section 3.3.2. As expected, the amount of i-EGR increases for both loads with intake valve advance. At part load with

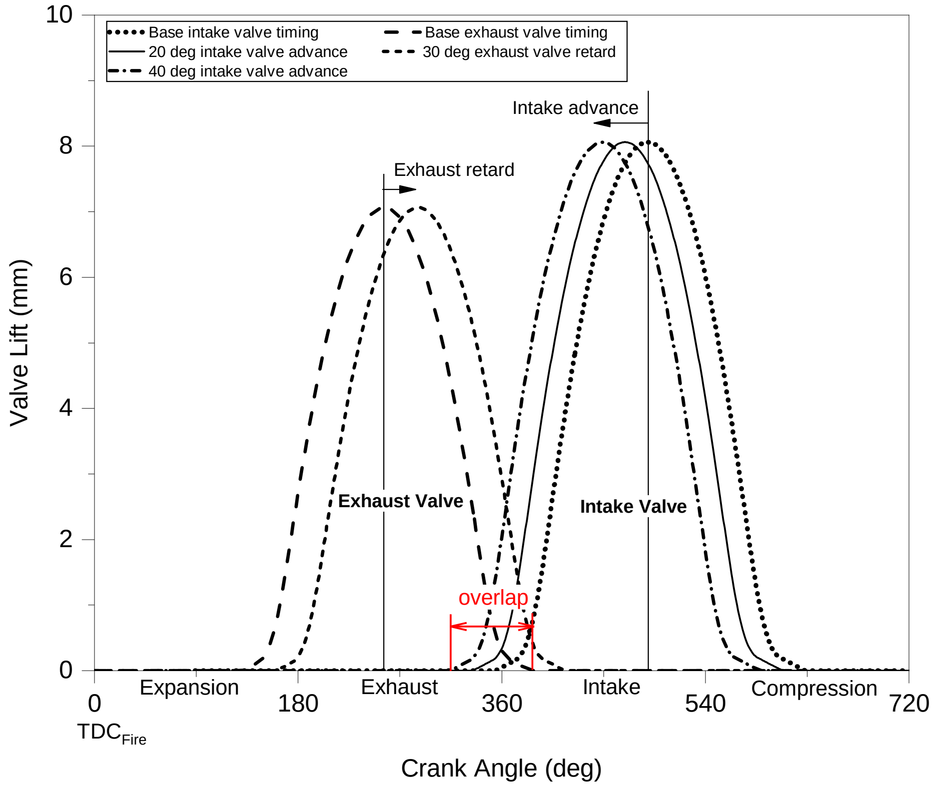

Figure 7.1: Valve lift profiles using intake valve advance and exhaust valve retard relative to base valve timing.

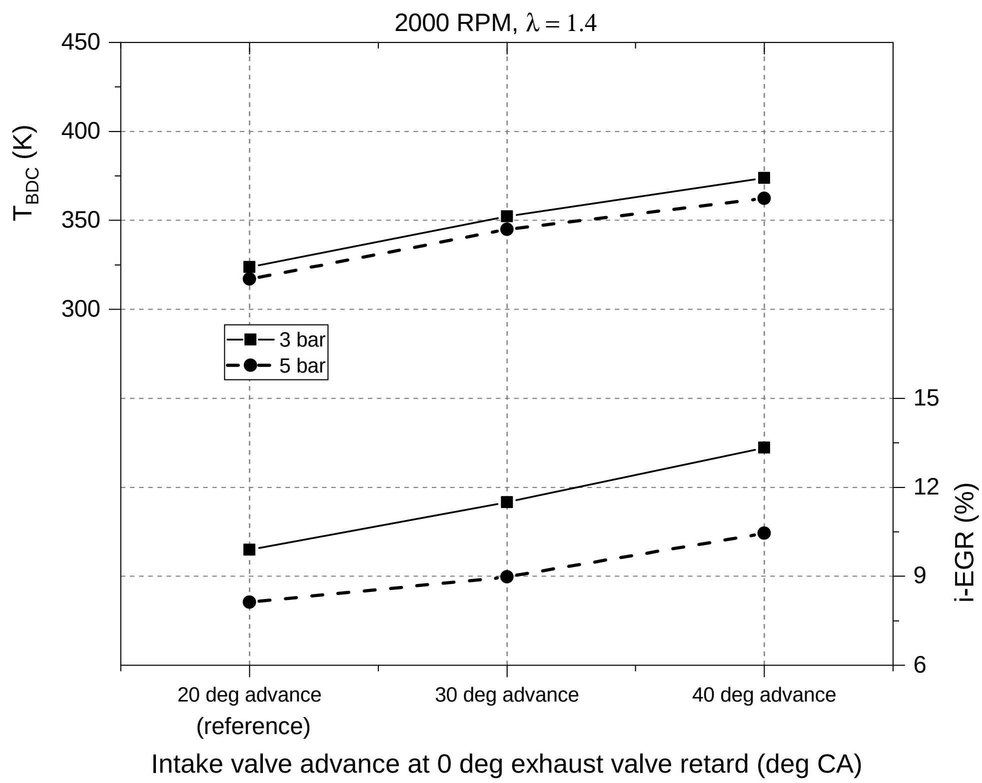

Figure 7.2: Effect of intake valve advance on simulated i-EGR rate and T_{BDC} at 2000 RPM, 3 and 5 bar BMEP, $\lambda = 1.4$ and valve timing as per Table 7.1.

intake valve advance and no boost, more exhaust gas flows back into the intake manifold through the intake valve and fills the cylinder in the subsequent intake stroke, resulting in higher internal residual gases [172]. The increased i-EGR with intake valve advance is also consistent with the increased T_{BDC} results for both loads.

Figure 7.3 shows the measured UHC emissions and BTE as a function of i-EGR via the intake valve advance. As shown, UHC emissions increase with intake valve advance despite the higher in-cylinder T_{BDC}. This is likely due to the adverse impact of additional inert species on the flame speed and post combustion temperature, resulting in higher UHC emissions [173]. Furthermore, there is no significant change in BTE with this variation of i-EGR.

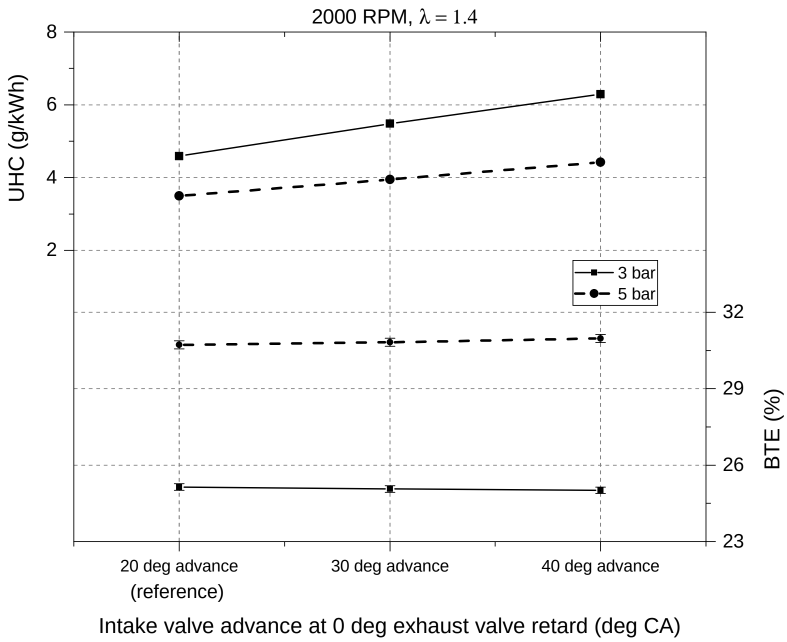

Figure 7.3: Effect of intake valve advance on measured UHC and BTE at 2000 RPM, 3 and 5 bar BMEP, $\lambda = 1.4$ and valve timing as per Table 7.1

The energy balance approach, as described in Section 3.4.2, is used to further analyse these trends. Figures 7.4 (a) and (b) compare the input fuel energy balance and heat loss distribution, respectively, for the extreme intake valve advances shown in Table 7.1 at 2000 RPM and 3 bar BMEP. With 40 deg intake valve advance, the benefits of reduced pumping losses, $\dot{Q}_{Pump}$ and lower heat transfer rates, $\dot{Q}_{In-Cyl}$ with increased internal dilution are offset by higher combustion inefficiency (i.e., higher $\dot{H}_{UBF}$) and higher energy lost in the exhaust (i.e., $\dot{H}_{Exh} + \dot{Q}_{misc}$) due to longer burn durations (Fig.7.5). The overall result is a BTE similar to the reference intake valve advance of 20 deg, as shown in Fig. 7.3.

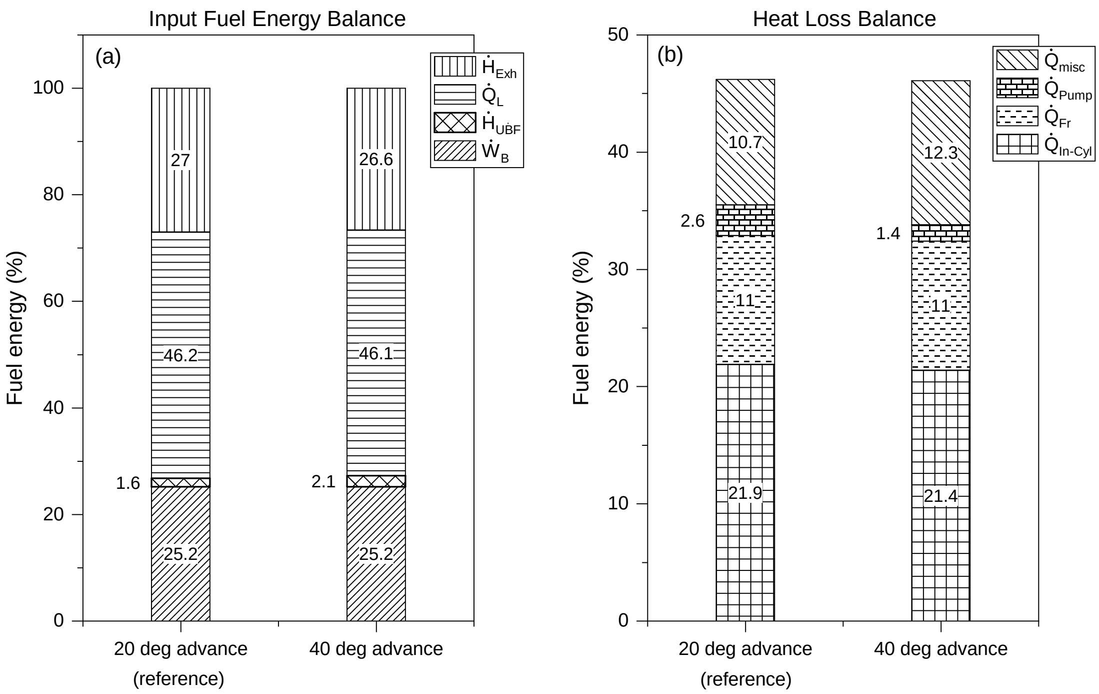

Figure 7.4: Comparison of (a) input fuel energy balance and (b) heat loss distribution at 2000 RPM and 3 bar BMEP for CNG fuelled operation with valve timing as per Table 7.1.

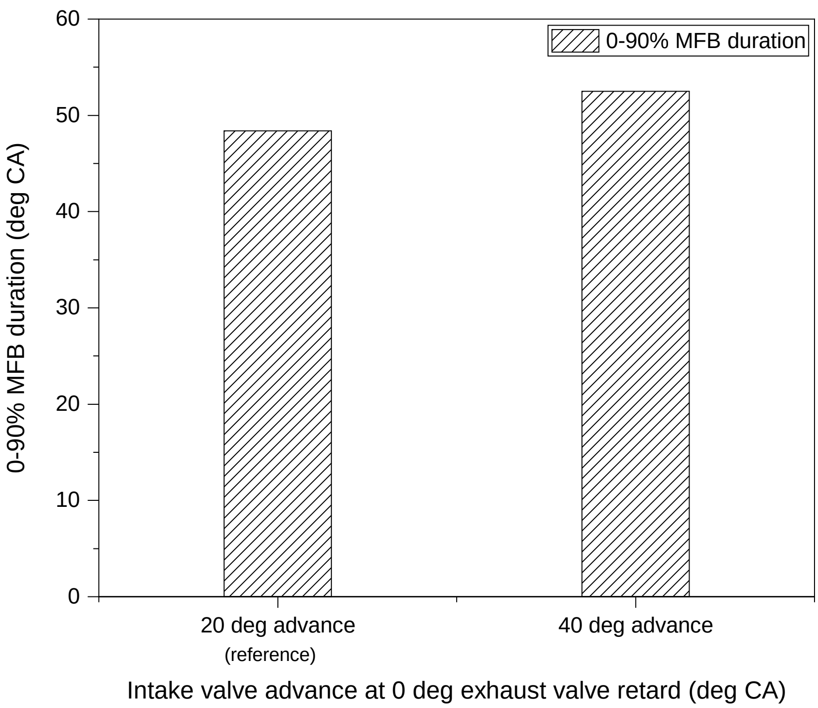

Figure 7.5: Effect of intake valve advance on 0-90% MFB duration at 2000 RPM, 3 bar BMEP with valve timing as per Table 7.1.

7.1.2 Effect of exhaust valve retard

The effect of exhaust valve retard on UHC emissions is now examined with a fixed 20 deg intake valve advance as this timing demonstrated the minimum UHC emissions among the tested intake valve timings. The details of these tests are presented in Table 7.1. Figure 7.6 shows the UHC emissions and BTE as a function of exhaust valve retard for fixed 20 deg intake valve advance phasing. Over this range of exhaust valve retard, both UHC and BTE again demonstrate insignificant variation, though a slight increase in UHC emissions is observed at the most retarded exhaust position.

Overall, both intake valve advance and exhaust valve retard suggest that the higher internal residuals are not effective in reducing UHC emissions and increasing BTE at these particular engine operating conditions.

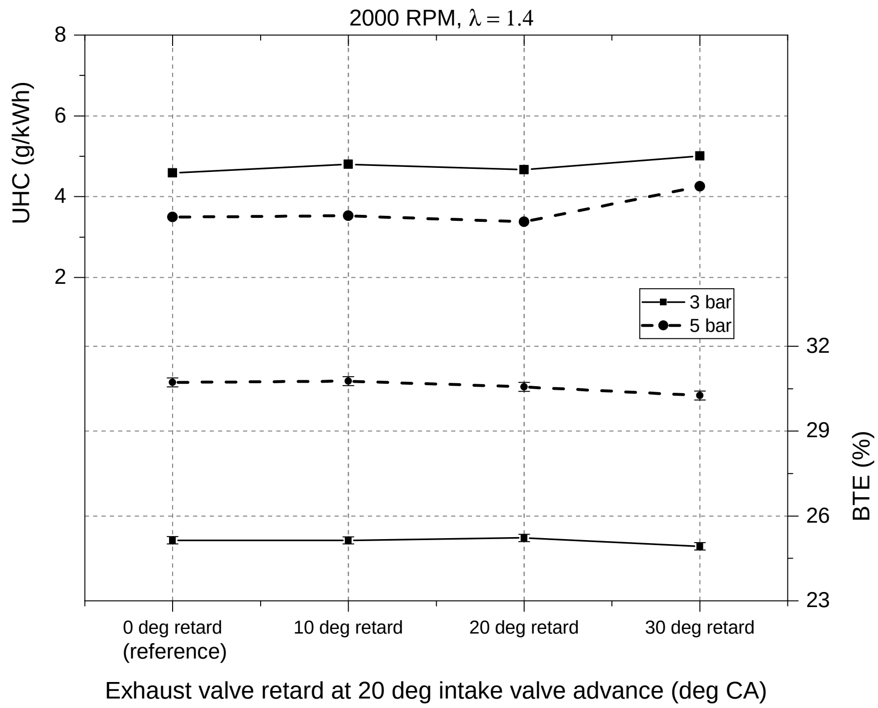

Figure 7.6: Effect of exhaust valve retard on UHC and BTE at 2000 RPM, 3 and 5 bar BMEP, $\lambda = 1.4$ with valve timing as per Table 7.1.

7.2 Impact of multiple injection strategies on engine performance

A dual injection strategy is a possible method to counter UHC emissions. With this strategy, the start of primary injection is placed in the intake stroke to create a more homogeneous mixture, and a secondary small injection takes place closer to the ignition timing to encourage more stable combustion with low UHC emissions. Such an approach has been shown by others to improve DI CNG engine performance in some cases [80, 129]. In this work, both the timing of the secondary fuel pulse and the split of mass between the two pulses are considered, and their impact on engine performance is analyzed. Note that this multiple injection strategy with CNG fuelling is only possible in the DI CNG engine, not with the CNG PFI system.

The secondary injection timing and different fuel mass splitting percentage (FSP) strategies are investigated for both stoichiometric and lean operating conditions. The FSP metric defines the fuel mass percentage of the primary and secondary injections; for example, FSP 60/40 means 60% of total fuel mass is injected during the primary injection and the remaining 40% is in the secondary injection. The minimum percentage of injected fuel mass in either injection is controlled by the dynamics of the injector, which sets the minimum injector opening time, and the engine operating condition, which sets the injection duration. As such, variations in FSP will be hardest to achieve at part load and low engine speeds with any form of dilution. Using the current injector, approximately 40% of the total charge could be injected in either the primary or secondary injection at the studied engine operating conditions.

7.2.1 Effect of secondary injection timing

This section examines how the start of secondary injection (SOI2) timing for a fixed FSP and start of primary injection (SOI1) timing impact engine performance. As shown in Fig. 7.7, the position of SOI2 is varied from the later part of the intake stroke through the compression stroke and approaching the ignition point. The most retarded position of SOI2 is limited to 90 deg bTDC$_{Fire}$ as excessive combustion

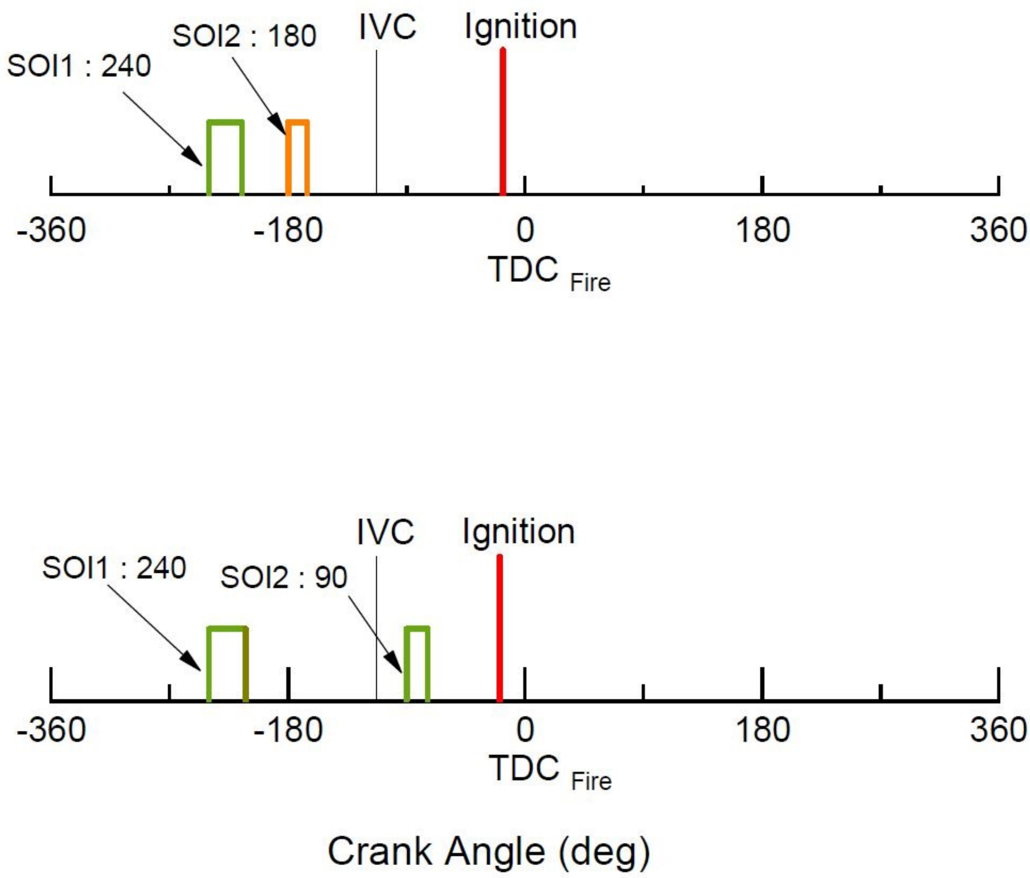

Figure 7.7: Dual injection strategy, showing advanced (top) and retarded (bottom) secondary injections with FSP=60/40 and relative to other significant timing parameters.

instability is observed with further retard. The position of SOI1 is fixed in the intake stroke at 240 deg bTDC$_{Fire}$ due to its mixing, as demonstrated in Chapter 4. The minimum percentage of secondary fuel mass is limited to 40% at 6 bar BMEP due to the limitation of the DI CNG injector opening time.

Figure 7.8 shows the BTE, COV$_{IMEP}$, and UHC emissions as a function of SOI2 timing with a FSP of 60/40 using stoichiometric and lean operation at 2000 RPM for different loads. The result for the single injection at 240 deg bTDC$_{Fire}$ is also plotted as a reference. UHC trend increases from the single injection value irrespective of the load and λ as SOI2 moves towards ignition. This can likely be attributed to a less homogeneous in-cylinder mixture distribution due to the decreased mixing time for a portion of the fuel charge, particularly with the most retarded SOI2. This is consistent with the results of the SOI variation tests using the single injection strategy as shown in Fig. 4.5 of Chapter 4, where retarded injection also demonstrated higher UHC emissions. The impact of secondary injection timing on BTE and COV_{IMEP} is also shown in Fig. 7.8, which again demonstrates diminished engine performance with SOI2 retard compared to the reference single injection.

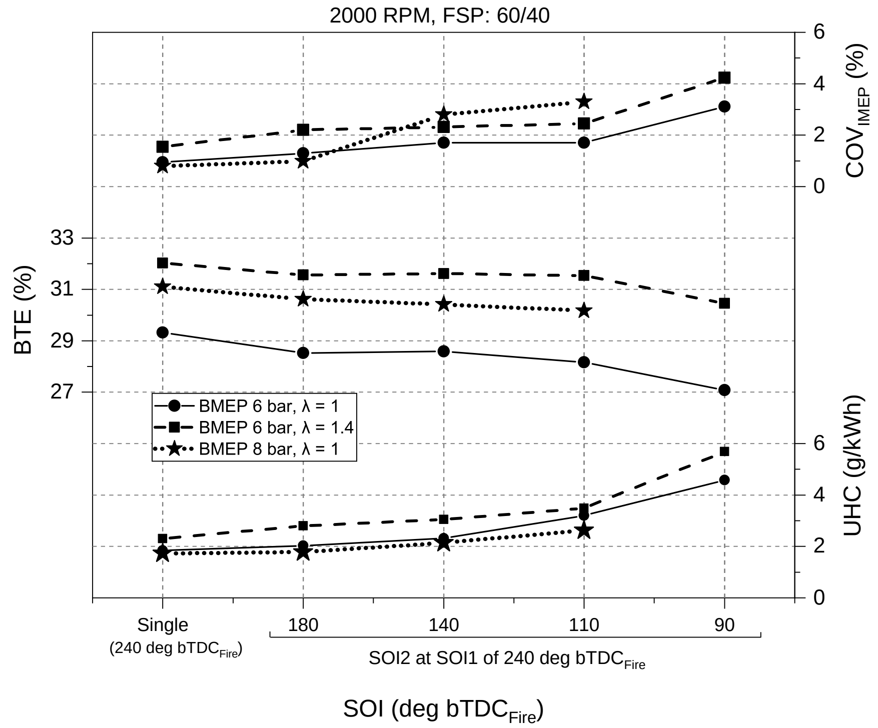

Figure 7.8: Effect of secondary injection (SOI2) timing on UHC emissions, BTE, and COV_{IMEP} at 2000 RPM with FSP = 60/40.

7.2.2 Effect of secondary injection fuel mass

Figure 7.9 demonstrates the impact of two different fuel mass splits (i.e., FSP 60/40 and FSP 40/60) on UHC and BTE at 2000 RPM, 6 bar, and $\lambda = 1.4$. UHC emissions increase with both FSP when SOI2 is retarded towards ignition, and FSP 40/60 case exhibits higher UHC compared to FSP 60/40 case for a given SOI2. This can be attributed to a reduction in mixture homogeneity due to higher secondary injection fuel mass for a given SOI2. As to be expected, the FSP 40/60 case also demonstrates lower BTE due to the lower combustion efficiency associated with this higher UHC.

The impact of FSP on UHC and BTE is further shown in Figure 7.10 for 2000 RPM, 8 bar and $\lambda = 1$ condition. An engine load of 8 bar BMEP is chosen

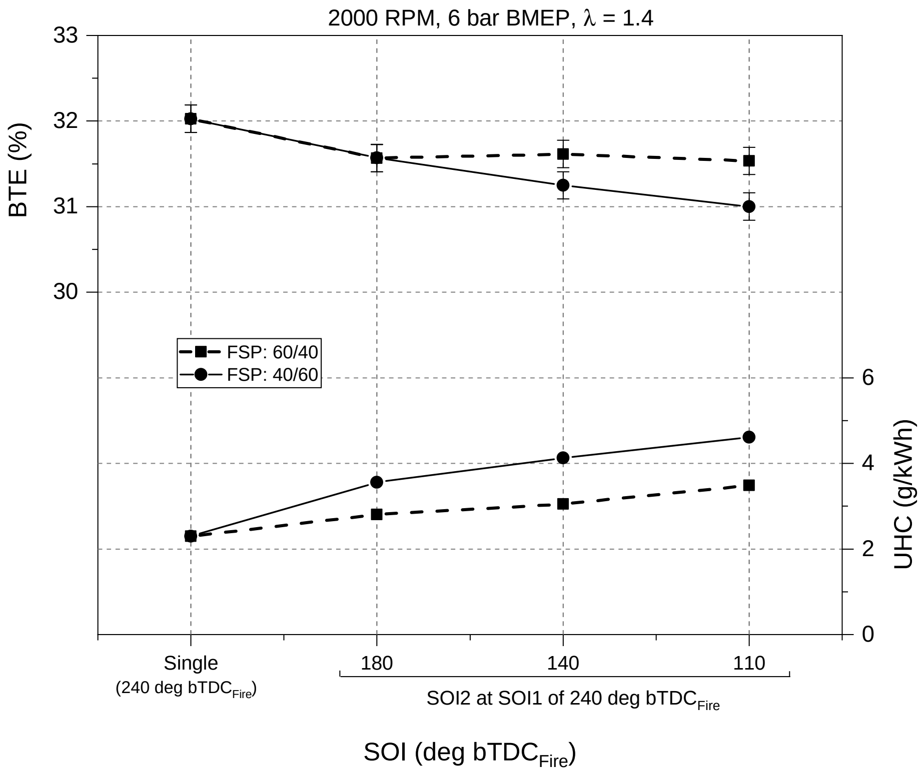

Figure 7.9: Effect of FSP on UHC emissions and BTE at 2000 RPM, 6 bar BMEP and $\lambda = 1.4$.

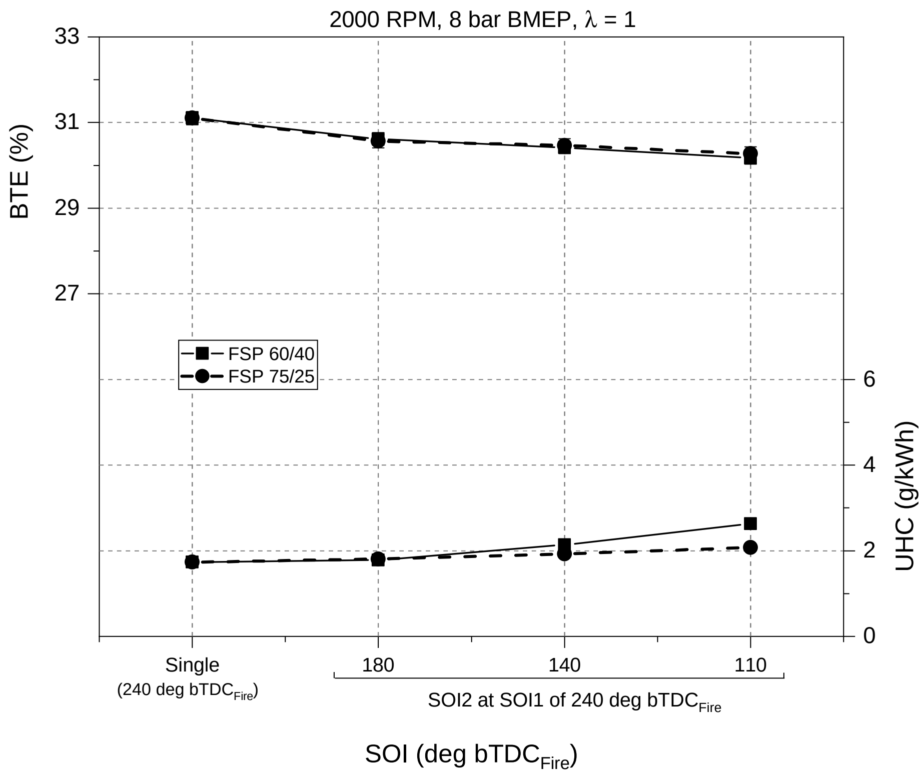

Figure 7.10: Effect of FSP on UHC emissions and BTE at 2000 RPM, 8 bar BMEP and $\lambda = 1$.

for this test as it provides the flexibility for a FSP of 75/25 due to a sufficiently long injection duration during the second fuel pulse. As shown in Fig. 7.10, UHC emissions increase with both FSP when SOI2 is retarded towards ignition. However, the increase of UHC emissions for FSP 75/25 relative to those of a single injection is not as significant as those of FSP 60/40 over the range of SOI2 timing. This indicates that further decreasing the proportion of fuel in the secondary fuel injection could prove beneficial if the injector was able to do this. These results suggest that additional investigations into multi-pulsing with DI CNG might be warranted using a more flexible injection hardware than was available in the present study, as others have recently found [129].

7.3 Combined dilution strategy

Chapter 6 showed that CNG fuelled lean-burn operation close to the lean limit at low loads has high UHC emissions despite the fuel economy benefits. Lean-burn operation was also shown to suffer from high NO_x emissions near stoichiometry, suggesting a potential benefit of using EGR dilution at high loads. Therefore, Fig. 7.11 presents a strategy for combined dilution at part loads ranging from 3 to 8 bar BMEP. The strategy consists of the following:

(a) use lean operation with $\lambda = 1.4$ and throttling for engine loads ranging from 3 to 6 bar BMEP to maintain high fuel efficiency and avoid high UHC emissions. Note that the use of EGR dilution is not an option at low loads because UHC emissions were high at these conditions, as shown in Chapter 5.

(b) use stoichiometric, EGR dilute operation for loads from 6 bar to 8 bar BMEP as lean operation close to stoichiometry suffered from high NO_x emissions (Fig. 6.8). The EGR rates for this combined dilution strategy are similar to the rates used for EGR dilution in Chapter 5 at the same conditions.

7.3.1 Fuel economy and engine-out emissions

Figure 7.12 compares the brake thermal efficiency of the combined strategy along with the results for the lean and EGR dilute operation demonstrated in previous

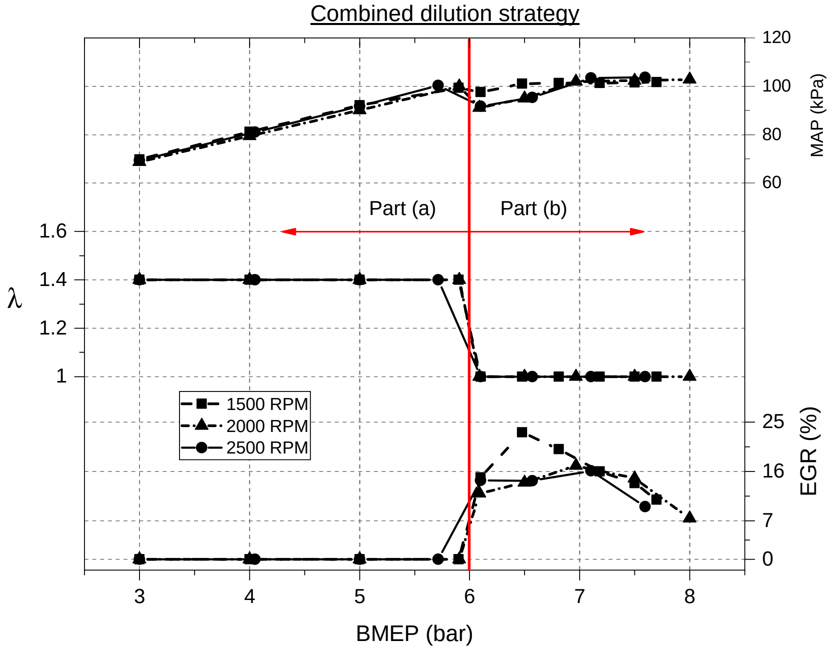

Figure 7.11: Variation of λ, EGR rate, and MAP for the combined dilution strategy over a range of part load operation with CNG fuelling

chapters at three different engine speeds. The combined strategy has intermediate BTE, which is unsurprising given its combined use of air and EGR dilution. At low loads, combined dilution demonstrates a considerable reduction in UHC emissions relative to lean operation, as shown in Fig. 7.13. Furthermore, NO_x emissions are lower than the lean results at all three engine speeds, as shown in Fig. 7.14, particularly at higher loads where the use of EGR and stoichiometric combustion results in much lower NO_x emissions than lean-burn.

Total CO_2 equivalent emissions are now used to assess if the combined dilution strategy can provide an overall benefit, where the UHC and NO_x emissions are again used in CO_{2e} calculation, as defined in Eq. 3.5.1. Fig. 7.15 shows that, depending on the speed and load, CO_{2e} emissions can be lower with the combined strategy since it incorporates attractive aspects of these two other strategies.

Of course, as discussed in Section 6.4, the choice of after-treatment system is key to determining whether a given strategy is best in a vehicle. As the combined strategy uses air dilution at part load, it is not thought prospective for use with a three-way catalyst, suggesting that a similar approach to the air dilution case will be preferable. This will most likely involve an oxidation catalyst and selective catalytic reduction (SCR). Since the primary benefit of the combined strategy

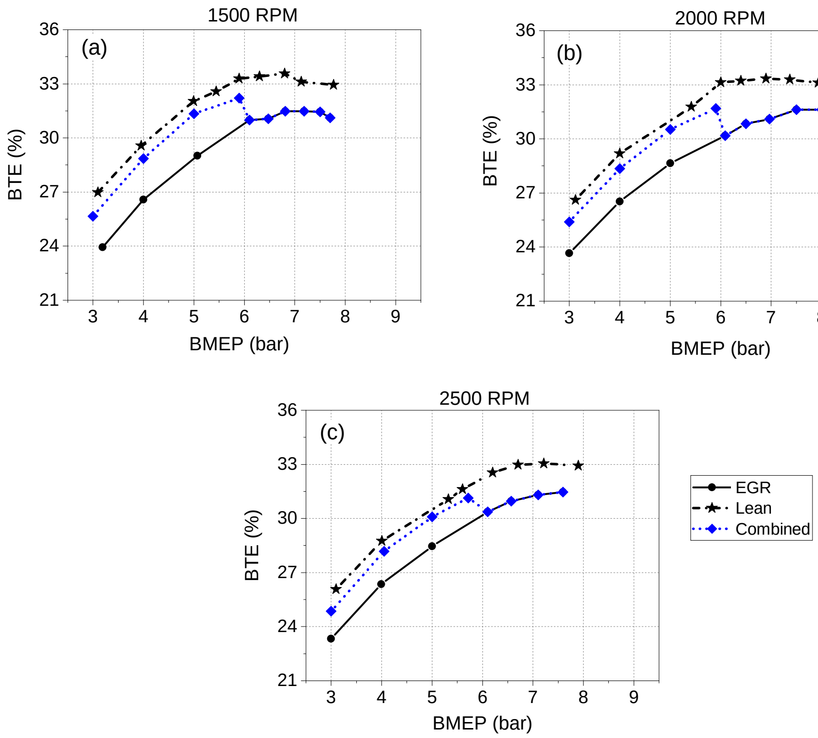

Figure 7.12: Comparison of part load BTE for EGR, lean, and combined dilution operation with CNG fuelling as a function of BMEP at (a) 1500 RPM, (b) 2000 RPM, and (c) 2500 RPM.

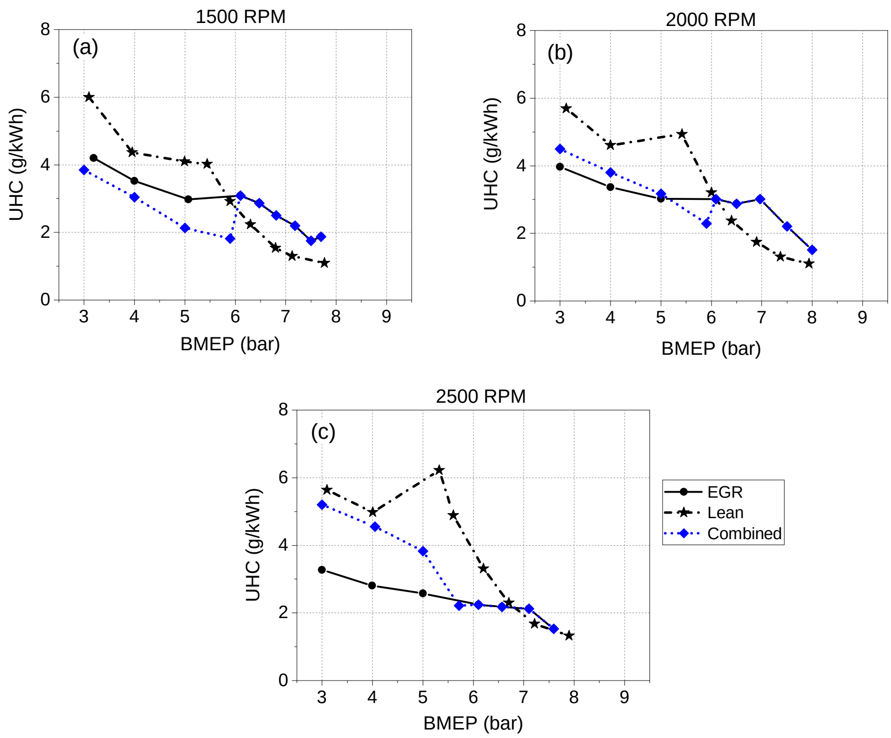

Figure 7.13: Comparison of part load UHC for EGR, lean, and combined dilution operation with CNG fuelling as a function of BMEP at (a) 1500 RPM, (b) 2000 RPM and (c) 2500 RPM.

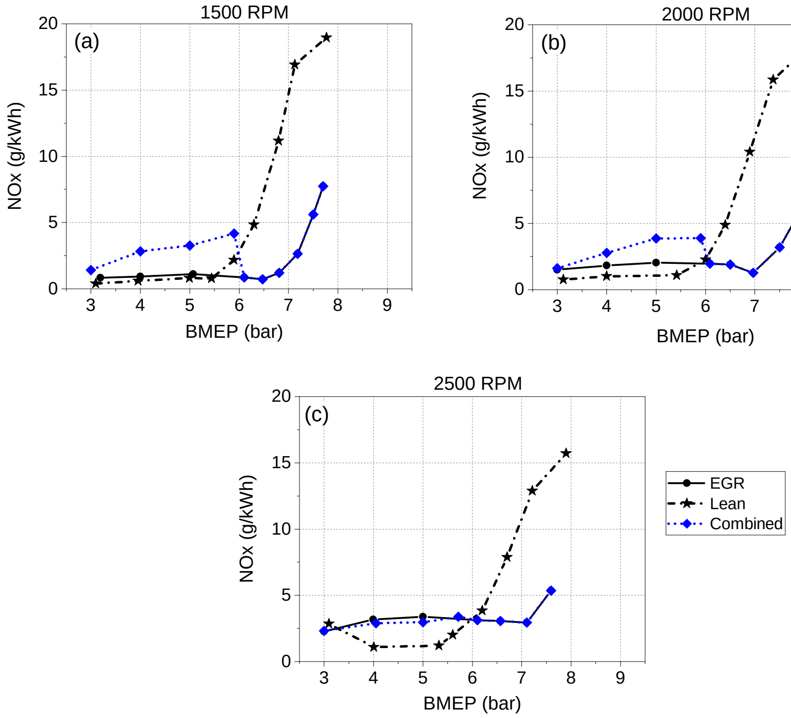

Figure 7.14: Comparison of part load NO_x for EGR, lean, and combined dilution operation with CNG fuelling as a function of BMEP at (a) 1500 RPM (b) 2000 RPM, and (b) 2500 RPM.

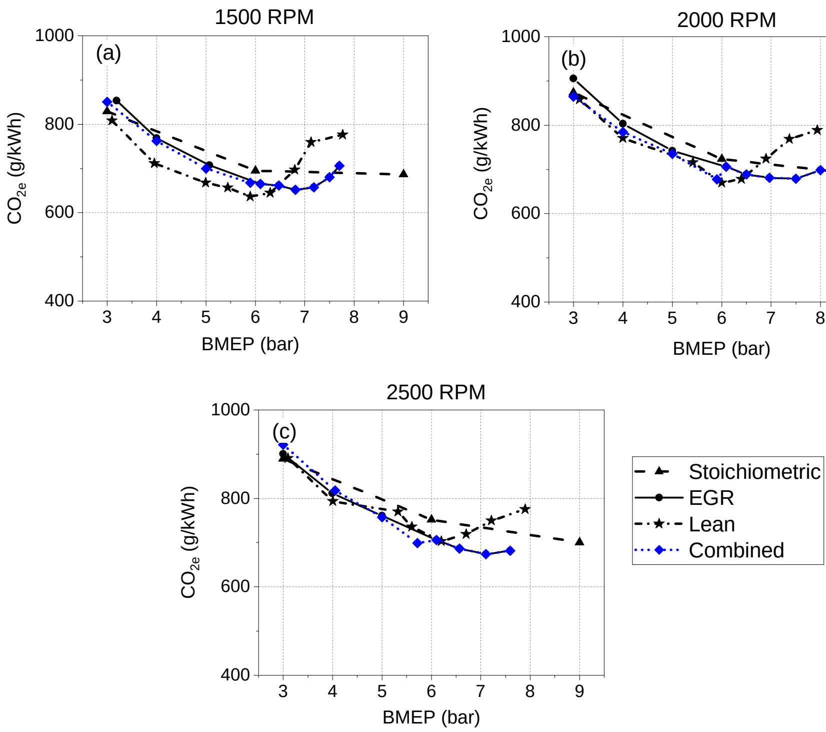

Figure 7.15: Part load CO_{2e} considering the GWP of CO_2, CH_4 and NO_x at (a) 1500 RPM, (b) 2000 RPM, and (c) 2500 RPM for CNG fuelled operation with stoichiometric, lean, EGR, and combined dilution.

appears to be its avoidance of high engine-out NO_x emissions, the SCR system should be smaller and therefore involving lower operational cost than a SCR system for a pure, lean-burn engine. However, since the BTE of the combined strategy is lower than that of the air dilution strategy, further work is required to determine whether the combined strategy will be preferable overall to either the air dilution or EGR dilution approaches.

7.4 Summary

This chapter investigated various, more advanced engine control strategies that might enhance DI CNG engine performance relative to the earlier studies of dilution with air and EGR. The impact of hot internal residual gases (i-EGR) on BTE and engine-out UHC emissions was first examined by controlling the phasing of the intake valve advance and exhaust valve retard. It was observed that varying the i-EGR rate in this manner has little effect on BTE and was not effective in mitigating engine-out UHC emissions.

The effect of split injections on UHC emissions was then examined at part loads by varying the secondary injection timing and the split of fuel mass between the two injections. In contrast to other published studies [80, 129], these experiments also did not show an improvement in BTE and UHC emissions versus the reference single injection, suggesting that the injection hardware may need to have a faster dynamic response to exploit such opportunities.

Finally, a combined dilution strategy was examined in an attempt to combine some of the favorable characteristics of both air and EGR dilution. In some cases, this combined strategy was able to achieve lower CO_{2e} emissions at part load than the other approaches studied, while also avoiding some of the extremes in the UHC and NO_x emissions that result from air and EGR dilution in different parts of the engine map. However, since the BTE of the combined strategy is always lower than that of the air dilution strategy, further work that considers vehicle tailpipe emissions in the field is required to determine whether the combined strategy will be preferable overall to either the air or EGR dilution approaches.

Chapter 8

Conclusions and Recommendations

8.1 Conclusions

This work presented an experimental and numerical study of the performance of a 4-cylinder, downsized and boosted, spark-ignited production engine when employing directly injected compressed natural gas (DI CNG) and gasoline direct injection (GDI). Three different charge preparation strategies were investigated for both fuels over a range of engine speeds and loads: stoichiometric engine operation without external dilution, stoichiometric operation with external exhaust gas recirculation (EGR), and lean burn. Furthermore, the impact of internal residual gases, multiple fuel injections per cycle, and the combined use of air and recirculated exhaust gas dilution on engine performance were also explored. The key findings of the work are as follows.

1. An optimized DI CNG engine was shown to have comparable performance to a gasoline-fuelled equivalent at stoichiometric conditions, but without the peak torque loss that is characteristic of CNG PFI systems.

Three different injection strategies were first investigated for DI CNG at part load under stoichiometric conditions. It was observed that mixture homogeneity was desirable for fuel economy and emissions, with intermediate SOI timings exhibiting the best performance due to the combined effect of sufficient mixing time and reduced pumping losses.

Next, the stoichiometric part load performance of DI CNG with intermediate SOI timings was compared with equivalent gasoline fuelled operation. At part load, both DI CNG and GDI were able to achieve MBT timing and showed similar thermal efficiencies. This was because the higher combustion efficiency and lower pumping losses of DI CNG were offset by its higher compression stroke work compared to that of GDI operation.

However, this work also demonstrated that directly injecting CNG after IVC using a highly retarded SOI timing produced the same peak torque as the gasoline fuelled engine. A substantial improvement in fuel economy was also observed with DI CNG relative to GDI at this higher load operation under stoichiometric conditions. This was primarily because MBT timing was maintained for CNG due to its superior knock resistance, whereas ignition timing was retarded for gasoline to avoid auto-ignition at these conditions.

2. The use of charge dilution demonstrated improved fuel efficiency with DI CNG and GDI operation, with lean-burn and EGR each outperforming the other at different operating conditions when using different performance metrics.

The impact of charge dilution using EGR or excess air with DI CNG and GDI operation was examined and compared with the stoichiometric operation without dilution. It was suggested that optimization of the fuel efficiency with either form of dilution required a balance between the positive impact of lower in-cylinder heat losses and less pumping work, and the negative impact of higher energy lost to the exhaust, either via sensible enthalpy or unburned fuel. For equivalent quantities of charge dilution with CNG fuelling, higher BTE was observed with lean-burn relative to EGR dilution primarily due to shorter combustion duration and lower unburned fuel energy. Furthermore, both DI CNG and GDI lean-burn operation exhibited similar thermal efficiency at a given air dilution level, whereas EGR dilution demonstrated higher BTE with GDI than with DI CNG at the same EGR rate due to gasoline's faster flame speed.

The engine-out total CO_2 equivalent emissions for the part load performance of DI CNG under stoichiometric, EGR and air dilution conditions were then assessed. DI CNG operation with EGR dilution exhibited slightly better greenhouse gas emissions relative to stoichiometric operation without dilution. CNG fuelled lean-burn operation demonstrated a significant reduction in CO_2 emissions compared to the other two modes, though total CO_2 equivalent emissions were not as favourable due to lean-burn's higher NO_x emissions near stoichiometry and significant UHC emissions at low loads. However, while the GHG emissions from these different dilution with DI CNG were lower than those from stoichiometric GDI operation, assessment of which is superior requires consideration of the after-treatment system before a final choice of combustion strategy is made.

3. Using turbulent premixed flame theory, the modelled onset of bulk flame quenching correlated with measured indicators of combustion quality across a range of different engine operating conditions.

Premixed turbulent combustion simulations were performed for both DI CNG and GDI under stoichiometric and dilute conditions, where the latter included EGR and lean-burn. The flame speed results demonstrated decreasing trends with the increase of dilution levels for both fuels, and this effect was most pronounced with CNG. At similar dilution levels with CNG fuelling, lean-burn exhibited higher flame speed than that with stoichiometric EGR operation due to improved mixture heating value in the presence of excess oxygen.

The premixed turbulent flame theory of Bradley [60, 62, 70] was then utilized to model the severity of turbulent flame quenching. This showed that the substitution of gasoline with CNG, an increase in charge dilution, or a higher engine speed all increased the impact of flame quenching. For both fuels and both charge dilution strategies, a correlation was observed between the modelled onset of flame quenching and increased UHC emissions and COV_{IMEP}, particularly at the early stages of combustion. This provided physical insight into the role of charge dilution on combustion and engine performance.

4. The combined use of air and EGR dilution avoided high engine-out NO_x emissions at some operating conditions, and may be superior to the use of solely air or EGR dilution.

A combined dilution strategy that incorporated the favorable characteristics of both air and EGR dilution was investigated with DI CNG at part load, and was shown to achieve lower engine-out GHG emissions in some cases. Since the primary benefit of this strategy appeared to be its avoidance of high engine-out NO_x emissions, its lower BTE compared to pure, air dilution necessitates further study with an after-treatment system in place to determine its performance relative to air or EGR dilution.

8.2 Recommendations for future work

8.2.1 Investigation in a high compression ratio DISI engine designed for DI CNG operation

In this thesis, DI CNG work was performed in a test engine based on a modern, GDI engine, which had a relatively low compression ratio of 9.3 and was designed for wall-guided, DI liquid fuel. This engine design was not ideal for probing the maximum fuel efficiency attainable with DI CNG, as it could not test CNG at the autoignition limit and the in-cylinder mixing strategy was optimized for liquid fuel injection. It is proposed that future work utilizes a higher compression ratio engine and a combustion chamber design better-suited to gaseous fuel DI. In addition, valve lifts and the associated intake and exhaust valve timings should be investigated in this future work. These are not studied in detail in this thesis; however, they are expected to have an impact on engine performance.

8.2.2 Drive cycle analysis for GHG footprint using post-catalyst emissions

This work assessed the efficacy of a particular engine operating strategy in terms of fuel efficiency and engine-out GHG emissions without regard to the after-treatment system. However, exhaust gas conditions such as EGT varied significantly with different engine operating modes, particularly with external diluent operation. These factors are likely to have a significant impact on the performance of a conventional catalyst and, therefore, on the tailpipe-out emissions. This is potentially problematic for UHC emissions with DI CNG operation due to methane's high light-off temperature. Future work is therefore required to perform drive cycle analysis of a conventional powertrain using the measured post-catalyst GWP emissions, which will provide an overall GHG footprint for different engine operating modes with DI CNG. This work can be further extended to estimate the GHG emissions reduction with hybrid powertrain configurations. Furthermore, energy consumption associated with the storing of natural gas at 200 bar for vehicle use may have a significant implication on GHG footprint. Therefore, a life-cycle analysis of CNG vehicles is necessary to demonstrate the overall GHG footprint of CNG as an automotive fuel.

8.2.3 Implementation of advanced strategies for methane based UHC emissions reduction

This work demonstrated a significant fuel economy improvement potential with DI CNG, mainly using lean-burn operation. However, this benefit cannot be fully realized due to potential increase in GWP emissions, particularly methane-based UHC emissions. Various in-cylinder techniques, such as the utilization of hot i-EGR, multiple-injections, and combined dilution, were briefly examined in this study to address these issues. The resolution of this UHC issue can be investigated in future work using a more effective multiple injection system (i.e., the capability to inject less fuel in the first pulse) or with a pre-chamber ignition concept. In addition, a catalyst heating strategy for methane oxidation can be explored.

References

[1] J. Teter, P. Feuvre, M. Gorner, and S. Scheffer, "Tracking transport report," tech. rep., International energy agency (IEA), 2019.

[2] J. Graichen, "Targets for the non-ETS sectors in 2040 and 2050," tech. rep., Öko-Institut e.V., 2016.

[3] G. Bartsch, R. Friedfeldt, U. Heiter, U. Kramer, M. Lauterbach, T. Schorn, and S. Siebrandt, "3-cylinder SI engine with fully variable valve train upvalve on intake and exhaust side," in *Gas ON, Europe*, 2017.

[4] *www.theicct.org/info-tools/global-passenger-vehicle-standards.*

[5] P. Mock, J. Kühlwein, U. Tietge, V. Franco, A. Bandivadekar, and J. German, "The WLTP: How a new test procedure for cars will affect fuel consumption values in the EU," *International council on clean transportation*, vol. 9, pp. 35–47, 2014.

[6] EIA, "International energy outlook," tech. rep., U.S. Energy Information Administration, 2019.

[7] Thinkstep, "Greenhouse gas emissions from natural gas in transport," tech. rep., www.ngvemissionsstudy.eu, 2017.

[8] *NGVA Europe, https://www.ngva.eu/medias/decarbonizing-passenger-cars-with-cng/.*

[9] R. Otten and R. Mangold, "Audi e-fuels: energy revolution in tank," *Advanced Fuels for Sustainable Mobility*, 2014.

[10] Standard, "N.N. diesel fuel EN 590," tech. rep., Europe, 2014.

[11] Standard, "N.N. gasoline fuel EN 228, 2014," tech. rep., Europe, 2014.

[12] U. Kramer, T. Lorenz, C. Hofmann, H. Ruhland, R. Klein, and C. Weber, "Methane number effect on the efficiency of a downsized, dedicated, high performance compressed natural gas (CNG) direct injection engine," in *SAE Technical Paper*, SAE International, 03 2017.

[13] R. Bechtold, *Alternative Fuels Guide Book*. SAE Innternational, 1997.

[14] M. I. Khan, T. Yasmeen, M. I. Khan, M. Farooq, and M. Wakeel, "Research progress in the development of natural gas as fuel for road vehicles: a bibliographic review (1991–2016)," *Renewable and Sustainable Energy Reviews*, vol. 66, pp. 702–741, 2016.

[15] *World wide natural gas vehicle market share, NGV Global.*

[16] *NGVA Europe, https://www.ngva.eu/medias/renewable-gas-in-transport-and-methane-emissions/.*

[17] IGU, "Natural gas – the fuel of choice towards clean mobility," tech. rep., International Gas Union, 2018.

[18] U. Kramer, R. Klein, C. Hofmann, H. Stoffels, O. Berkemeier, and C. Weber, "Extreme downsizing of CNG engines–opportunities and challenges," in *Proceedings of the 1st International Conference "Advanced Fuels for Sustainable Mobility", Haus der Technik, Nürburgring*, 2014.

[19] GDI, "https://www.greencarcongress.com/2019/04/20190416-gdi.html," tech. rep., Green Car Congress, 2019.

[20] F. Zhao, M.-C. Lai, and D. L. Harrington, "Automotive spark-ignited direct-injection gasoline engines," *Progress in energy and combustion science*, vol. 25, no. 5, pp. 437–562, 1999.

[21] Y. Takagi, "The role of mixture formation in improving fuel economy and reducing emissions of automotive SI engines," *FISITA Technical Paper*, no. P0109, 1996.

[22] C. Stovell, R. Matthews, B. E. Johnson, H. Ng, and B. Larsen, "Emissions and

fuel economy of a 1998 Toyota with a direct injection spark ignition engine," *SAE Transactions*, vol. 108, pp. 1124–1141, 1999.

[23] *Australian Energy Market Operator, https://aemo.com.au/energy-systems/gas/declared-wholesale-gas-market-dwgm/data-dwgm/daily-dwgm-reports.*

[24] BP, "Statistical review of world energy," tech. rep., https://www.bp.com/, 2019.

[25] A. Das and H. C. Watson, "Development of a natural gas spark ignition engine for optimum performance," *Proceedings of the Institution of Mechanical Engineers, Part D: Journal of Automobile Engineering*, vol. 211, no. 5, pp. 361–378, 1997.

[26] R. Motor, "Design storage system, engine and subsystem installation," tech. rep., GasON, 2019.

[27] C. Reynolds, R. Evans, L. Andreassi, S. Cordiner, and V. Mulone, "The effect of varying the injected charge stoichiometry in a partially stratified charge natural gas engine," in *SAE Technical Paper*, SAE International, 04 2005.

[28] B. M. Shasby, "Alternative fuels: incompletely addressing the problems of the automobile," Master's thesis, Virginia Tech, 2004.

[29] M. L. Poulton, *Alternative fuels for road vehicles.* Computational Mechanics, Inc., Billerica, MA (United States), 12 1994.

[30] O. Lang, K. Habermann, R. Thiele, and F. Fricke, "Gasoline combustion with future fuels," in *SAE Technical Paper*, The Automotive Research Association of India, 01 2007.

[31] *EPA Tier 3 Cert Fuel Regular, GAGE Company.*

[32] S. Pischinger, M. Umierski, and B. Hüchtebrock, "New CNG concepts for passenger cars: High torque engines with superior fuel consumption," in *SAE Technical Paper*, SAE International, 06 2003.

[33] S. S. Takagaki and R. R. Raine, "The effects of compression ratio on nitric

oxide and hydrocarbon emissions from a spark-ignition natural gas fuelled engine," *SAE Transactions*, vol. 106, pp. 701–707, 1997.

[34] A. E. Catania, D. Misul, E. Spessa, and A. Vassallo, "Analysis of combustion parameters and their relation to operating variables and exhaust emissions in an upgraded multivalve bi-fuel CNG SI engine," *SAE Transactions*, vol. 113, pp. 682–703, 2004.

[35] N.N., "Automotive fuels - compressed natural gas - requirements and test methods," tech. rep., German Fuel Standard (English version) DIN 51624, 2007.

[36] N.N., "Natural gas and biomethane for use in transport and biomethane for injection in the natural gas network - part 2: Automotive fuel specifications," tech. rep., CEN Draft European Standard, 2014.

[37] J. Heywood, *Internal Combustion Engine Fundamentals.* McGraw-Hill, Inc., 1988.

[38] P. Atibeh, "Performance of a spark ignition, lean burn, natural gas internal combustion engine," Master's thesis, Department of Mechanical Engineering, The University of Melbourne, 2012.

[39] S. Matsuok and H. Tasaka, "The evaporation of fuel and its effect on volumetric efficiency," *JARI technical memorandum*, no. 2, pp. 17–22, 1971.

[40] O. Akindele, D. Bradley, P. Mak, and M. McMahon, "Spark ignition of turbulent gases," *Combustion and Flame*, vol. 47, pp. 129–155, 1982.

[41] D. Bradley and F.-K. Lung, "Spark ignition and the early stages of turbulent flame propagation," *Combustion and Flame*, vol. 69, no. 1, pp. 71–93, 1987.

[42] L. Gillespie, M. Lawes, C. G. W. Sheppard, and R. Woolley, "Aspects of laminar and turbulent burning velocity relevant to SI engines," *SAE Transactions*, vol. 109, pp. 13–33, 2000.

[43] D. Ballal and A. Lefebvre, "The structure and propagation of turbulent flames," *Proceedings of the Royal Society of London. A. Mathematical and Physical Sciences*, vol. 344, no. 1637, pp. 217–234, 1975.

[44] S. Merdjani and C. G. W. Sheppard, “Gasoline engine cycle simulation using the leeds turbulent burning velocity correlations,” in *SAE Technical Paper*, SAE International, 10 1993.

[45] N. C. Blizard and J. C. Keck, “Experimental and theoretical investigation of turbulent burning model for internal combustion engines,” *SAE Transactions*, vol. 83, pp. 846–864, 1974.

[46] J. R. Smith, “Turbulent flame structure in a homogeneous-charge engine,” *SAE Transactions*, vol. 91, pp. 150–164, 1982.

[47] J. B. Heywood, “Combustion and its modeling in spark-ignition engines,” in *International symposium COMODIA*, vol. 94, pp. 1–15, 1994.

[48] R. J. Tabaczynski, C. R. Ferguson, and K. Radhakrishnan, “A turbulent entrainment model for spark-ignition engine combustion,” *SAE Transactions*, vol. 86, pp. 2414–2433, 1977.

[49] R. J. Tabaczynski, F. H. Trinker, and B. A. Shannon, “Further refinement and validation of a turbulent flame propagation model for spark-ignition engines,” *Combustion and Flame*, vol. 39, no. 2, pp. 111–121, 1980.

[50] A. L. Jones and R. L. Evans, “Comparison of burning rates in a natural-gas-fueled spark ignition engine,” *Journal of Engineering for Gas Turbines and Power*, vol. 107, no. 4, pp. 908–913, 1985.

[51] H. E. Jääskeläinen and J. S. Wallace, “Performance and emissions of a natural gas-fueled 16 valve DOHC four-cylinder engine,” in *SAE Technical Paper*, SAE International, 03 1993.

[52] P. A. Atibeh, P. A. Dennis, P. J. Orbaiz, M. J. Brear, and H. C. Watson, “Lean burn performance of a natural gas fuelled, port injected, spark ignition engine,” in *SAE Technical Paper*, SAE International, 04 2012.

[53] A. E. Hassaneen, K. S. Varde, A. H. Bawady, and A.-A. Morgan, “A study of the flame development and rapid burn durations in a lean-burn fuel injected natural gas SI engine,” in *SAE Technical Paper*, SAE International, 05 1998.

[54] T. Yamato, H. Sekino, T. Ninomiya, and M. Hayashida, “Stratification of

in-cylinder mixture distributions by tuned port injection in a 4-valve SI gas engine," in *SAE Technical Paper*, SAE International, 03 2001.

[55] T. Thurnheer, P. Soltic, and P. D. Eggenschwiler, "SI engine fuelled with gasoline, methane and methane/hydrogen blends: heat release and loss analysis," *International Journal of Hydrogen Energy*, vol. 34, no. 5, pp. 2494–2503, 2009.

[56] D. B. Rhodes and J. C. Keck, "Laminar burning speed measurements of indolene-air-diluent mixtures at high pressures and temperatures," *SAE Transactions*, vol. 94, pp. 23–35, 1985.

[57] JANAF, "Thermochemical tables, 2d ed., nsrds-nb537," tech. rep., U.S. National Bureau of Standards, 1971.

[58] A. Klimov, "Flame propagation under conditions of strong turbulence," *SPhD*, vol. 20, p. 168, 1975.

[59] P. A. Libby and F. A. Williams, "Structure of laminar flamelets in premixed turbulent flames," *Combustion and Flame*, vol. 44, no. 1-3, pp. 287–303, 1982.

[60] R. Abdel-Gayed, D. Bradley, and F.-K. Lung, "Combustion regimes and the straining of turbulent premixed flames," *Combustion and Flame*, vol. 76, no. 2, pp. 213–218, 1989.

[61] R. Abdel-Gayed, D. Bradley, and M. Lawes, "Turbulent burning velocities: a general correlation in terms of straining rates," *Proceedings of the Royal Society of London. A. Mathematical and Physical Sciences*, vol. 414, no. 1847, pp. 389–413, 1987.

[62] D. Bradley, A. Lau, M. Lawes, and F. Smith, "Flame stretch rate as a determinant of turbulent burning velocity," *Philosophical Transactions of the Royal Society of London. Series A: Physical and Engineering Sciences*, vol. 338, no. 1650, pp. 359–387, 1992.

[63] D. Bradley, R. Hicks, M. Lawes, C. Sheppard, and R. Woolley, "The measurement of laminar burning velocities and markstein numbers for iso-octane–air and iso-octane–n-heptane–air mixtures at elevated temperatures

and pressures in an explosion bomb," *Combustion and flame*, vol. 115, no. 1-2, pp. 126–144, 1998.

[64] J. Abraham, F. A. Williams, and F. V. Bracco, "A discussion of turbulent flame structure in premixed charges," *SAE Transactions*, vol. 94, pp. 128–143, 1985.

[65] R. Stephen, *An introduction to combustion: concepts and applications.* McGraw-Hill, 1996.

[66] F. Williams, "Asymptotic methods in turbulent combustion," *AIAA journal*, vol. 24, no. 6, pp. 867–875, 1986.

[67] R. Borghi, "On the structure and morphology of turbulent premixed flames," in *Recent advances in the Aerospace Sciences*, pp. 117–138, Springer, 1985.

[68] N. Peters, "Laminar flamelet concepts in turbulent combustion," in *Symposium (International) on Combustion*, vol. 21, pp. 1231–1250, Elsevier, 1988.

[69] V. Zimont, "Theory of turbulent combustion of a homogeneous fuel mixture at high reynolds numbers," *Combustion, Explosion and Shock Waves*, vol. 15, no. 3, pp. 305–311, 1979.

[70] R. Abdel-Gayed, K. Al-Khishali, and D. Bradley, "Turbulent burning velocities and flame straining in explosions," *Proceedings of the Royal Society of London. A. Mathematical and Physical Sciences*, vol. 391, no. 1801, pp. 393–414, 1984.

[71] B. Karlovitz, D. Denniston Jr, D. Knapschaefer, and F. Wells, "Studies on turbulent flames: A. flame propagation across velocity gradients b. turbulence measurement in flames," in *Symposium (international) on combustion*, vol. 4, pp. 613–620, Elsevier, 1953.

[72] P. Abbasi Atibeh, M. J. Brear, P. A. Dennis, P. J. Orbaiz, and H. C. Watson, "Lean limit combustion analysis for a spark ignition natural gas internal combustion engine," *Combustion science and technology*, vol. 185, no. 8, pp. 1151–1168, 2013.

[73] M. A. Kalam, H. H. Masjuki, T. Mahlia, M. Fuad, K. Halim, A. Ishak, M. Khair, A. Yusoff, and A. Shahrir, "Experimental test of a new compressed natural gas engine with direct injection," *SAE International Powertrains, Fuels and Lubricants Meeting*, 2009.

[74] A. Shah, S. S. Thipse, A. Tyagi, S. D. Rairikar, K. P. Kavthekar, N. V. Marathe, and P. Mandloi, "Literature review and simulation of dual fuel diesel-CNG engines," in *SAE Technical Paper*, The Automotive Research Association of India, 01 2011.

[75] L. Harry, "Direct injection of CNG for driving performance with low CO_2," in *23rd Aachen Colloquium Automobile and Engine Technology*, 2014.

[76] P. Hofmann, T. Hofherr, G. Hoffmann, and J.-F. Preuhs, "Potential of CNG direct injection for downsizing engines," *MTZ worldwide*, vol. 77, no. 7-8, pp. 28–35, 2016.

[77] K. Zeng, Z. Huang, B. Liu, L. Liu, D. Jiang, Y. Ren, and J. Wang, "Combustion characteristics of a direct-injection natural gas engine under various fuel injection timings," *Applied thermal engineering*, vol. 26, no. 8-9, pp. 806–813, 2006.

[78] A. Boretti, P. Lappas, B. Zhang, and S. K. Mazlan, "CNG fueling strategies for commercial vehicles engines - a literature review," in *SAE Technical Paper*, SAE International, 11 2013.

[79] D. E. Wang and H. C. Watson, "Direct injection compressed natural gas combustion and visualisation," in *SAE Technical Paper*, SAE International, 06 2000.

[80] C. Hu and S. Hou, "Investigations on combustion process of low-pressure CNG compound direct injection spark-ignited engines," in *SAE Technical Paper*, SAE International, 09 2010.

[81] M. Ferrera, "Highly efficient natural gas engines," in *SAE Technical Paper*, SAE International, 09 2017.

[82] A.-R. A-Aziz and Firmansyah, "The effect of fuel rail pressure on the

performance of a CNG-direct injection engine," in *SAE Technical Paper*, SAE International, 04 2009.

[83] *VEHICLE CATALOGUE, https://www.ngva.eu/medias/vehicle-catalogue-2019/.*

[84] P. Einewall, P. Tunestål, and B. Johansson, "Lean burn natural gas operation vs. stoichiometric operation with EGR and a three way catalyst," in *SAE Technical Paper*, SAE International, 04 2005.

[85] P. Corbo, M. Gambino, S. Iannaccone, and A. Unich, "Comparison between lean-burn and stoichiometric technologies for CNG heavy-duty engines," *SAE Transactions*, vol. 104, pp. 20–22, 1995.

[86] Y. Nakajima, K. Sugihara, Y. Takagi, and S. Muranaka, "Effects of exhaust gas recirculation on fuel consumption," *Proceedings of the Institution of Mechanical Engineers*, vol. 195, no. 1, pp. 369–376, 1981.

[87] A. Manivannan, P. Tamil, and S. Chandrasekaran, "Lean burn natural gas spark ignition engine – an overview," *SAE International*, 2003.

[88] F. A. Ayala, M. D. Gerty, and J. B. Heywood, "Effects of combustion phasing, relative air-fuel ratio, compression ratio, and load on SI engine efficiency," *SAE Transactions*, vol. 115, pp. 177–195, 2006.

[89] B. Peters, "Mass burning rates in a spark ignition engine operating in the partial burn regime," in *Paper C92/79 Proceedings of IMechE Conference on Fuel Economy and Emissions in Lean Burn Engines*, p. 63, 1979.

[90] D. Agarwal, S. K. Singh, and A. K. Agarwal, "Effect of exhaust gas recirculation (EGR) on performance, emissions, deposits and durability of a constant speed compression ignition engine," *Applied energy*, vol. 88, no. 8, pp. 2900–2907, 2011.

[91] L. Rouleau, D. Serrano, B. Lecointe, F. Ravet, G. Coma, and P. Christou, "CNG direct injection spark-ignition engine with high turbulence and high compression ratio: numerical and experimental investigations," in *12th*

Conference of Gaseous-Fuel Powered Vehicles, (Stuttgart, Germany), FKFS, Oct. 2017.

[92] H. Wei, T. Zhu, G. Shu, L. Tan, and Y. Wang, "Gasoline engine exhaust gas recirculation–a review," *Applied energy*, vol. 99, pp. 534–544, 2012.

[93] M. Kaiser, U. Krueger, R. Harris, and L. Cruff, "Doing more with less - the fuel economy benefits of cooled EGR on a direct injected spark ignited boosted engine," in *SAE Technical Paper*, SAE International, 04 2010.

[94] D. Tomazic and A. Pfeifer, "Cooled EGR - a must or an option for 2002/04," *SAE Transactions*, vol. 111, pp. 1650–1658, 2002.

[95] T. Kato, K. Saeki, H. Nishide, and T. Yamada, "Development of CNG fueled engine with lean burn for small size commercial van," *JSAE review*, vol. 22, no. 3, pp. 365–368, 2000.

[96] H. Kuroda, Y. Nakajima, K. Sugihara, Y. Takagi, and S. Muranaka, "The fast burn with heavy EGR, new approach for low NO_x and improved fuel economy," *SAE Transactions*, vol. 87, pp. 1–15, 1978.

[97] H. H. Geok, T. I. Mohamad, S. Abdullah, Y. Ali, A. Shamsudeen, and E. Adril, "Experimental investigation of performance and emission of a sequential port injection natural gas engine," *European Journal of Scientific Research*, vol. 30, no. 2, pp. 204–214, 2009.

[98] H. Hamid and A. Ahmad, "Development of monofuelled natural gas vehicles: a malaysian experience," *Malaysia: Special Project of Petronas Research*, p. 10, 2002.

[99] M. I. Jahirul, H. H. Masjuki, R. Saidur, M. Kalam, M. Jayed, and M. Wazed, "Comparative engine performance and emission analysis of CNG and gasoline in a retrofitted car engine," *Applied Thermal Engineering*, vol. 30, no. 14-15, pp. 2219–2226, 2010.

[100] M. Aslam, H. Masjuki, M. Kalam, H. Abdesselam, T. Mahlia, and M. Amalina, "An experimental investigation of CNG as an alternative fuel for a retrofitted gasoline vehicle," *Fuel*, vol. 85, no. 5-6, pp. 717–724, 2006.

[101] W. S. Wayne, N. N. Clark, and C. M. Atkinson, “A parametric study of knock control strategies for a bi-fuel engine,” *SAE Transactions*, vol. 107, pp. 1387–1398, 1998.

[102] K. Kato, K. Igarashi, M. Masuda, K. Otsubo, A. Yasuda, K. Takeda, and T. Sato, “Development of engine for natural gas vehicle,” *SAE Transactions*, vol. 108, pp. 939–947, 1999.

[103] R. L. Evans, F. Goharian, and P. G. Hill, “The performance of a spark-ignition engine fuelled with natural gas and gasoline,” in *SAE Technical Paper*, SAE International, 02 1984.

[104] C. Bach, C. Lämmle, R. Bill, P. Soltic, D. Dyntar, P. Janner, K. Boulouchos, C. Onder, T. Landenfeld, L. Kercher, O. Seel, and J. D. Baronick, “Clean engine vehicle a natural gas driven Euro-4/SULEV with 30% reduced CO_2 emissions,” in *SAE Technical Paper*, SAE International, 03 2004.

[105] J. Hall, M. Bassett, B. Hibberd, and S. Streng, “Heavily downsized demonstrator engine optimised for CNG operation,” *SAE International Journal of Engines*, vol. 9, no. 4, pp. 2250–2261, 2016.

[106] J. Lee, C. Park, J. Bae, Y. Kim, S. Lee, and C. Kim, “Comparison between gasoline direct injection and compressed natural gas port fuel injection under maximum load condition,” *Energy*, vol. 197, p. 117173, 2020.

[107] T. Kar and A. K. Agarwal, “Development of a single cylinder CNG direct injection engine and its performance, emissions and combustion characteristics,” *International Journal of Oil, Gas and Coal Technology*, vol. 10, no. 2, pp. 204–220, 2015.

[108] S. S. Thipse, S. B. Sonawane, A. F. D. Souza, S. D. Rairikar, K. K. Kavathekar, and N. V. Marathe, “Injection strategies, optimization and simulation techniques on DI CNG technology,” in *SAE Technical Paper*, SAE International, 01 2015.

[109] P. Zoldak and J. Naber, “Spark ignited direct injection natural gas combustion in a heavy duty single cylinder test engine - start of injection and spark timing effects,” in *SAE Technical Paper*, SAE International, 09 2015.

[110] M. Baratta, D. Misul, J. Xu, A. Fuerhapter, R. Heindl, C. Peletto, J. Preuhs, and P. Salemi, "Development of a high performance natural gas engine with direct gas injection and variable valve actuation," *SAE International Journal of Engines*, vol. 10, no. 5, pp. 2535–2551, 2017.

[111] J. Sevik, M. Pamminger, T. Wallner, R. Scarcelli, R. Reese, A. Iqbal, B. Boyer, S. Wooldridge, C. Hall, and S. Miers, "Performance, efficiency and emissions assessment of natural gas direct injection compared to gasoline and natural gas port-fuel injection in an automotive engine," *SAE International Journal of Engines*, vol. 9, no. 2, pp. 1130–1142, 2016.

[112] D. Seboldt, D. Lejsek, and M. Bargende, "Studies on the influence of the start of injection and the direction of injection on the mixture formation and combustion on a gasoline engine with CNG direct injection," in *IAV Conference*, 2015.

[113] J. Song, M. Choi, D. Kim, and S. Park, "Combustion characteristics of methane direct injection engine under various injection timings and injection pressures," *Journal of Engineering for Gas Turbines and Power*, vol. 139, no. 8, 2017.

[114] J. Song, T. Kim, J. Jang, and S. Park, "Effects of the injection strategy on the mixture formation and combustion characteristics in a DISI (direct injection spark ignition) optical engine," *Energy*, vol. 93, pp. 1758–1768, 2015.

[115] A. R. A Aziz, F. Firmansyah, and R. S. Raja Shahzad, "Combustion analysis of a CNG direct injection spark ignition engine," *International Journal of Automotive and Mechanical Engineering (IJAME)*, vol. 2, pp. 157–170, 2010.

[116] C. Weber, U. Kramer, R. Friedfeldt, H. Ruhland, and F. Krämer, "Development of a new combustion engine dedicated to methane operation," in *39th International Vienna Motor Symposium, Vienna*, 2018.

[117] T. W. Ryan and S. S. Lestz, "The laminar burning velocity of isooctane, n-heptane, methanol, methane, and propane at elevated temperature and pressures in the presence of a diluent," *SAE Transactions*, vol. 89, pp. 652–664, 1980.

[118] N. Ozdor, M. Dulger, and E. Sher, "Cyclic variability in spark ignition engines a literature survey," *SAE Transactions*, vol. 103, pp. 1514–1552, 1994.

[119] G. R. Neame, D. P. Gardiner, R. W. Mallory, V. K. Rao, M. F. Bardon, and V. Battista, "Improving the fuel economy of stoichiometrically fuelled SI engines by means of EGR and enhanced ignition - a comparison of gasoline, methanol and natural gas," *SAE Transactions*, vol. 104, pp. 1062–1076, 1995.

[120] S. K. Chen and N. J. Beck, "Gas engine combustion principles and applications," in *SAE Technical Paper*, SAE International, 08 2001.

[121] L. H. Borges, C. Hollnagel, and W. Muraro, "Development of a Mercedes-Benz natural gas engine M 366 LAG, with a lean burn combustion system," in *SAE Technical Paper*, SAE International, 10 1996.

[122] D. S.-K. Ting and M. D. Checkel, "The effects of turbulence of spark-ignited, ultra lean, premixed methane-air flame growth in a combustion chamber," in *SAE Technical Paper*, SAE International, 10 1995.

[123] P. Soltic, T. Hilfiker, S. Hänggi, R. Hutter, M. Weissner, A. Volkswagen, and A. Konzernforschung, "Ignition and combustion concepts for lean operated passenger car natural gas engines," *Sustain. Altern., FKFS, Stuttgart*, 2017.

[124] D. R. Lancaster, R. B. Krieger, S. C. Sorenson, and W. L. Hull, "Effects of turbulence on spark-ignition engine combustion," *SAE Transactions*, vol. 85, pp. 689–710, 1976.

[125] Y. Liu and B. Lenze, "The influence of turbulence on the burning velocity of premixed CH_4-H_2 flames with different laminar burning velocities," in *Symposium (International) on Combustion*, vol. 22, pp. 747–754, Elsevier, 1989.

[126] H. M. Cho and B.-Q. He, "Spark ignition natural gas engines—a review," *Energy conversion and management*, vol. 48, no. 2, pp. 608–618, 2007.

[127] W. Pulkrabek, *Engineering Fundamentals of the Internal Combustion Engine.* Prentice Hall, 1997.

[128] V. Ganeshan, *Internal Combustion Engines.* Tata McGraw Hill, 2012.

[129] D. Seboldt, D. Lejsek, and M. Bargende, “Injection strategies for low HC raw emissions in SI engines with CNG direct injection,” *Automotive and Engine Technology*, vol. 1, no. 1-4, pp. 81–91, 2016.

[130] *Worldwide emission standards for passenger cars and lightduty vehicles,” Delphi tech. rep., 2016-17.*

[131] R. L. Evans and J. Blaszczyk, “A comparative study of the performance and exhaust emissions of a spark ignition engine fuelled by natural gas and gasoline,” *Proceedings of the Institution of Mechanical Engineers, Part D: Journal of Automobile Engineering*, vol. 211, no. 1, pp. 39–47, 1997.

[132] R. Tilagone and S. Venturi, “Development of natural gas demonstrator based on an urban vehicle with a down-sized turbocharged engine,” *Oil and gas science and technology*, vol. 59, no. 6, pp. 581–591, 2004.

[133] A. E. Catania, S. d’Ambrosio, A. Mittica, and E. Spessa, “Experimental investigation of fuel consumption and exhaust emissions of a 16V pent-roof engine fueled by gasoline and CNG,” *SAE Transactions*, vol. 110, pp. 1213–1233, 2001.

[134] M. Frailey, P. Norton, N. N. Clark, and D. W. Lyons, “An evaluation of natural gas versus diesel in medium-duty buses,” in *SAE Technical Paper*, SAE International, 10 2000.

[135] P. L. Mtui and P. G. Hill, “Ignition delay and combustion duration with natural gas fueling of diesel engines,” in *SAE Technical Paper*, SAE International, 10 1996.

[136] K. G. Darrow, “Light duty vehicle full fuel cycle emissions analysis,” tech. rep., Energy International, Inc., Bellevue, WA (United States), 1994.

[137] U. Kramer and K. Dylong, “Development of a C-segment vehicle dedicated to methane operation,” in *Gas Powered Vehicles Congress*, 2019.

[138] Y. Sakai, H. Mtyazaki, and K. Mukai, “The effect of combustion chamber shape on nitrogen oxides,” *SAE International*, 1973.

[139] M. Ferrera and S. Zandiri, “Assessment of combustion system development,” tech. rep., InGAS, 2011.

[140] M. Ferrera, “Boundary definition for aftertreatment,” tech. rep., InGas, 2008.

[141] E. Schwarzer, “Investigation of mechanisms of catalytic methane reduction,” tech. rep., FVV Project, 2014.

[142] D. Engler, K. Glück, E. Lox, and A. Schäfer-Sindlinger, “Catalyst development for stoichiometric and lean burn natural gas engines,” in *Proceedings of the Seminar on Gas engines for Cogeneration, I MECH E*, pp. 19–27, 1993.

[143] J. Lapetz, D. McCarthy, N. Greenfield, R. Czapski, T. Geftos, J. Rosson, S. Couture, B. Nelson, R. Schaefer, R. Klein, and P. Kuechler, “Development of the Ford QVM CNG Bi-fuel 4.9L F-series pickup truck,” in *SAE Technical Paper*, SAE International, 02 1996.

[144] S. Phillipi, “DI CNG injector,” Tech. Rep. EP 3 153 693 A1, Continental Automotive, 2017.

[145] D. Rogers, *Engine Combustion: Pressure Measurement and Analysis.* SAE International, 2010.

[146] Z. Zhou, *The Significance of Research and Motor Octane Numbers to Anti-Knock Performance and Fuel Efficiency of Modern Spark-Ignition Engines.* PhD thesis, The University of Melbourne, 2020.

[147] K. Kim and K. Kruger, “Optimization of in-cylinder pressure filter for engine research,” tech. rep., Vehicle Technology Directorate, ARL, 2017.

[148] T. Foong, *On the Autoignition of Ethanol/Gasoline Blends in Spark-Ignition Engines.* PhD thesis, The University of Melbourne, 2013.

[149] P. Dennis, *A Study of the Performance of Hydrogen Fueled Internal Combustion Engines and Vehicles.* PhD thesis, The University of Melbourne, 2015.

[150] *AutoGas Five Gas Analyzer, User Manual version 1.31, AUTO TEST Pty. Ltd.*

[151] *GT-Suite Engine Performance Application Manual, Gamma Technologies, 2018.*

[152] *GT-Suite Engine Performance Tutorials, Gamma Technologies.*

[153] *GEM3D Tutorials - Building an Intake Manifold from an STL File, Gamma Technologies.*

[154] G. M. Rassweiler and L. Withrow, "Motion pictures of engine flames correlated with pressure cards," *SAE Transactions*, vol. 33, pp. 185–204, 1938.

[155] T. Morel and R. Keribar, "A model for predicting spatially and time resolved convective heat transfer in bowl-in-piston combustion chambers," *SAE Transactions*, vol. 94, pp. 77–93, 1985.

[156] B. Milton and J. Keck, "Laminar burning velocities in stoichiometric hydrogen and hydrogen-hydrocarbon gas mixtures," *Combustion and Flame*, vol. 58, no. 1, pp. 13–22, 1984.

[157] *GT-SUITE Optimization Manual, Version 2018, Gamma Technologies.*

[158] P. Orbaiz and M. Brear, "Energy balance of a spark ignition engine running on hydrogen, synthesis gas and natural gas," in *SAE Technical Paper*, SAE International, 04 2014.

[159] P. A. Atibeh, P. A. Dennis, P. J. Orbaiz, M. J. Brear, and H. C. Watson, "Lean burn performance of a natural gas fuelled, port injected, spark ignition engine," in *SAE Technical Paper*, SAE International, 04 2012.

[160] C. change group, "Global warming potentials - IPCC fourth assessment report," tech. rep., United Nations, 2019.

[161] G. Lammel and H. Graßl, "Greenhouse effect of NO_X," *Environmental Science and Pollution Research*, vol. 2, no. 1, pp. 40–45, 1995.

[162] R. R. Raine, G. Zhang, and A. Pflug, "Comparison of emissions from natural gas and gasoline fuelled engines - total hydrocarbon and methane emissions and exhaust gas recirculation effects," in *SAE Technical Paper*, SAE International, 02 1997.

[163] E. Hu, Z. Huang, B. Liu, J. Zheng, and X. Gu, "Experimental study on combustion characteristics of a spark-ignition engine fueled with natural gas–hydrogen blends combining with EGR," *International journal of hydrogen energy*, vol. 34, no. 2, pp. 1035–1044, 2009.

[164] J. M. Luján, H. Climent, R. Novella, and M. E. Rivas-Perea, "Influence of a low pressure EGR loop on a gasoline turbocharged direct injection engine," *Applied Thermal Engineering*, vol. 89, pp. 432–443, 2015.

[165] G. Andrews and D. Bradley, "The burning velocity of methane-air mixtures," *Combustion and Flame*, vol. 19, no. 2, pp. 275–288, 1972.

[166] L. Manofsky, J. Vavra, D. N. Assanis, and A. Babajimopoulos, "Bridging the gap between HCCI and SI: Spark-assisted compression ignition," in *SAE Technical Paper*, SAE International, 04 2011.

[167] H. B.-Q. Cho Haeng Muk, "Combustion and emission characteristics of a natural gas engine under different operating conditions," *Environmental Engineering Research*, vol. 14, no. 2, pp. 95–101, 2009.

[168] A. Ibrahim and S. Bari, "A comparison between EGR and lean-burn strategies employed in a natural gas SI engine using a two-zone combustion model," *Energy Conversion and Management*, vol. 50, no. 12, pp. 3129–3139, 2009.

[169] J. A. Caton, "A comparison of lean operation and exhaust gas recirculation: Thermodynamic reasons for the increases of efficiency," in *SAE Technical Paper*, SAE International, 04 2013.

[170] S. Pischinger and J. B. Heywood, "A model for flame kernel development in a spark-ignition engine," in *Symposium (international) on Combustion*, vol. 23, pp. 1033–1040, Elsevier, 1991.

[171] V. B. Pedrozo, I. May, T. D. Lanzanova, and H. Zhao, "Potential of internal EGR and throttled operation for low load extension of ethanol–diesel dual-fuel reactivity controlled compression ignition combustion on a heavy-duty engine," *Fuel*, vol. 179, pp. 391–405, 2016.

[172] M. Jankovic and S. W. Magner, "Variable cam timing: Consequences to

automotive engine control design," *IFAC Proceedings Volumes*, vol. 35, no. 1, pp. 271–276, 2002.

[173] S. Szwaja, E. Ansari, S. Rao, M. Szwaja, K. Grab-Rogalinski, J. D. Naber, and M. Pyrc, "Influence of exhaust residuals on combustion phases, exhaust toxic emission and fuel consumption from a natural gas fueled spark-ignition engine," *Energy Conversion and Management*, vol. 165, pp. 440–446, 2018.

Appendices

Appendix A

Calculation procedure

A.1 Burn parameter based on 'Rassweiler and Withrow' method

The calculation procedure for the burn rate and related parameters based on 'Rassweiler and Withrow' method [37, 154] are as follows:

1. Selection of crank angle resolved representative in-cylinder pressure data, positions of intake valve closing (IVC), exhaust valve opening (EVO), and ignition timing.

2. Estimation of the end of combustion (EOC) position, which is the crank angle at which the first derivative of pressure with crank angle is zero (i.e., $\frac{dP}{d\theta} \approx 0$).

3. Calculation of compression index, n_{com} and expansion index, n_{exp} based on the linear regression fit using pressure and volume data from IVC to spark and from EOC to EVO, respectively.

4. Calculation of combustion polytropic index, n_c over the crank angle duration from spark to EOC using Eq. A.1.1.

$$n_c(i) = n_{com} + [\theta(i) - \theta_{spark}] * \frac{n_{exp} - n_{com}}{\theta_{EOC} - \theta_{spark}}. \tag{A.1.1}$$

5. Estimation of the pressure rise (ΔP_c) due to combustion and then the mass

fraction burned (x_b) at the end of the i^{th} crank angle using the following Eqs. A.1.2 and A.1.3, respectively. This will provide the crank angle location of 50% MFB and 10-90% MFB duration.

$$\Delta P_c(i) = \left[P(i+1) - P(i) * \left(\frac{V(i)}{V(i+1)} \right)^{n_c(i)} \right] * \frac{V(i)}{V_{clearence}}. \tag{A.1.2}$$

$$x_b(i) = \frac{m_b(i)}{m_b(total)} = \frac{\sum\limits_{Spark}^{i} \Delta P_c(i)}{\sum\limits_{Spark}^{EOC} \Delta P_c(i)}. \tag{A.1.3}$$

6. Finally, the curve fitting of estimated burn profile in the following Wiebe function Eq. A.1.4 to obtain the Wiebe exponent, m.

$$x_b = 1 - e^{\left[-a \left(\frac{\theta(i) - \theta_{spark}}{\theta_{total}} \right)^{m+1} \right]}. \tag{A.1.4}$$

Appendix B

Additional experimental results

B.1 Effect of different turbomachinery control modes

The effectiveness of two turbomachinery control modes mentioned in Section 3.2.3 is examined at 1500 RPM over the loads ranging from 5 to 8.2 bar BMEP using excess air diluent and maintaining MAP of 1 atm. Two control modes are: Mode 1 corresponding to normal turbomachinery operation with factory settings, and Mode 2 representing turbomachinery operation with a fully open wastegate. Fig. B.1 shows the operating λ and BTE for both Mode 1 and Mode 2 over the loads, where Mode 2 allows higher λ for a given load, resulting in improved BTE than Mode 1.

Furthermore, as shown in Fig. B.2, higher exhaust gas pressure and temperature are measured downstream of the turbomachinery with Mode 2 operation relative to Mode 1 as exhaust gas enthalpy is not utilized by the turbine in Mode 2 due to the fully open wastegate operation.

The increased $\mathrm{Pr}_{Exhaust}$ can be helpful to recirculate the exhaust gas back into the intake system during EGR dilute operation. In addition, higher EGT can be beneficial for catalytic converter. This indicates that the Mode 2 operation is more effective than the Mode 1 at part load. Note that the engine operation with Mode 2 is applicable over the range of part load if the boosting is not mandatory.

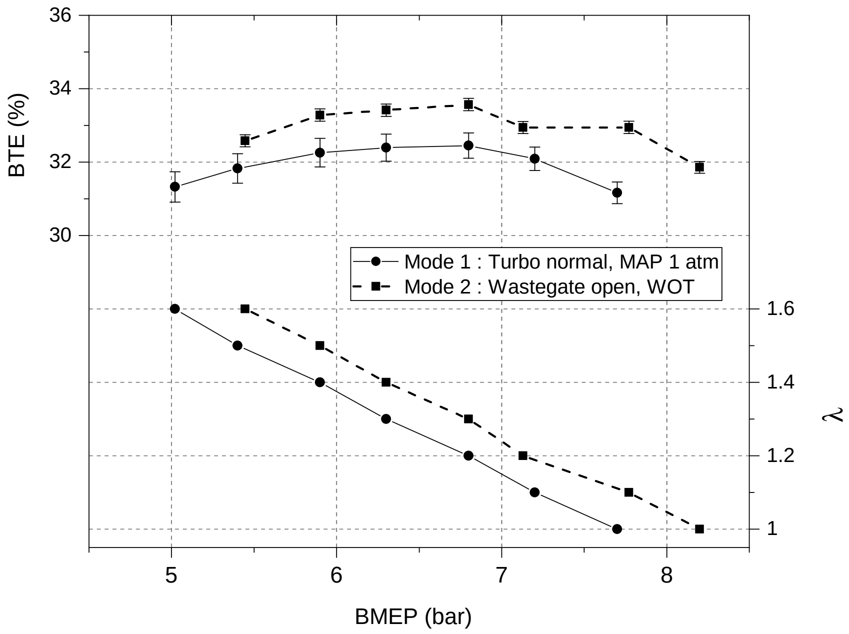

Figure B.1: Comparison of λ and corresponding BTE over the range of part load at 1500 RPM for two different turbomachinery control modes.

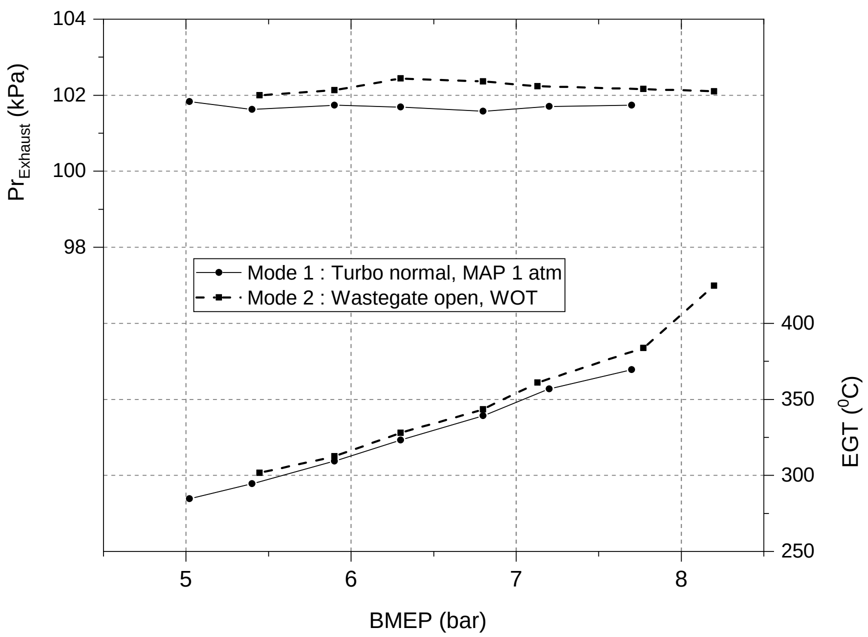

Figure B.2: Comparison of exhaust pressure ($\mathrm{Pr}_{Exhaust}$) and exhaust gas temperature (EGT) over the range of part load with excess air dilution at 1500 RPM for two different turbomachinery control modes.

B.2 Effect of injection timing with dilute operation

The effect of the start of injection timing on engine performance for dilute operation are examined over a range of part load at 1500 RPM with two different SOI of 240 and 280 deg bTDC$_{Fire}$. The two SOI examined here are from the range of injection timings that yielded optimal engine performance at part load for stoichiometric DI CNG operation. Figure B.3 shows that both the SOI timings demonstrate a similar brake thermal efficiency for a given λ under the same part load. This indicates that the variation of λ has minimal influence on the impact of SOI.

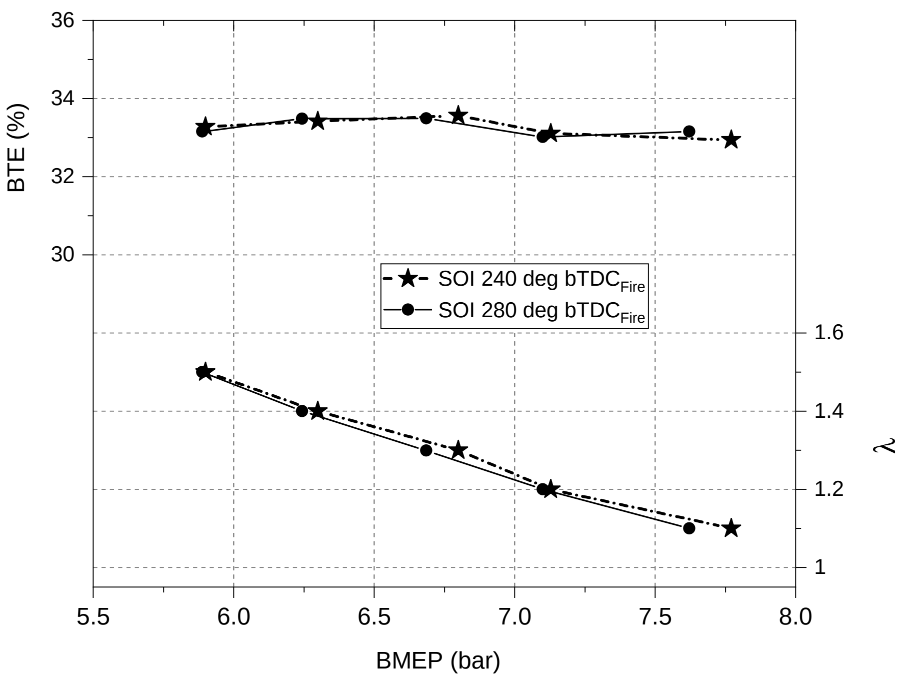

Figure B.3: Comparison of BTE and corresponding λ over the part loads at 1500 RPM for two different start of injection (SOI) timings with CNG fuelling.

Appendix C

Technical Drawing

C.1 Engine Mounting

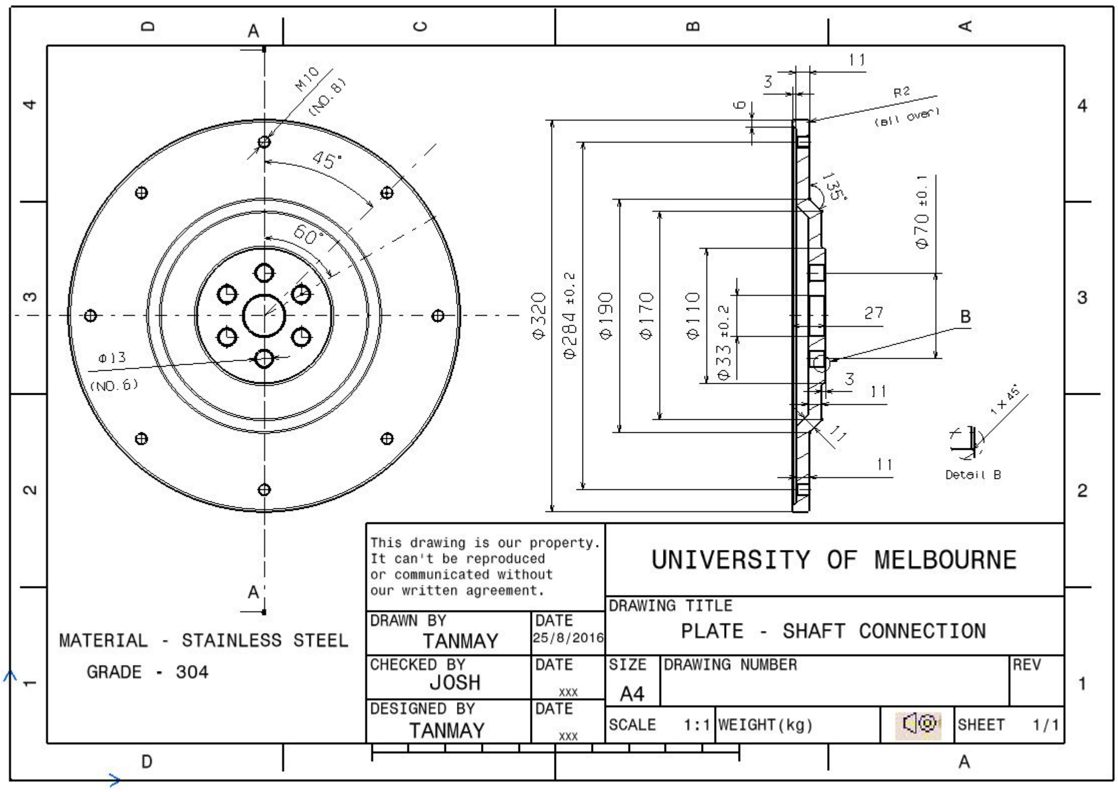

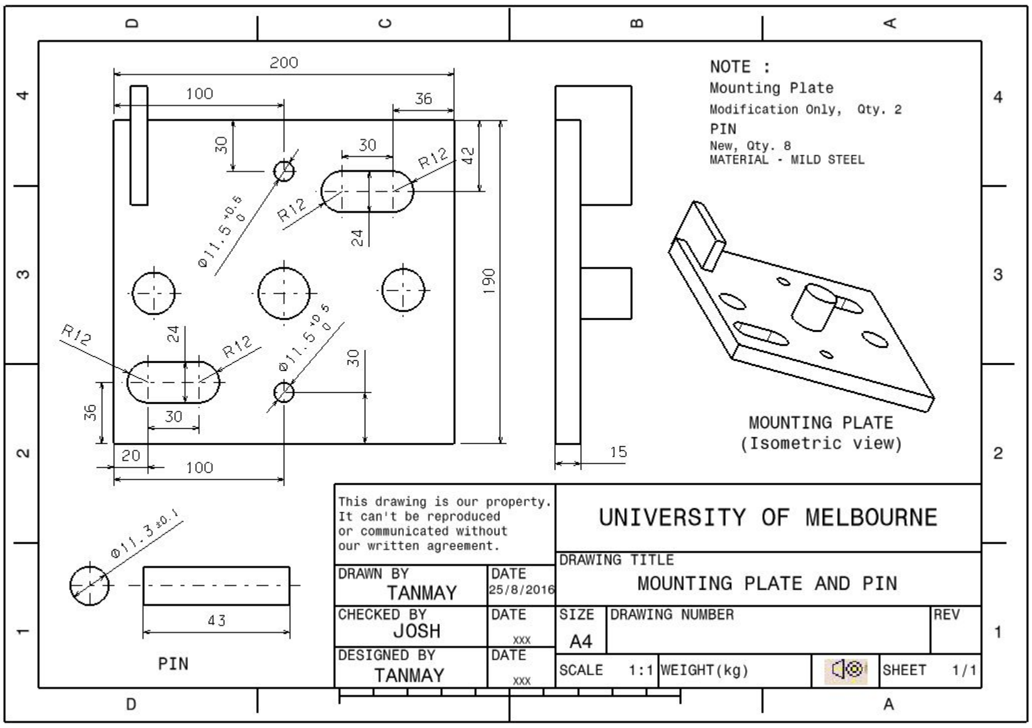
NOTE :
Mounting Plate
Modification Only, Qty. 2
PIN
New, Qty. 8
MATERIAL - MILD STEEL
MOUNTING PLATE
(Isometric view)
PIN
This drawing is our property.
It can't be reproduced
or communicated without
our written agreement.
UNIVERSITY OF MELBOURNE
DRAWING TITLE
MOUNTING PLATE AND PIN
DRAWN BY
TANMAY
DATE
25/8/2016
CHECKED BY
JOSH
DATE
xxx
DESIGNED BY
TANMAY
DATE
xxx
SIZE
A4
DRAWING NUMBER
REV
SCALE 1:1
WEIGHT(kg)
SHEET 1/1

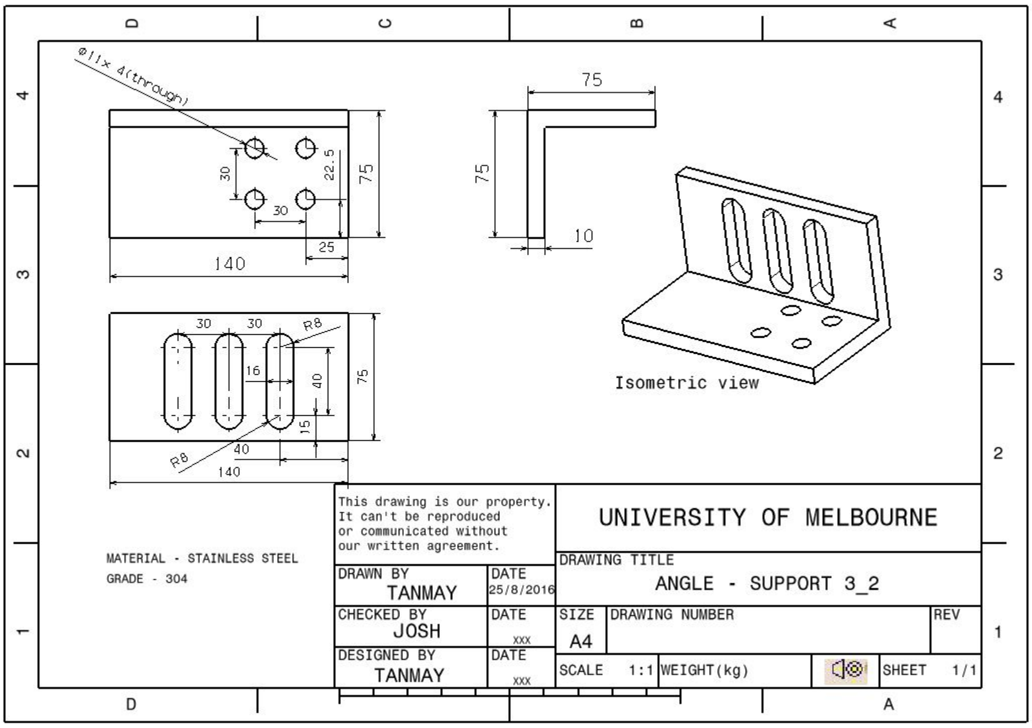
Ø11x 4(through)
Isometric view
MATERIAL - STAINLESS STEEL
GRADE - 304
This drawing is our property.
It can't be reproduced
or communicated without
our written agreement.
UNIVERSITY OF MELBOURNE
DRAWING TITLE
ANGLE - SUPPORT 3_2
DRAWN BY
TANMAY
DATE
25/8/2016
CHECKED BY
JOSH
DATE
xxx
DESIGNED BY
TANMAY
DATE
xxx
SIZE
A4
DRAWING NUMBER
REV
SCALE 1:1
WEIGHT(kg)
SHEET 1/1

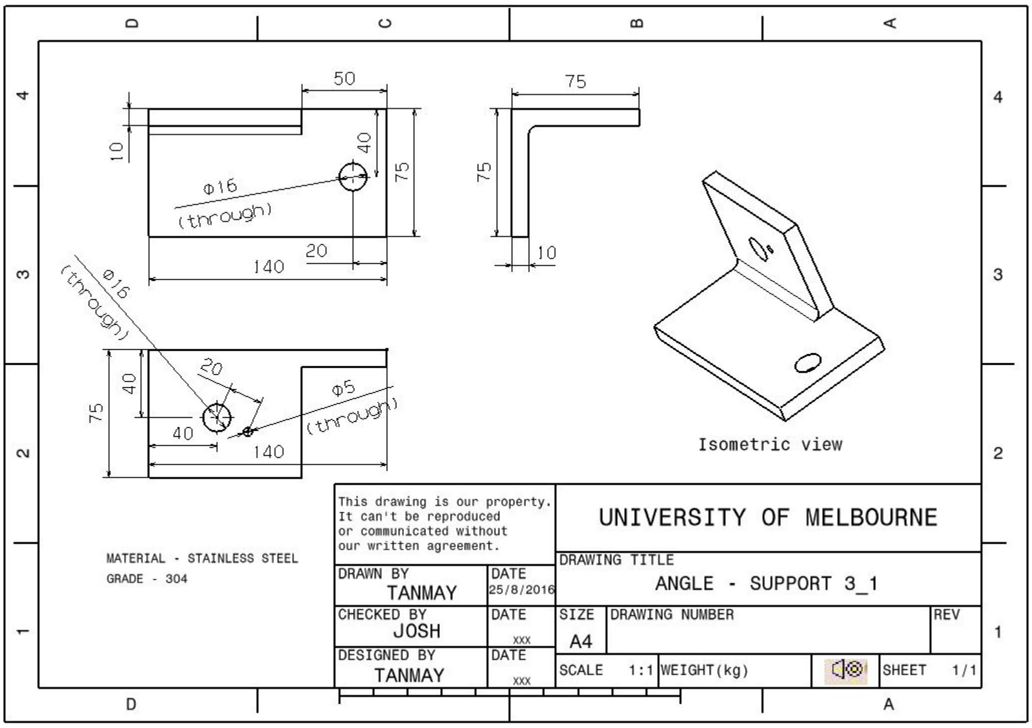
50
10
40
Φ16
(through)
75
140
20
75
75
10
Φ16
(through)
20
40
75
40
Φ5
(through)
140
Isometric view
MATERIAL - STAINLESS STEEL
GRADE - 304
This drawing is our property. It can't be reproduced or communicated without our written agreement.
UNIVERSITY OF MELBOURNE
DRAWING TITLE
ANGLE - SUPPORT 3_1
DRAWN BY TANMAY
DATE 25/8/2016
CHECKED BY JOSH
DATE xxx
DESIGNED BY TANMAY
DATE xxx
SIZE A4
DRAWING NUMBER
REV
SCALE 1:1
WEIGHT(kg)
SHEET 1/1

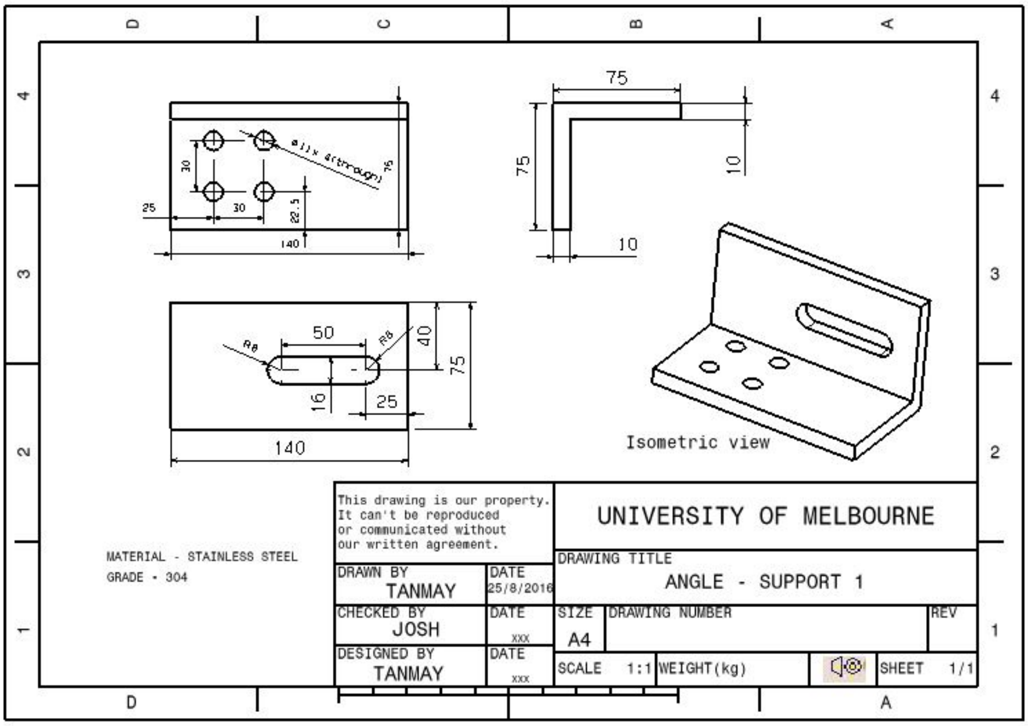
75
10
75
10
30
25
30
22.5
140
50
R8
R8
40
75
16
25
140
Isometric view
MATERIAL - STAINLESS STEEL
GRADE - 304
This drawing is our property. It can't be reproduced or communicated without our written agreement.
UNIVERSITY OF MELBOURNE
DRAWING TITLE
ANGLE - SUPPORT 1
DRAWN BY TANMAY
DATE 25/8/2016
CHECKED BY JOSH
DATE xxx
DESIGNED BY TANMAY
DATE xxx
SIZE A4
DRAWING NUMBER
REV
SCALE 1:1
WEIGHT(kg)
SHEET 1/1

C.2 DI CNG Injector drawing